11A

DOE/ET/34215-29
PNL-4337

UC-78

Fuel Performance Improvement Program

Power-Ramp Testing and Postirradiation Examination of PCI-Resistant LWR Fuel Rod Designs

September 1982

Consumers
Power
Company

EXXON NUCLEAR
COMPANY, Inc.

Battelle
Pacific Northwest Laboratory

DISCLAIMER

Work on this program is performed for the
UNITED STATES DEPARTMENT OF ENERGY
by
CONSUMERS POWER COMPANY and EXXON NUCLEAR COMPANY, INC.
Under Contract DE-AC02-76ET34215
and by
PACIFIC NORTHWEST LABORATORY, *Operated by* BATTELLE MEMORIAL INSTITUTE;
Under Contract DE-AC06-76RLO 1830

Printed in the United States of America
Available from
National Technical Information Service
United States Department of Commerce
5285 Port Royal Road
Springfield, Virginia 22151

NTIS Price Codes
Microfiche A01

Printed Copy

Pages	Price Codes
001-025	A02
026-050	A03
051-075	A04
076-100	A05
101-125	A06
126-150	A07
151-175	A08
176-200	A09
201-225	A010
226-250	A011
251-275	A012
276-300	A013

DOE/ET/34215-29
PNL-4337
UC-78

FUEL PERFORMANCE IMPROVEMENT PROGRAM

Power-Ramp Testing and Postirradiation Examination of PCI-Resistant LWR Fuel Rod Designs

September 1982

J. O. Barner
R. J. Guenther

Pacific Northwest Laboratory
Richland, WA 99352

This report was prepared for the Department of Energy by Pacific Northwest Laboratory, operated by Battelle Memorial Institute, under Contract DE-AC06-76RLO 1830

ACKNOWLEDGMENTS

This report summarizes work conducted for the U.S. Department of Energy (DOE) through the joint efforts of Consumers Power Company (CPC) and Exxon Nuclear Company, Inc. (ENC), under Contract DE-AC02-76ET34215 and Pacific Northwest Laboratory (PNL) under Contract DE-AC06-76RLO 1830. The authors acknowledge the support and guidance of the following people: P. M. Lang, DOE; A. S. Mehner, DOE; F. W. Buckman, CPC; and G. F. Pratt, CPC.

C. E. Crouthamel (ENC), K. N. Woods (ENC), and M. D. Fresnley (PNL) provided program direction. The contributions of R. K. Welty and his colleagues at ENC for rod design and fabrication are also acknowledged. Appreciation is also extended to A. Hanevik of the Institutt for Energiteknikk (IFE), Halden, Norway, and especially to R. W. Miller(a) and A. D. Appelhans,(a) the U.S. Nuclear Regulatory Commission (NRC) representatives at Halden, for assistance in test design, irradiation testing, nondestructive examinations, and data handling. The assistance of J. B. Rich and D. J. Clough of the United Kingdom Atomic Energy Authority (UKAEA), Harwell, England, during the post-irradiation examination is gratefully acknowledged.

The authors also appreciate the assistance of the technical editor, S. K. Edler, and the data and graphics technical specialist, W. D. Bennett.

(a) On assignment to IFE from EG&G Idaho, Inc., Idaho Falls, Idaho.

ACKNOWLEDGMENTS

This report summarizes work conducted for the U.S. Department of Energy (DOE) through the joint efforts of Consumers Power Company (CPC) and Exxon Nuclear Company, Inc. (ENC), under Contract DE-AC02-76NE18215 and Pacific Northwest Laboratory (PNL) under Contract DE-AC06-76RLO 1830. The authors acknowledge the support and guidance of the following people: R. M. Lang, USDOE; S. Mehner, USDOE; F. W. Buckman, CPC; and J. E. Pratt, CPC.

C. E. Crouthamel (ENC), K. R. Woods (ENC), and M. D. Freshley (PNL) provided program direction. The contributions of R. K. Welty and his colleagues at ENC for rod design and fabrication are also acknowledged. Appreciation is also extended to A. Hanevik of the Institutt for Energiteknikk (IFE), Halden, Norway, and especially to R. W. Miller(a) and A. D. Appelhans,(a) the U.S. Nuclear Regulatory Commission (NRC) representatives at Halden, for assistance in test design, irradiation testing, nondestructive examinations, and data handling. The assistance of J. B. Rich and D. J. Clough of the United Kingdom Atomic Energy Authority (UKAEA), Harwell, England, during the post-irradiation examination is gratefully acknowledged.

The authors also appreciate the assistance of the technical editor, S. K. Edler, and the data and graphics technical specialist, W. D. Bennett.

(a) On assignment to IFE from EG&G Idaho, Inc., Idaho Falls, Idaho.

ABSTRACT

This report describes the power-ramp testing results from 10 fuel rods irradiated in the Halden Boiling Water Reactor (HBWR), Halden, Norway. The work is part of the Fuel Performance Improvement Program (FPIP), which is sponsored by the U.S. Department of Energy (DOE) and is conducted through the joint efforts of Consumers Power Company, Exxon Nuclear Company, Inc., and Pacific Northwest Laboratory. The objective of the FPIP is to identify and demonstrate fuel concepts with improved pellet-cladding interaction (PCI) behavior that will be capable of extended burnup. The postirradiation examination results obtained from one nonramped rod are also presented. The power-ramping behavior of three basic fuel rod types--rods with annular-pellet fuel, sphere-pac fuel, and dished-pellet (reference) fuel--are compared in terms of mechanisms known to promote PCI failures. The effects of graphite coating on the inside cladding surface and helium pressurization in rods with annular fuel are also evaluated.

ABSTRACT

This report describes the power-ramp testing results from 10 fuel rods irradiated in the Halden Boiling Water Reactor (HBWR), Halden, Norway. The work is part of the Fuel Performance Improvement Program (FPIP), which is sponsored by the U.S. Department of Energy (DOE) and is conducted through the joint efforts of Consumers Power Company, Exxon Nuclear Company, Inc., and Pacific Northwest Laboratory. The objective of the FPIP is to identify and demonstrate fuel concepts with improved pellet-cladding interaction (PCI) behavior that will be capable of extended burnup. The postirradiation examination results obtained from one nonramped rod are also presented. The power-ramping behavior of three basic fuel rod types--rods with annular-pellet fuel, sphere-pac fuel, and dished-pellet (reference) fuel--are compared in terms of mechanisms known to promote PCI failures. The effects of graphite coating on the inside cladding surface and helium pressurization in rods with annular fuel are also evaluated.

SUMMARY

The Fuel Performance Improvement Program (FPIP) has the objectives of: 1) developing advanced light-water reactor (LWR) fuel rod designs with improved pellet-cladding interaction (PCI) failure resistance and 2) providing the technical support needed to design and license lead test assemblies of these concepts for irradiation in commercial LWRs. The FPIP is conducted for the U.S. Department of Energy (DOE) through the joint efforts of Consumers Power Company, Exxon Nuclear Company, Inc., and Pacific Northwest Laboratory. The advanced fuel rod designs incorporate 1) annular fuel pellets with and without graphite coating on the inside cladding surface and helium pressurization and 2) sphere-pac fuel with helium pressurization. The pressurization level in the pressurized rods was 0.45 MPa (4.5 atm). Fuel rods with standard solid pellets and a pressurization level of 0.10 MPa (1 atm) are included for comparison.

Results from power-ramp testing in the Halden Boiling Water Reactor (HBWR) of 10 irradiated fuel rods and the postirradiation examination (PIE) of these rods and one nonramped rod are reported and compared in terms of PCI resistance. Although none of the fuel rods failed during the power-ramp testing to maximum linear heat generation rates (LHGRs) of ~70 kW/m, fuel rod elongation measurements obtained from nine rods and an internal rod pressure measurement from one rod provided PCI-related performance data. Information required to determine the LHGR and its axial distribution as a function of testing time was also collected. PIE data consisted of visual, eddy-current, diametral, neutron radiographic, gross gamma scanning, spectral gamma scanning, fission gas release, ceramographic, burnup, and scanning electron microscope examinations.

The most significant results from the power-ramp testing and PIE are summarized as follows:

- During power-ramping, the maximum axial stress levels in the cladding of rods containing annular fuel pellets were lower than in the rods with reference fuel. Permanent axial elongation of the cladding occurred in only one of four rods with annular fuel but occurred in all three reference rods that were tested.

- At the terminal LHGR, the axial stress in rods containing annular fuel was relieved rapidly by plastic deformation of the hot central portion of the fuel.
- The cladding hoop stress during power-ramping of rods with annular fuel was low compared with rods with reference fuel.
- The presence of a graphite coating on the inside cladding surface apparently had little effect on the general stress condition in the cladding of rods containing annular fuel. However, the graphite coating apparently acted as a barrier to fission products in terms of accessibility to the cladding surface.
- The fission gas release during power-ramping of rods with annular fuel was slightly higher than for reference rods due to the formation of a midradius crack that acted as a heat transfer barrier in the annular pellets.
- During power-ramping, while the maximum axial stresses in the cladding were less in the sphere-pac rods than in the reference rods, the hoop stresses were comparable. The resultant stress condition in the sphere-pac rods caused permanent shortening of the cladding in one of two rods tested. Permanent diametral deformation of the cladding was indicated in the sphere-pac rod that underwent permanent shortening and in all three reference rods.
- For sphere-pac and reference rods power-ramped to the same LHGR, the fission gas release and the implied fuel temperatures were lower for the sphere-pac rods than for the reference rods.

CONTENTS

FIGURES

TABLES

CONVERSION TABLE FOR U.S. CUSTOMARY TO SI UNITS(a)

	To convert from	to	Use the equation
Temperature	degree Fahrenheit (°F)	degree Celsius (°C)	$°C = (°F - 32)/1.8$
	degree Fahrenheit (°F)	Kelvin (K)	$K = (°F + 459.67)/1.8$
	degree Celsius (°C)	Kelvin (K)	$K = °C + 273.15$

	To convert from	to	Multiply by
Time	hour (h)	second (s)	3.600×10^{3}
	day (d or day)	second (s)	8.640×10^{4}
Length	inch (in.)	meter (m)	2.540×10^{-2}
Area	inch^2 (in.^{2})	meter^2 (m^2)	6.452×10^{-4}
Volume	inch^3 (in.^{3})	meter^3 (m^3)	1.639×10^{-5}
Pound-Mass	lbm	kilogram (kg)	4.536×10^{-1}
Pound-Force	lbf	newton (N)	4.448
Pressure or Stress	psi (lbf/in.^{2})	pascal (Pa)	6.895×10^{3}
Energy	British thermal unit (Btu)	joule (J)	1.055×10^{3}
	calorie (cal)	joule (J)	4.187
	watt-second (W-s)	joule (J)	1.000
Linear Heat Rating	kilowatts/ft (kW/ft)	kilowatts/meter (kW/M)	3.281
Burnup	megawatt-day/kilogram of heavy metal(b) (MWd/kgM)	gigajoule/kg of heavy metal(b) (GJ/kgM)	86.4

Prefix	SI Symbol	Multiplication Factors
tera	T	$1\ 000\ 000\ 000\ 000 = 10^{12}$
giga	G	$1\ 000\ 000\ 000 = 10^{9}$
mega	M	$1\ 000\ 000 = 10^{6}$
kilo	k	$1\ 000 = 10^{3}$
hecto(f)	h	$100 = 10^{2}$
deka(f)	da	$10 = 10^{1}$
deci(f)	d	$0.1 = 10^{-1}$
centi(f)	c	$0.01 = 10^{-2}$
milli	m	$0.001 = 10^{-3}$
micro	µ	$0.000\ 001 = 10^{-6}$
nano	n	$0.000\ 000\ 001 = 10^{-9}$
pico	p	$0.000\ 000\ 000\ 001 = 10^{-12}$
femto	f	$0.000\ 000\ 000\ 000\ 001 = 10^{-15}$
atto	a	$0.000\ 000\ 000\ 000\ 000\ 001 = 10^{-18}$

(a) Conversions are based on ASTM Metric Practice Guide E380-74. The SI prefixes, SI symbols, and associated multiplication factors are given above.

(b) M is normally the SI symbol for mega; an exception in this report is the additional use of M in burnup units to denote heavy metal.

DESCRIPTION OF FUEL ROD TYPES[a]

Fuel Type	Description
Standard	Standard ENC "product-line." Solid, cylindrical, dished-end fuel pellet.
Reference	Solid, cylindrical, dished-end, chamferred-corner (except HBWR Series H-1) fuel pellet.
Annular	Cylindrical, flat-ended, chamferred-corner (except HBWR Series H-1) fuel pellet with a central hole equivalent to 10 vol% of a solid, undished pellet.
Vipac	Packed-particle fuel composed of high-density, angular fuel shards, produced by high-energy pneumatic compaction (Dynapak). The rods are pressurized with 0.45 MPa of helium, except in the HBWR Series H-1, and the lower segments of the BRPR segmented rods.
Sphere-pac	Packed-particle fuel composed of high-density, spherical particles produced by the sol-gel process. The rods are pressurized with 400 to 500 kPa of helium.
Coated-cladding	Cladding coated with Dag 4[b] graphite, except HBWR Series H-1, which utilized Dag 154[b] graphite.
Pressurized	Rods pressurized with 0.45 MPa of helium.
Reference-coated	Reference fuel pellets combined with coated cladding.
Annular-coated	Annular fuel pellets combined with coated cladding.
Reference-pressurized	Reference fuel pellets in a pressurized rod.
Annular-coated-pressurized	Annular fuel pellets combined with coated cladding in a pressurized rod.

(a) All rods are clad with cold-worked and stress-relieved Zircaloy-2 cladding.
(b) Product of Acheson Colloids Corp., Port Huron, Michigan.

1.0 INTRODUCTION

Results from power-ramp testing of 10 fuel rods in the Halden Boiling Water Reactor (HBWR) and the postirradiation examination (PIE) of these rods and one nonramped rod are presented in this report. The work is part of the Fuel Performance Improvement Program (FPIP) and is sponsored by the U.S. Department of Energy (DOE) and performed by Consumers Power Company (CPC), Exxon Nuclear Company, Inc. (ENC), and Pacific Northwest Laboratory (PNL).(a) The objectives of the FPIP are to identify and demonstrate fuel concepts with improved pellet-cladding interaction (PCI) resistance and to provide the supportive technical bases for licensing lead test assemblies of the improved concepts for operation in commercial light-water reactors (LWRs). As a result of improved performance, the fuel concepts being developed are expected to be capable of achieving higher discharge burnups, which will enhance uranium utilization. A complete description of the FPIP and other work accomplished under this program is provided in References 1-3.

A review of the PCI phenomenon(4) and an assessment of design improvements that could result in improved PCI resistance(5) led to the selection of several possible design modifications. The fuel design modifications selected for investigation as part of the FPIP were:

- annular pellets - an annular-pellet design with a central hole equivalent to 10 vol% of a solid, nondished pellet
- coated cladding - an ~6-μm graphite coating applied to the inner surface of the cladding
- pressurization - helium pressurization of 0.45 MPa (4.5 atm) in the sealed fuel rod
- sphere-pac fuel - a packed bed of high-density spherical fuel particles.

Ultimately, a combination of potential improvements consisting of annular fuel, graphite coating, pressurization, and pellet chamfers (the annular-coated-

---

(a) Operated for DOE by Battelle Memorial Institute.

pressurized design) was selected as the primary design to be developed. The combination of spherical fuel particles and pressurization (the sphere-pac design) was chosen as a secondary design. Fuel rods incorporating individual design changes or other combinations, e.g., annular fuel, nonpressurized particle fuel, and annular fuel with graphite-coated cladding, were also included in the testing program. In all cases, a dished, solid pellet (reference) design that was pressurized with 0.10 MPa (1 atm) of helium was included in the program for comparison.

In-reactor experiments have included both steady-state and power-ramp testing of instrumented rods in the HBWR, which is located in Halden, Norway. All of the rods were previously irradiated in the HBWR under steady-state conditions (see References 6 and 7). The results presented in this report were obtained from the power-ramp tests that were conducted after the steady-state irradiations to compare the PCI behavior of the different fuel types. The power-ramp tests included annular, annular-coated, annular-coated-pressurized, sphere-pac, and reference designs. Data are also presented from the PIE of the power-ramped rods and one sphere-pac rod that received only steady-state base irradiation.

2.0 CONCLUSIONS

The following conclusions concerning the power-ramp behavior of the rods are based on in-reactor length measurements and PIE results.

- High cladding stresses in both the axial and hoop directions develop in dished-pellet reference rods during power-ramp testing. The axial stress can be sufficient to cause permanent cladding elongation.
- During power-ramping, the rods with annular fuel, i.e., the annular, annular-coated, and annular-coated-pressurized designs, exhibit significantly less cladding stress in both the axial and hoop directions compared with the reference rods. The cladding stress is primarily axial immediately after achieving the peak ramping linear heat generation rate (LHGR), but the axial stress rapidly decreases by plastic deformation of the hot central portion of the fuel during the peak-power holding period. Rods with annular fuel have much less tendency to permanently elongate during ramping compared with rods with reference fuel.
- During power-ramping, sphere-pac rods develop cladding hoop stresses similar to those in reference rods whereas axial stresses are lower in the sphere-pac rods than in the reference rods. The resulting stress configuration can cause a small amount of permanent cladding shortening.
- No graphite-fuel reaction occurs during the power-ramping of rods with graphite-coated cladding to high LHGRs (~70 kW/m).
- Graphite coating appears to prevent significant amounts of fission products from coming in contact with the cladding.
- The graphite coating does not appear to have any significant effect on the general FCMI behavior of annular fuel during power-ramping.
- Fuel temperatures are lower in sphere-pac rods than in reference rods that were power-ramped to the same LHGR, as evidenced by lower fission gas release and less fuel restructuring.

- The mechanism by which fresh and slightly irradiated sphere-pac rods are conditioned to the previous peak LHGR by the fracturing of small particles and by central fuel sintering is apparently not operative during power-ramping of irradiated sphere-pac rods to higher LHGRs than previously attained.
- During power-ramping to comparable LHGRs, the central fuel temperatures in rods with annular fuel are higher than in rods with sphere-pac and reference fuel due to the formation of a midradius circumferential crack that acts as a heat transfer barrier.

3.0 DESCRIPTION OF EXPERIMENT

3.1 OBJECTIVES

The objectives of the power-ramp tests were to compare the differences in performance limits and general rod behavior between the improved and reference rod designs. Because none of the 10 rods failed during the power-ramp tests in the HBWR, direct comparisons could not be made on a fail/no-fail criterion. Comparisons for this report were therefore based primarily on fuel rod length measurements made during the ramp tests and on nondestructive and destructive PIE.

3.2 FUEL ROD DESIGNS

The basic design characteristics for the rods were based on a standard BWR 8 x 8 fuel rod design. The 10 fuel rods that were power-ramped and the non-ramped sphere-pac rod are identified in Table 1. The cladding for all the rods came from the same lot of 0.902-mm (0.0355-in.) thick cold-worked and stress-relieved tubing. Pellet fuel densities were nominally 95.5% of theoretical density (TD), and the sphere-pac smear density was nominally 87% TD. The annular pellets were flat-ended with a small chamfer and had a central hole equivalent to 10 vol% of a solid pellet. The reference pellets contained dishes on each end with each dish nominally equivalent to 0.5 vol% of a solid pellet. The spheres for the sphere-pac fuel were nominally 1200, 400, and 25 μm in diameter; and sphere densities were >98% TD. Nominal diametral pellet-to-cladding gaps were 0.25 mm (0.010 in.) for the rods containing pellets. The fuel was enriched to 11% ^{235}U to achieve the desired LHGRs. Helium pressurization levels were nominally 0.1 MPa (1 atm) for the annular, annular-coated, and reference rods and nominally 0.45 MPa (4.5 atm) for the annular-coated-pressurized and sphere-pac rods. The graphite coating was nominally 6.4 μm thick; Dag 154[a] was used in the annular-coated rods and Dag 4[a] was used in the annular-coated-pressurized rods.

(a) Dags 4 and 154 are products of the Acheson Colloids Corp., Port Huron, Michigan.

TABLE 1. Fuel Rod Descriptions

Rod Number and Type(a)	Rod Instrumentation(b)	Steady-State Rig No.(c)	Rod-Average Burnup, MWd/kgM(d)	Characterization Report Reference	Steady-State Irradiation Reference
1980 Power-Ramp Tests					
R1 (H1LCR001)	E(T)	517.1	7.1	8	7
R2 (H1LCR002)	E(T)	518.1 (LC)	9.7	8	6
A6 (H1LCA006)	E(T)	518.1 (LC)	10.7	8	6
AC9 (H1LCG009)	E(T)	518.1 (LC)	10.8	8	6
AC10 (H1LCG010)	P	518.1 (LC)	10.6	8	6
S40 (H2SPS040)	E	517.1	7.0	9	7
S41 (H2XXS041)	E(T)	517.1	7.1	9	7
1981 Power-Ramp Tests					
R3 (H1UCR003)	E	518.1 and 518.2 (UC)	14	8	6,12
AC11 (H1LCG011)	E	518.1 and 518.2 (UC)	16	8	6,12
ACP27 (H2UCG027)	E	518.2 (LC)	9 1/2	9	12
Nonramped Rod					
S42 (H2XXS042)	P(T)	517.1	7.1	9	7

(a) R = reference
A = annular
AC = annular-coated
ACP = annular-coated-pressurized
S = sphere-pac.
See fuel rod definitions on p. xx. The rods are identified by a simplified alphanumeric, e.g., AC9. The same rods may be described in other reports by the actual alphanumeric that was engraved on the end plug of each rod, e.g., H1LCG009.

(b) E = elongation sensor
P = pressure sensor
(T) = W/Re thermocouple that operated only during the steady-state irradiation.

(c) 518.1 = instrumented fuel assembly (IFA)-518.1 (first loading)
518.2 = IFA-518.2 (second loading)
517.1 = IFA-517.1 (only steady-state loading)
LC = lower cluster
UC = upper cluster.

(d) Values with decimals are based on burnup analyses. Values without decimals are based on power calculations.

Gas-to-fuel volume ratios were larger in the test rods than in commercial rods to accommodate the fuel rod instrumentation. Nine of the power-ramped rods contained combination elongation/failure detectors (Table 1), while the tenth power-ramped rod and the nonramped sphere-pac rod contained internal pressure sensors. Additional design and fabrication data for the rods are given in the references listed in Table 1.

3.3 STEADY-STATE IRRADIATION SUMMARY

Five of the power-ramped rods were irradiated in the first loading of the IFA-518 test rig (IFA-518.1), and two rods were irradiated in both the first and second loadings of IFA-518 (see Table 1). The three remaining ramped rods and the nonramped sphere-pac rod were irradiated in the first loading of IFA-517 test rig (IFA-517.1). Although there were many power ascensions and descensions during these tests, there were long periods of essentially steady-state operation. IFA-517 was later used for all the ramp tests. Detailed descriptions of the steady-state irradiations have been published and are referenced for each rod in Table 1.

The IFA-518 rig contained two six-rod clusters of test rods with the clusters located approximately symmetrically on either side of the reactor core midplane. There was a silver absorber shield in the IFA-518.1 test rig that could be alternately placed over either cluster to reduce the power in that cluster by about 40%, thus permitting power cycling of both clusters. This absorber shield was removed for IFA-518.2 to increase the burnup rate. For either cluster, the peak-to-average LHGR in the test rods was ~1.10 to 1.15 (Figure 1). Some power peaking occurred at the ends of the rods when they were shielded and the power profile was axially reversed between the two clusters. The lower smear density rods with annular fuel were located nearer the core centerline than the other rods to take advantage of the flux tilt across the assembly to equilibrate the LHGRs between rods. Typical rod-average LHGRs during steady-state irradiation in IFA-518.1 and IFA-518.2 were ~35 kW/m.

The IFA-517.1 test contained a single cluster of four fuel rods centered at the reactor core midplane. The peak-to-average LHGR was about 1.03, i.e., the axial power profile was relatively flat; and the rod-average LHGRs during steady-state irradiation were ~40 kW/m.

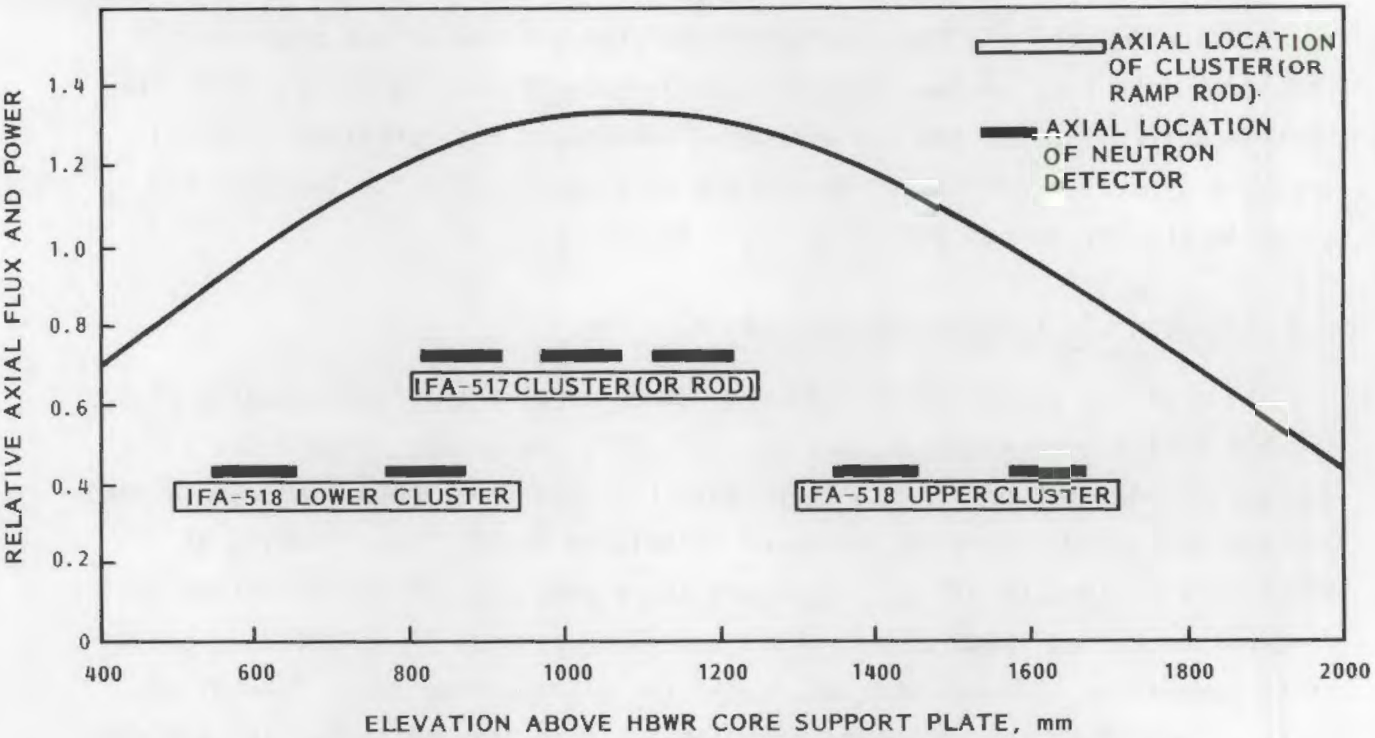

FIGURE 1. Relative Axial Power Profile in IFA-517 and IFA-518 Test Assemblies

3.4 POWER-RAMP TESTING SUMMARY

The 10 power-ramp tests were conducted in the HBWR using the IFA-517 test rig. Seven rods were tested between May and August 1980, and the three remaining tests were conducted in August and September 1981. The test rig nad the capability of pneumatically inserting each test rod from a low-power "parking" position near the top of the HBWR core into the power-ramp position at the midplane of the reactor core. Each test rod was also removed from the core pneumatically. Both maneuvers were completed while the reactor was at or near zero power.

During both normal operation and the power-ramp tests, the HBWR was cooled and moderated by heavy water. The coolant pressure was nominally 3.4 MPa (500 psi), and the saturation temperature was usually 240°C although it ranged as low as 230°C during the tests. The normal mode of flow for tests is by natural convection; however, forced circulation was used during the ramp tests to assure adequate cooling at the hign LHGRs.

Each power-ramped rod was individually tested according to the general scheme depicted in Figure 2. After an initial reactor power ascension, the rod was maintained at a peak LHGR of ~28 kW/m [see zone (a) in Figure 2] by using either reduced reactor power or ^{3}He pressurization in the coils surrounding the test rod. The 28-kW/m power level was maintained for 24 h to condition the rod to the reactor environment after the significant amount of handling it had experienced during preramp examinations. The conditioning power hold was followed by a reactor-power-induced LHGR increase in the rod to the 35- to 40-kW/m level [see zone (b)]. (Reactor power was about 15 MW at this time, which was significantly above the 11- to 12-MW level at which it had operated for several previous reactor cycles.) Immediately after the reactor achieved full power, an additional rapid LHGR increase [see zone (c)] was induced by depressurization of the ^{3}He in the coils surrounding the test rod. Ramp rates during this period were from 3.5 to 4.5 kW/m-min. The target rod-average LHGR at the

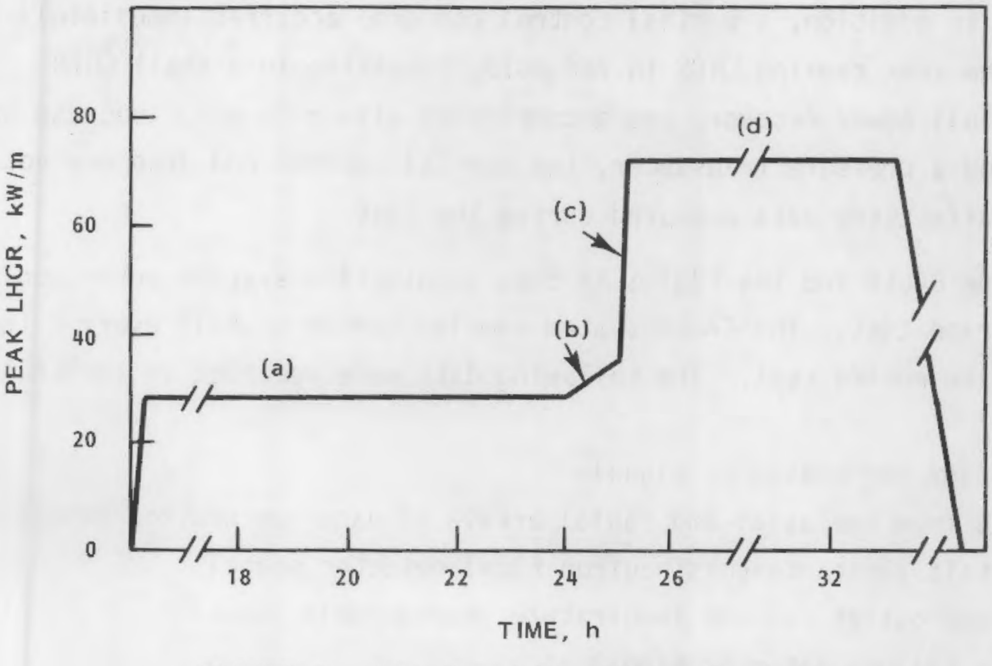

FIGURE 2. Idealized Power-Ramping Scheme

end of the rapid power-ramp was $\geq$68 kW/m, which is equivalent to a peak pellet LHGR of $\geq$70 kW/m. The target LHGR was maintained for 8 h [see zone (d)], followed by a relatively slow reactor power decension to near zero power over several hours.

The testing sequence was planned to permit flexibility and decision making in the event of an unexpected result, e.g., the failure of an annular-coated rod. The improved rod designs, especially the annular designs, were power-ramped before the reference rods so that the peak LHGR of the improved designs could be repeated for the reference design. As much as possible, the two sets of rods at different burnups and different steady-state power histories were treated separately. Two major deviations from this plan occurred: 1) reference Rod R2 was inadvertently over-ramped to a rod-average LHGR of ~75 kW/m (the target was the ~68 kW/m that had been achieved in annular-coated rods AC9 and AC10) and 2) annular Rod A6 was under-ramped to a rod-average LHGR of only 66.5 kW/m. In addition, a partial control rod drop occurred immediately after achieving the peak ramping LHGR in rod AC10, resulting in a small LHGR decrease. Full power recovery was accomplished within 10 min. Because this rod contained a pressure transducer, the partial control rod drop did not significantly affect the data measured during the test.

Both the CALIB and the FAST-SCAN data acquisition systems were used for each power-ramp test. The CALIB system sampled sensor signals every 3 to 5 min throughout the entire test. The following data were recorded on the CALIB system:

- elongation (or pressure) signals
- signals from the axial and radial arrays of vanadium neutron detectors
- the cobalt (instantaneous neutron flux) detector signal
- inlet and outlet coolant temperature thermocouple signals
- the rig failure detector signal
- reactor power
- ^{3}He pressure
- time and date.

The FAST-SCAN system was used during critical portions of the test. For the 1980 tests, this period was from the beginning of the reactor ramp until about 1 h into the peak-power holding period. For the 1981 tests, this period was extended to include the entire peak-power holding period and the power descension. All the signals listed above, except for those from the vanadium neutron detectors, were recorded on the FAST-SCAN system approximately every 2 s. Because the delay time for the vanadium detectors is long in comparison to the sampling time, correction to a real-time basis during the rapid ramp would have been extremely uncertain. Therefore, vanadium detector data were deleted from the FAST-SCAN data set and the cobalt detector was used instead.

The presence of only one rod in the ramping position at any time disrupted the forced subcooled water flow in such a way that a heat balance could not be obtained for each rod. Therefore, individual LHGRs in the test rods were determined as described in Appendix A. The derived LHGRs for the FAST-SCAN data set were spliced into the CALIB data (see Appendix A) to provide the best overall description of each test as a function of time. Individual ramp test characteristics are listed in Table 2. The LHGR for each test as a function of time is presented in Section 4.1.

3.5 PRERAMP AND POSTRAMP NONDESTRUCTIVE EXAMINATION AT HALDEN

Preramp and postramp nondestructive examinations (NDEs) were conducted in a hot cell adjacent to the HBWR. These examinations were conducted to ascertain any changes in the general physical characteristics of the rods as a result of the power-ramp tests; they consisted of visual, eddy-current, and profilometry tests.

3.5.1 Visual Examination

Preramp and postramp visual examinations of the rods were conducted through a hot cell window.

3.5.2 Eddy-Current Examination

Preramp and postramp eddy-current examinations were conducted to determine if defects, e.g., cracks, had formed in the cladding as a result of the power-ramp tests.

TABLE 2. Individual Ramp Test Characteristics

Rod Number	Test Sequence,(a) Date	Coolant Temperature, °C	Axial Peak-to-Average LHGR Ratio	^{3}He Ramp Rate, kW/m-min	Rod-Average Holding Period LHGR, kW/m
1980 Power-Ramp Tests					
R1	7 (9/80)	240 to 241	1.03	3.68	$70.6^{+1.8}_{-3.5}$
R2	6 (8/80)	230 to 232	1.03	4.16	$74.2^{+3.2}_{-2.2}$
A6	5 (7/80)	240 to 242	1.03	3.75	$66.5^{+1.7}_{-1.6}$
AC9	3 (5/80)	235 to 236.5	1.04	3.65	$67.2^{+3.3}_{-1.2}$
AC10	4 (7/80)	240.5 to 241.5	1.04	4.44	$69.3^{+1.9}_{-1.5}$
S40	8 (9/80)	240 to 241.5	1.03	4.50	$70.9^{+1.3}_{-3.2}$
S41	2 (5/80)	235 to 237	1.04	4.04	$70.9^{+3.3}_{-1.6}$
1981 Power-Ramp Tests					
R3	10 (9/81)	240 to 241	1.02	3.33	$67.8^{+1.0}_{-1.6}$
AC11	9 (9/81)	241.5	1.02	3.64	$66.3^{+1.5}_{-2.0}$
ACP27	11 (9/81)	240.5 to 241.5	1.01	2.11	$70.0^{+2.0}_{-1.5}$

(a) Vipac Rod V13 was tested first to check out the power-ramp system. Results for this test are not reported in this document.

The eddy-current testing device consisted of twin coils that were differentially connected and surrounded the fuel rod. The coils formed one-half of an AC bridge that was completed outside the hot cell. The bridge was excited with a variable-frequency power source (10 to 60 kHz). Cladding defects would produce a bridge imbalance as the coils passed over them, and the amplitude and phase relationships of this imbalance are characteristic for various types of defects. Cracks, ridging, and significant changes in local ovality of the cladding, if present, can be detected and separated from each other by comparison of the amplitude and phase relationships. However, as of the date of the measurements, calibrations of the magnitudes of each type of measurement had not been completed.

The standard method for eddy-current examination at Halden is to perform the initial examination of a fuel rod at the lowest frequency (10 kHz) because it provides the best sensitivity for detecting defects. If a defect is located at 10 kHz, the fuel rod is reexamined at higher frequencies because better separation between types of defects can be made at higher frequencies. No defects were found in any of the test rods during the preramp and postramp eddy-current examinations at 10 kHz.

3.5.3 Profilometry

Preramp and postramp diameter measurements were made on the test rods to ascertain any dimensional changes that occurred as a result of the ramp tests. Measurements were made at four azimuthal orientations that were 45° apart using an apparatus that azimuthally positioned the fuel rods in the same orientation during the preramp and postramp examinations.

The diameter measurements were made using variable-gap differential transformers. For each orientation, axial traces in both the up and down directions were generated. There were no statistical differences in sensitivity in the up or down direction; therefore, only data from the upward traces are presented in this report. Because zero offsets occurred over the several days that it took for the measurements, all the postramp diameter traces were shifted in magnitude to match the preramp diameter of the lower end plug. The axial position of the diameter data was determined using a differential transformer that produced a sinusoidal signal with a pitch of 4.499 mm. The estimated uncertainty of the axial position of any set of diameter data was ±0.1 mm. The diameter and axial position data were recorded on magnetic tape to facilitate data handling.

3.6 POSTRAMP EXAMINATIONS AT HARWELL

Nondestructive and destructive postramp examinations were conducted at the United Kingdom Atomic Energy Authority (UKAEA)-Harwell hot cell facilities on rods from the 1980 tests (see Table 2). Descriptions and the objectives of each examination are presented below. The examinations that were completed on individual rods are summarized in Table 3.

3.6.1 Neutron Radiography

Neutron radiographs were made on the annular-coated and sphere-pac rods to assess the effects of power-ramping on the fuel. Of particular interest was 1) whether or not axial fuel relocation occurred within the central hole of the annular fuel and 2) confirmation of positioning of the centerline thermocouples used during the steady-state testing of the sphere-pac rods. Axial fuel relocation within the central hole of annular fuel rods by spalling during handling and/or steady-state and power-ramp operation could cause perturbations in the axial power profile of the fuel rod. Similarly, axial fuel movement in the central hole during power-ramp operation by some other mechanism, e.g., vaporization-condensation, could affect the axial power profile.

Rods AC9, AC10, S41, and S42 were neutron radiographed using the DIDO reactor facility using a 170-mm diameter horizontal neutron beam with a neutron flux at the specimen of 5×10^7 n/cm^2-s. The limited diameter of the beam necessitated four overlapping exposures to cover the fueled length of the rod. Rods AC9 and AC10 were radiographed in only one orientation, while Rods S41 and S42 were radiographed in two orientations that were 90° apart to ascertain the position of the thermocouples.

Each rod was loaded into a sealed aluminum container before radiography. The rods were radiographed vertically using an indirect transfer method. The rod and the container were positioned between the reactor and an indium foil, and the foil was placed in close proximity to the fuel rod. After exposure to the neutron beam, the irradiated foil was placed in contact with x-ray film; and the activation image was transferred to the film. The developed film produced a negative image of the fuel rod.

3.6.2 Visual Examination

Each fuel rod was visually examined at a magnification of 2X using equipment that slowly rotated the fuel rod.

TABLE 3. Postirradiation Examinations on Fuel Rods Irradiated in the HBWR[(a)]

Rod Number	Neutron Radiography	Visual and Photo	Gross Gamma Scan	Spectral Gamma Scan	Eddy-Current Exam	Profilometry	Fission Gas Release	Ceramography	Burnup Analysis	Longitudinal Cladding Exam	Special SEM
R1	–	X	X	X	X	X	X	X	X	X	–
R2	–	X	X	X	X	X	X	X	X	–	–
A6	–	–	–	–	–	X	X	–	–	X	–
AC9	X	X	X	–	X	X	X	X	–	X	X
AC10	X	X	X	X	X	X	X	–	–	X	–
S40	–	–	–	–	–	X	–	–	–	–	–
S41	X	X	X	X	X	X	X	X	–	–	X
S42	X	X	X	X	X	X	X	X	–	–	X

(a) X denotes examination; – denotes examination not planned.

3.6.3 Gross and Spectral Gamma Scanning

Fuel rods were axially scanned for gross gamma activity to determine the axial burnup distribution and to obtain an indication of whether or not fission product migration occurred during the ramp tests. Spectral gamma scanning was performed on selected rods to determine where selected volatile fission products such as cesium were located.

The rods were scanned using a standard technique. Each fuel rod was placed on a horizontal table and moved in front of a fixed 0.25-mm wide by 12.7-mm high collimator at a rate of 0.0064 mm/s using pulsed stepping motors. The gamma activity was detected and measured using a Ge(Li)-diodide detector and modular nucleonic equipment. An analog-to-digital conversion system with a single-channel analyzer and rate meters automatically corrected for dead time, which permitted ready comparison of the burnup in different fuel rods. The amplified detector output pulses were processed by a digital pulse processor with built-in stabilization. At a rate of 100 count per second (cps), the standard deviation for a measurement was ±2.3%; at 1000 cps, the standard deviation was ±1%. The gain was digitally set at 0.40 keV/channel. The digital single-channel analyzers were set precisely as follows:

gross gamma	440 to 850 keV
^{137}Cs	658 to 666 keV
^{95}Nb	762 to 770 keV

For the ^{137}Cs peak, the background continuum under the photo peak was automatically subtracted.

Fuel stack lengths were determined by counting at 0.13-mm intervals near the ends of the fuel stack. The nominal 2.78% ^{235}U enriched pellets at each end of the fuel stack were included in the measurement. It was assumed that the ends of the fuel stack corresponded to the half height position after background was subtracted. The standard deviation for the measurements of the total fuel stack length was estimated to be 0.13 mm.

3.6.4 Eddy-Current Examination

Six fuel rods were examined for incipient cladding cracks using eddy-current techniques. An encircling-type coil was used for examination at three frequencies: 10, 50, and 125 kHz. The coil was mounted on a gimble assembly that permitted it to follow the shape of the fuel rod as the axial scans were performed. The rod being examined was also rotated about its axis, and a probe-type sensor was used to determine the azimuthal position of any particular feature. A 255-mm long standard, which was prepared from the same lot of tubing as the rods, was prepared with several machined features (e.g., internal and external notches, small holes, and a region with reduced wall thickness).

No defects were detected in the cladding although the equipment was sensitive enough to detect the wall thickness changes resulting from the "rocking" that had occurred during tubing manufacture. The regions at the tips of the thermocouple in the pelletized rods and at the tip of the thermocouple wells in the sphere-pac rods were also detected.

3.6.5 Profilometry

Profilometry measurements were made at Harwell at four azimuthal orientations. Two of these orientations were as near to the original pretest orientations for profilometry measurements made at Kjeller, Norway, as visually possible. Because the four orientations of the preramp and postramp profilometry measurements at Halden were better known and controlled than the Kjeller and the Harwell measurements, the Halden results were used for data presentation and analysis for this report (see Sections 3.5.3 and 4.2.3).

3.6.6 Fission Gas Release

Seven rods were punctured to determine the internal pressure, gas composition, and free volume of the fuel rods. A rod-puncturing head in a hot cell was used, and the head was connected by a flexible stainless steel tube to an external gas collecting and measuring system.

The gases were first released into the evacuated puncturing head assembly. The released gases were then pumped into evacuated, calibrated storage vessels; and the pressure in the vessels was measured using a high-precision pressure transducer. Four 5-cm^3 samples of the gas were removed for mass spectrographic analysis for the gas species. In general, there was excellent agreement between the sets of measurements with the volume percentage of the major constituents falling within ±0.4% of the average of the four measurements. The estimated precisions for the species analyses are estimated to be ±1% at the 10 vol% (or greater) level, falling to ±10% at the 0.01 vol% level.

The internal rod volume was measured by filling the evacuated rod and punctured head assembly with helium at atmospheric pressure, pumping the gas into calibrated vessels, measuring the pressure rise, and, finally, subtracting the volume of the puncturing head. The original fuel rod pressure was then derived from the measured volume of gas collected and the measured internal rod volume. At least three separate measurements of the fuel rod volume were made for each rod with very little scatter ($<0.1\ cm^3$). The accuracy of the internal rod volume and pressure measurements was calculated to be ±1% and ±2%, respectively, at the 1σ confidence level.

3.6.7 Ceramography

Both transverse and longitudinal ceramographic sections were prepared from several fuel rods. Before cutting the rods with a nonlubricated diamond-bonded cutting wheel, a line was scribed axially on each rod at the 0° orientation marked on the lower end plug. This mark is visible in the transverse section. During the cutting sequences, the rods were impregnated with a slow-setting epoxy and a penetrating cyanoacrylate resin to minimize "pull-out." This technique was only marginally successful for the sphere-pac rods; therefore, additional samples were prepared from Rods S41 and S42 using a vacuum impregnation and mounting technique. Pull-out was significantly improved for these specimens.

After sectioning, the transverse and longitudinal specimens were mounted in a slow-setting epoxy resin. During sectioning, the transverse sections had been cut 2 mm away from the desired inspection surface. The mounts contained depth markers for 2 mm and 3 mm. The specimens were ground to a level between these two markers so that the level to be inspected would be within ±0.5 mm of the specified surface.

The longitudinal sections were mounted in a step gauge designed to indicate the centerline of the section (fuel rod) to within ±0.5 mm. The sections were mounted with the scribed surface uppermost and then ground to within the step gauge limits.

The specimens were prepared conventionally by grinding progressively on SiC papers of 240, 320, 400, and 600 grit. Final polishing was accomplished with diamond compounds of 14- and 1-μm particle size. Throughout the grinding and polishing operations the specimens were frequently reimpregnated with quick-setting cyanoacrylate adhesive and slow-setting epoxy resin.

The UO_2 fuel surface of the specimens was etched using an attack polish consisting of γ alumina, 20% H_2O_2 and 80% H_2O. The etched Zircaloy-2 cladding surfaces were prepared using an attack polish consisting of γ alumina, 45-cm^3 H_2O, 4.5-cm^3 HNO_3, 1-cm^3 HF, and 50-cm^3 H_2O.

3.6.8 Burnup Analyses

Burnup analyses were completed on Rod R1 from the IFA-517.1 test rig and Rod R2 from IFA-518.1. Because the burnup during the power-ramp tests was small and such analyses are costly, these two burnup values were used to determine the burnup accumulated during steady-state irradiation in the sibling rods by normalizing the measured burnups to the values calculated from the power histories.(6,7) The burnups were measured using the ^{148}Nd method; because of the relatively low levels, the fissions in plutonium were not determined. In making the conversion from burnup units of atom% to MWd/kgM, a value of 190 MeV/fission was assumed. For both Rods R1 and R2, the burnup sample was taken at the midplane of the fueled length, which was estimated to be the position of the rod-average burnup for both rods as determined from steady-state axial power distributions.

3.6.9 Longitudinal Cladding Examination

Samples were prepared to examine the inner cladding surfaces of annular-coated, annular, sphere-pac, and reference rods. Both visual and scanning electron microscope (SEM) examinations were conducted. The examinations were performed to ascertain if the graphite coating was intact on the annular-coated rods and if there was any evidence of sphere-cladding mechanical interaction in the ramped and nonramped sphere-pac rods. Reference rod specimens were prepared for comparison.

The cladding samples were prepared by longitudinally slitting sections of ~50-mm long fuel rods. The slits were made slightly off the axial centerline to maintain a portion of the fuel in the original position. The smaller "clamshell" was then lifted off, and the exposed fuel was photographed. The fuel was then removed, and the inner cladding surfaces of the clamshells were photographed.

Smaller specimens (~10 to 15 mm long) were cut from the clamshells for examination on the SEM. In some cases, these samples were extremely radioactive and even smaller samples were required; e.g., scrapings of the graphite and fission product layers from the annular-coated rods were used.

4.0 DESCRIPTION OF TEST RESULTS

The results from power-ramp testing and fuel rod examinations are presented in this section. Especially meaningful results for individual rod types or those needing clarification are discussed and evaluated. Where evaluation of the behavior of a fuel rod type requires results from more than one test or examination or comparison between rod types are made, the results are evaluated in Section 5.0.

4.1 POWER-RAMP TEST RESULTS

The power-ramp tests were conducted in four loadings of the IFA-517 test rig from May 1980 to September 1981 (see Table 2). Burnup levels for the rods at the time of ramping are listed in Table 1, and the general ramping scheme is illustrated in Figure 2. The axial power for the ramp tests generally increased with rod length, starting at the bottom; and peak-to-average ratios ranged from 1.03 to 1.05.

The LHGR as a function of test time, the elongation signal as a function of test time, and the elongation signal as a function of LHGR are illustrated in Figures 3 through 11 for Rods R1, R2, R3, A6, AC9, AC11, ACP27, S40, and S41, respectively. The projected elongation due to free cladding thermal expansion is shown in each elongation versus LHGR figure as a dashed line. The LHGR as a function of test time, the pressure signal as a function of test time, and the pressure signal as a function of LHGR for Rod AC10 are shown in Figure 12.

The bellows-type transducers used for the elongation sensor in each of the rods responded to the internal rod pressure (i.e., lifted off) if this pressure was sufficiently high. An analysis of which transducers were affected by the internal rod pressure and over what ranges the elongation signals were valid is presented in Appendix B. The conclusions from this analysis are presented in Table 4. In the elongation versus LHGR plots in Figures 3 through 11, squares (□) show valid elongation signals from the start of the test until they are affected by the internal pressure, triangles (Δ) show elongation signals that are affected by the internal rod pressure, and diamonds (◊) show valid elongation signals after the signal was no longer affected by the rod pressure.

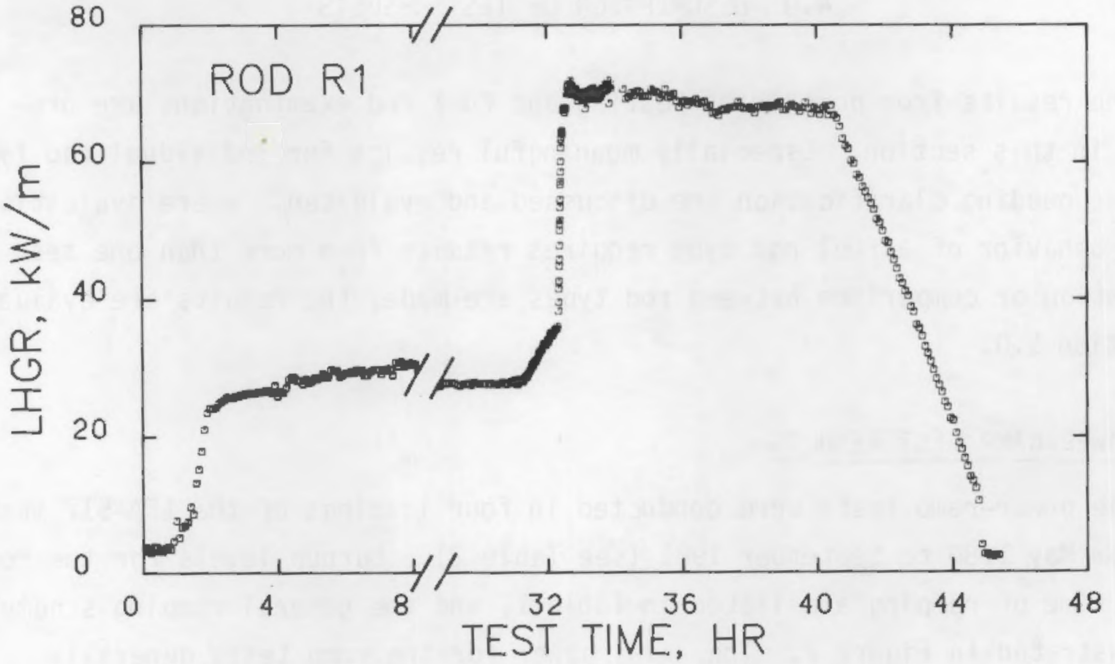

a) LHGR Versus Time

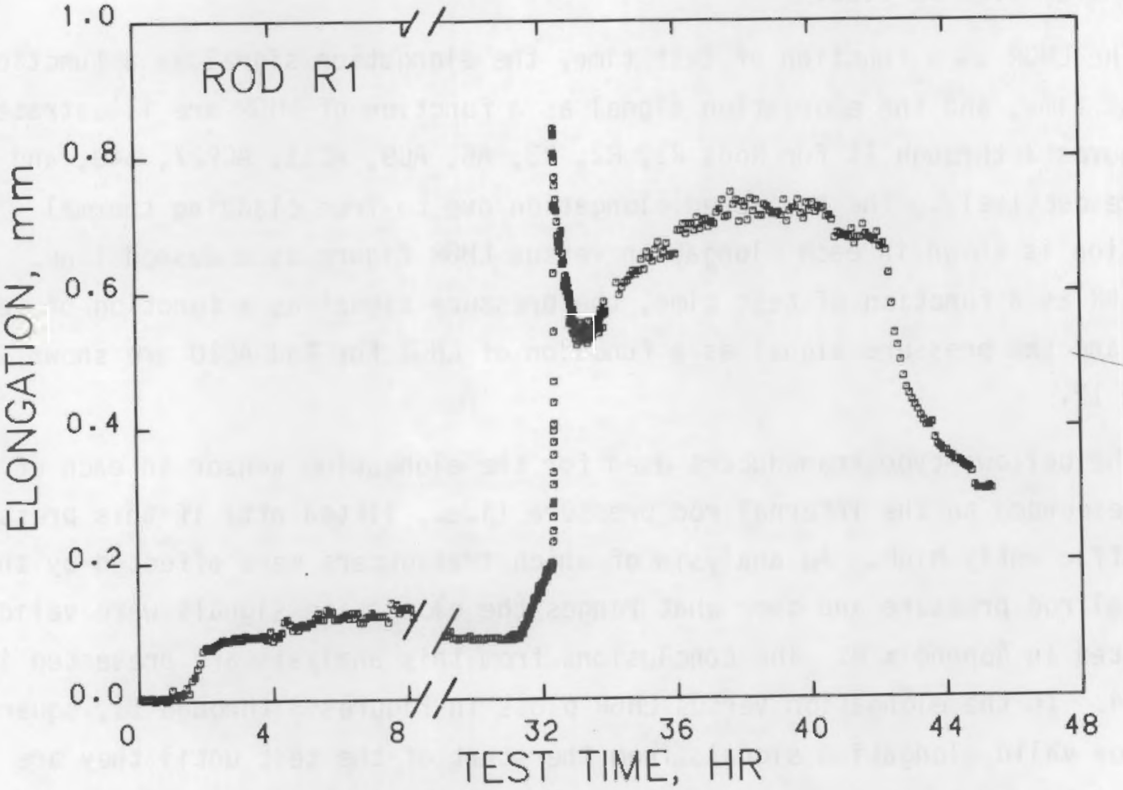

b) Elongation Versus Time

FIGURE 3. Elongation Signal During Power-Ramping of Rod R1 (see Table 4)

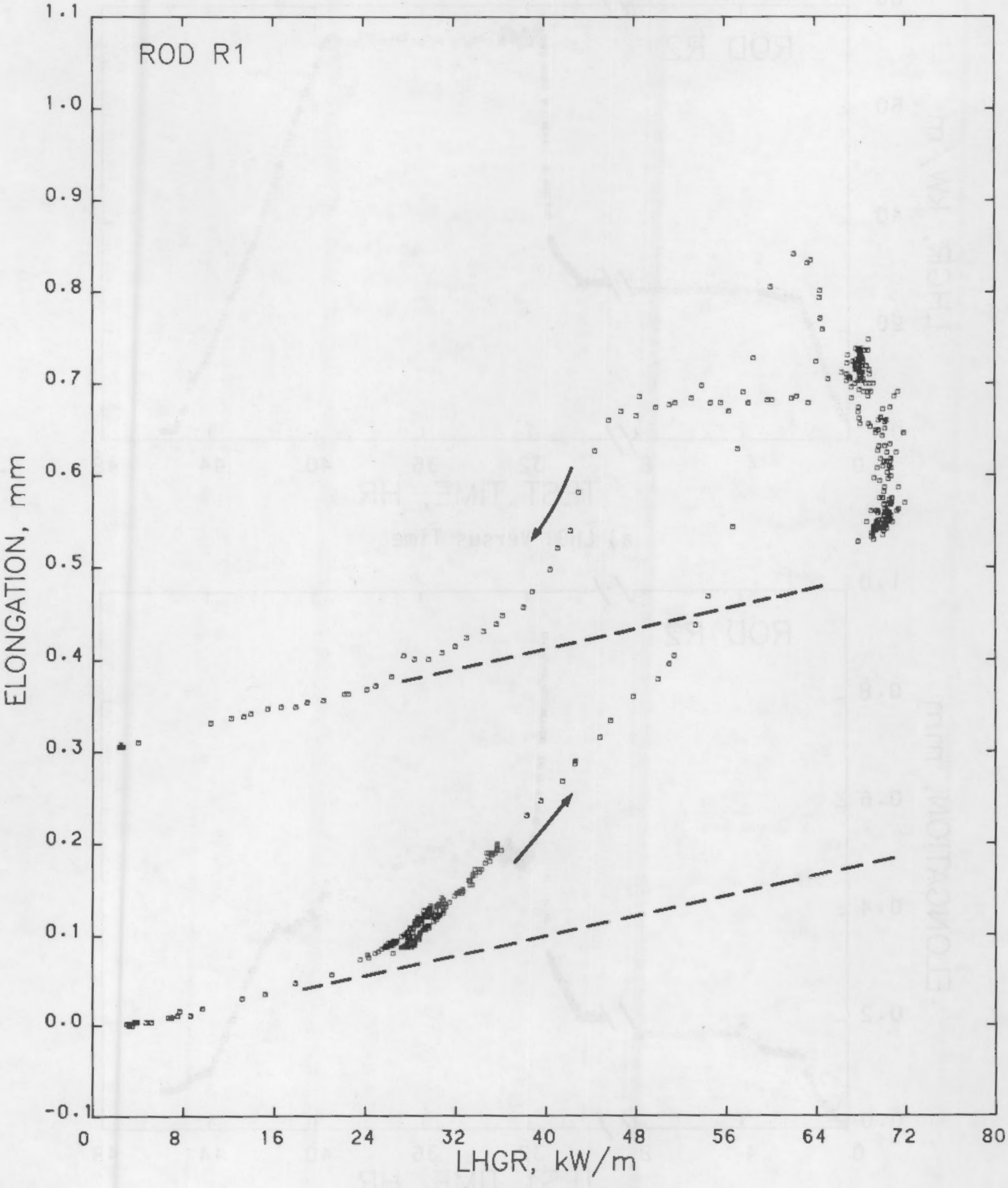

c) Elongation Versus LHGR

FIGURE 3. (contd)

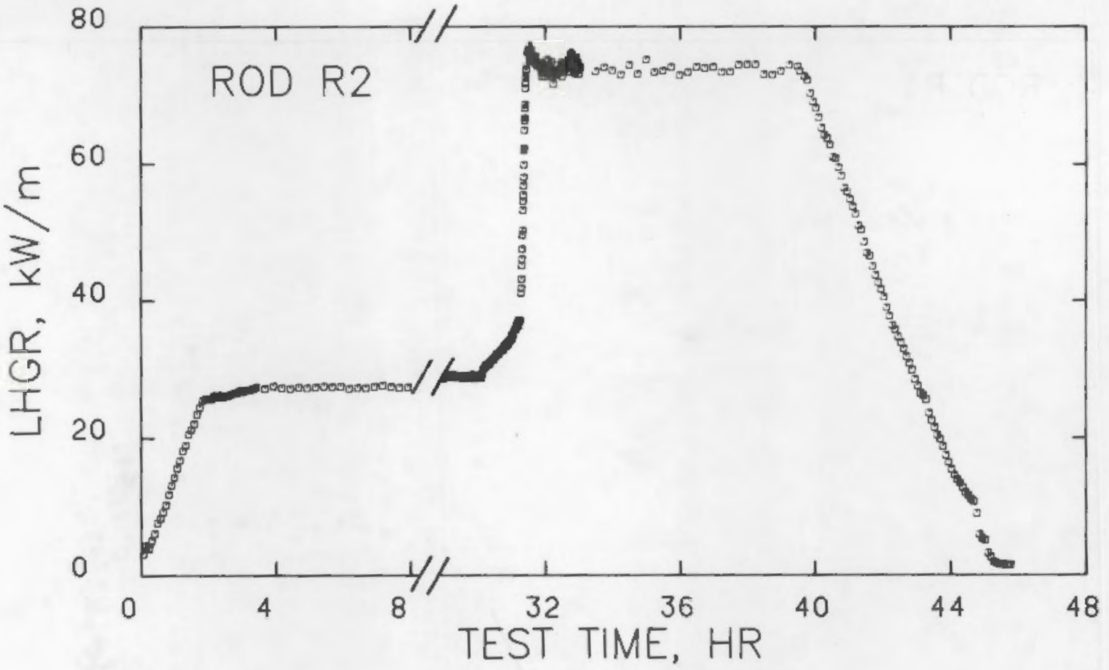

a) LHGR Versus Time

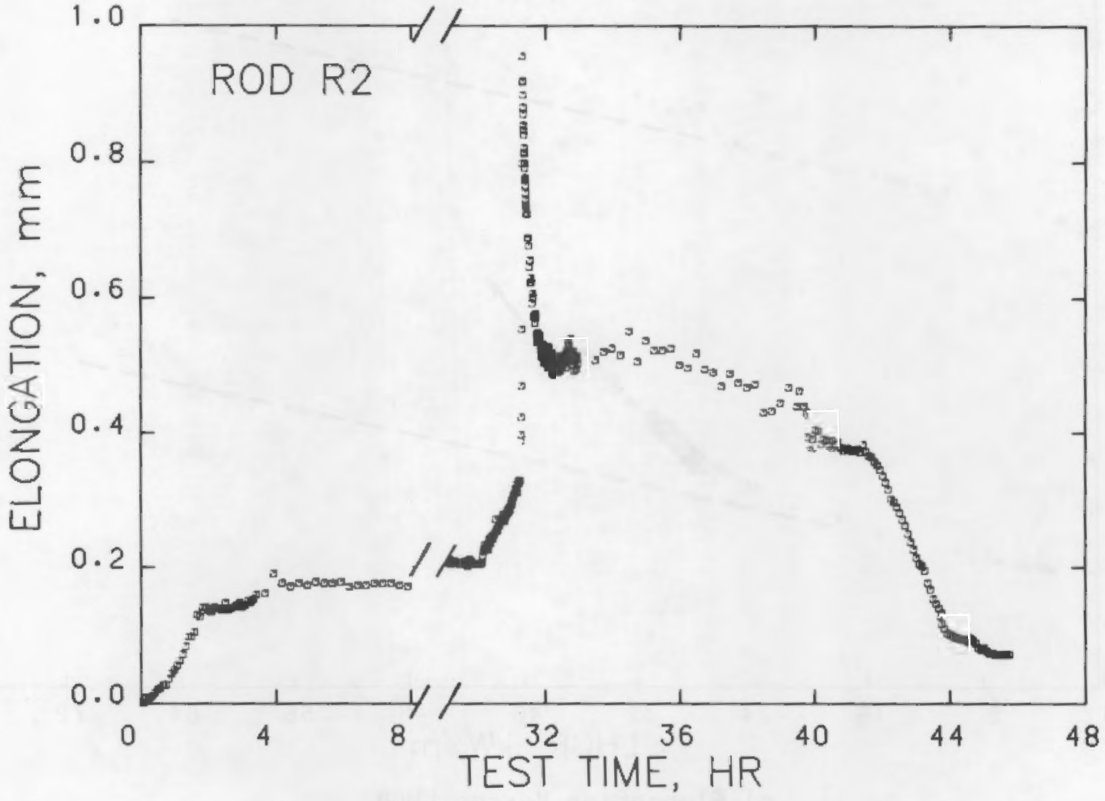

b) Elongation Versus Time

<u>FIGURE 4.</u> Elongation Signal During Power-Ramping of Rod R2 (see Table 4)

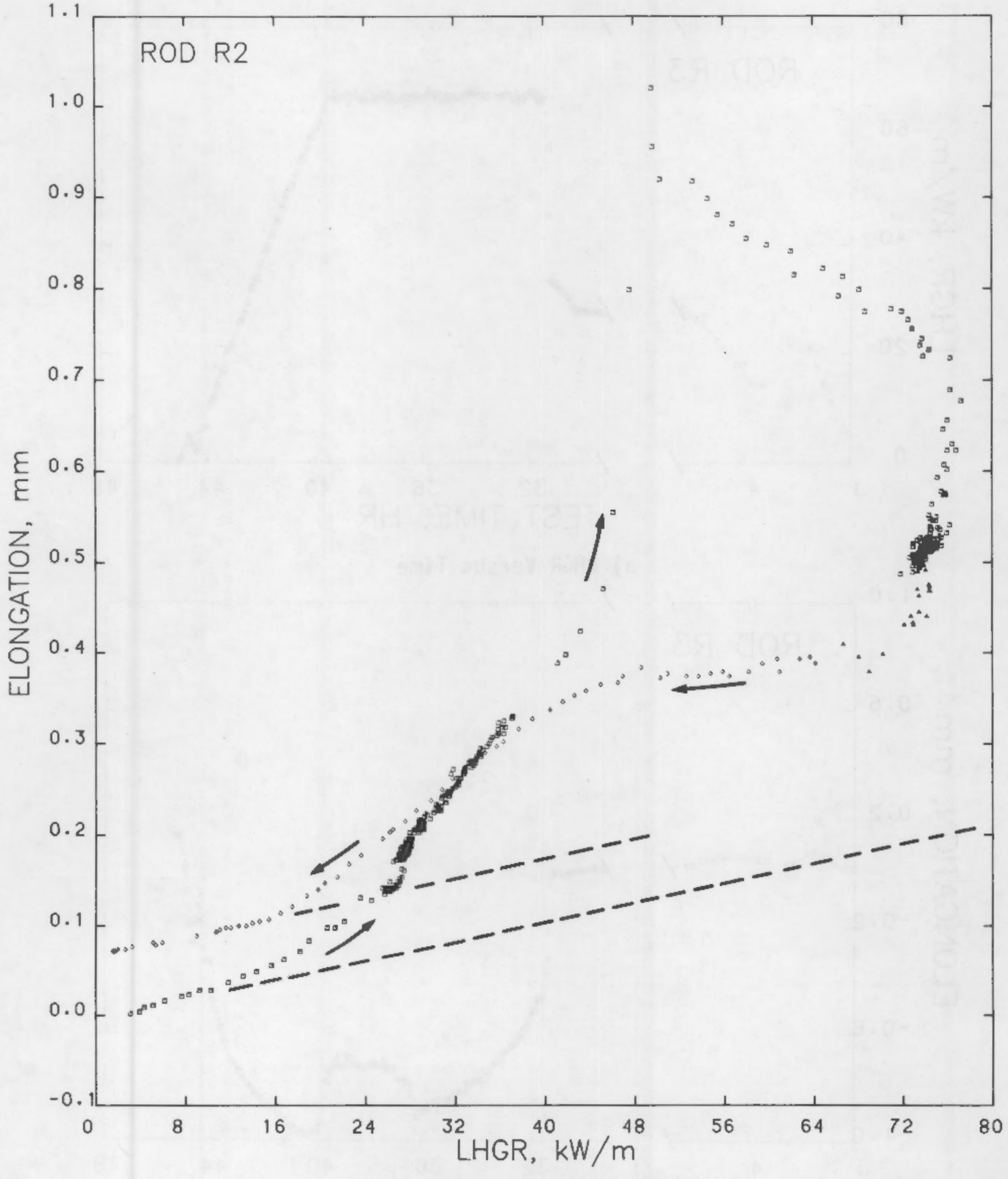

c) Elongation Versus LHGR

FIGURE 4. (contd)

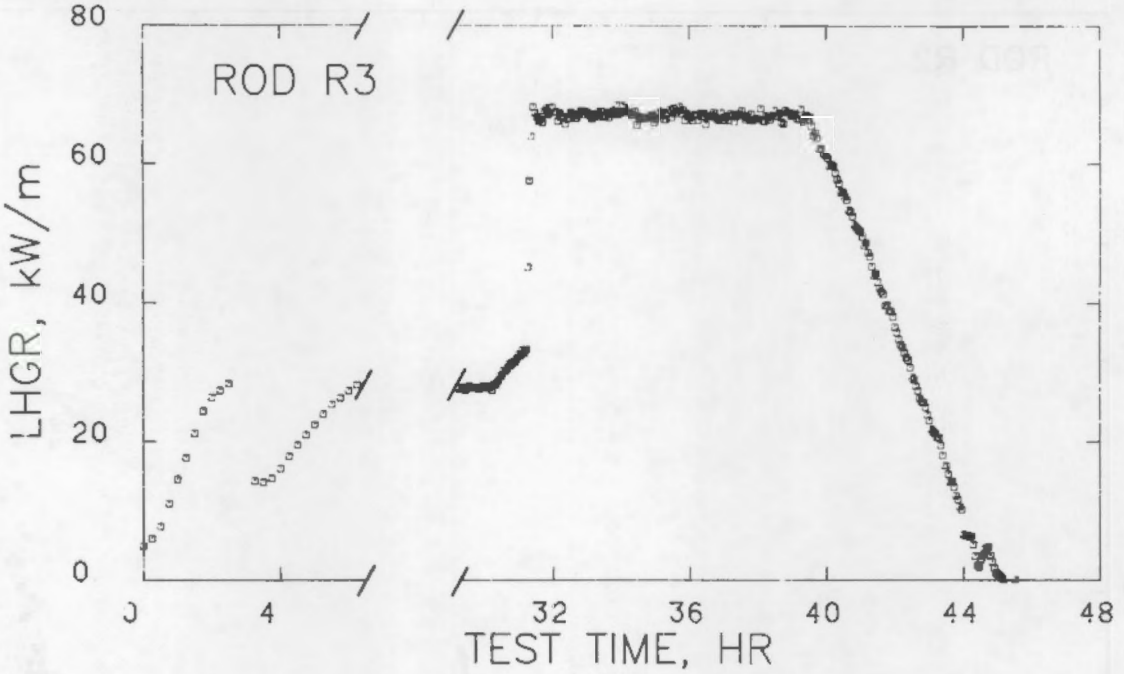

a) LHGR Versus Time

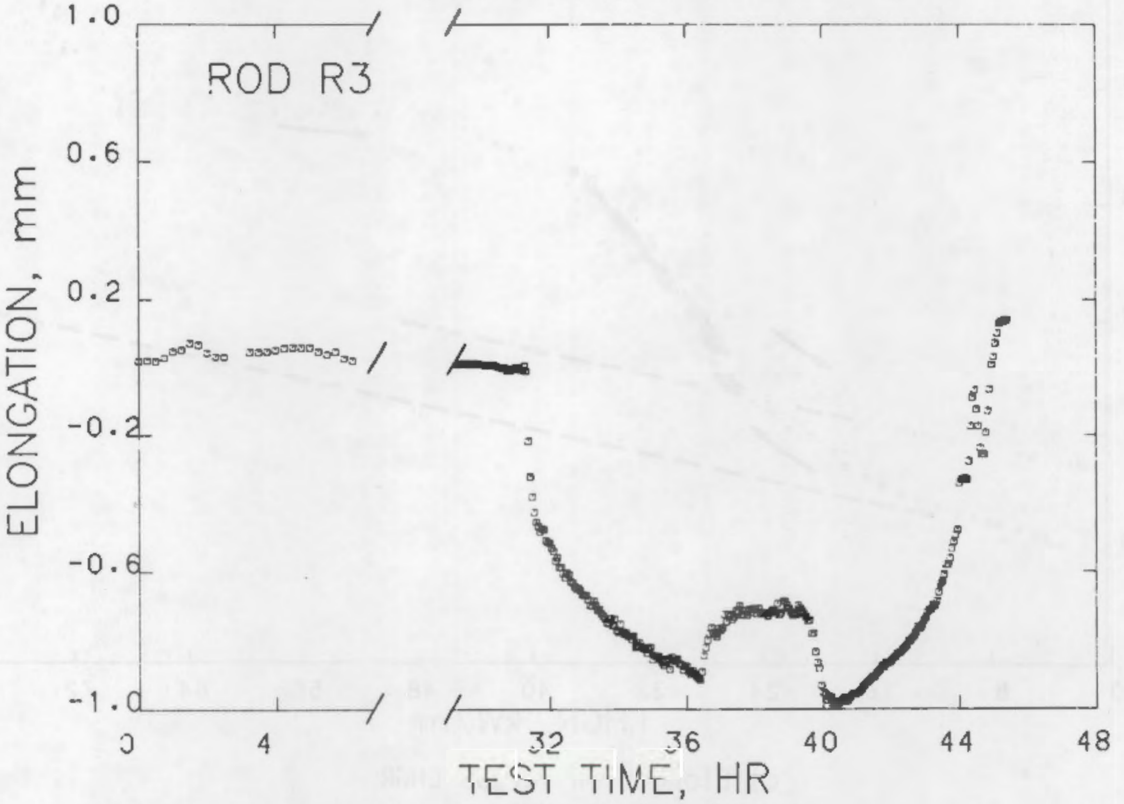

b) Elongation Versus Time

FIGURE 5. Elongation Signal During Power-Ramping of Rod R3 (see Table 4)

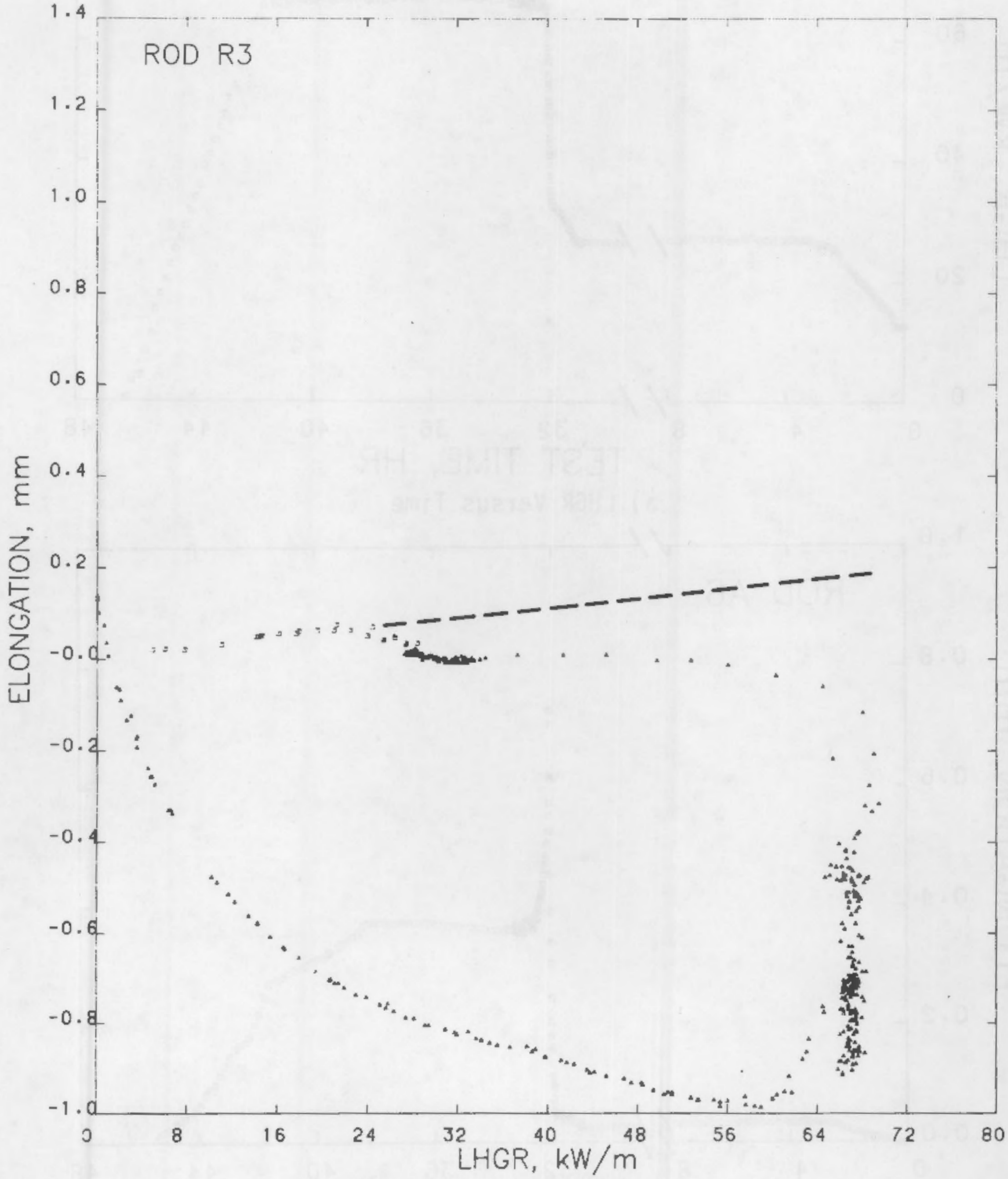

c) Elongation Versus LHGR

FIGURE 5. (contd)

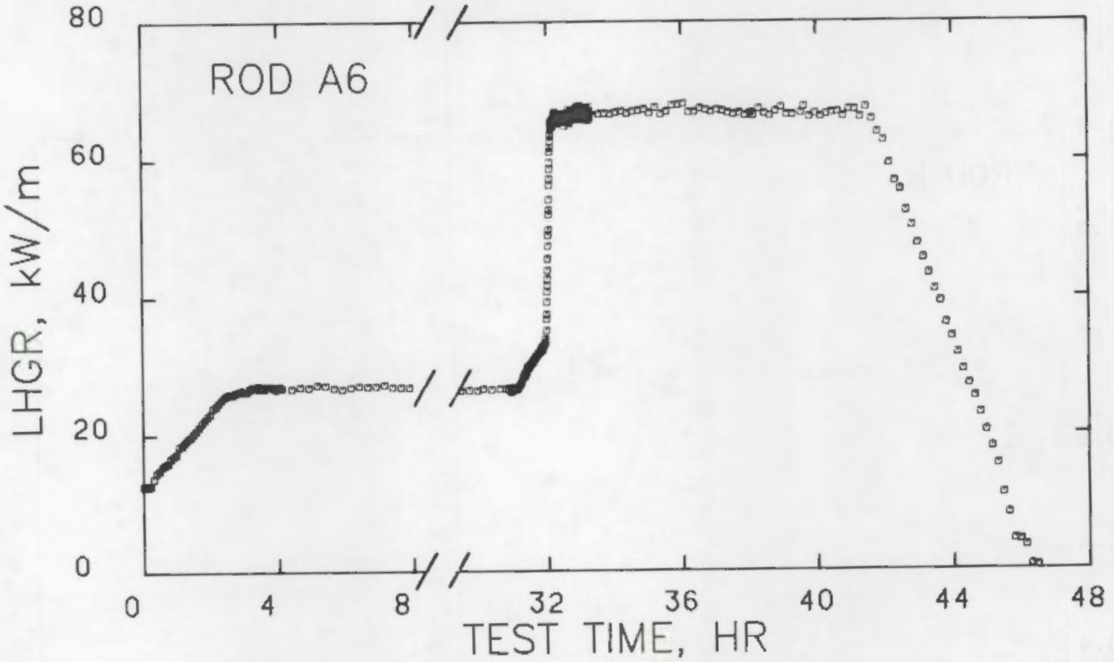

a) LHGR Versus Time

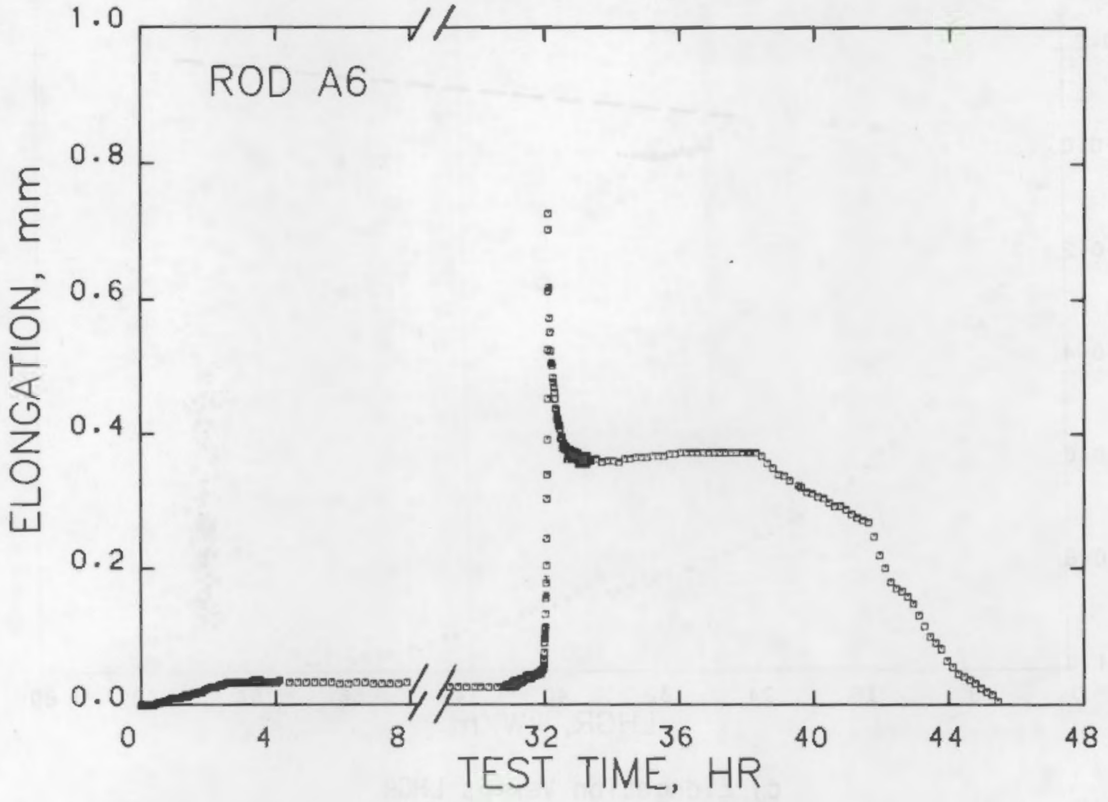

b) Elongation Versus Time

FIGURE 6. Elongation Signal During Power-Ramping of Rod A6 (see Table 4)

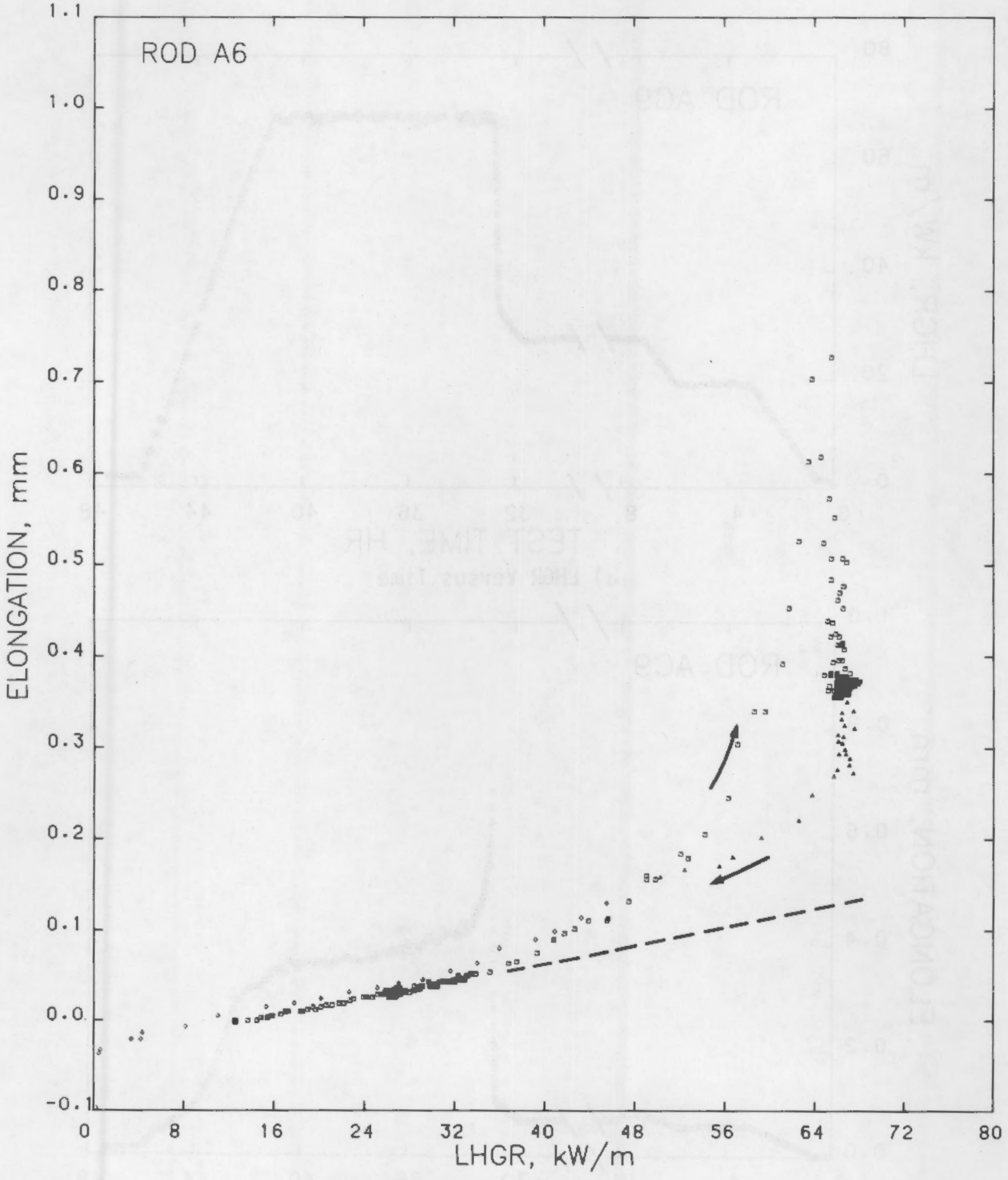

c) Elongation Versus LHGR

FIGURE 6. (contd)

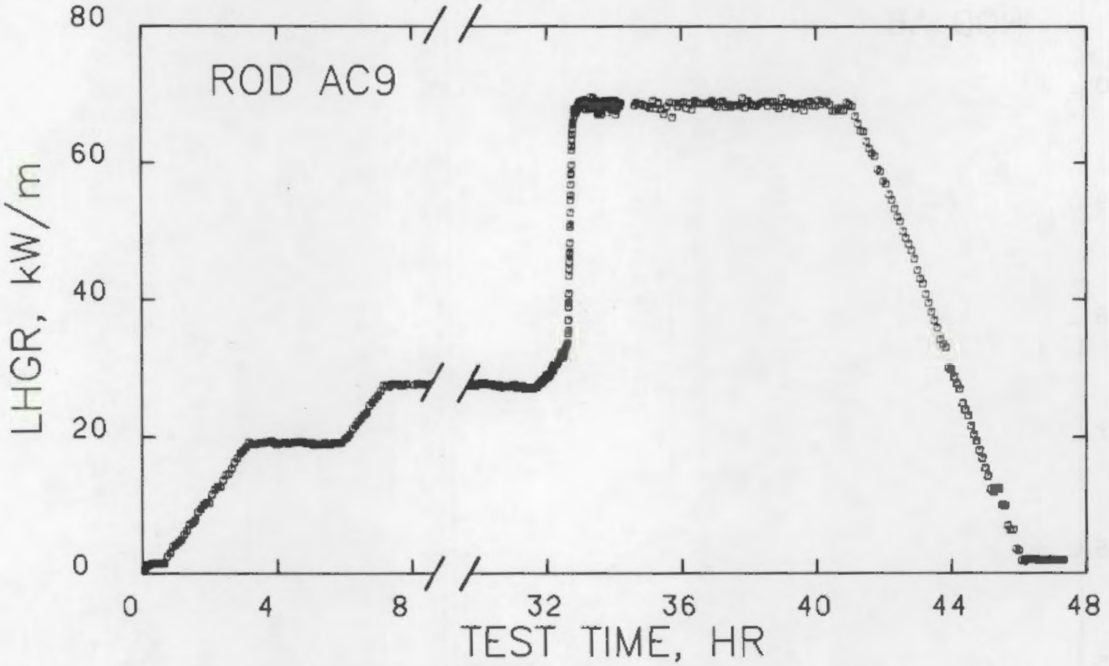

a) LHGR Versus Time

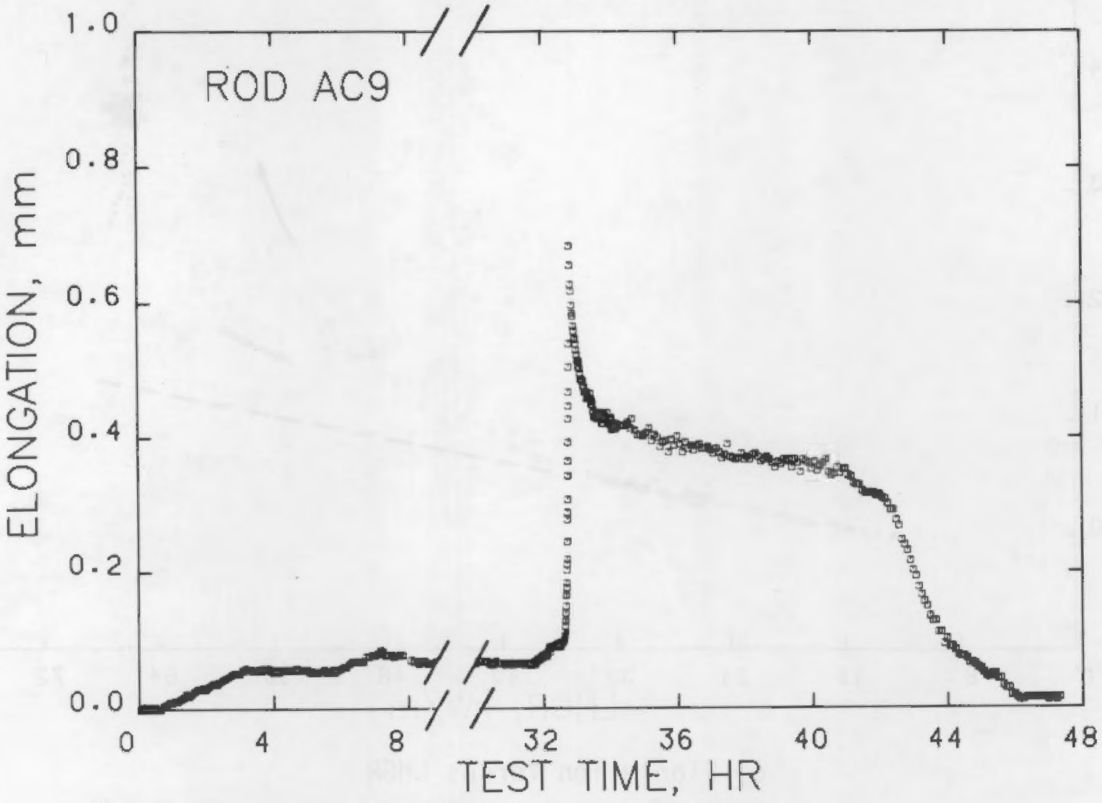

b) Elongation Versus Time

FIGURE 7. Elongation Signal During Power-Ramping of Rod AC9 (see Table 4)

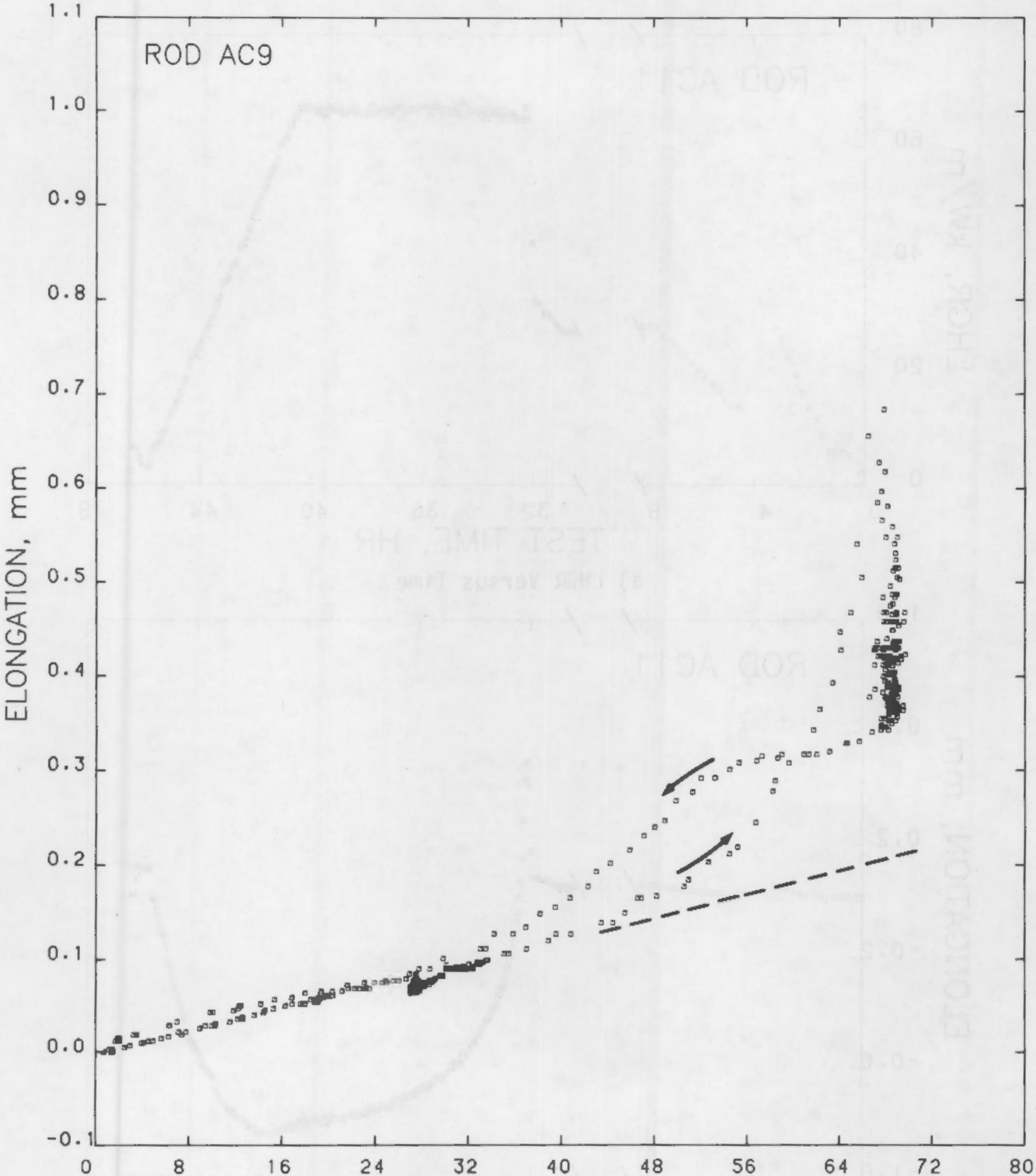

c) Elongation Versus LHGR

<u>FIGURE 7</u>. (contd)

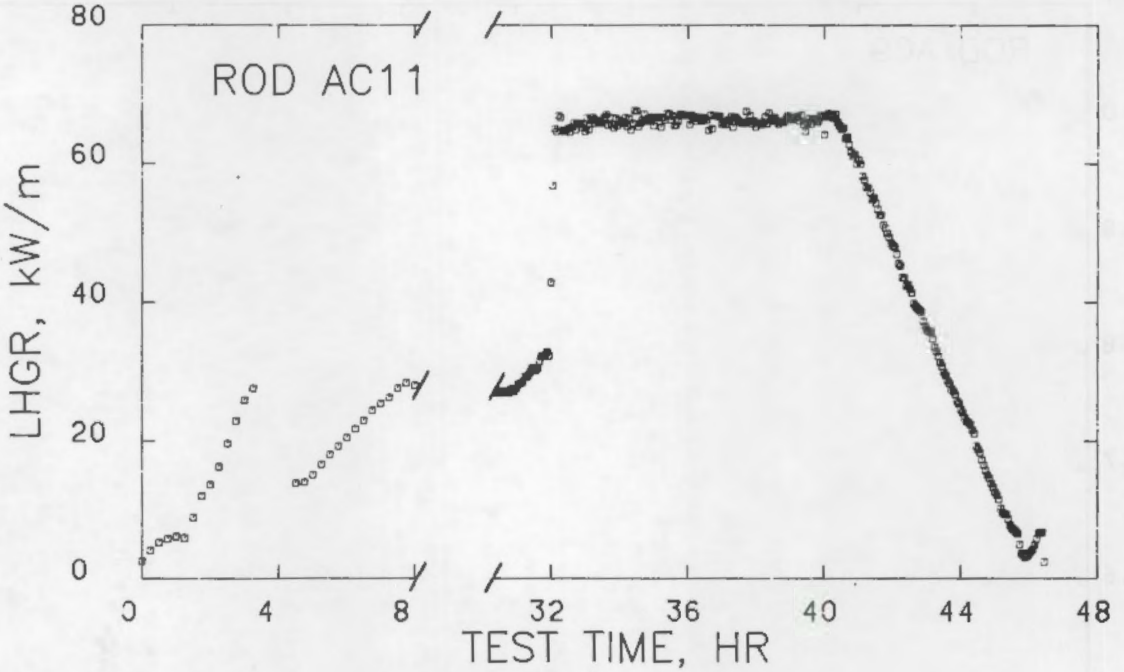

a) LHGR Versus Time

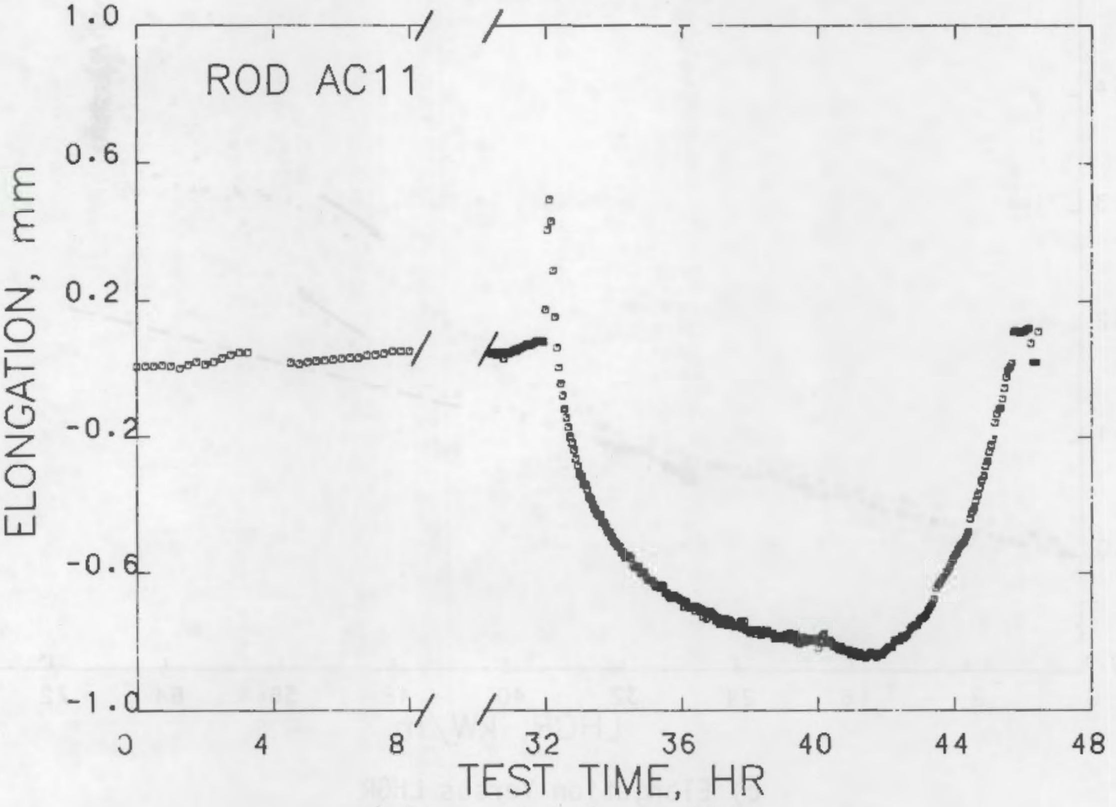

b) Elongation Versus Time

FIGURE 8. Elongation Signal During Power-Ramping of Rod AC11 (see Table 4)

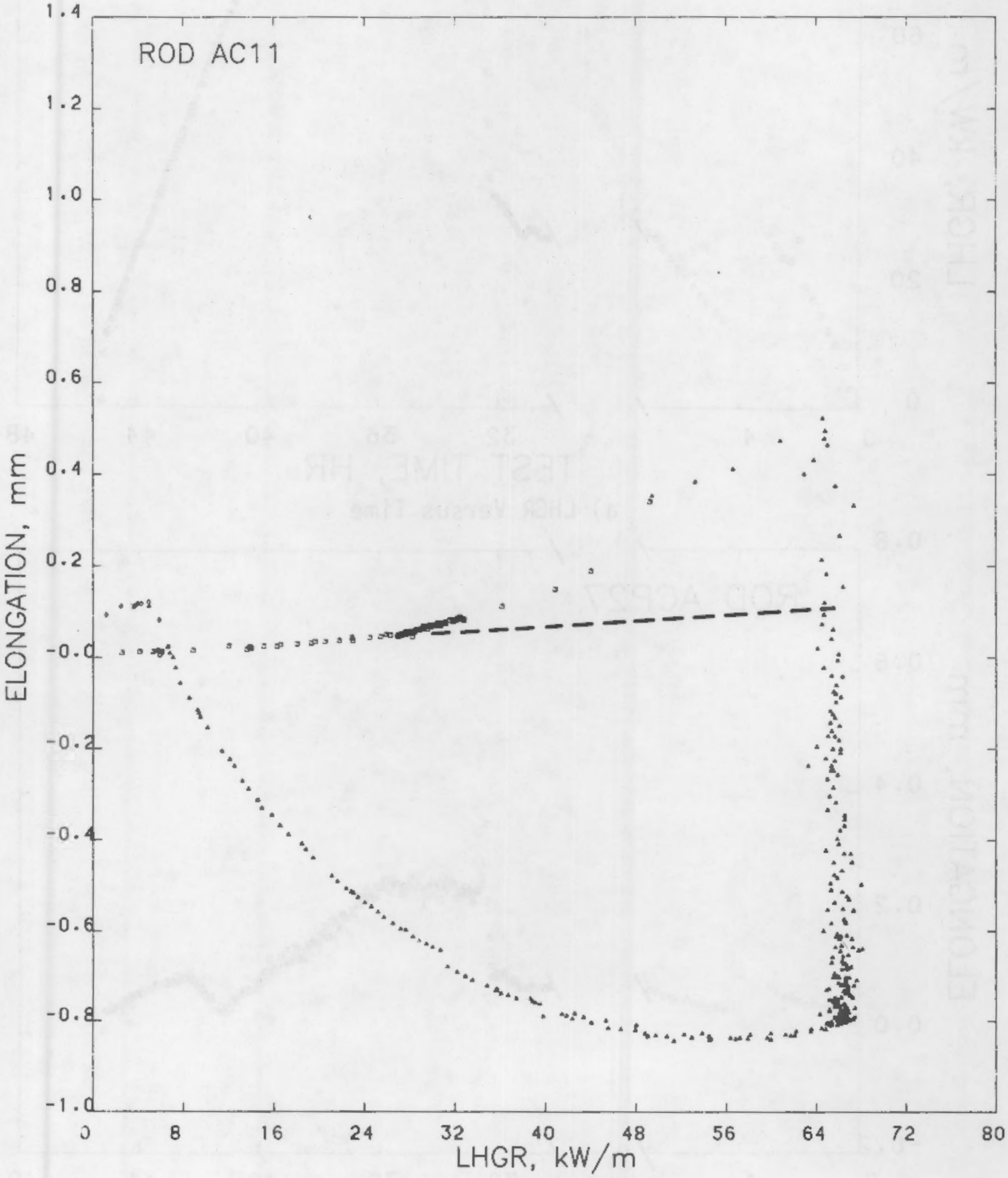

c) Elongation Versus LHGR

FIGURE 8. (contd)

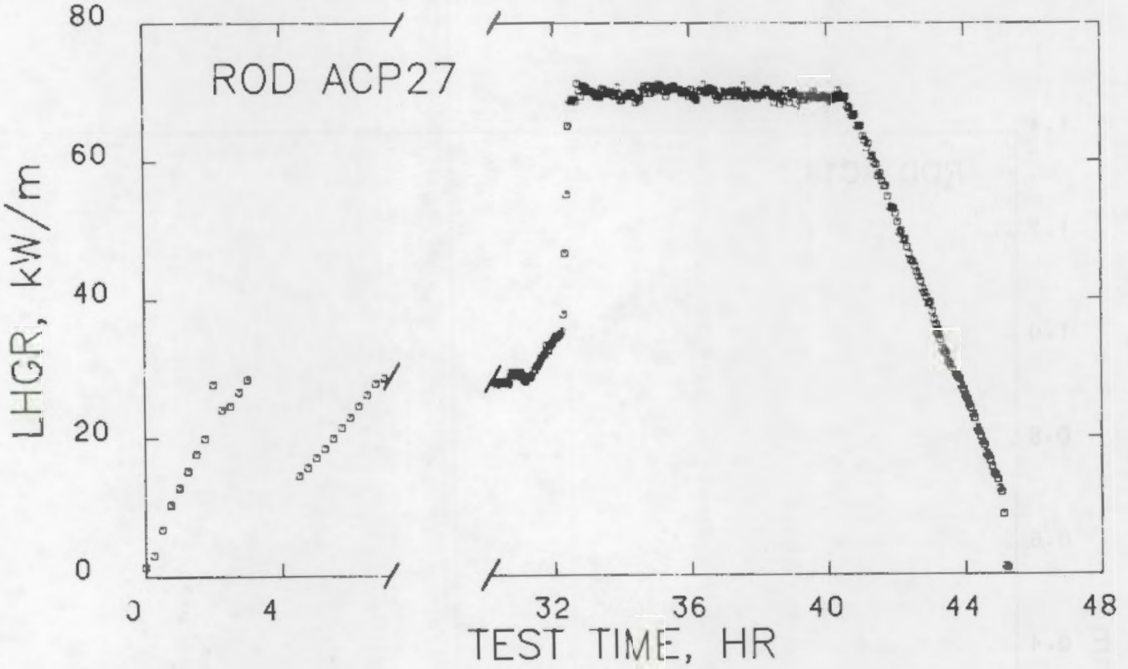

a) LHGR Versus Time

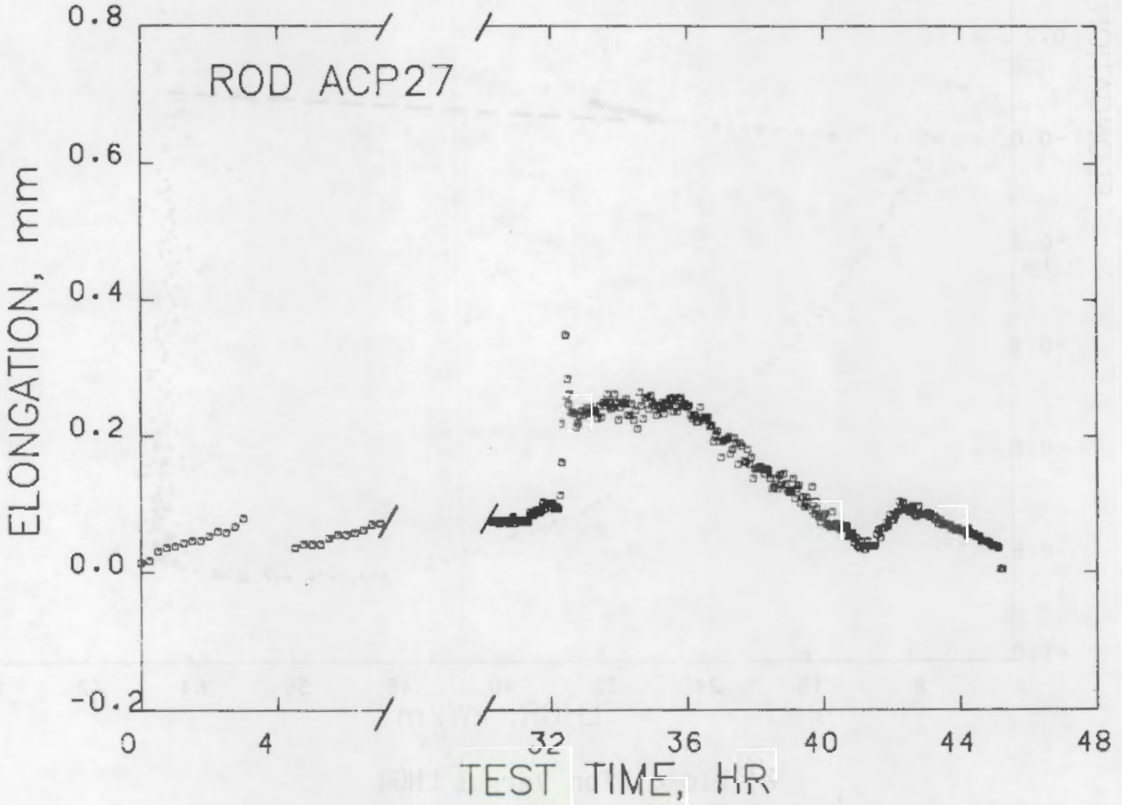

b) Elongation Versus Time

FIGURE 9. Elongation Signal During Power-Ramping of Rod ACP27 (see Table 4)

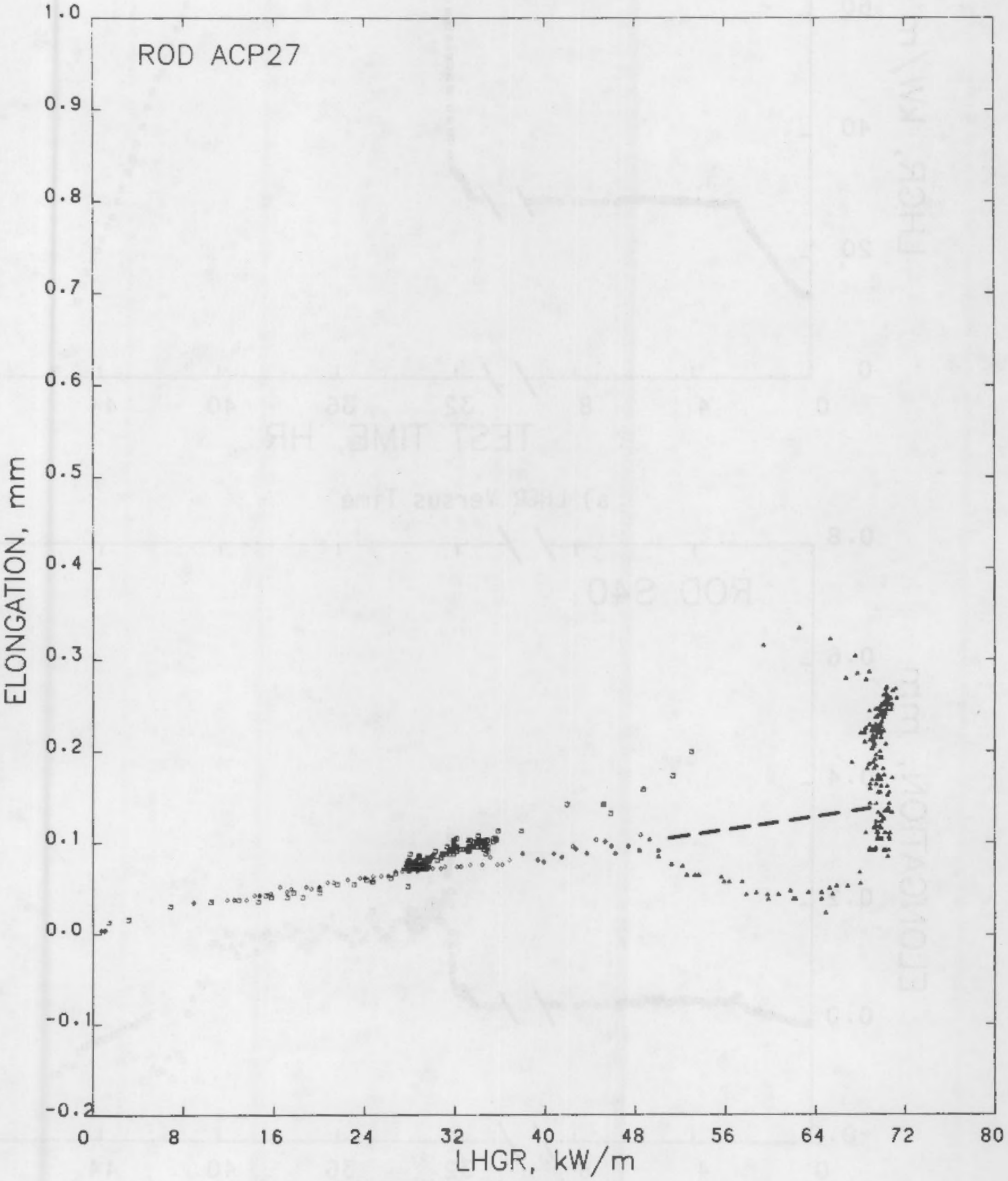

c) Elongation Versus LHGR

FIGURE 9. (contd)

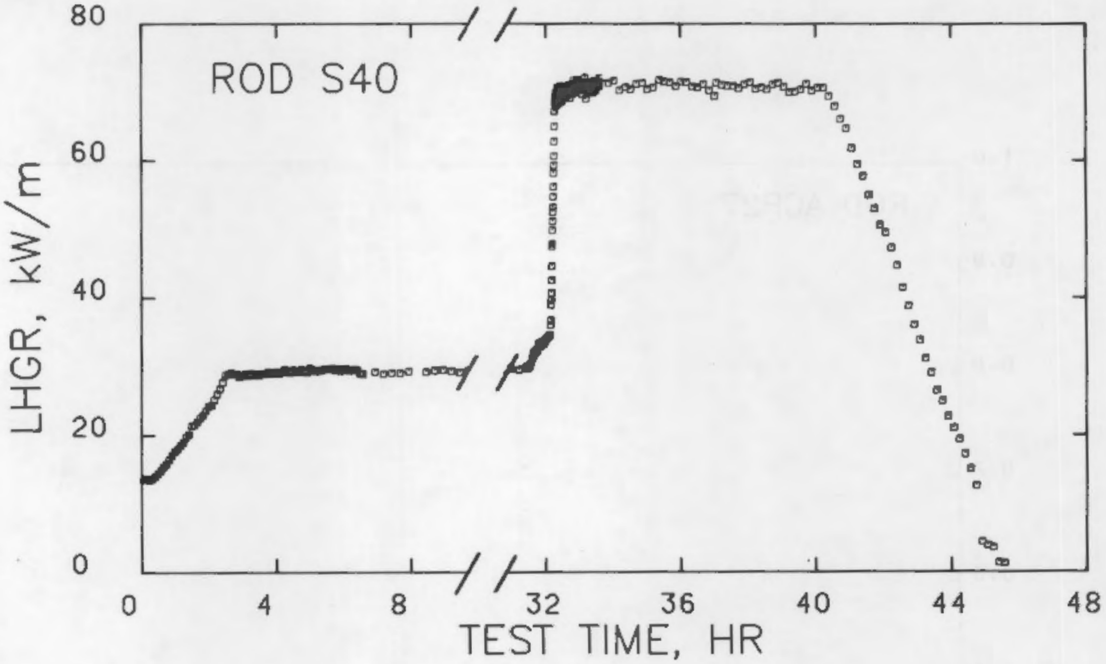

a) LHGR Versus Time

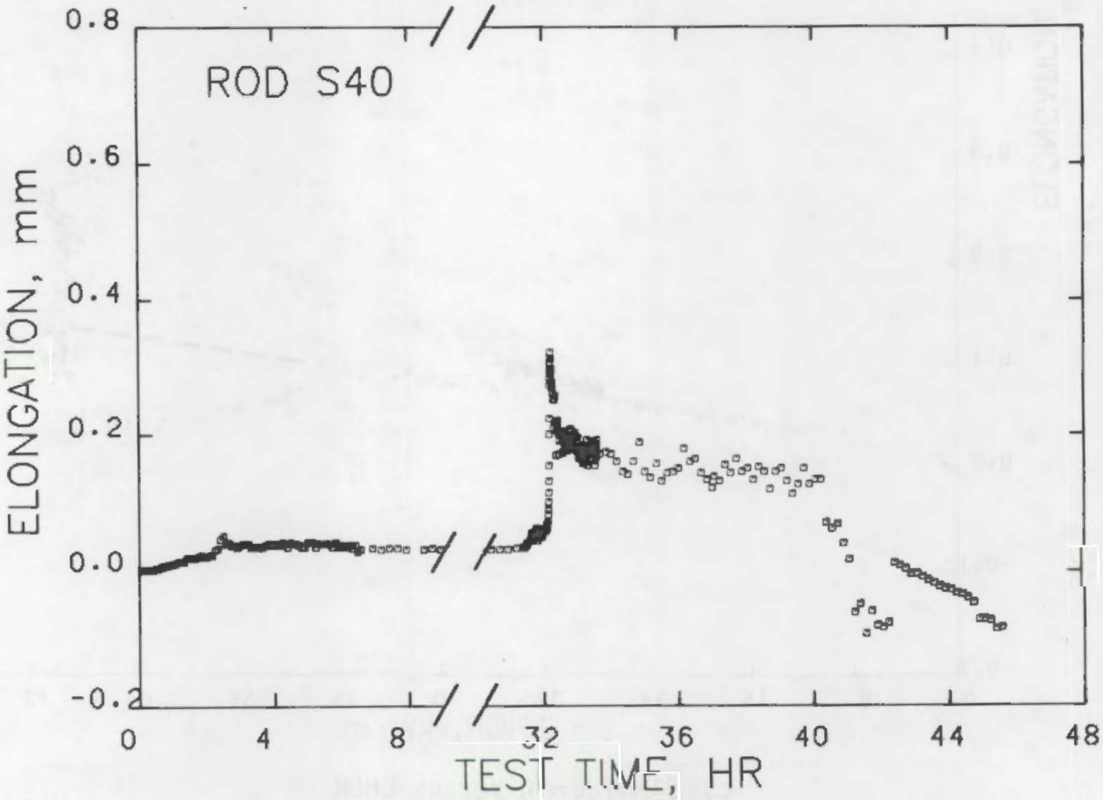

b) Elongation Versus Time

FIGURE 10. Elongation Signal During Power-Ramping of Rod S40 (see Table 4)

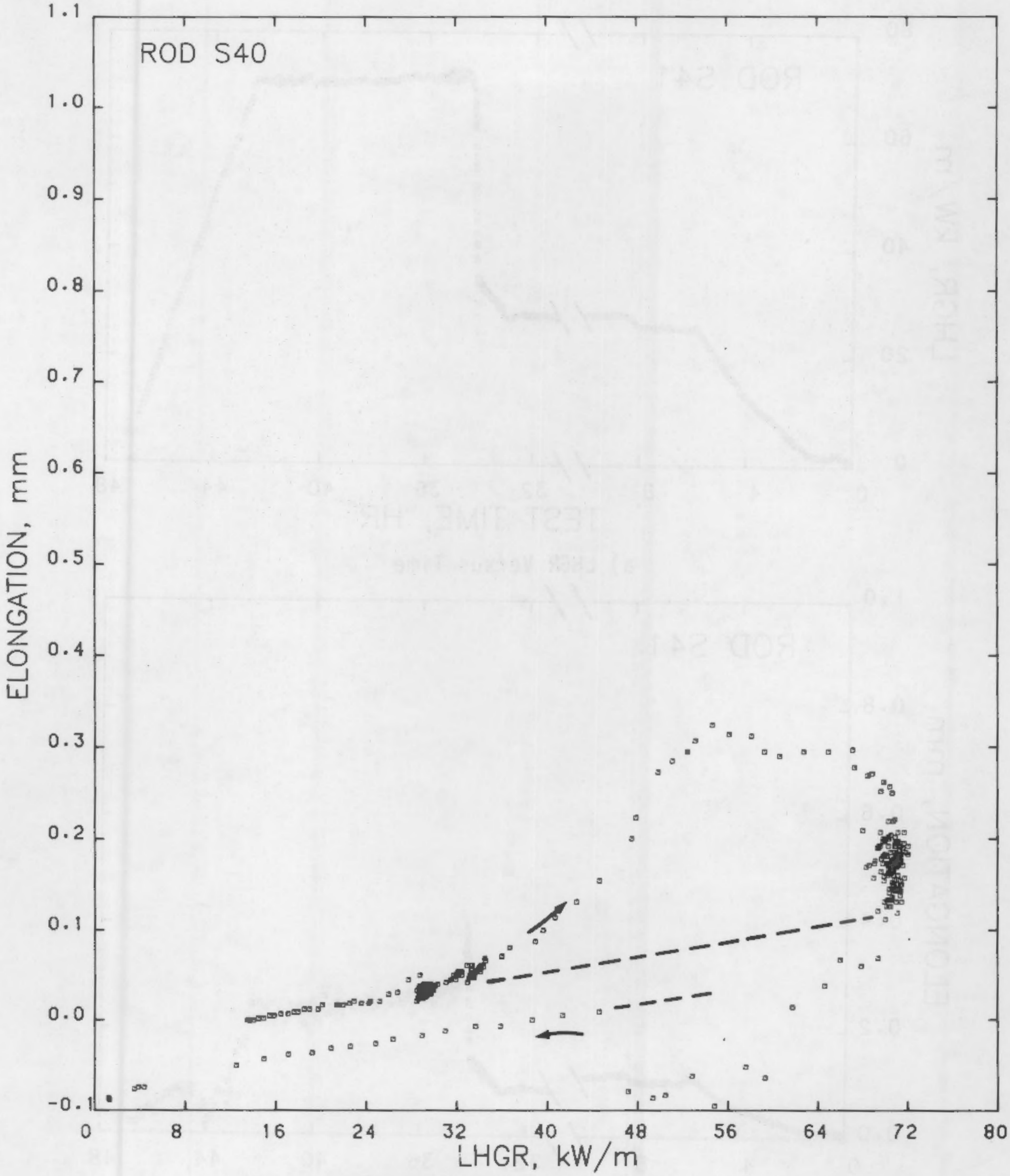

c) Elongation Versus LHGR

FIGURE 10. (contd)

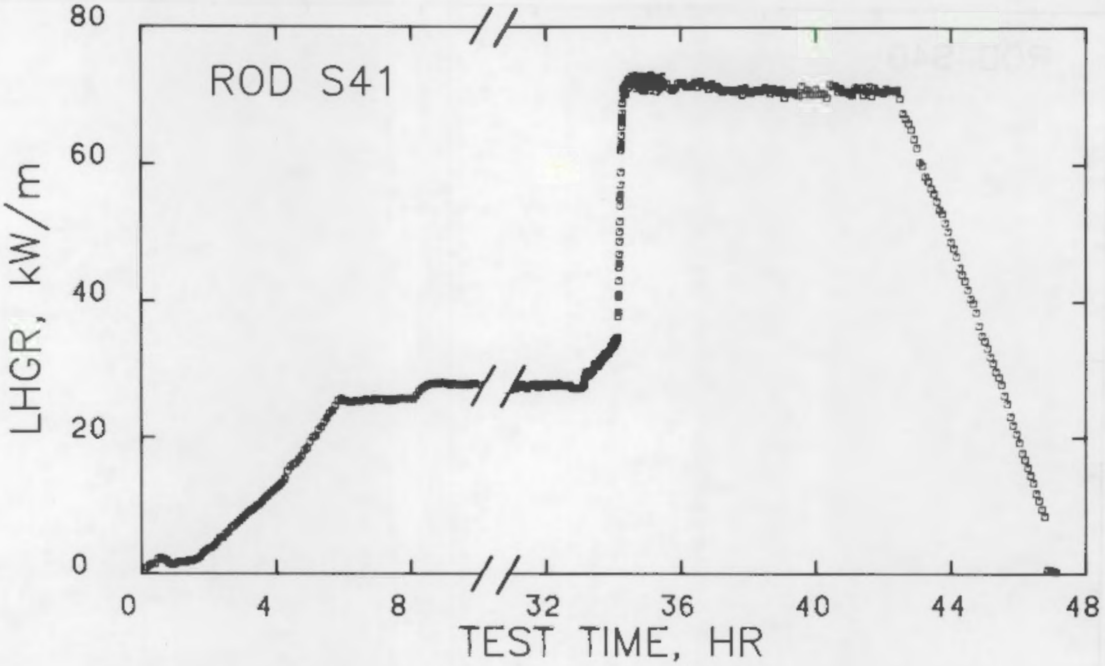

a) LHGR Versus Time

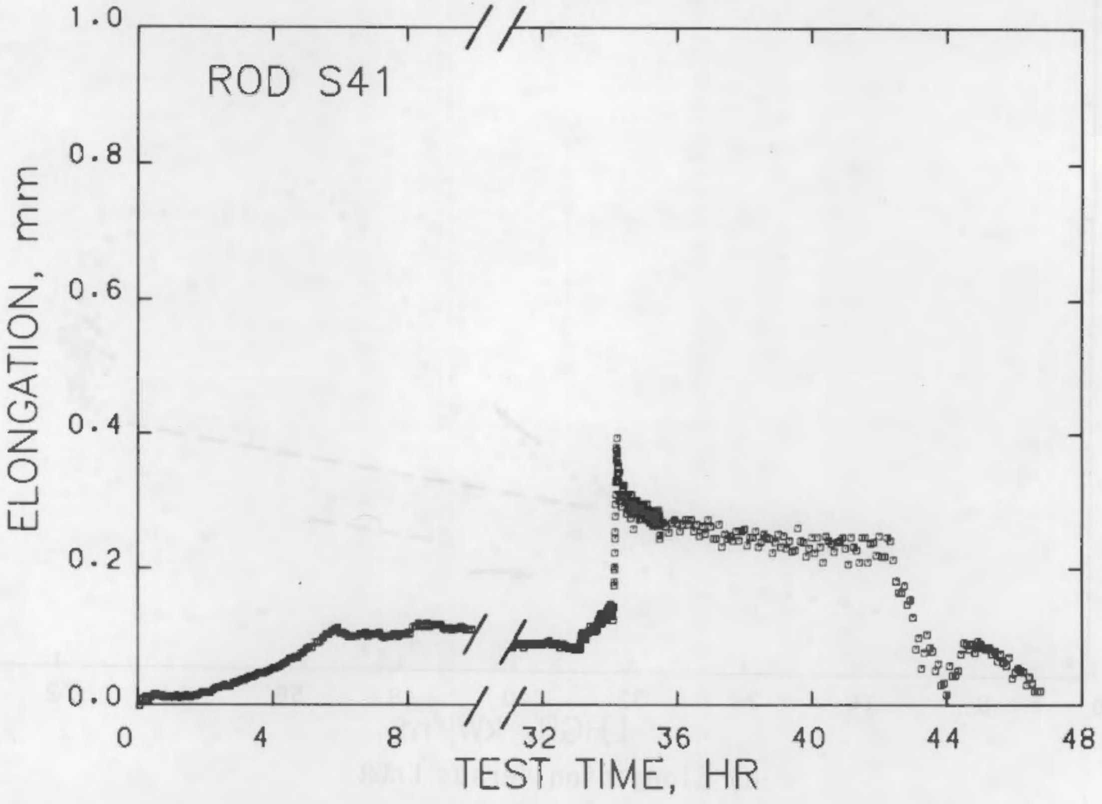

b) Elongation Versus Time

FIGURE 11. Elongation Signal During Power-Ramping of Rod S41 (see Table 4)

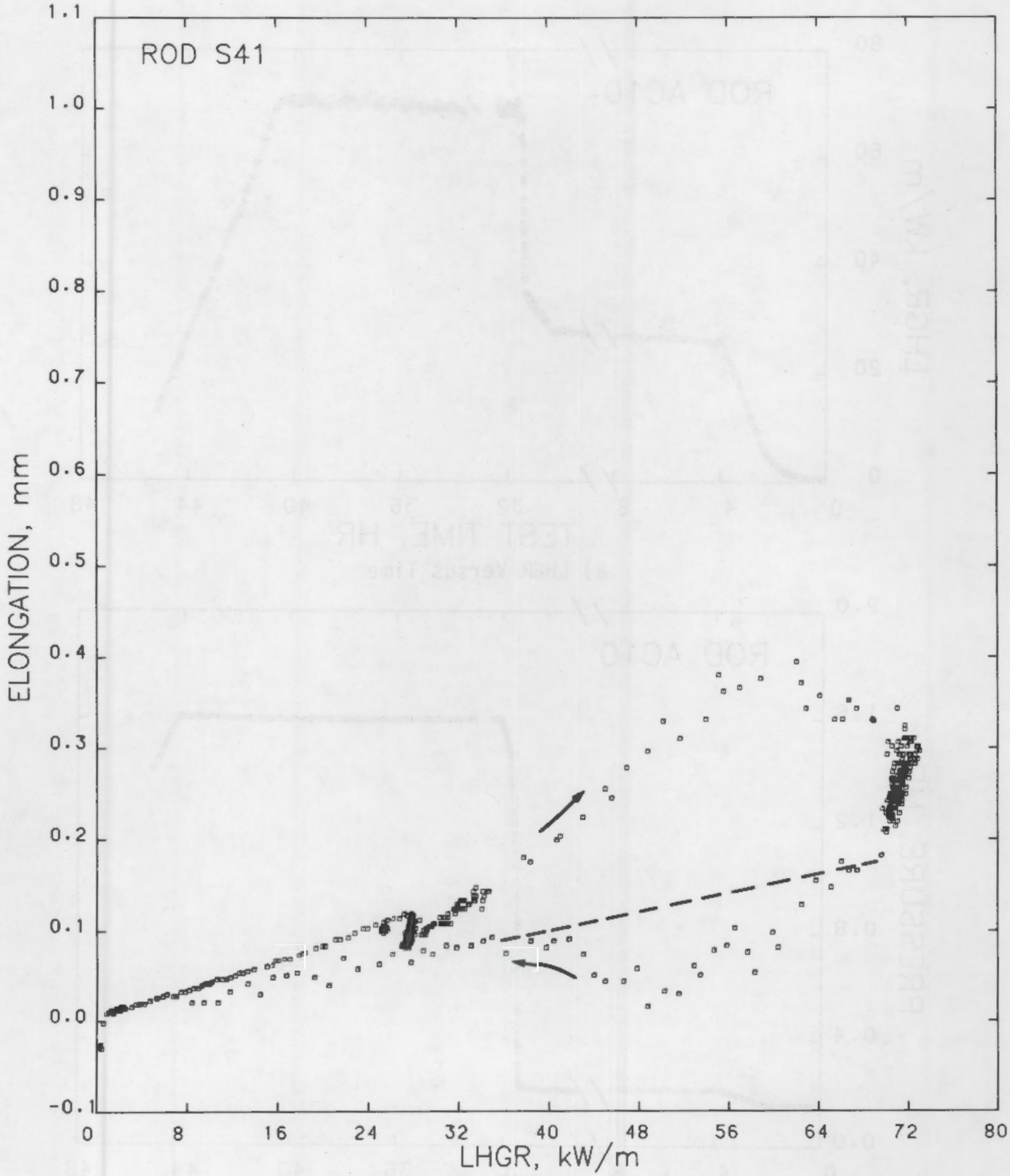

c) Elongation Versus LHGR

FIGURE 11. (contd)

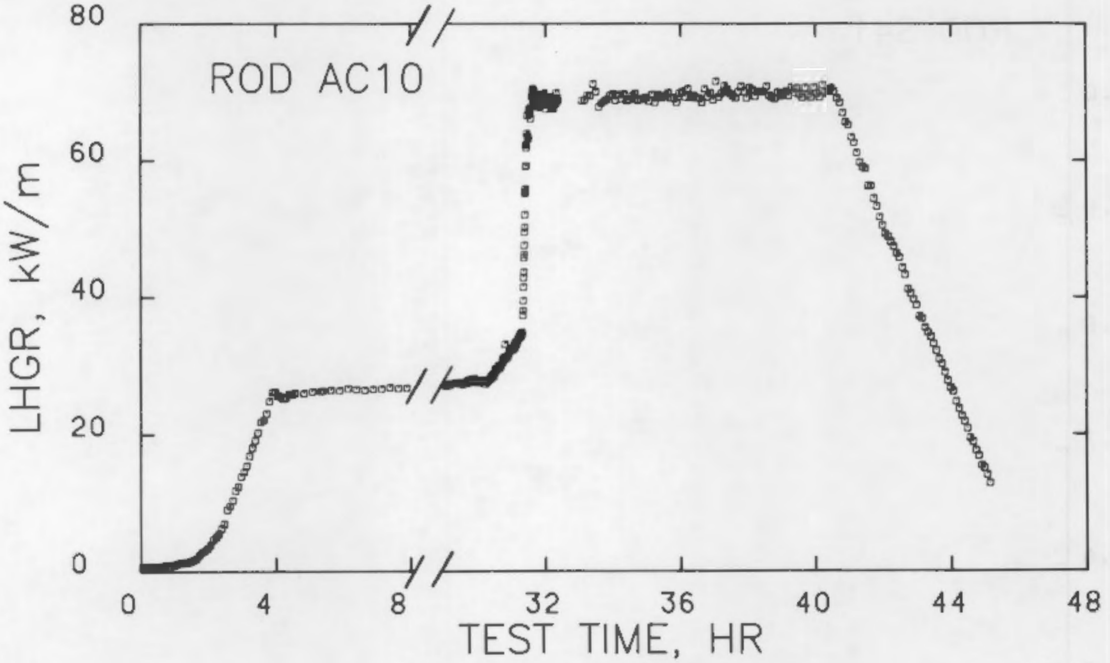

a) LHGR Versus Time

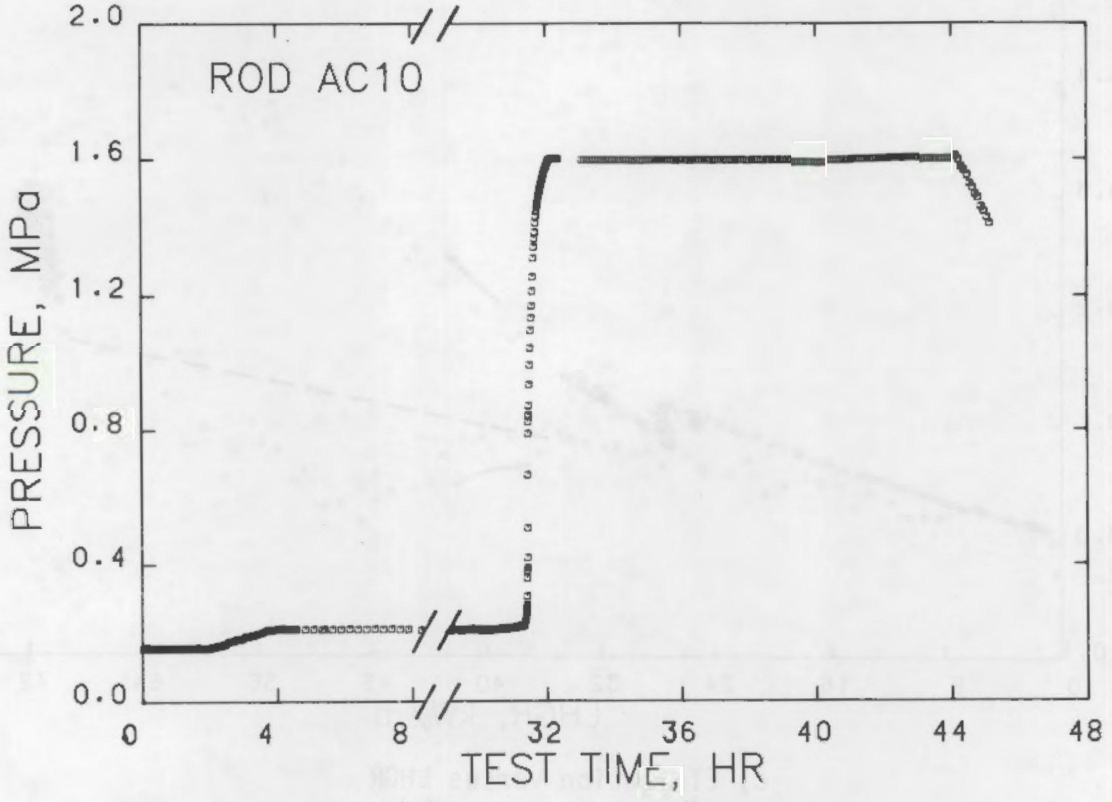

b) Pressure Versus Time

FIGURE 12. Pressure Signal During Power-Ramping of AC10

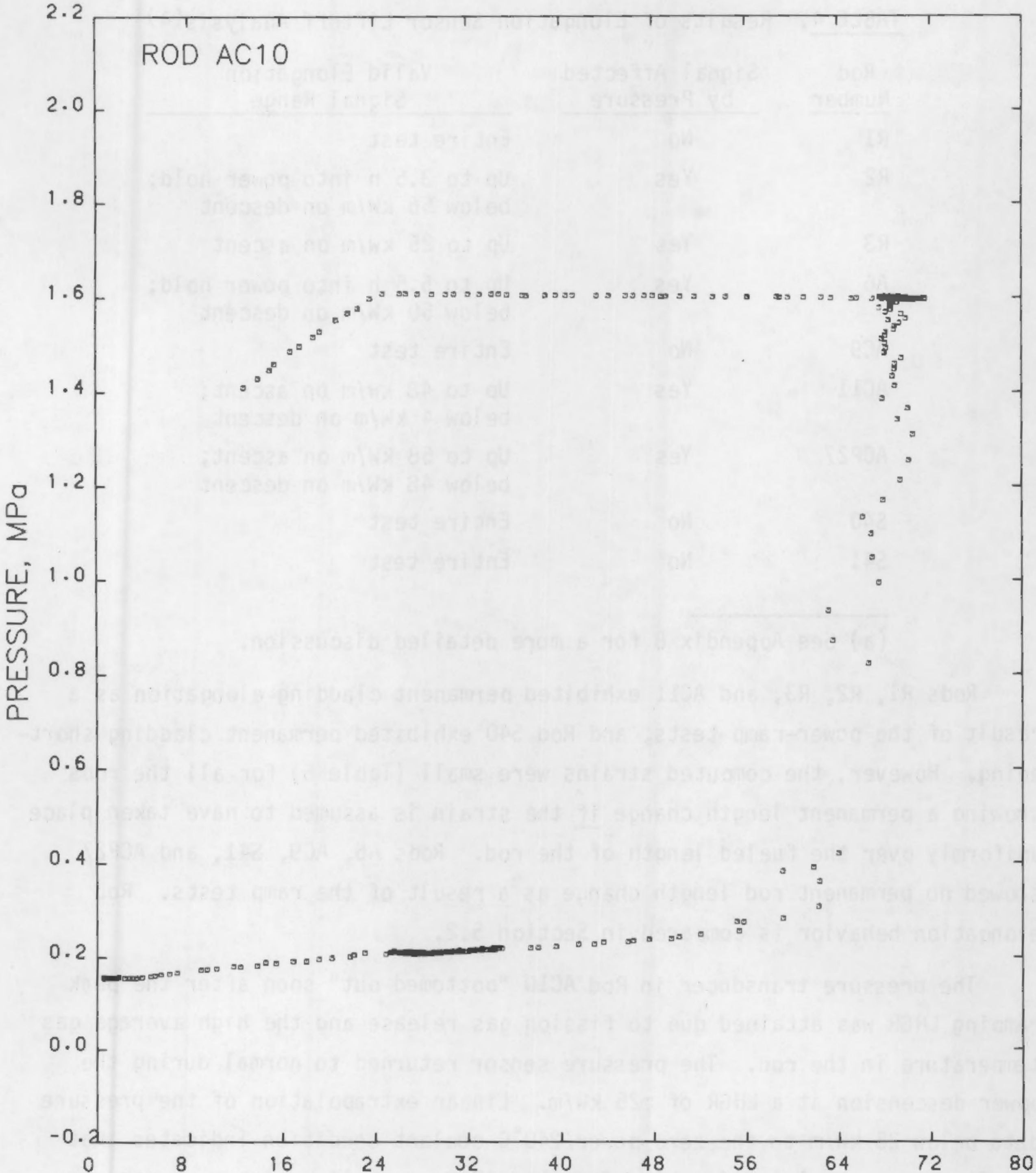

c) Pressure Versus LHGR

FIGURE 12. (contd)

TABLE 4. Results of Elongation Sensor Liftoff Analysis[a]

Rod Number	Signal Affected by Pressure	Valid Elongation Signal Range
R1	No	Entire test
R2	Yes	Up to 3.5 h into power hold; below 56 kW/m on descent
R3	Yes	Up to 25 kW/m on ascent
A6	Yes	Up to 5.5 h into power hold; below 50 kW/m on descent
AC9	No	Entire test
AC11	Yes	Up to 48 kW/m on ascent; below 4 kW/m on descent
ACP27	Yes	Up to 58 kW/m on ascent; below 48 kW/m on descent
S40	No	Entire test
S41	No	Entire test

(a) See Appendix B for a more detailed discussion.

Rods R1, R2, R3, and AC11 exhibited permanent cladding elongation as a result of the power-ramp tests; and Rod S40 exhibited permanent cladding shortening. However, the computed strains were small (Table 5) for all the rods showing a permanent length change <u>if</u> the strain is assumed to have taken place uniformly over the fueled length of the rod. Rods A6, AC9, S41, and ACP27 showed no permanent rod length change as a result of the ramp tests. Rod elongation behavior is compared in Section 5.2.

The pressure transducer in Rod AC10 "bottomed out" soon after the peak ramping LHGR was attained due to fission gas release and the high average gas temperature in the rod. The pressure sensor returned to normal during the power descension at a LHGR of ~25 kW/m. Linear extrapolation of the pressure data below 25 kW/m to the zero-power/240°C-coolant condition indicates that the fission gas release fraction from Rod AC10 was 0.44, which compares very well with the value obtained from the gas analysis during PIE (0.46). Based on a linear extrapolation, the peak pressure in the rod during the 8-h power

TABLE 5. Computed Cladding Strains Over Fueled Length of Rods Based on Elongation Sensor Data

Rod Number	Strain, %	Rod Number	Strain, %
R1	+0.06	A6	0
R2	+0.02	AC9	0
R3	>0.03	ACP27	0
AC11	+0.02	S41	0
S40	-0.02		

hold was between 2.2 and 2.3 MPa (Figure 12). The as-built gas volume of 9.8 cm^3 and a fission gas generation value of 31 cm^3 (STP)/MWd were used for the fission gas release calculation.

4.2 RESULTS OF NONDESTRUCTIVE EXAMINATIONS AT HALDEN

The methods used for the NDE of the fuel rods at Halden were described in Section 3.5. The results of visual, eddy-current, and profilometry examinations are presented in this section.

4.2.1 Visual Examination

Visual examinations were completed on all the rods after steady-state irradiation and again after the power-ramp tests. Nothing unusual--such as x-marks, corrosion, rod bowing, or significant scratches--was observed on any of the rods. All the rods were relatively uniformly gray, indicating a slight and expected oxidation of the cladding surface. The fuel rods were not autoclaved before irradiation; therefore, the slight oxidation occurred during steady-state irradiation.

4.2.2 Eddy-Current Examination

Eddy-current examinations were conducted at Halden before and after power-ramping as described in Section 3.5.2. Evidence of periodic cladding wall thickness changes produced by rocking during fabrication were observed during the examinations as was the presence of thermocouples in those rods with thermocouples. No signals indicative of incipient cladding defects, e.g., cracks or corrosion, were observed in any of the rods either before or after the power-ramp tests.

4.2.3 Profilometry

Preramp and postramp profilometry measurements were made at azimuthal orientations of 0°, 45°, 90°, and 135° along the length of the rods as described in Section 3.5.3. The same equipment and the same orientations were used for both measurements. Table 6 lists the appropriate figure numbers for each set of preramp and postramp profilometry traces for each rod. Data from the individual traces were also averaged as a function of rod length. The figure number for each of these averaged traces is also listed in Table 6.

The traces typically indicated an approximately sinusoidal feature on the cladding surface that was produced by rocking that had occurred during tubing manufacture. In general, the postramp traces followed the preramp rocking pattern both in shape and magnitude with a few exceptions: in Rod R1 from the 50- to the 300-mm levels in the 45° trace (Figure 14); in Rod R2 at the 225-mm level in the 0° trace (Figure 17) and the 315- and 410-mm levels in the 45° trace (Figure 18); in Rod AC9 at the 290-mm level in the 45° trace (Figure 30); in Rod S41 at the 85- and 315-mm levels in the 90° trace (Figure 51) and at the 415-mm level in the 0° trace (Figure 49). These deviations may be representative of localized FCMI of relatively short lengths in these rods. It is noteworthy that the rods that indicated the greatest cladding strains during the ramp tests, i.e., the reference and sphere-pac rods (see Table 5), had the most deviations from the rocking pattern. No definite ridging patterns, which would indicate significant amounts of localized mechanical interaction at pellet-pellet interfaces, were found superimposed on the rocking pattern of any of the

TABLE 6. Identification of Figure Numbers for Profilometry Data

	Figure Number for Profilometry Data				
Rod Number	0°	45°	90°	135°	Average
R1	13	14	15	16	53
R2	17	18	19	20	54
R3	21	22	23	24	55
A6	25	26	27	28	56
AC9	29	30	31	32	57
AC10	33	34	35	36	58
AC11	37	38	39	40	59
ACP27	41	42	43	44	60
S40	45	46	47	48	61
S41	49	50	51	52	62

rods with pellets. The lack of ridging is probably primarily due to the lack of cladding creepdown during the steady-state irradiation of the rods in the HBWR. However, the short pellets (length/diameter = 0.8) used in the reference and annular fuel designs would cause less hourglassing of the pellets and probably also contributed to the absence of ridges.

Examination of the profilometry traces for each rod reveals differing degrees of change in the surface or shape at any particular axial location as a result of the ramp test. In most cases, the shapes did not change to an ellipse or oval shape but to a more complicated egg-type shape. This trend is illustrated for Rod A6 where the 0° and 45° traces (Figures 25 and 26) show little change in diameter as a result of the ramp test while the traces at 90° and 135° (Figures 27 and 28) show the rod to be smaller in diameter after the ramp test. In most of the rods, the diameter changes were at different orientations as a function of length (e.g., all the pelletized rods) while in others the diameter changes were primarily in the same direction along the length of the rod (e.g., Rod S41). Because the shapes of the cladding tubes changed, no evidence could be ascertained for permanent hoop strain from the individual traces for any of the rods.

In an attempt to further determine if any permanent hoop strain had occurred, the four profilometry traces for each rod were averaged as a function of the length of the rod (see Table 6). The results of this averaging were also inconclusive because several averaged plots indicated that the rods were smaller in diameter as a result of the ramp tests while other plots indicated that the rods were the same or slightly larger in diameter after the ramp tests. Those rods that were apparently smaller (e.g., Rods A6, S40, and S41) exhibited no permanent rod lengthening during the ramp tests (see Figures 6, 10, and 11). In the absence of permanent lengthening, the only way the rods could be physically smaller in diameter would be for the wall to have become thicker. Given the postulated stress distribution during the ramp tests, i.e., axial and hoop tensile forces and a radial compressive force, it is impossible for the wall thickness to increase. Therefore, it is probable that the averaged plots represent a stochastic average where in some cases the four values that were sampled from the egg-shaped rods were less than the true average

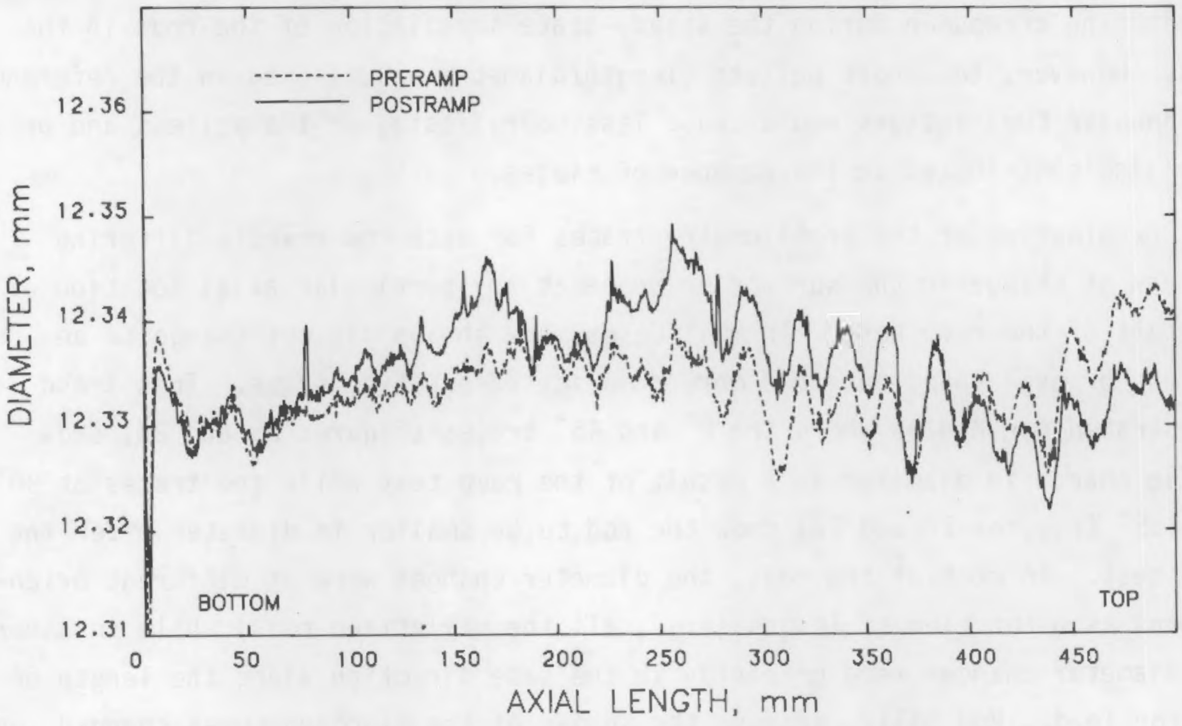

FIGURE 13. Preramp and Postramp Profilometry for Rod R1 at 0°

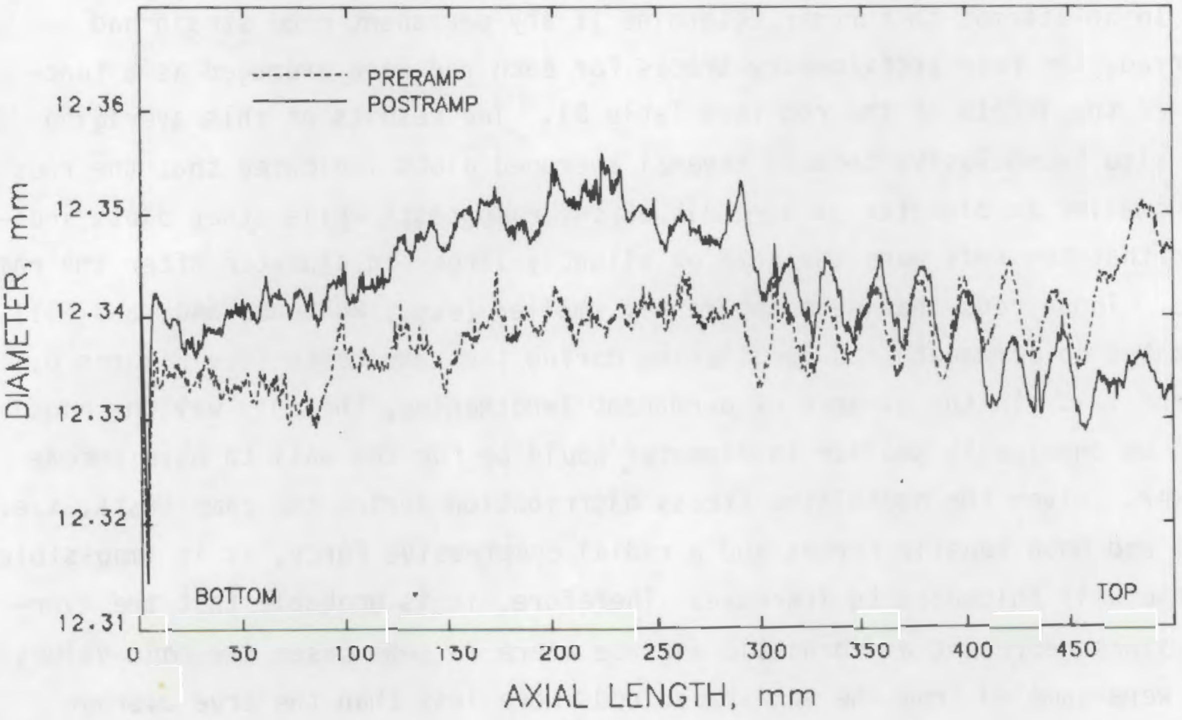

FIGURE 14. Preramp and Postramp Profilometry for Rod R1 at 45°

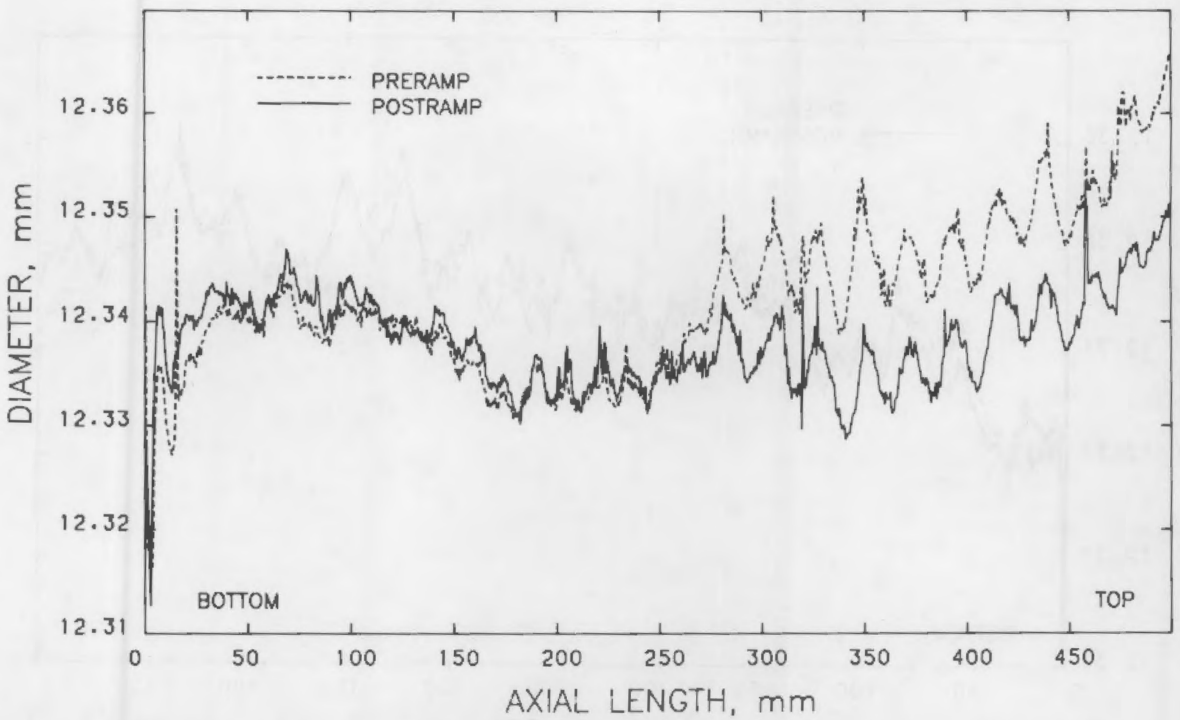

FIGURE 15. Preramp and Postramp Profilometry for Rod R1 at 90°

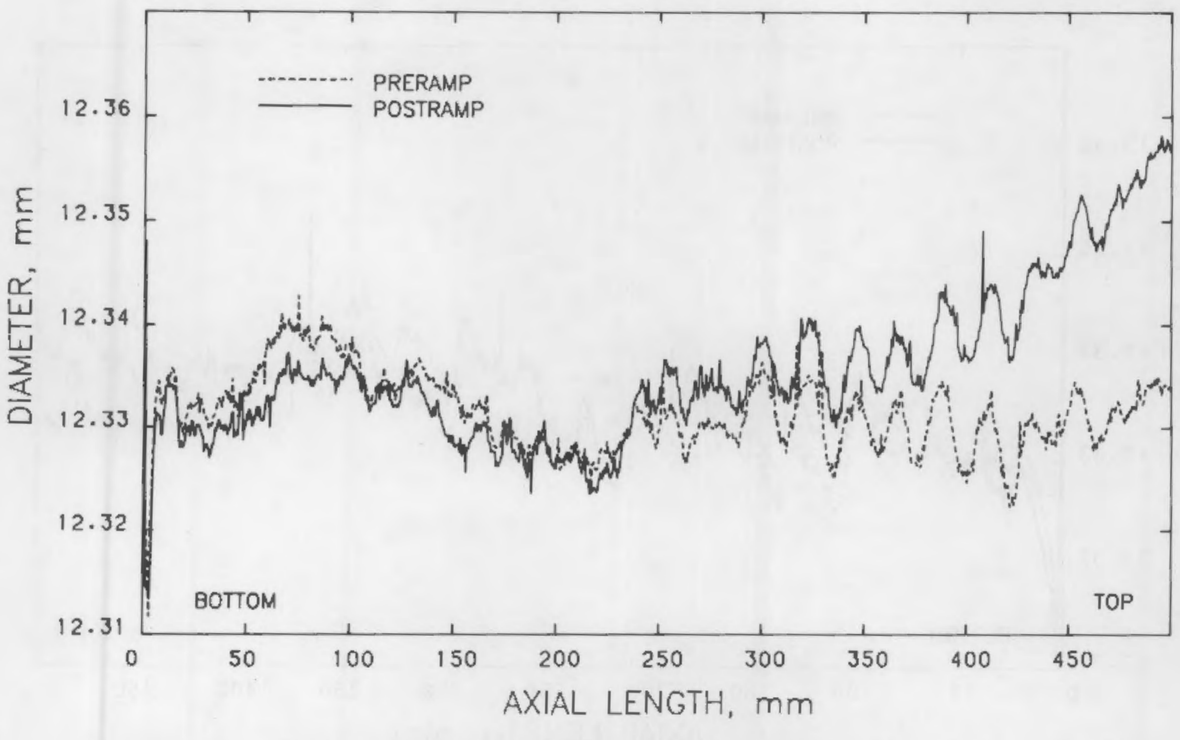

FIGURE 16. Preramp and Postramp Profilometry for Rod R1 at 135°

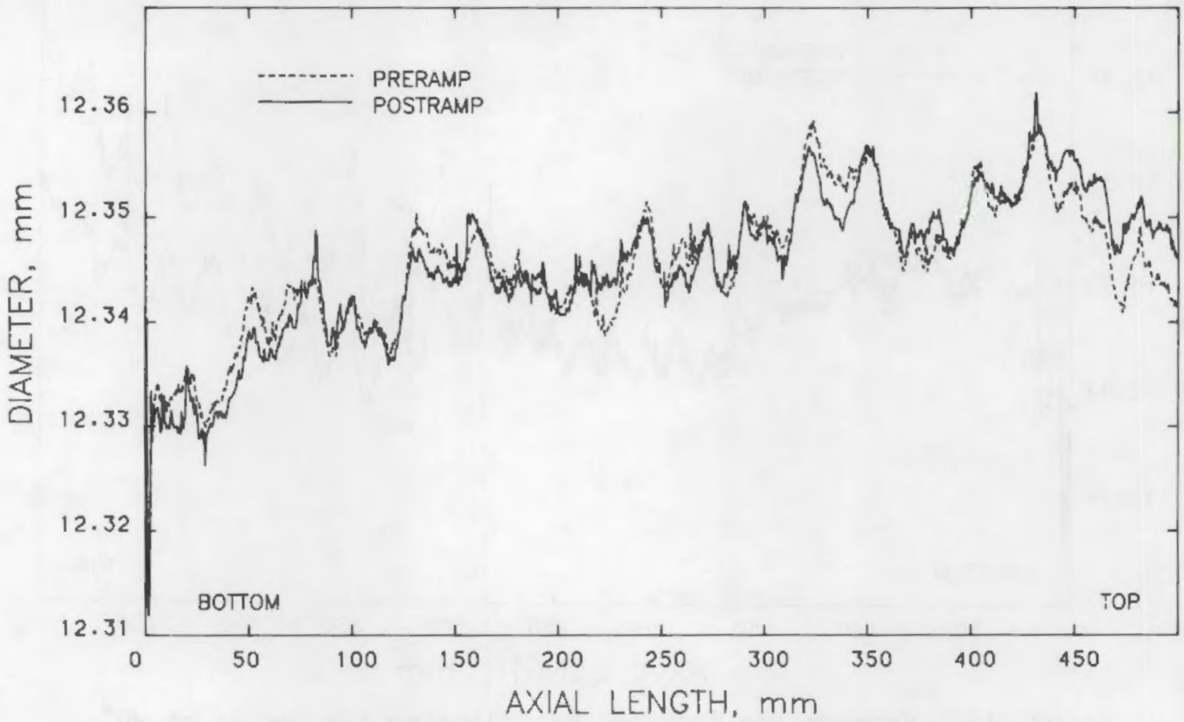

FIGURE 17. Preramp and Postramp Profilometry for Rod R2 at 0°

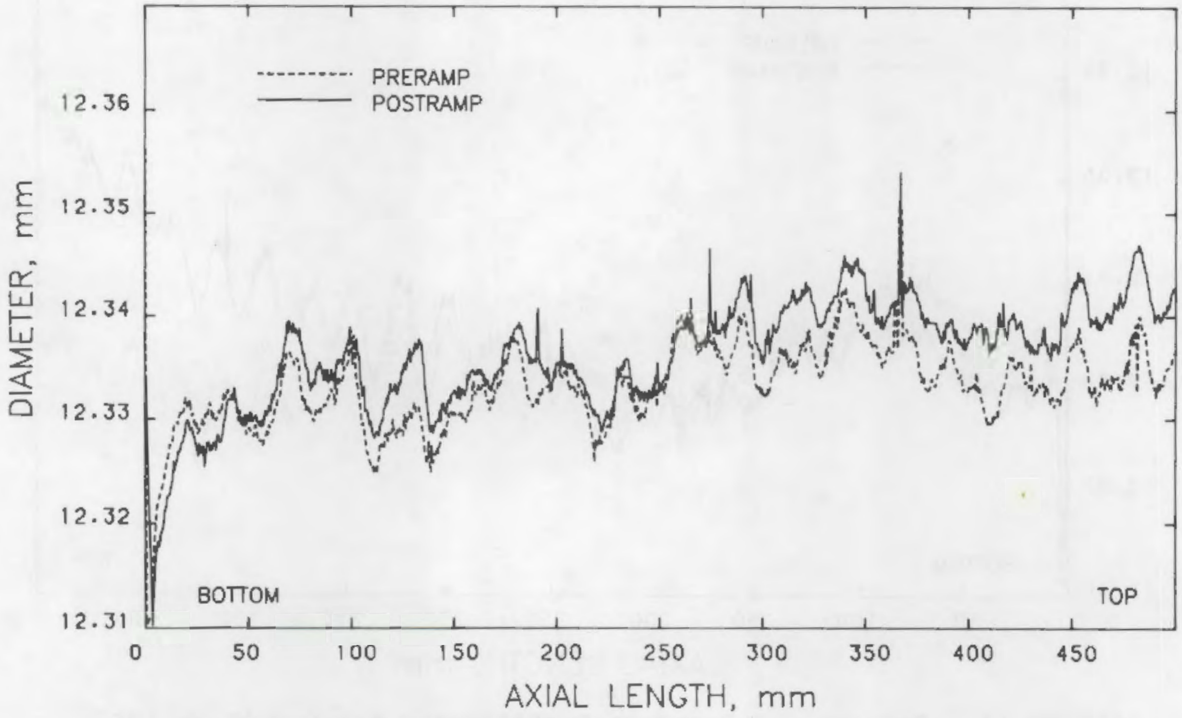

FIGURE 18. Preramp and Postramp Profilometry for Rod R2 at 45°

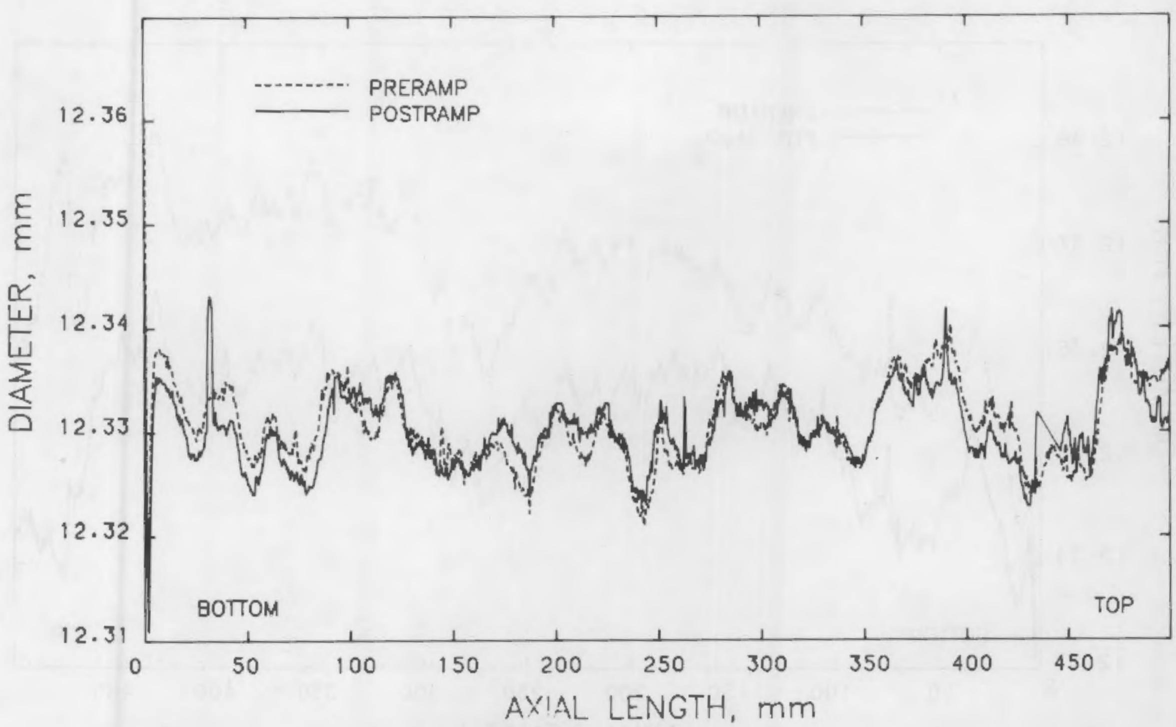

FIGURE 19. Preramp and Postramp Profilometry for Rod R2 at 90°

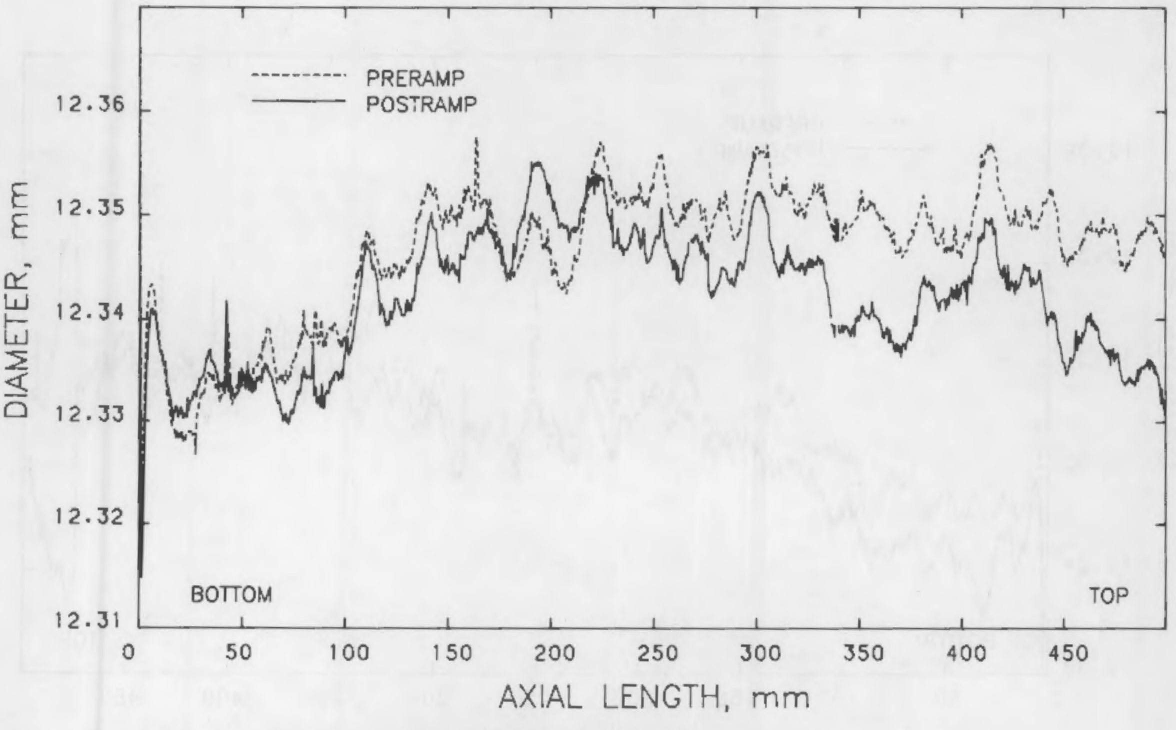

FIGURE 20. Preramp and Postramp Profilometry for Rod R2 at 135°

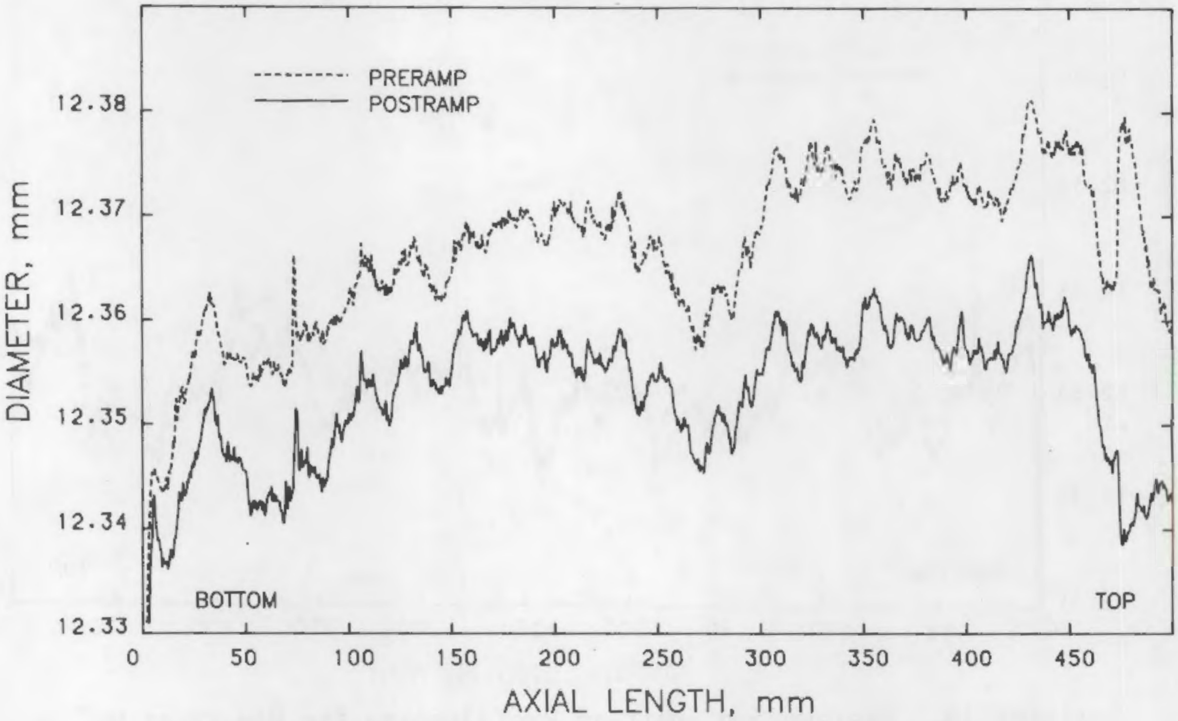

FIGURE 21. Preramp and Postramp Profilometry for Rod R3 at 0°

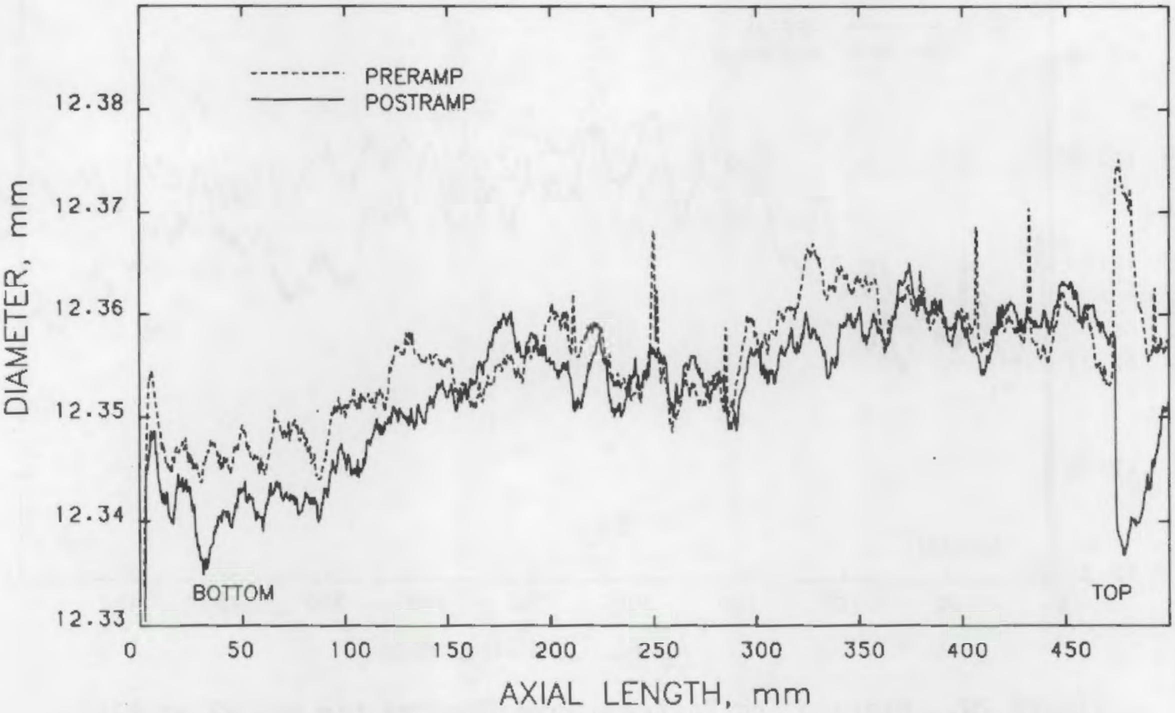

FIGURE 22. Preramp and Postramp Profilometry for Rod R3 at 45°

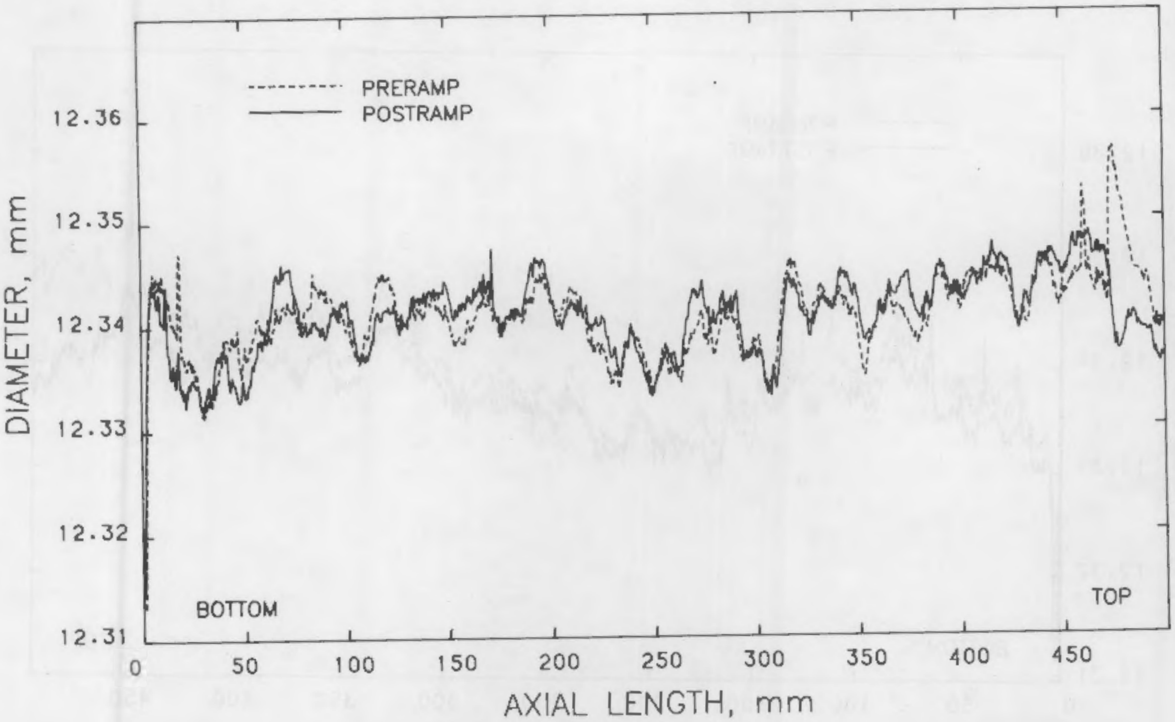

FIGURE 23. Preramp and Postramp Profilometry for Rod R3 at 90°

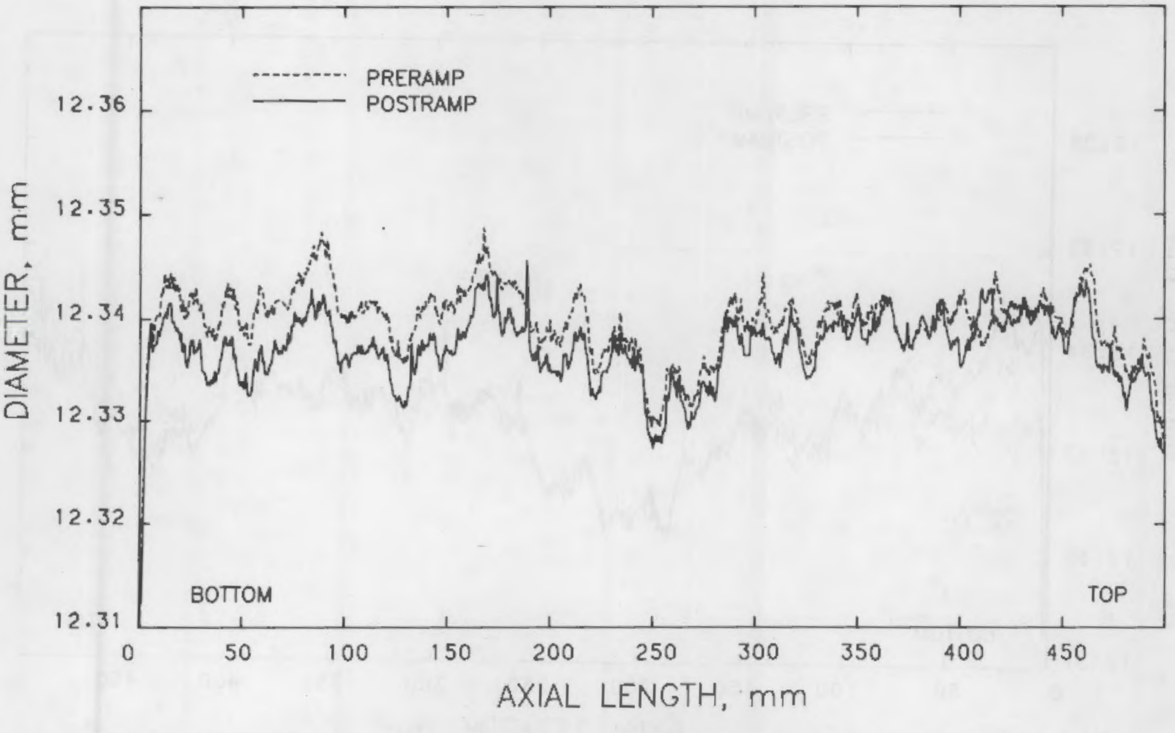

FIGURE 24. Preramp and Postramp Profilometry for Rod R3 at 135°

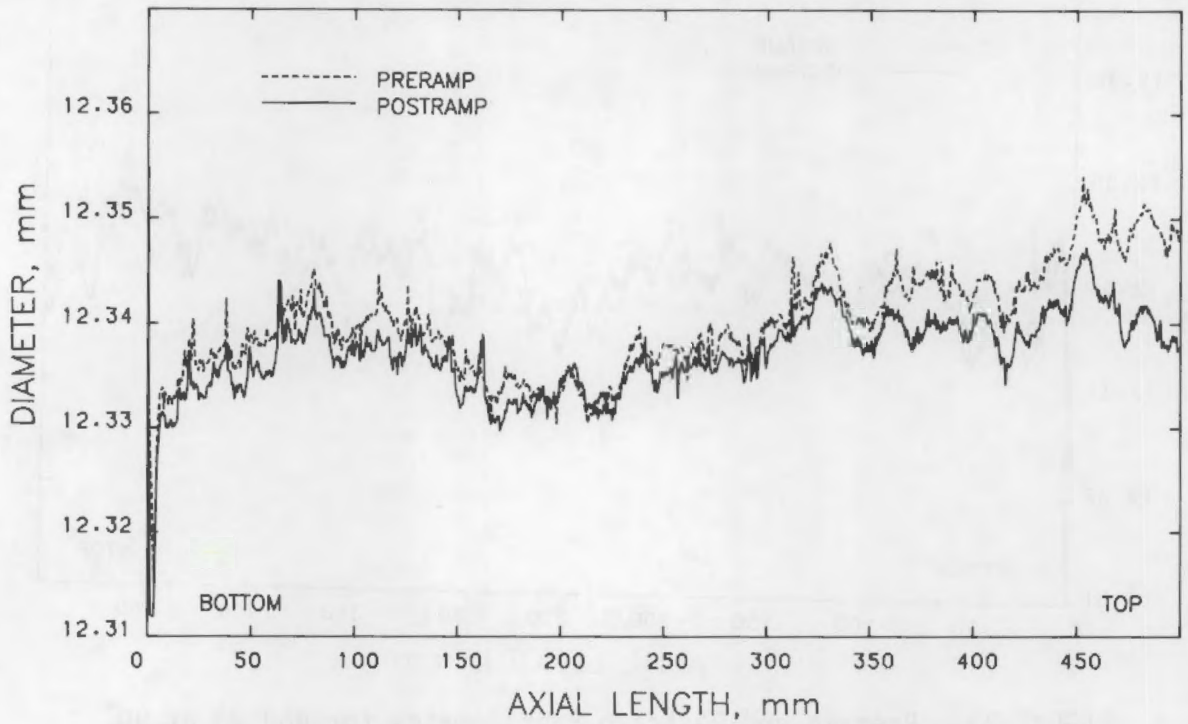

FIGURE 25. Preramp and Postramp Profilometry for Rod A6 at 0°

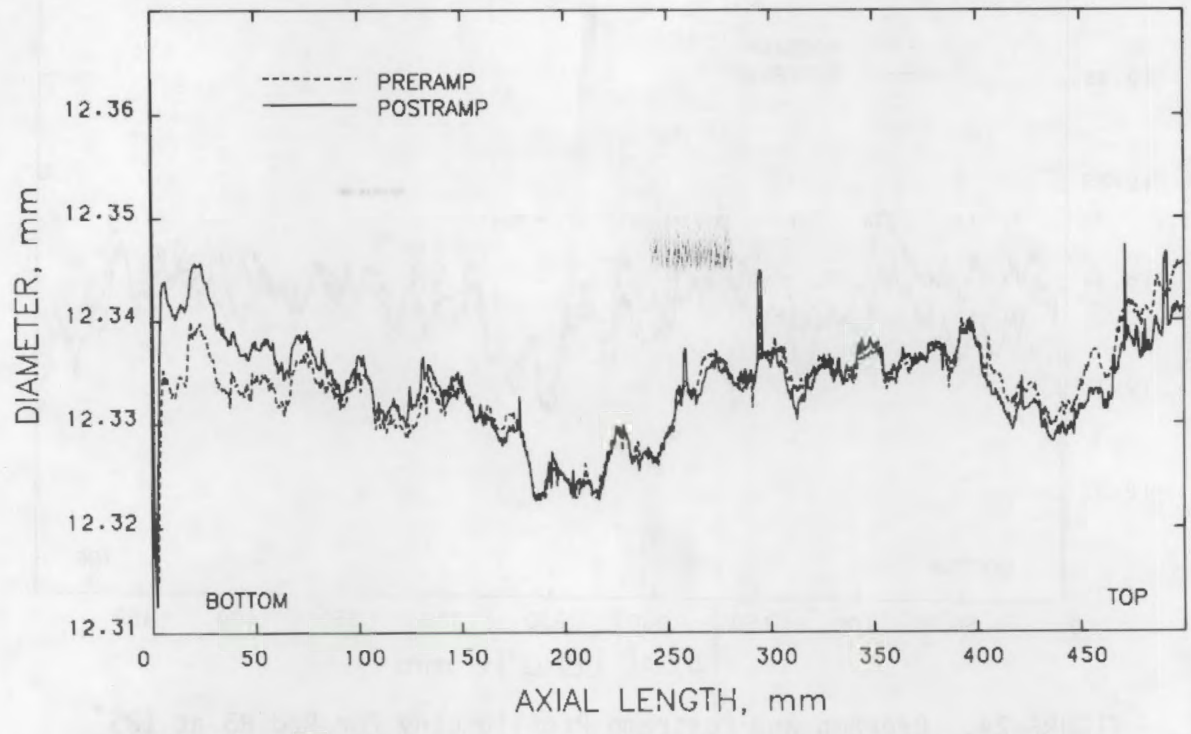

FIGURE 26. Preramp and Postramp Profilometry for Rod A6 at 45°

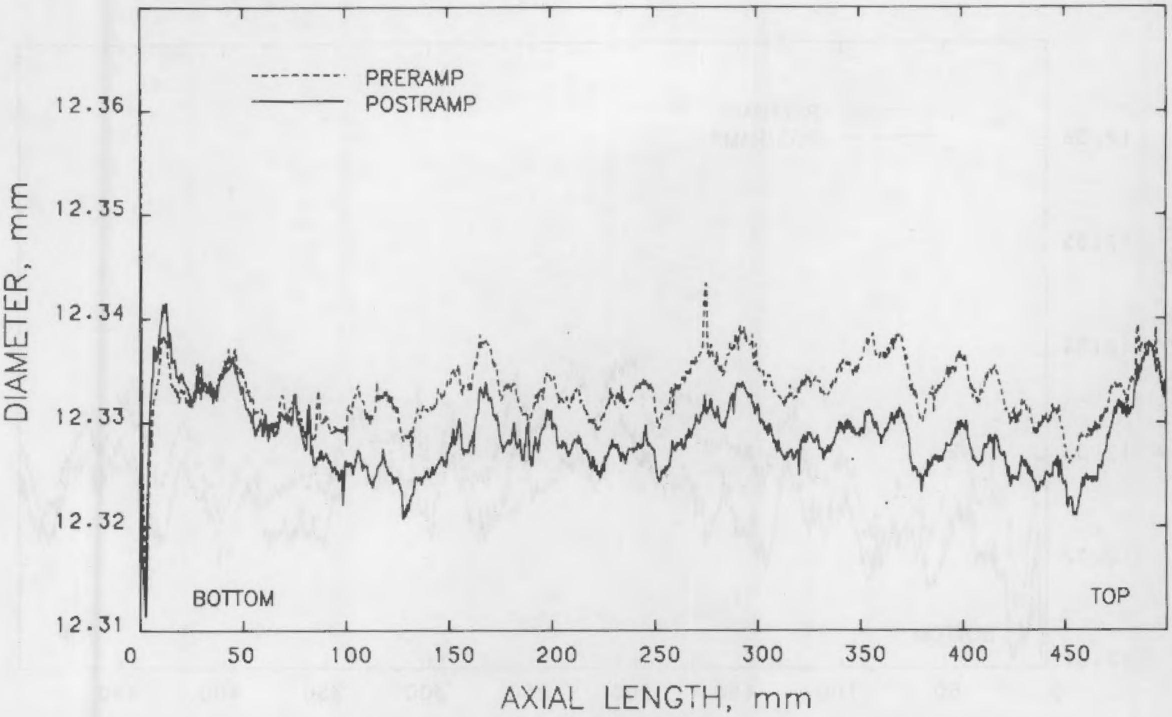

FIGURE 27. Preramp and Postramp Profilometry for Rod A6 at 90°

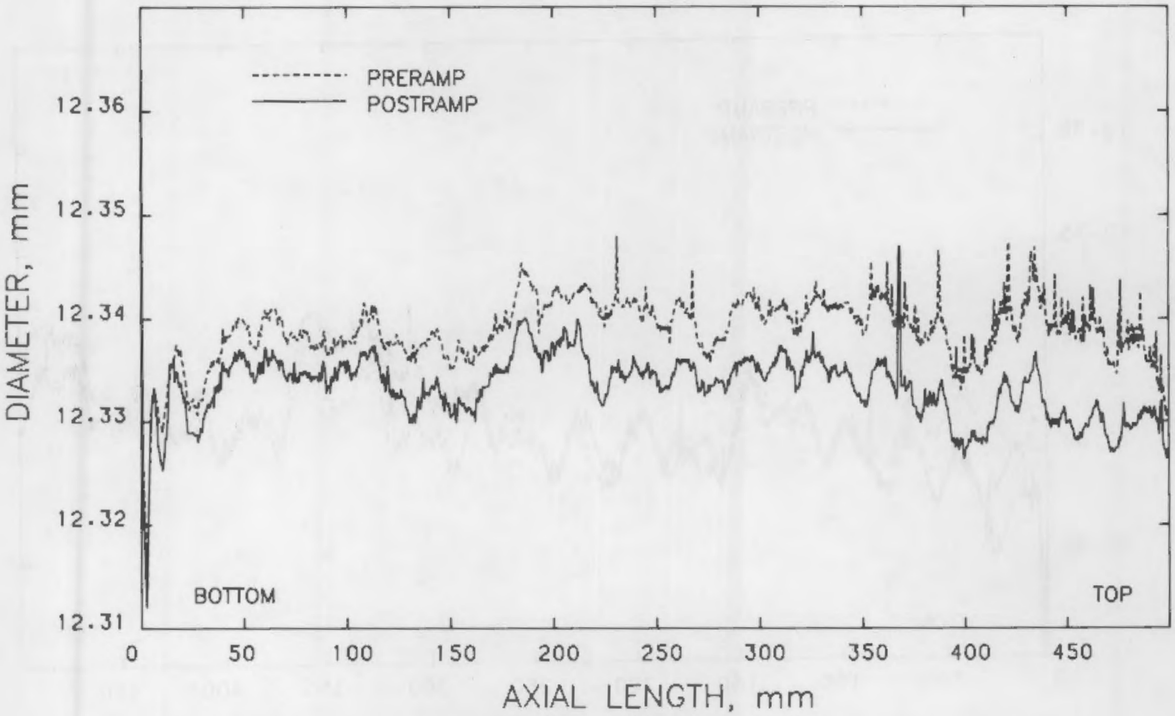

FIGURE 28. Preramp and Postramp Profilometry for Rod A6 at 135°

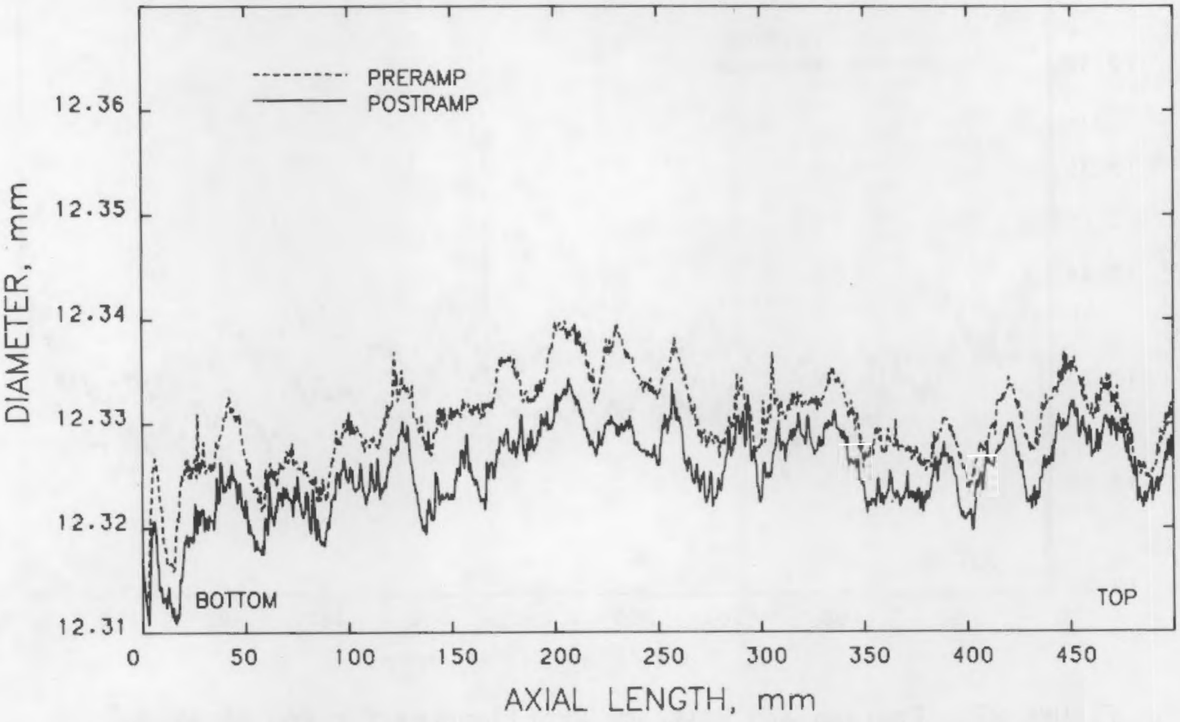

FIGURE 29. Preramp and Postramp Profilometry for Rod AC9 at 0°

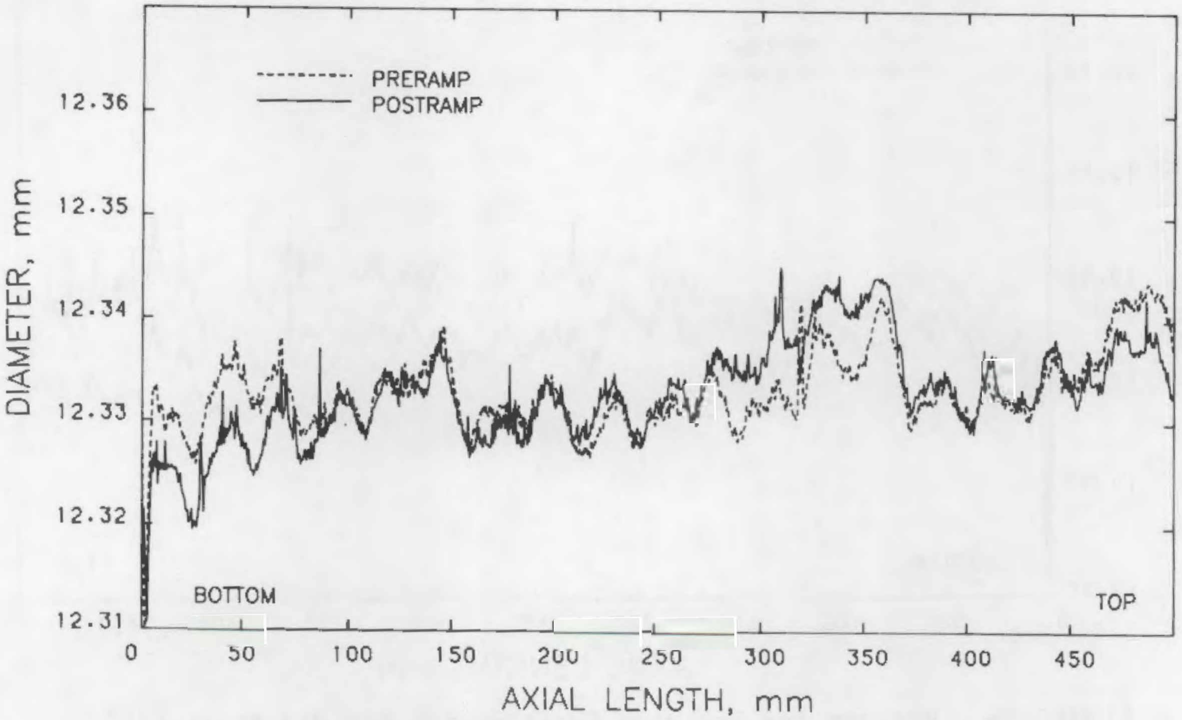

FIGURE 30. Preramp and Postramp Profilometry for Rod AC9 at 45°

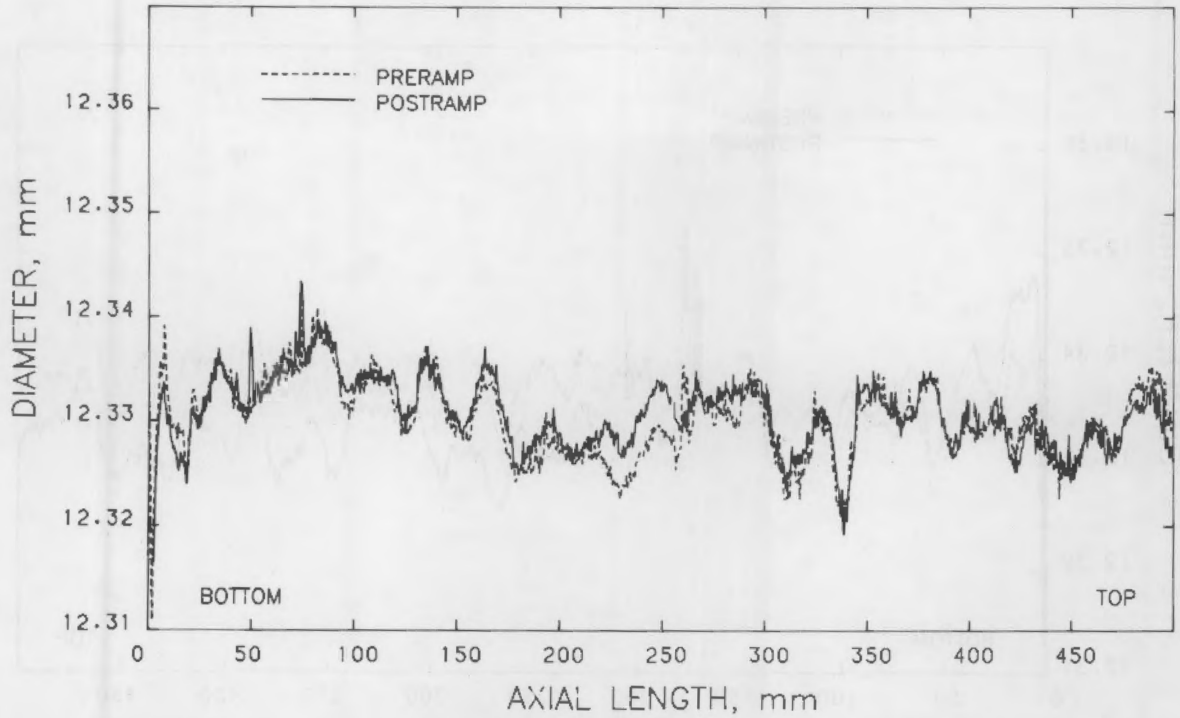

FIGURE 31. Preramp and Postramp Profilometry for Rod AC9 at 90°

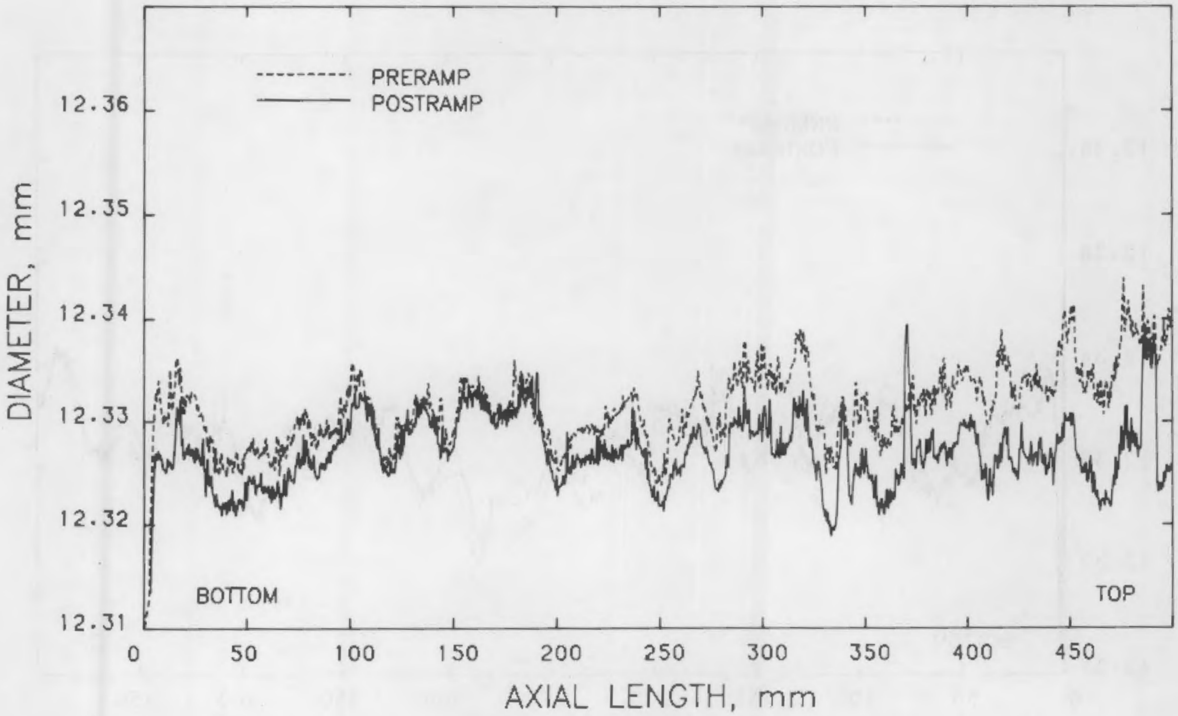

FIGURE 32. Preramp and Postramp Profilometry for Rod AC9 at 135°

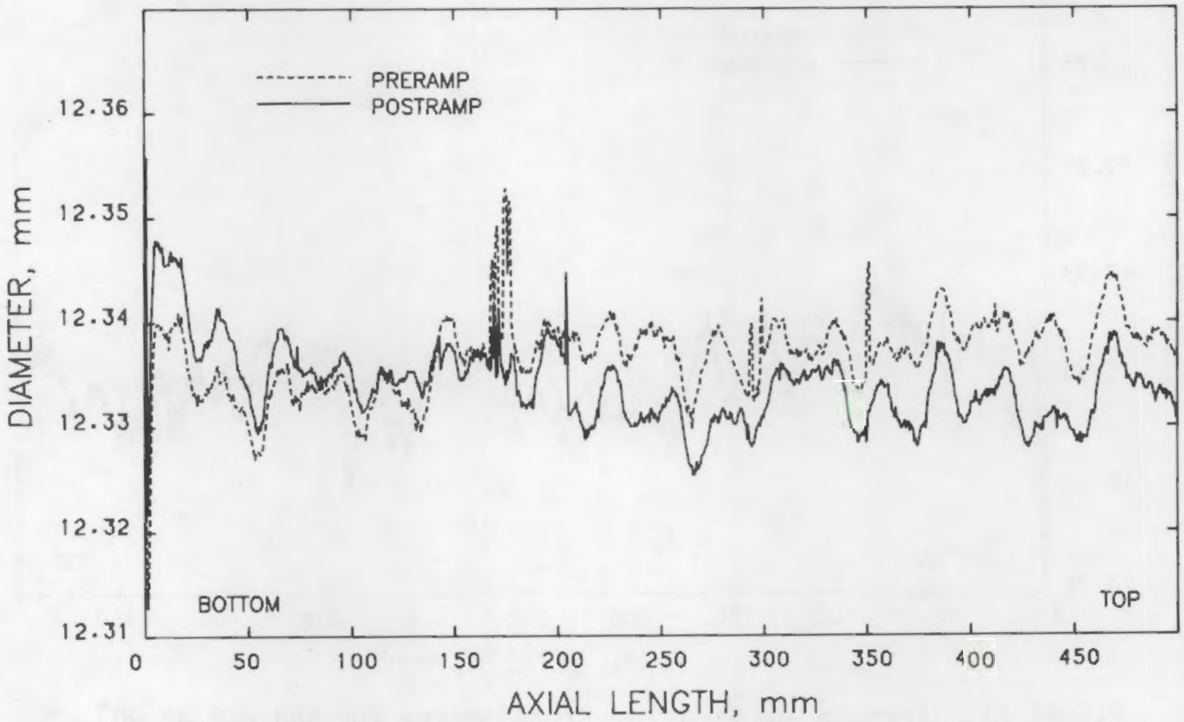

FIGURE 33. Preramp and Postramp Profilometry for Rod AC10 at 0°

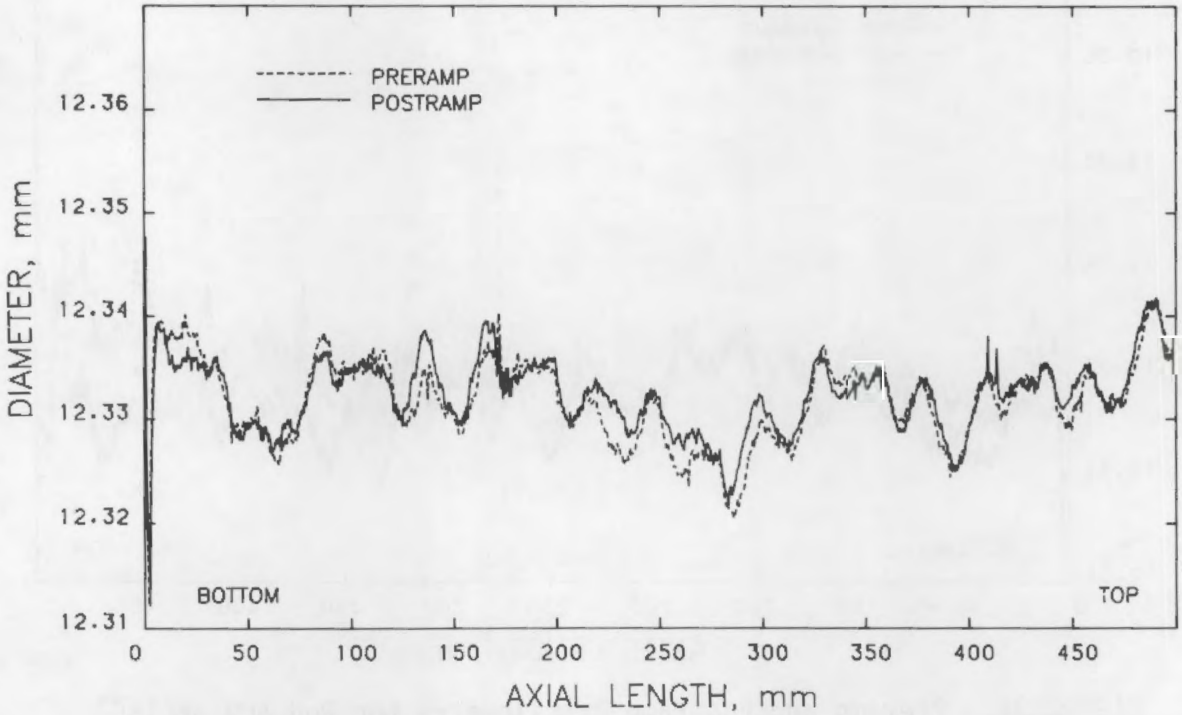

FIGURE 34. Preramp and Postramp Profilometry for Rod AC10 at 45°

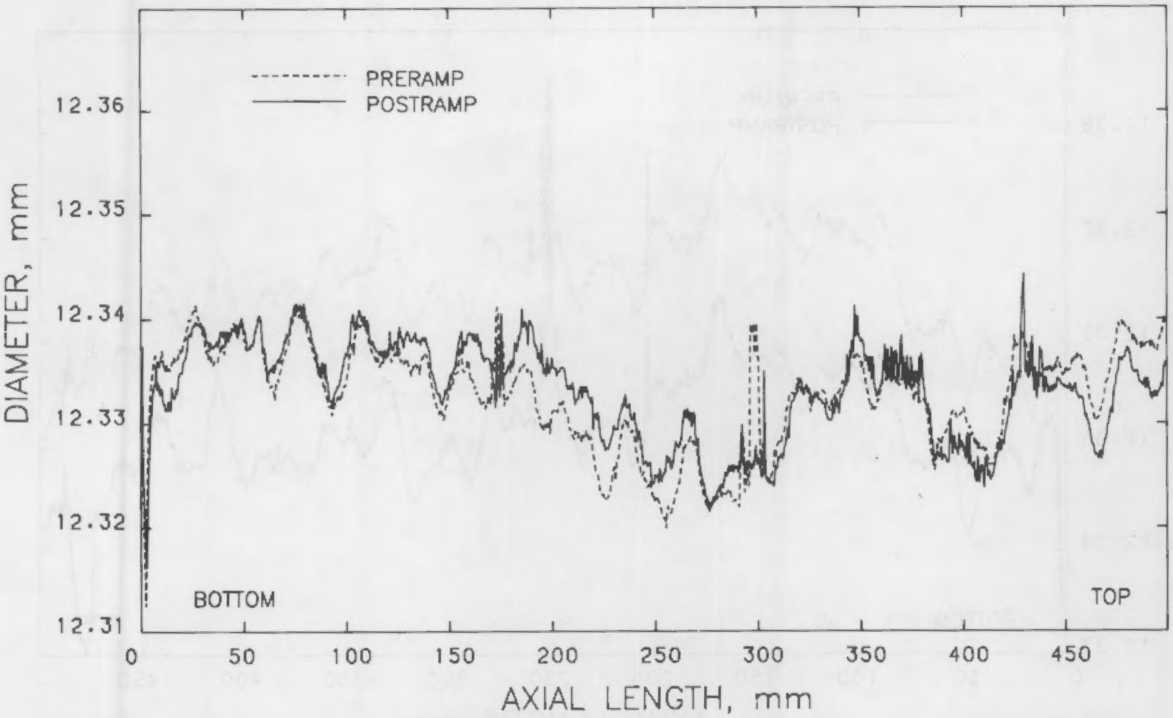

FIGURE 35. Preramp and Postramp Profilometry for Rod AC10 at 90°

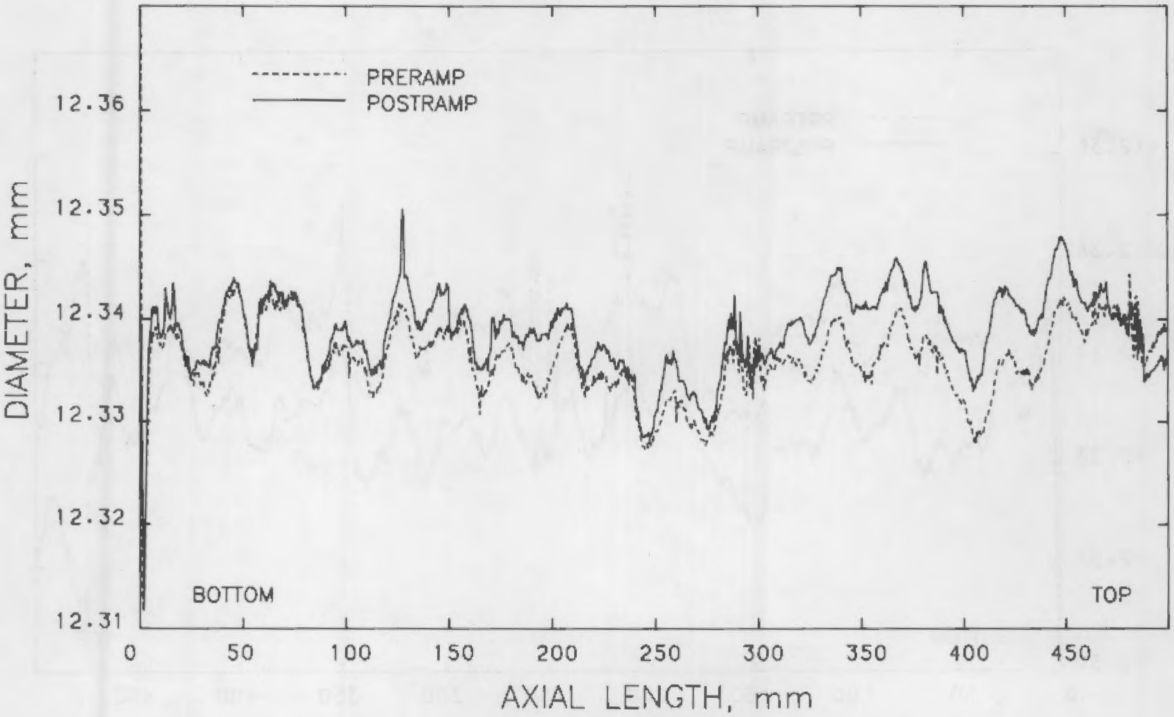

FIGURE 36. Preramp and Postramp Profilometry for Rod AC10 at 135°

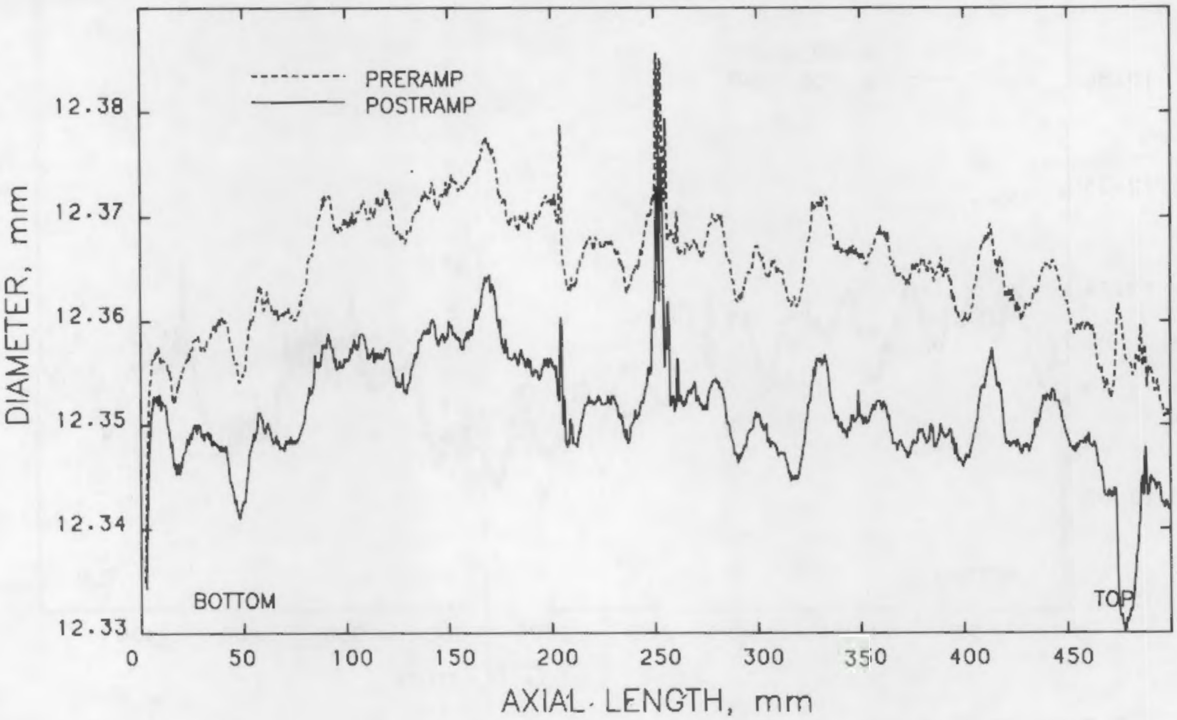

FIGURE 37. Preramp and Postramp Profilometry for Rod AC11 at 0°

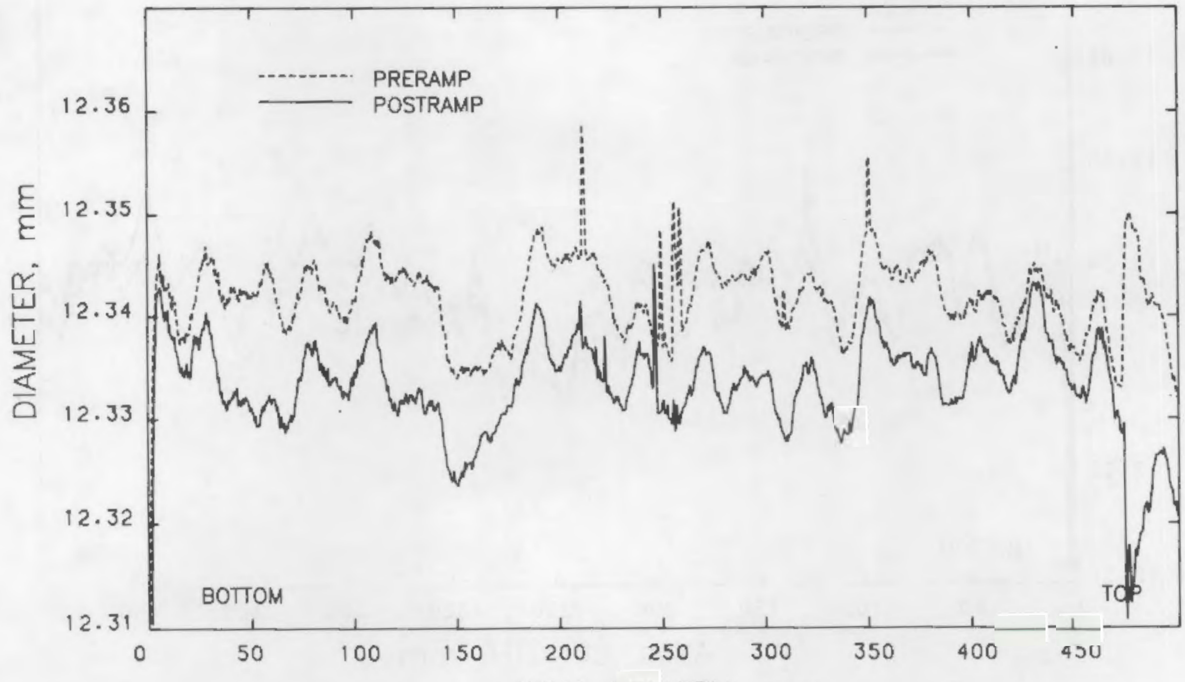

FIGURE 38. Preramp and Postramp Profilometry for Rod AC11 at 45°

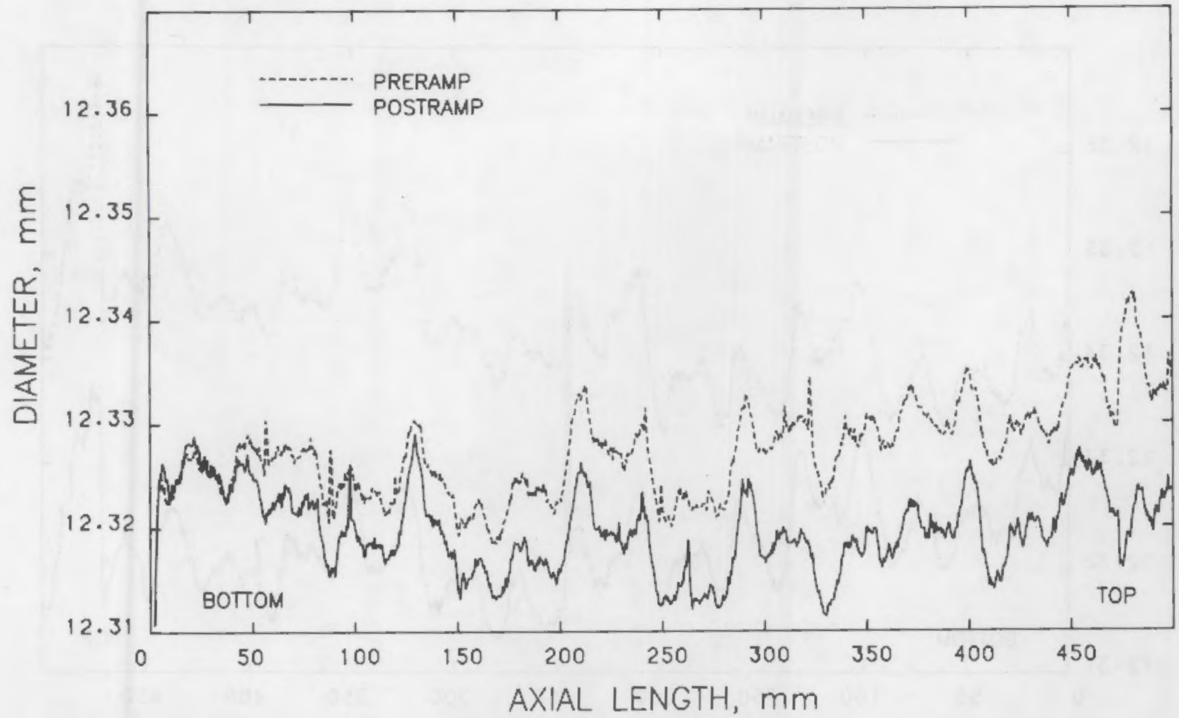

FIGURE 39. Preramp and Postramp Profilometry for Rod AC11 at 90°

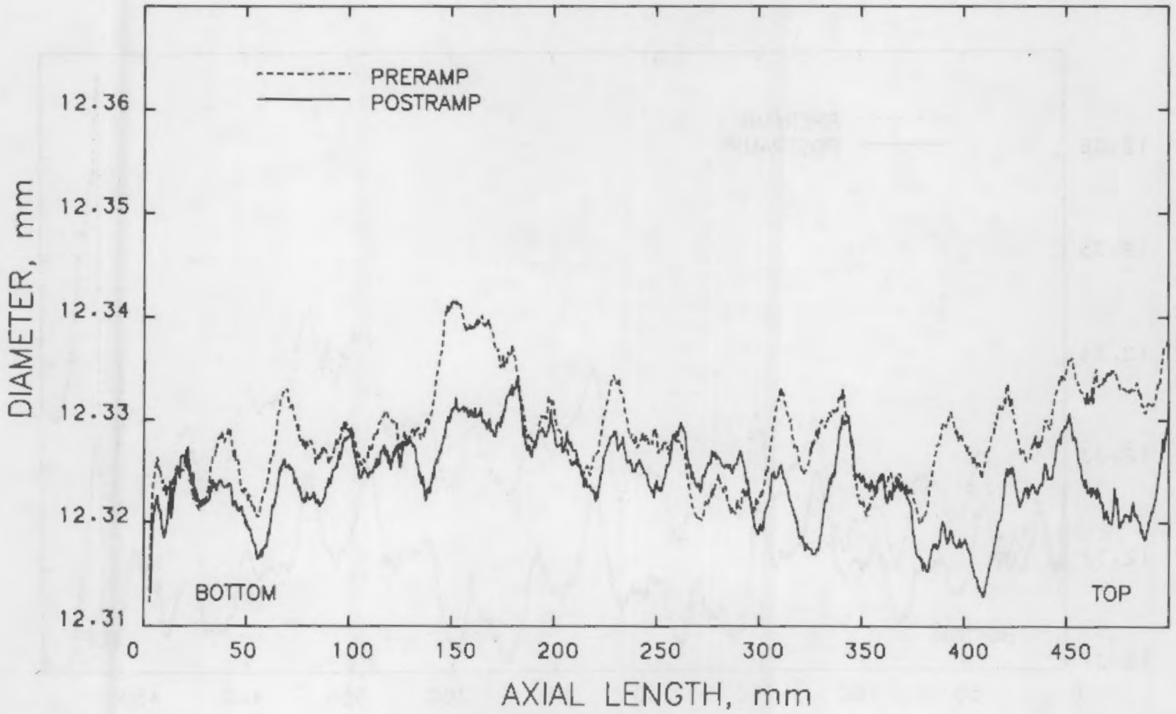

FIGURE 40. Preramp and Postramp Profilometry for Rod AC11 at 135°

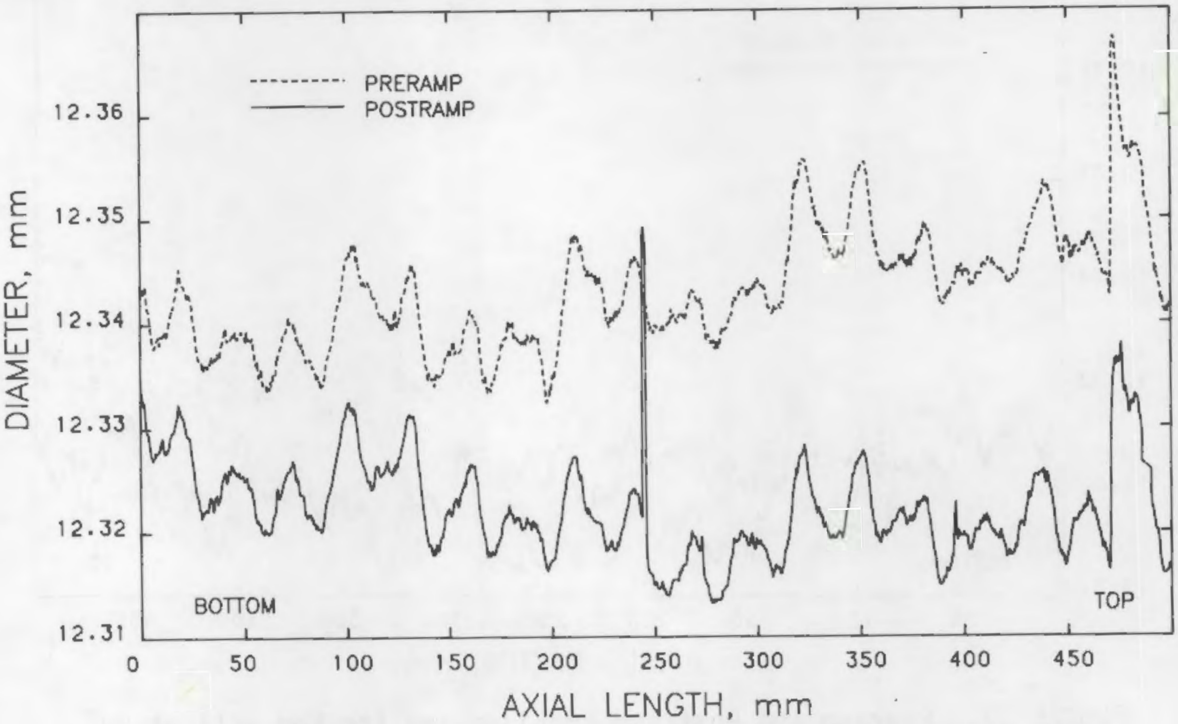

<u>FIGURE 41</u>. Preramp and Postramp Profilometry for Rod ACP27 at 0°

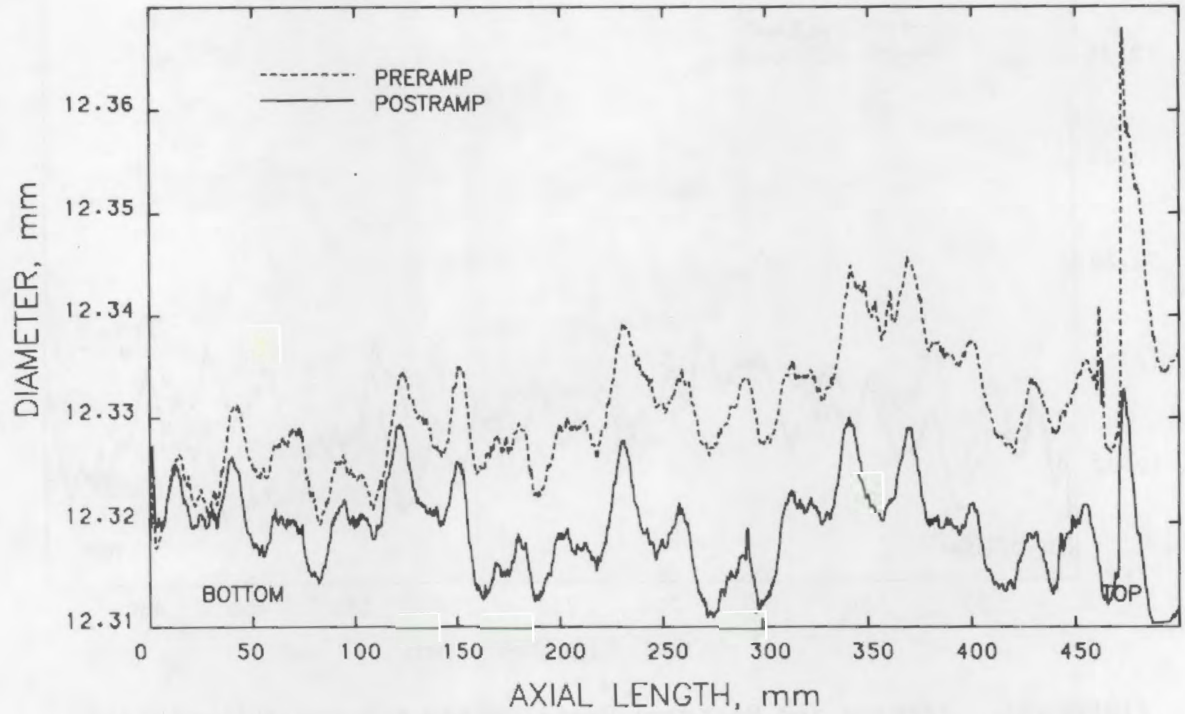

<u>FIGURE 42</u>. Preramp and Postramp Profilometry for Rod ACP27 at 45°

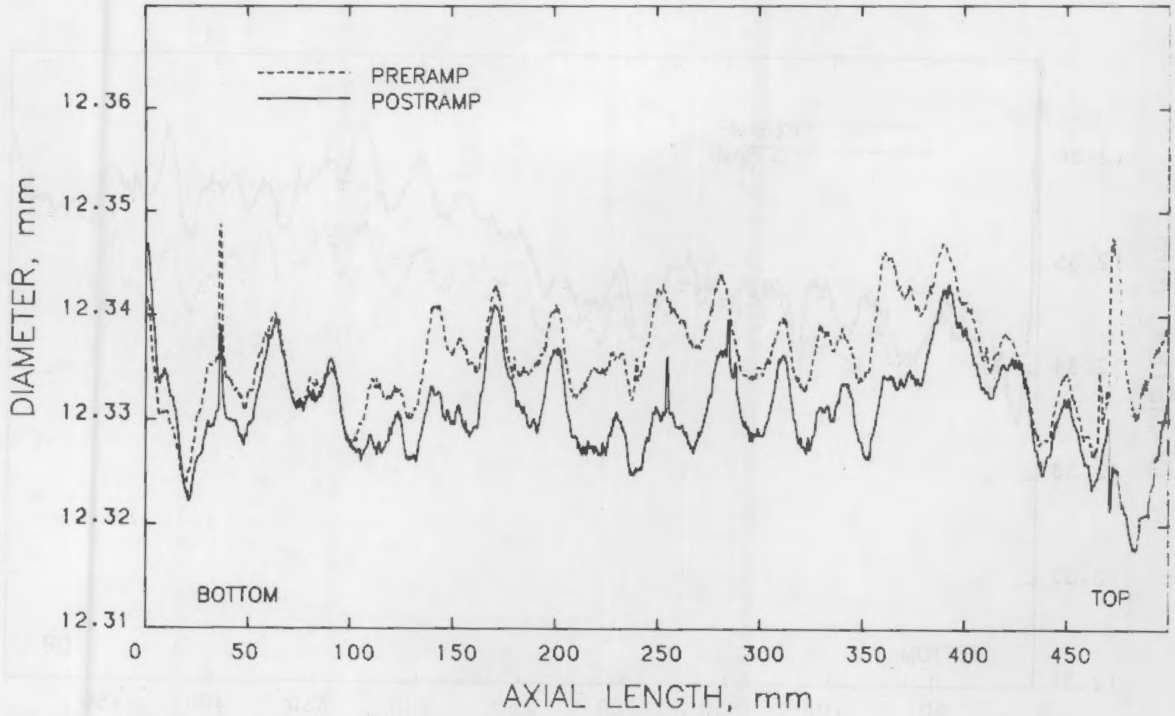

FIGURE 43. Preramp and Postramp Profilometry for Rod ACP27 at 90°

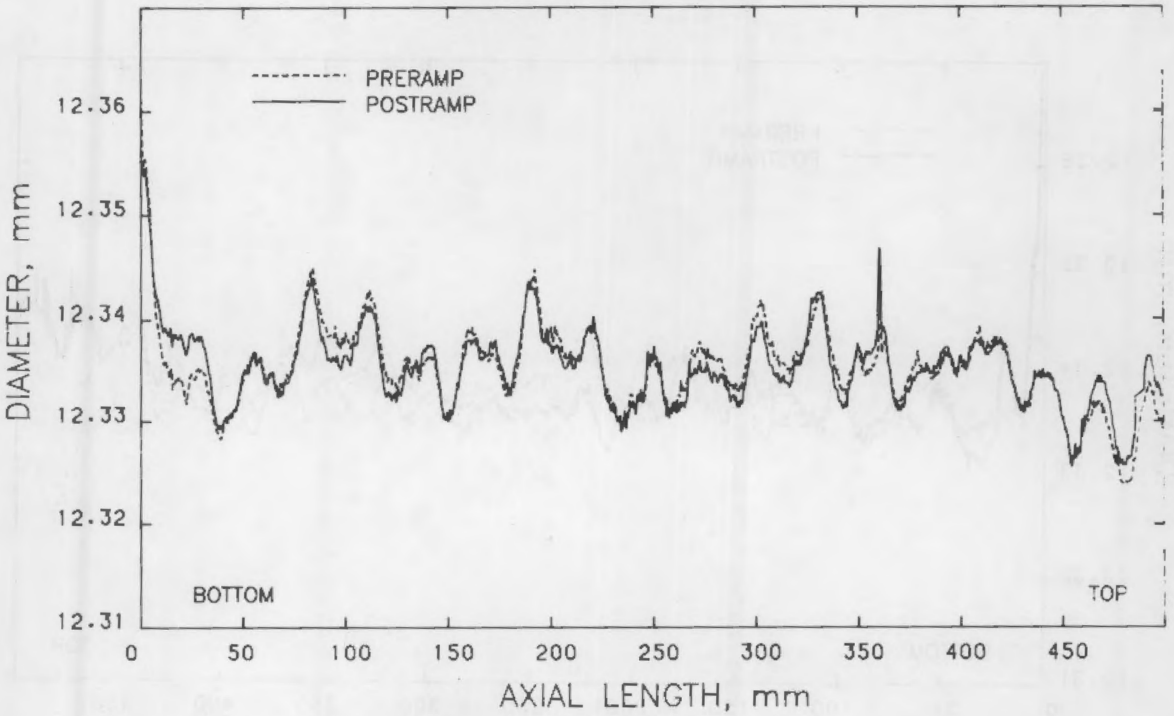

FIGURE 44. Preramp and Postramp Profilometry for Rod ACP27 at 135°

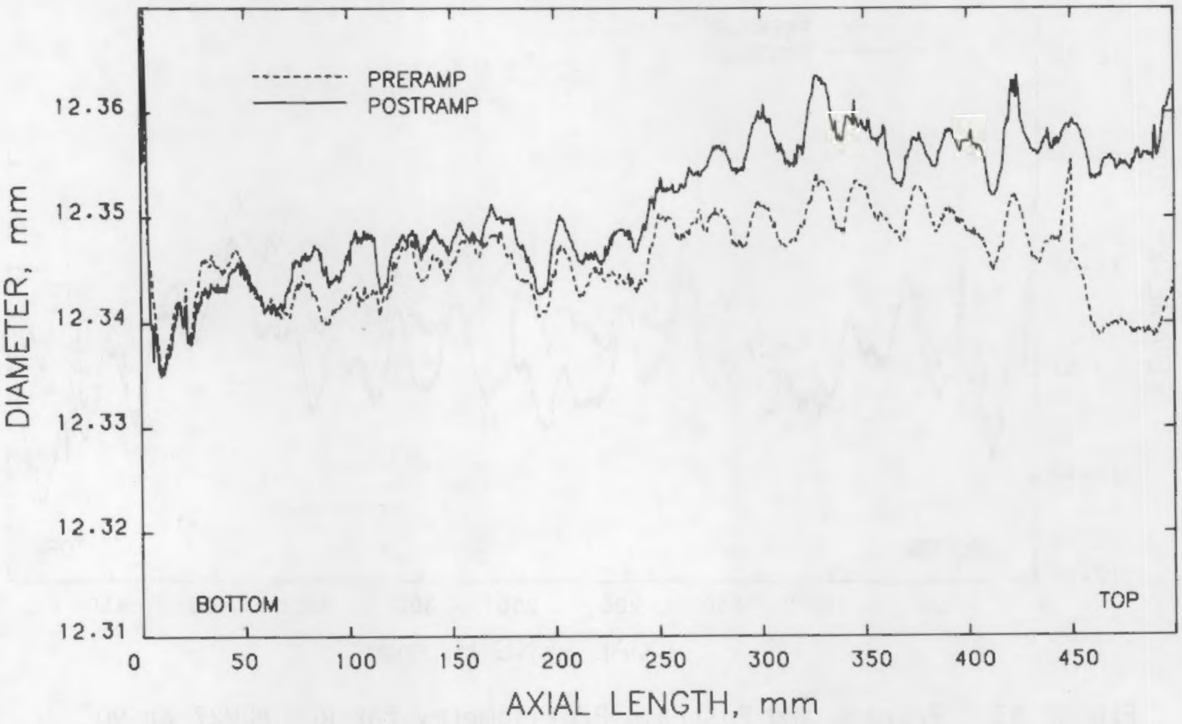

FIGURE 45. Preramp and Postramp Profilometry for Rod S40 at 0°

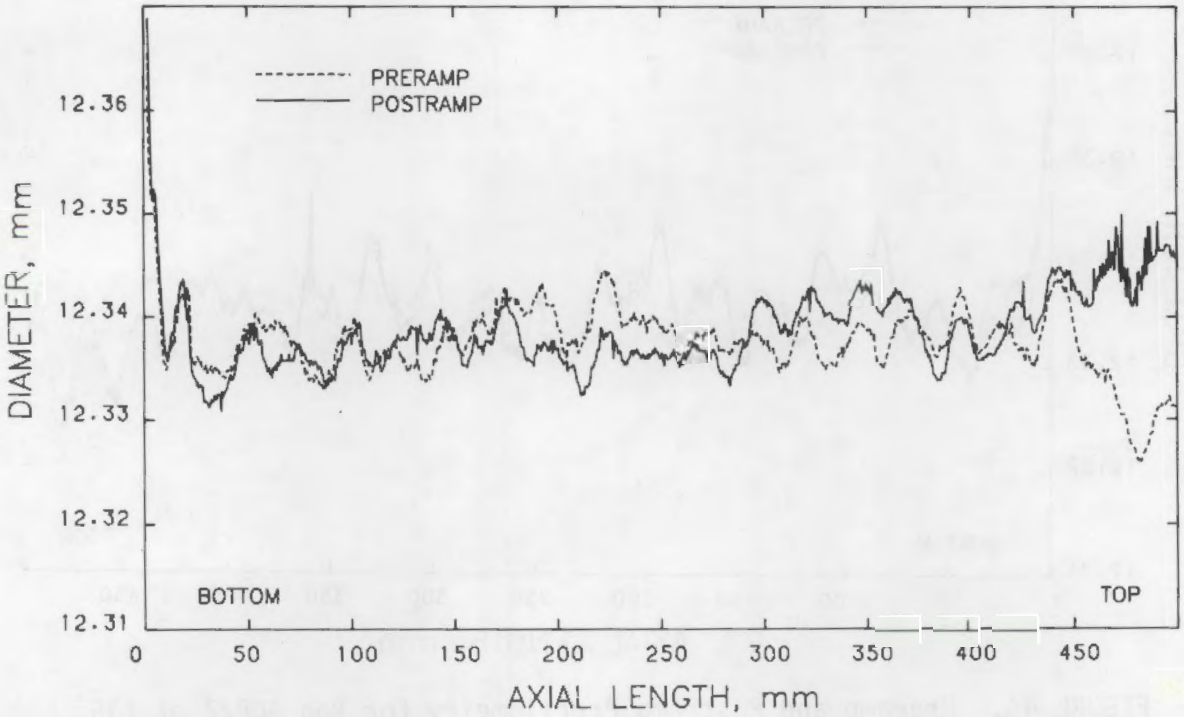

FIGURE 46. Preramp and Postramp Profilometry for Rod S40 at 45°

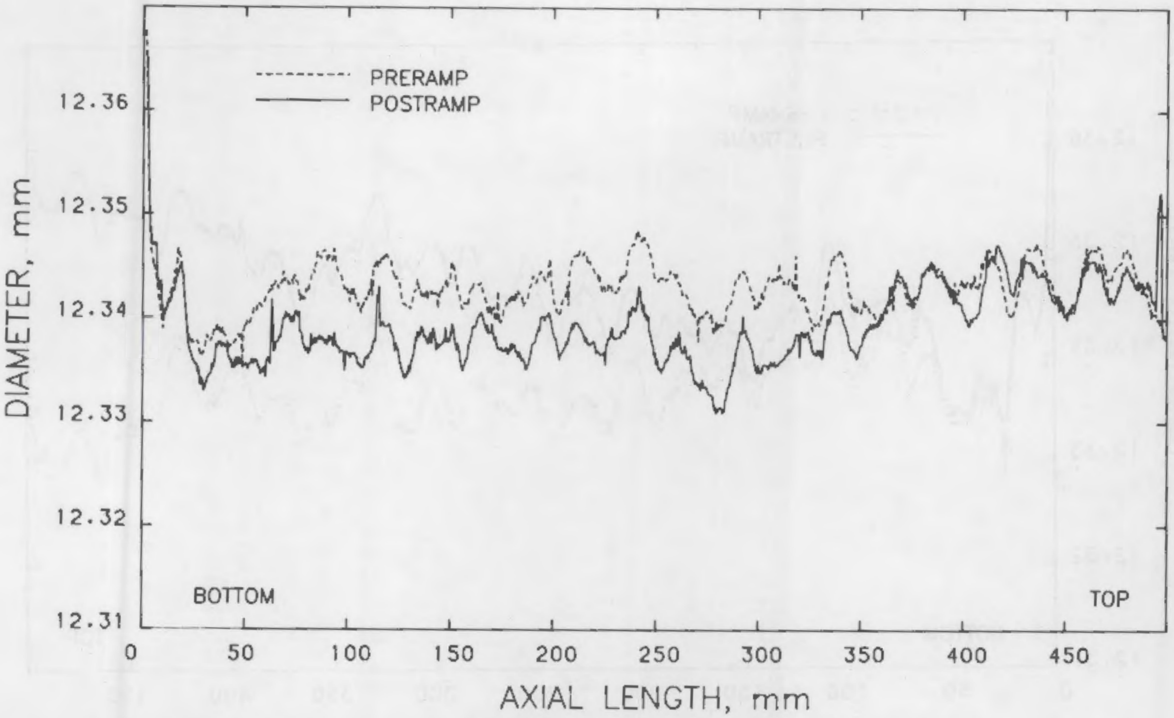

FIGURE 47. Preramp and Postramp Profilometry for Rod S40 at 90°

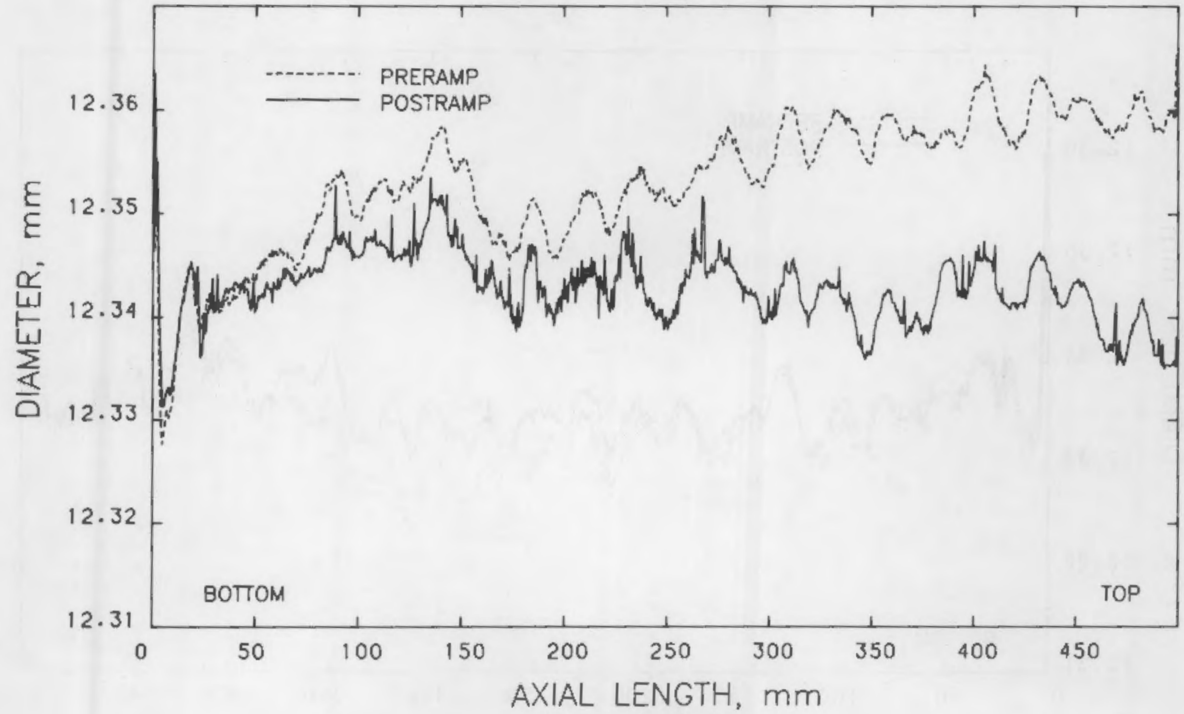

FIGURE 48. Preramp and Postramp Profilometry for Rod S40 at 135°

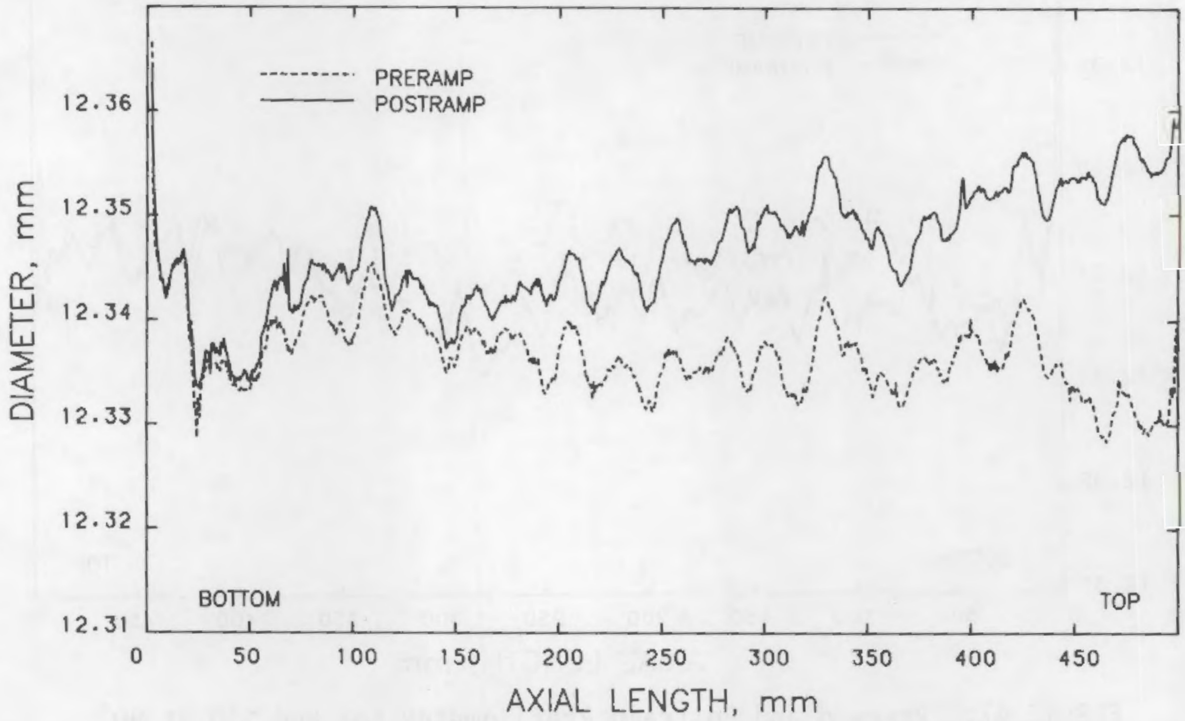

FIGURE 49. Preramp and Postramp Profilometry for Rod S41 at 0°

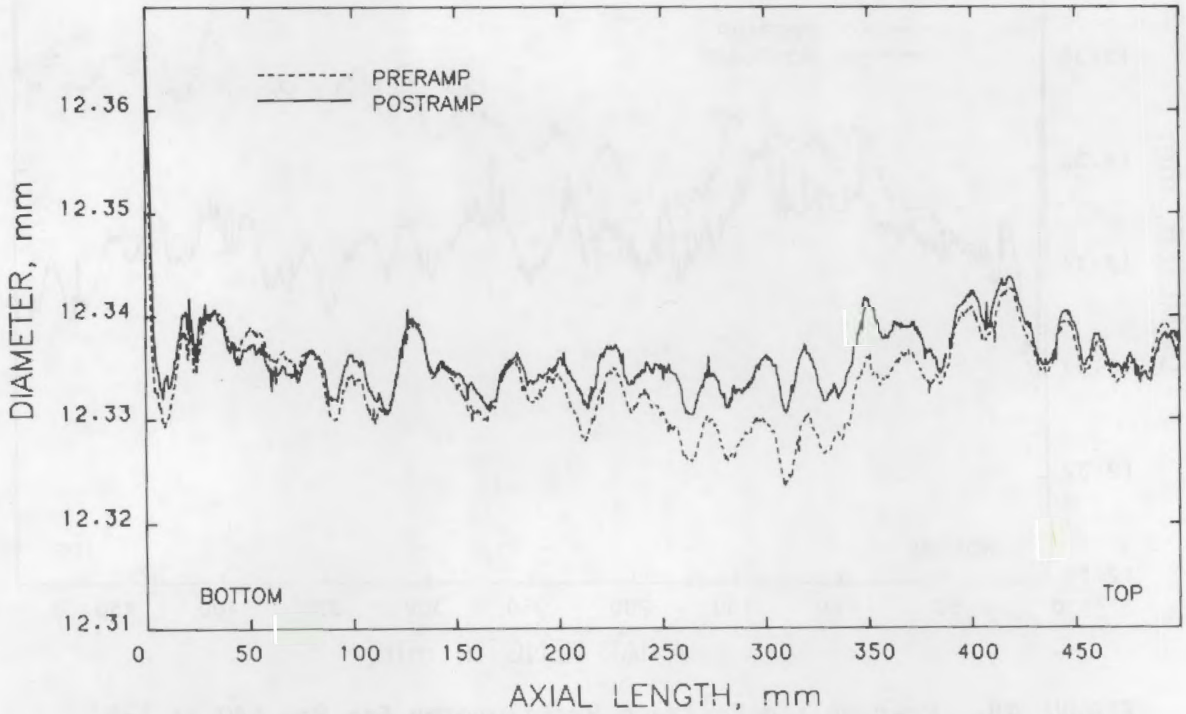

FIGURE 50. Preramp and Postramp Profilometry for Rod S41 at 45°

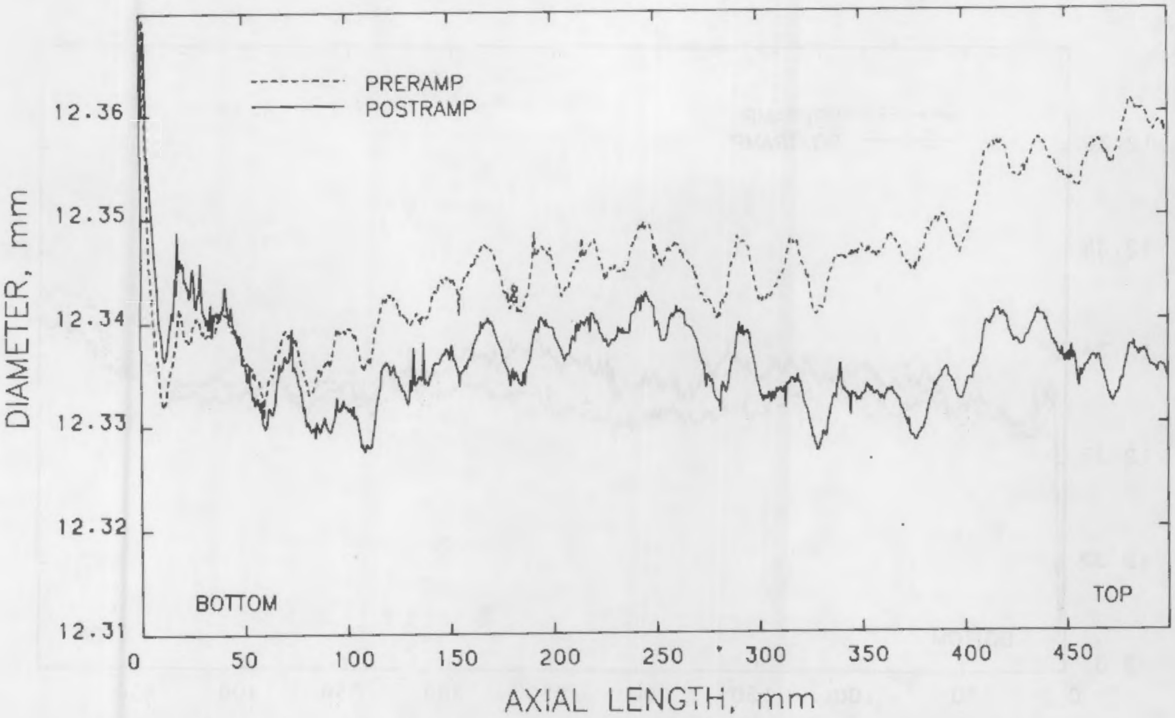

FIGURE 51. Preramp and Postramp Profilometry for Rod S41 at 90°

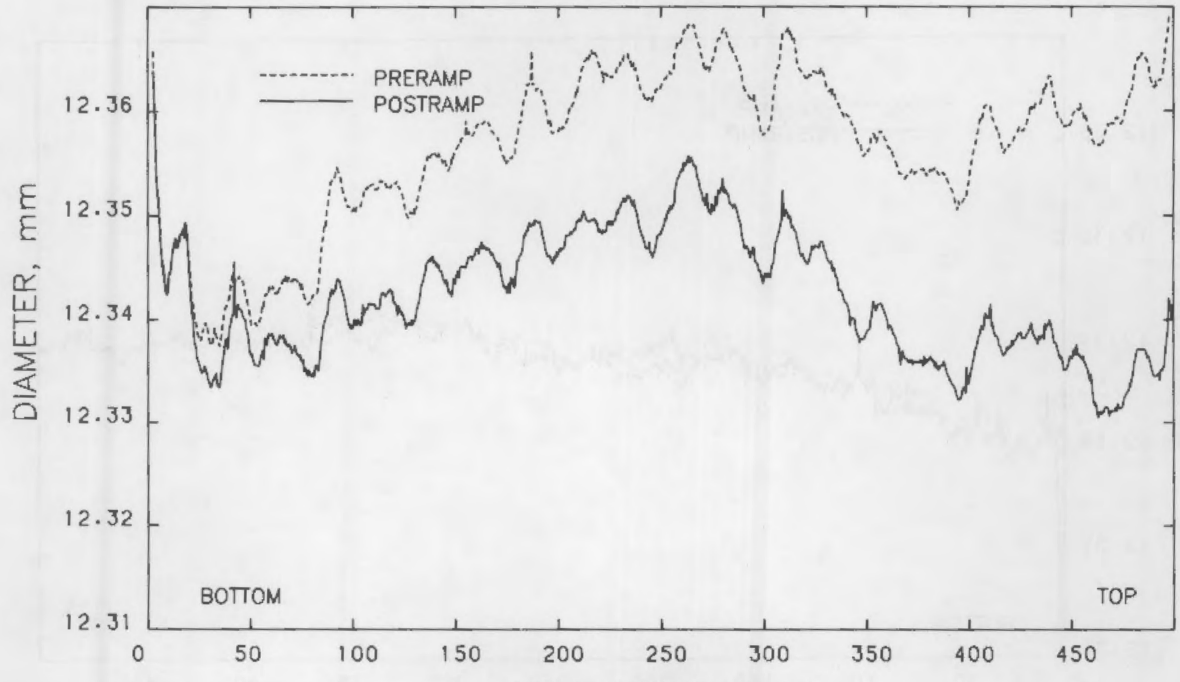

FIGURE 52. Preramp and Postramp Profilometry for Rod S41 at 135°

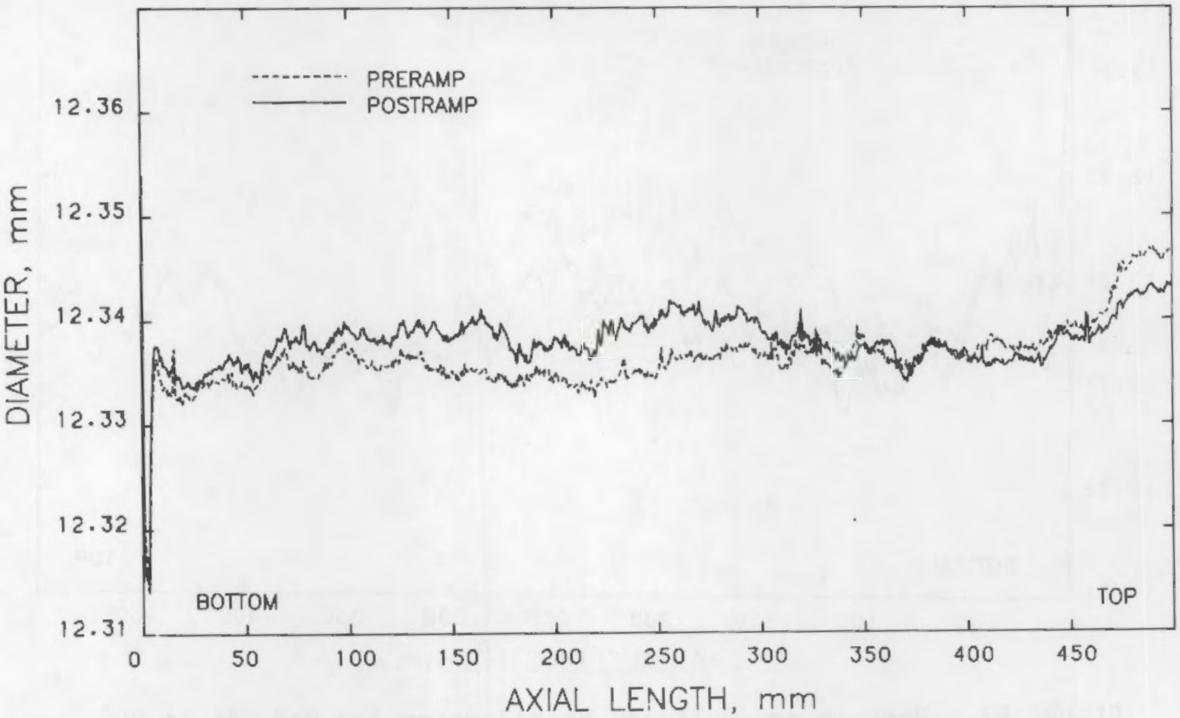

FIGURE 53. Preramp and Postramp Averaged Profilometry for Rod R1

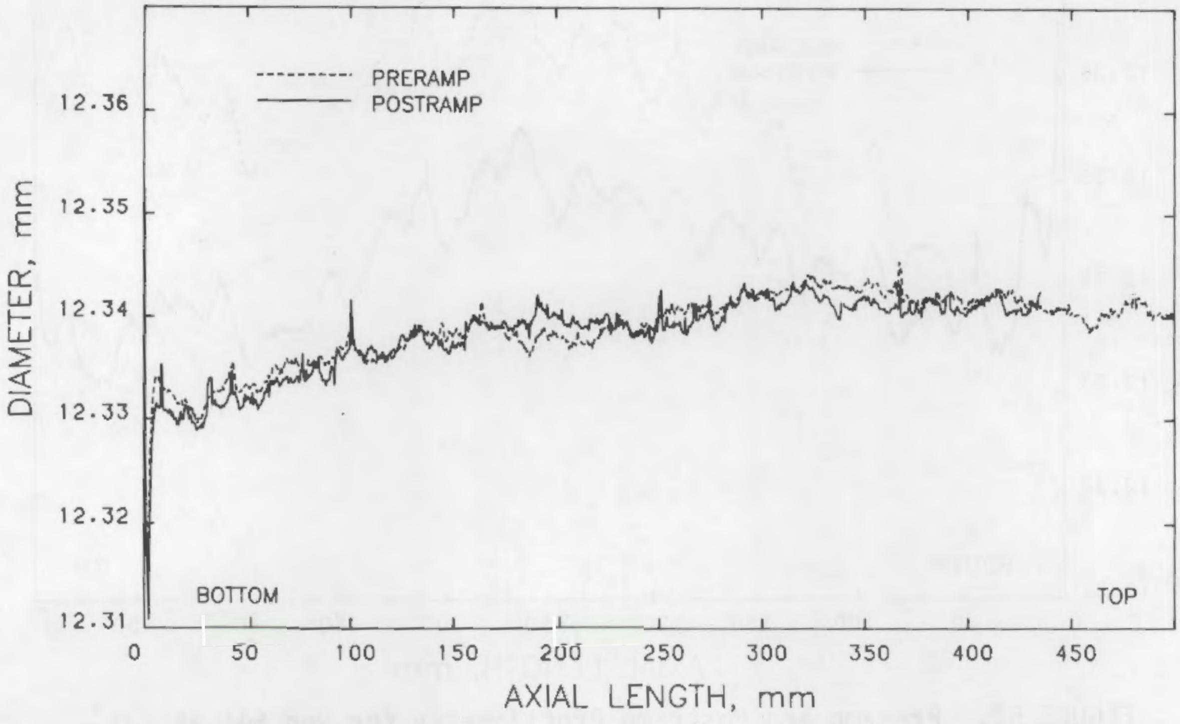

FIGURE 54. Preramp and Postramp Averaged Profilometry for Rod R2

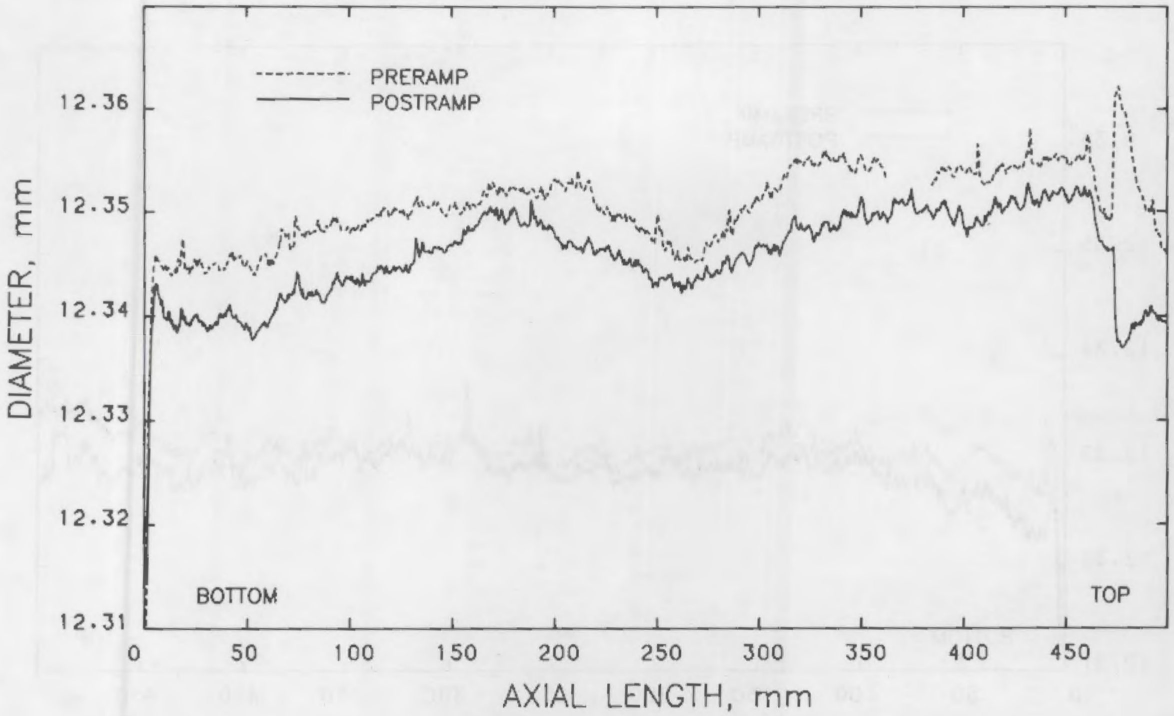

FIGURE 55. Preramp and Postramp Averaged Profilometry for Rod R3

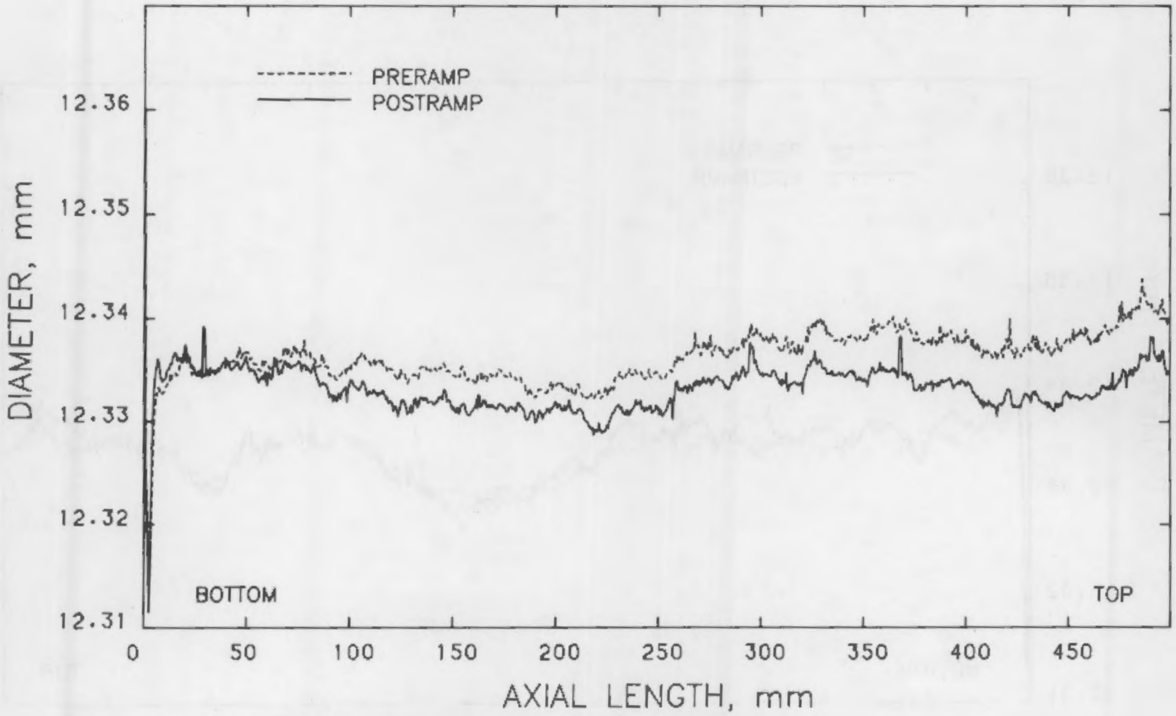

FIGURE 56. Preramp and Postramp Averaged Profilometry for Rod A6

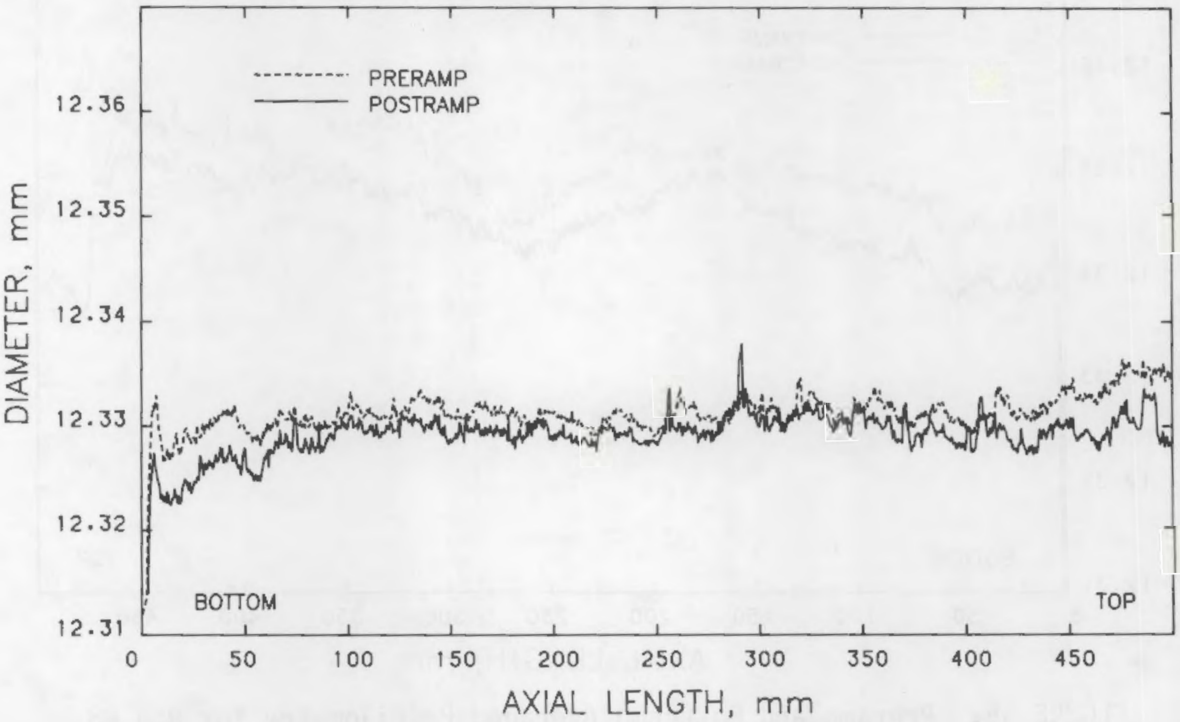

FIGURE 57. Preramp and Postramp Averaged Profilometry for Rod AC9

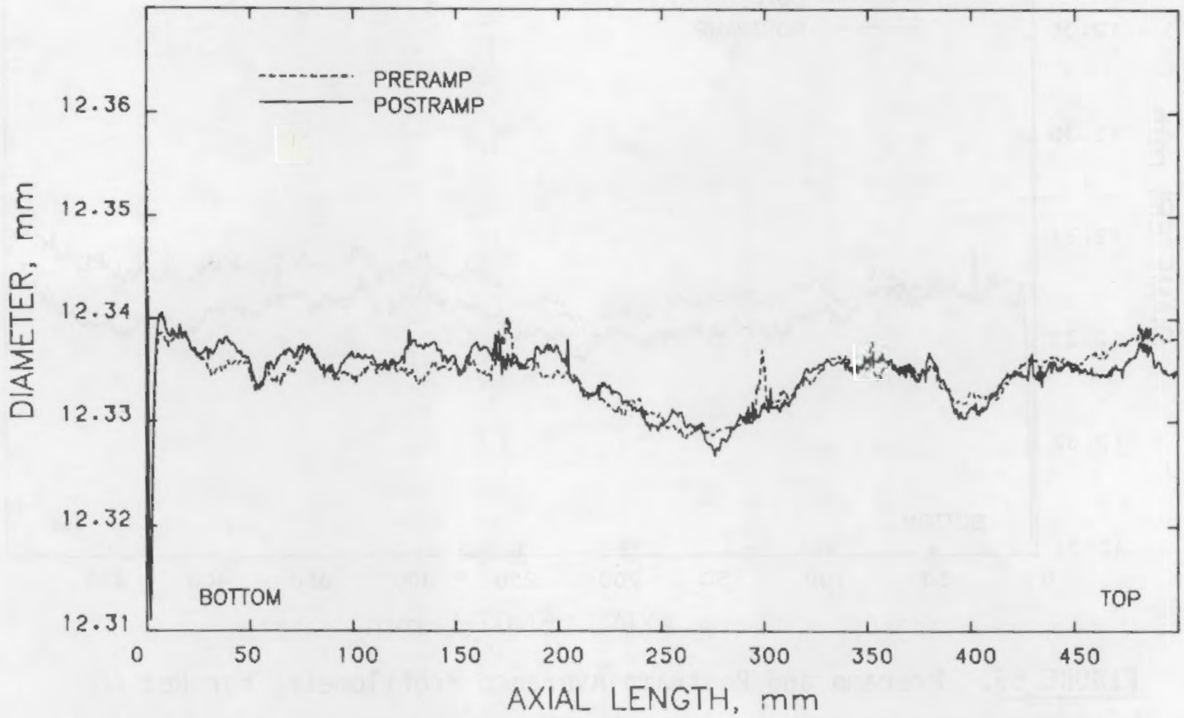

FIGURE 58. Preramp and Postramp Averaged Profilometry for Rod AC10

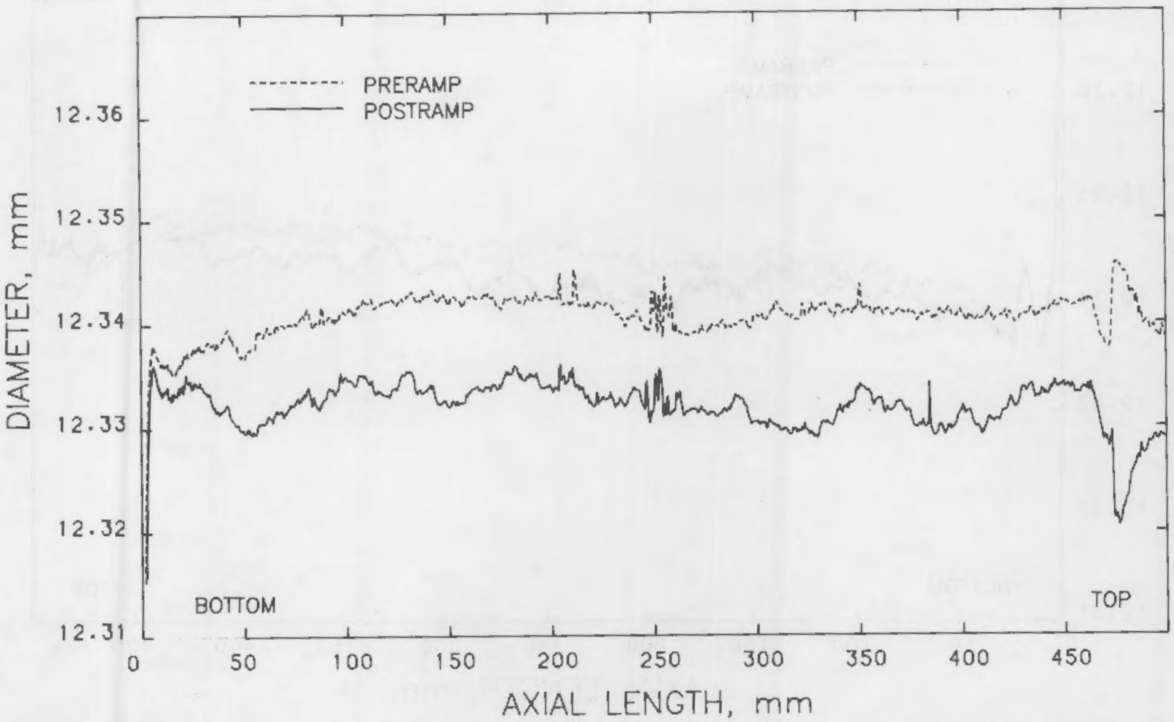

FIGURE 59. Preramp and Postramp Averaged Profilometry for Rod AC11

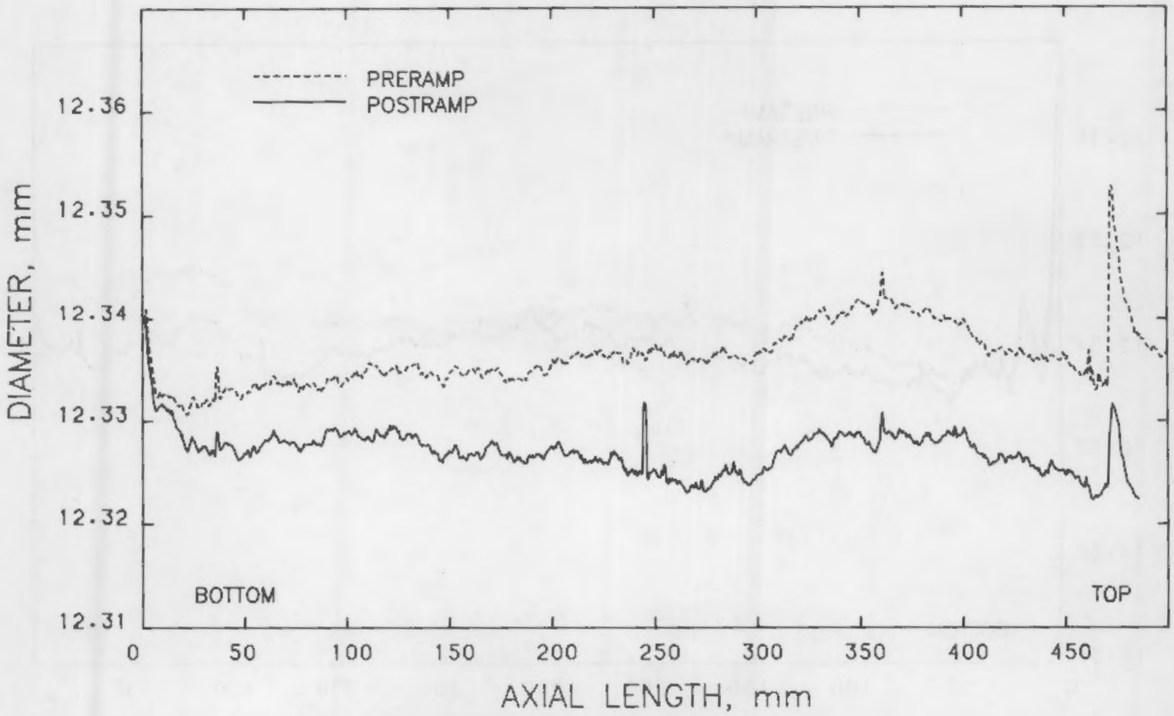

FIGURE 60. Preramp and Postramp Averaged Profilometry for Rod ACP27

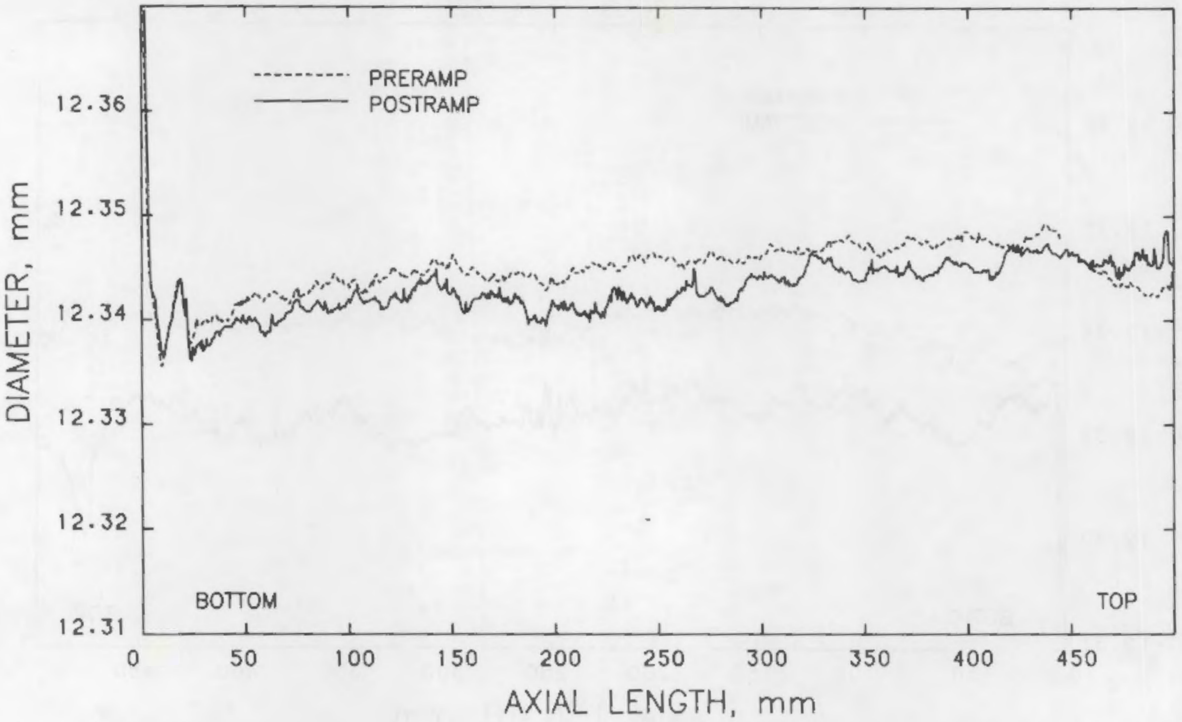

FIGURE 61. Preramp and Postramp Averaged Profilometry for Rod S40

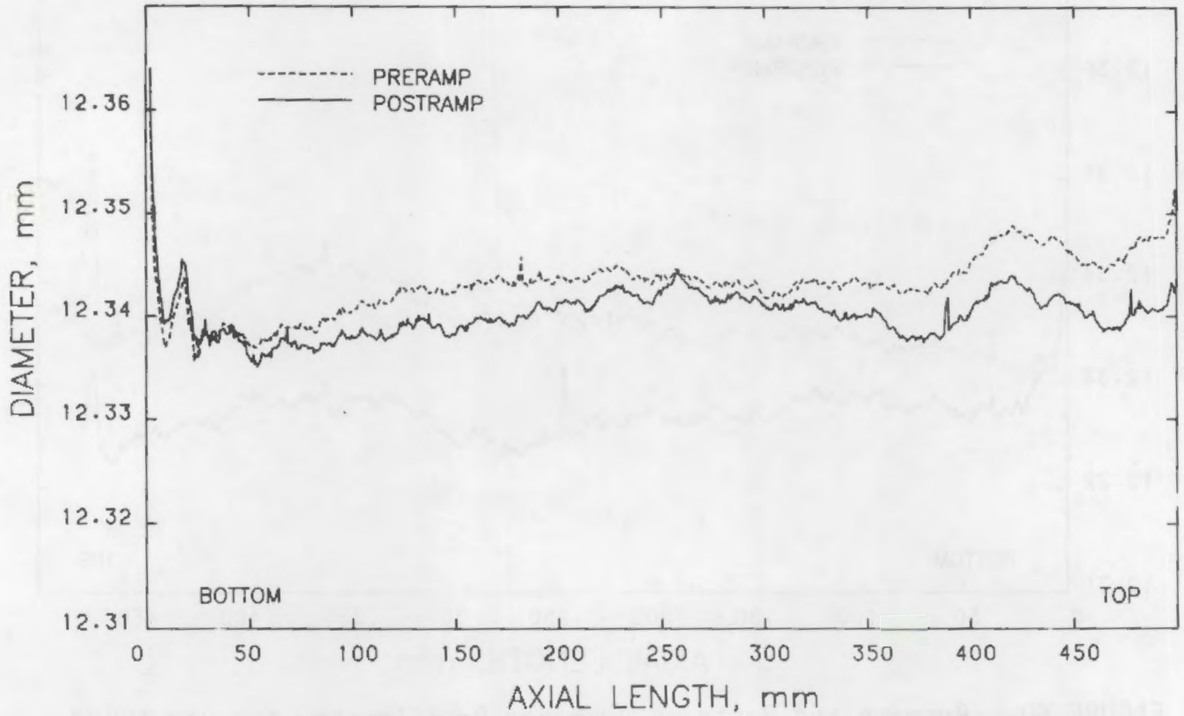

FIGURE 62. Preramp and Postramp Averaged Profilometry for Rod S41

while in other cases it was nearly equivalent or greater than the true average. As a result, no clear evidence of a permanent hoop strain was obtained from any of the rods.

4.3 RESULTS OF POSTIRRADIATION EXAMINATIONS AT HARWELL

Descriptions of the methods used for the nondestructive and destructive PIE at Harwell are presented in Section 3.6. This section presents the results from those examinations.

4.3.1 Neutron Radiography

Neutron radiographs were made of the ramped annular-coated Rods AC9 and AC10, the ramped sphere-pac Rod S41, and the nonramped sphere-pac Rod S42. The techniques used to produce the radiographs are presented in Section 3.6.1. Rods AC9 and AC10 (Figures 63 and 64) were radiographed in one orientation primarily to assess the degree of axial fuel relocation within the central hole. Rods S41 and S42 (Figures 65 and 66) were radiographed in two orientations that were 90° apart to assess the radial location of the thermocouples.

Axial fuel relocation within the central hole of rods with annular pellets could conceivably occur during handling or irradiation. Such relocation might cause localized areas of high power and high temperature during operation in a commercial reactor. The handling and irradiation history for Rods AC9 and AC10 is summarized as follows:

- fabricated by ENC in Richland, Washington
- trucked in DOT-6M container to Seattle, Washington
- air freighted to Oslo, Norway, via Copenhagen, Denmark
- trucked to Kjeller, Norway, for preirradiation NDE
- trucked to Halden, Norway
- irradiated in HBWR at rod-average LHGRs up to ~35 kW/m to a burnup of ~10.7 MWd/kgM
- nondestructively examined at Halden (preramp)
- power-ramp tested in HBWR
- nondestructively examined at Halden (postramp)

- trucked to Oslo in a cask
- freighted to England on ship
- trucked to the Harwell hot cells.

Even after this amount of handling and irradiation, the maximum fuel debris that accumulated at the bottom of the central hole in Rod AC9 was only 1.5 mm (0.06 in.) in depth (Figure 63).

Scrutiny of the radiographs of the annular-coated rods for phenomena other than axial fuel relocation revealed two other, apparently related features: 1) the central hole diameter in each pellet was smaller than the originally as-fabricated diameter and the shape of the central bore of each pellet usually had an hourglass shape (it was smaller at the middle than at the ends) and 2) each pellet exhibited a midradius circumferential crack that was generally barrel-shaped (it was larger at the middle than at the ends).

An illustration of the possible shape of an annular pellet while at power at the end of the ramp test is schematically shown in Figure 67. The apparent diameters of the central holes and circumferential cracks as a function of pellet location are shown in Figures 68 and 69. The measurements were made directly from the radiographs using a graduated magnifier. The precision of the magnifier was ±0.13 mm (0.005 in.). Only the diameter of the holes at the midpellet height are shown because the diameters at the ends were generally within ±0.13 mm (0.005 in.) and, even though hourglassing was observed, the diameter differences were not great enough to quantize. The diameters of the cracks at the middle and the ends of the pellet are shown because the differences in these diameters were generally greater than the precision of the measurement. The average hole diameter, the average crack diameter at the midpellet height, the average crack diameter at the ends of the pellet, and the respective standard deviations are listed in Table 7. The difference in the average hole diameters between the two rods is within the precision of the measurement, which indicates that the average hole diameters are essentially equivalent. The standard deviations for the hole measurements are only slightly larger than the precision, which indicates that there are no major trends in diameter with length. This is also indicated in Figures 68

BOTTOM TOP

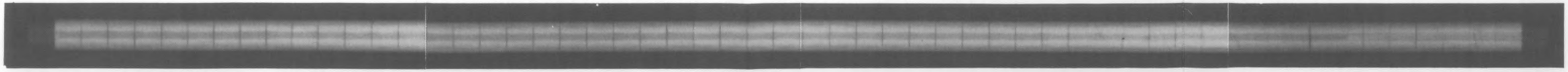

FIGURE 63. Postramp Neutron Radiography for Rod AC9 (one view)

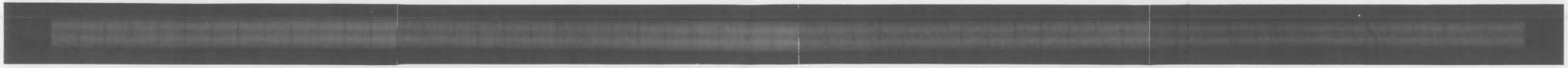

FIGURE 64. Postramp Neutron Radiography for Rod AC10 (one view)

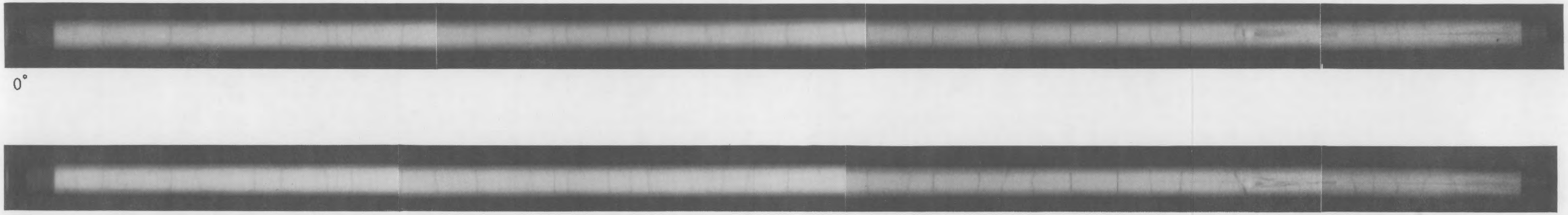

FIGURE 65. Postramp Neutron Radiography for Rod S41 at 0° and 90°

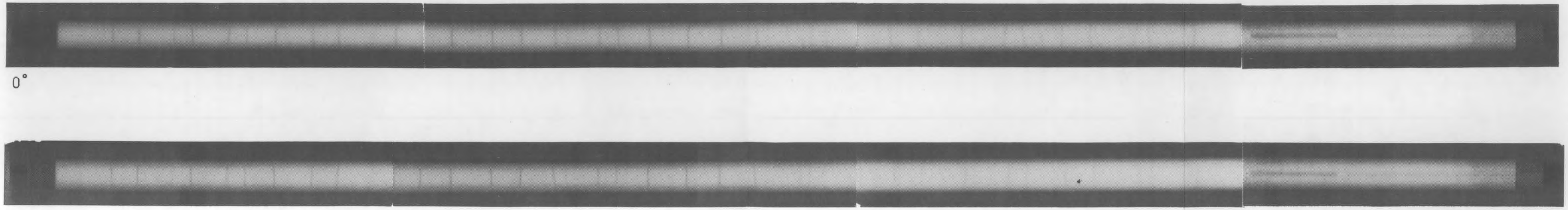

FIGURE 66. Neutron Radiography of Rod S42 After Steady-State Irradiation at 0° and 90°

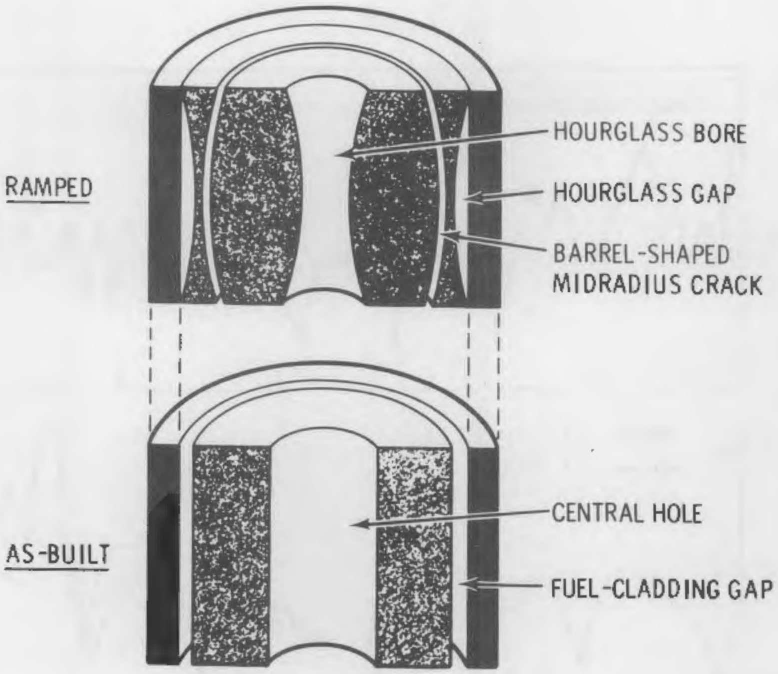

FIGURE 67. Geometry of Annular-Pellet Design During Ramp Test Compared with As-Built Geometry (idealized with no radial fuel cracks)

and 69, where only slight trends towards larger hole diameters at the top of the stack were observed. The change in hole diameters from the as-fabricated diameter represents a reduction in hole areas of ~60%.

The diametral differences of the midradius circumferential cracks at the middle and end of the pellet are significantly greater than the precision of the measurement and are therefore significant. The midpellet and end pellet crack diameters are both greater in Rod AC10 than in Rod AC9. These differences in crack diameter correlate well with the rod-average LHGRs during ramping, i.e., Rod AC10 had the higher ramping LHGR (see Table 2). The diameter of the midradius circumferential crack at the pellet ends and the midpellet height increased with increasing height of the fuel stack in both annular-coated rods (Figure 68 and 69). This increase in crack diameter with altitude in the fuel rods also correlates well with LHGR, i.e., the LHGR during ramping increased along the length of the rod from bottom to top.

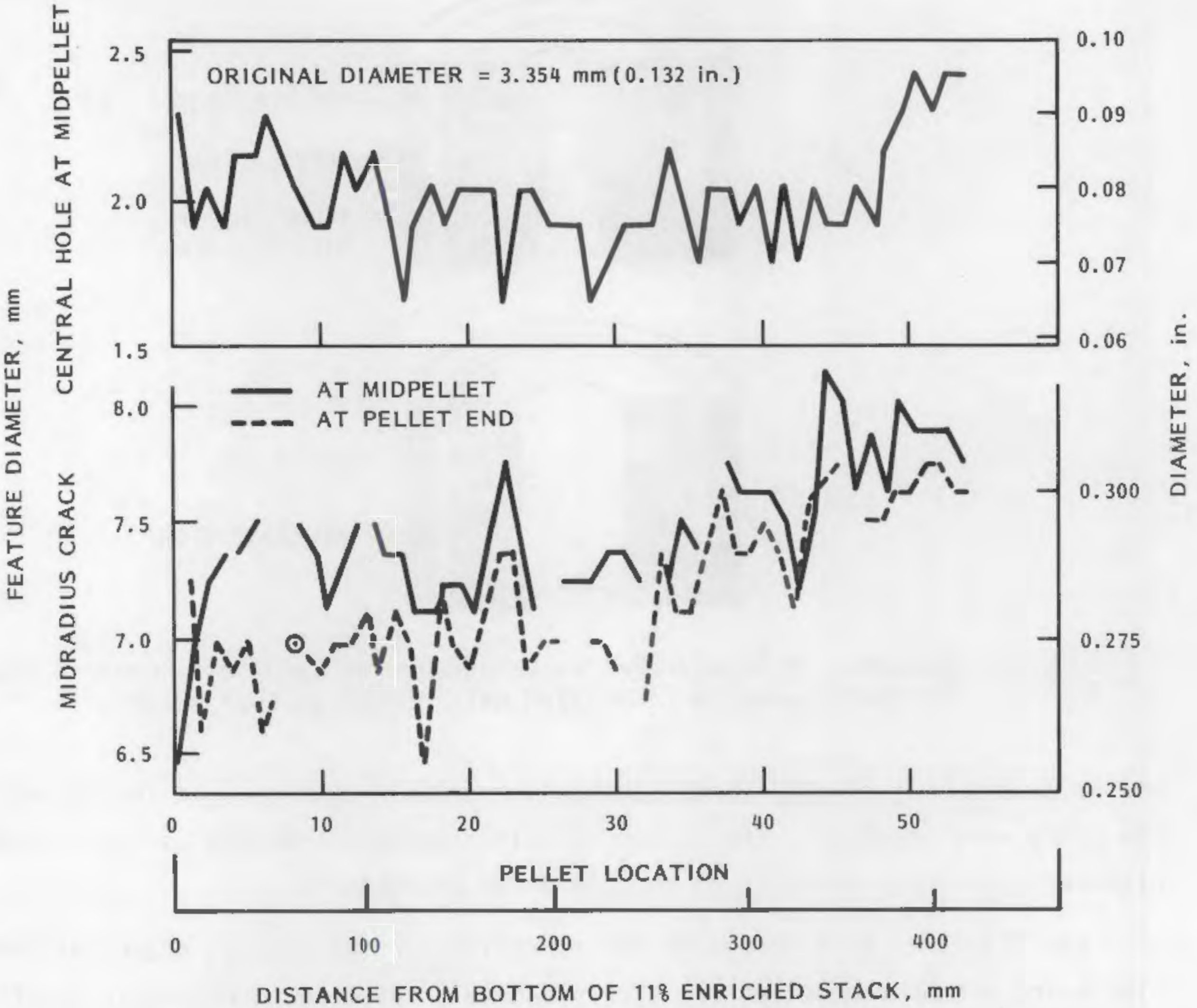

FIGURE 68. Diameters of Holes and Cracks in Rod AC9 as Measured from Neutron Radiographs

The thermocouple wells in ramped Rod S41 and nonramped Rod S42 were located on the fuel rod centerline (Figures 65 and 66), which substantiates that the temperatures measured during steady-state irradiation of these sphere-pac rods were correctly attributed to the maximum operating temperatures. The thermocouple in ramped Rod S41 melted/reacted during the ramp test and had relocated downwards into the thermocouple well, indicating that quite high fuel temperatures had occurred during the ramp test.

Examination of the neutron radiographs of the sphere-pac rods for other features revealed 1) the formation of a small central void in ramped Rod S41

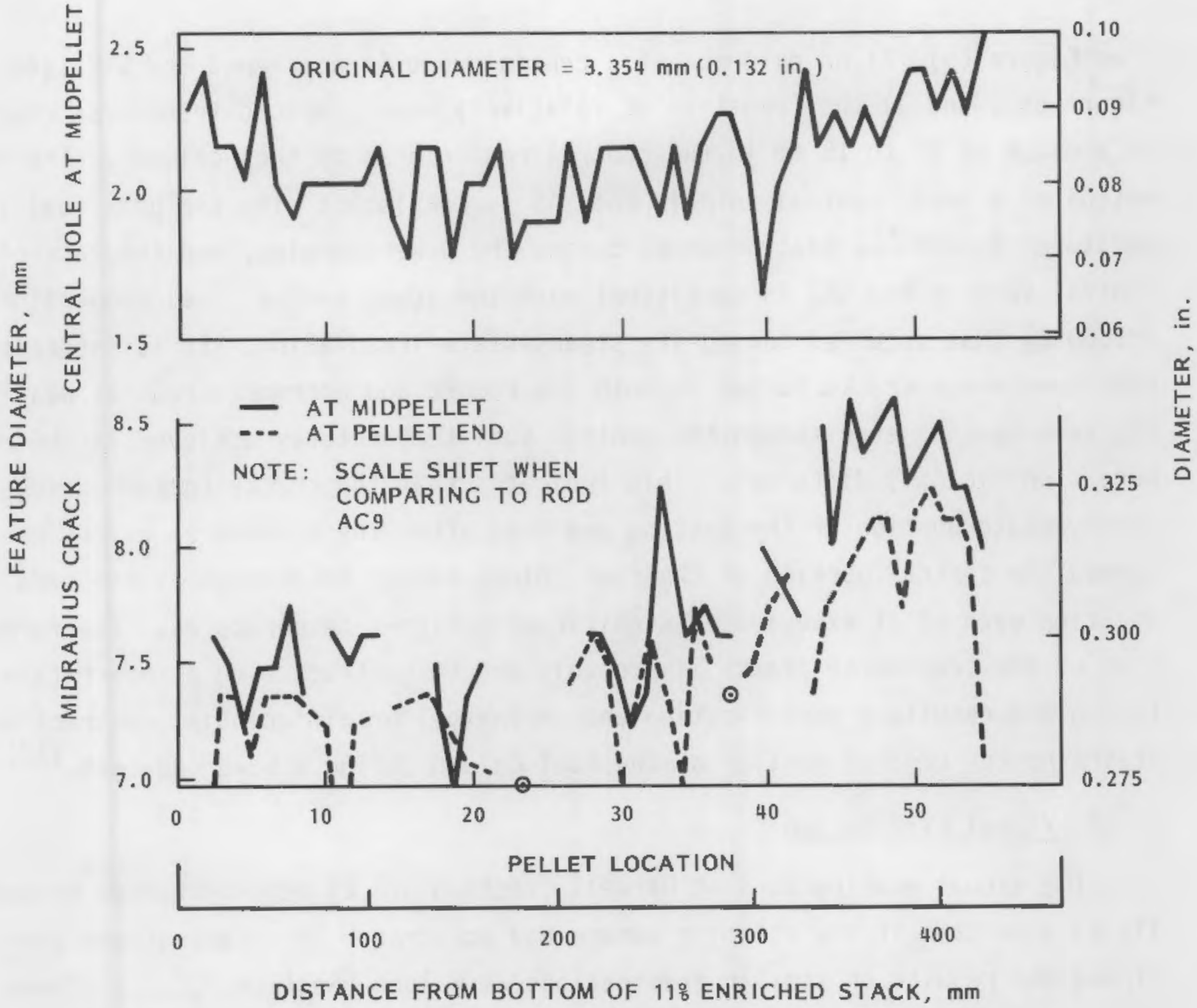

FIGURE 69. Diameters of Holes and Cracks in Rod AC10 as Measured from Neutron Radiographs

TABLE 7. Average Central Hole and Midradius Circumferential Crack Diameters in Rods AC9 and AC10 as Measured from Neutron Radiographs

	Diameter and Standard Deviation,[a] mm		
		Midradius Crack	
Rod Number	Central Hole	Midheight	Pellet End
AC9	2.01 (0.18)	7.44 (0.30)	7.16 (0.33)
AC10	2.11 (0.18)	7.80 (0.43)	7.54 (0.41)

(a) Standard deviations are in parentheses.

(see Figure 65), 2) no evidence of a central void in nonramped Rod S42 (see Figure 66), and 3) the formation of relatively evenly spaced transverse cracks at a pitch of 10 to 15 mm in the central region of both fuel columns. The formation of a small central void in Rod S41 is consistent with the peak fuel temperatures (>>2000°C) that occurred during the power-ramping, and the lack of a central void in Rod S42 is consistent with the lower central fuel temperatures (~1500°C) that occurred during its steady-state irradiation. It is interesting that transverse cracks formed in both the ramped and nonramped rods at nearly the same spacing even though the central fuel temperatures achieved in the rods were significantly different. This indicates that the cracks formed during the steady-state portion of the testing and that after the transverse cracks were formed the central portion of the fuel column tended to recrack at the same location even if it experienced significantly higher temperatures. The formation of the transverse cracks is probably due to restructuring at power (sintering and resultant densification and shrinkage) or differential contraction of the hotter central portion of the fuel column during a power descent.(12)

4.3.2 Visual Examination

The visual examinations at Harwell (Section 3.6.2) were performed primarily to ascertain if any shipping damage had occurred. The examinations confirmed the results of similar examinations at Halden (Section 4.2.1). There was no evidence of any shipping damage.

4.3.3 Gross Gamma Scanning

Gross gamma scans (Section 3.6.3) of the reference, annular-coated, and sphere-pac rods were made over the length of the fueled regions to 1) provide a general axial profile of the average LHGR during the irradiation of the rod by equating the power profile to the general axial activity distribution, 2) provide a general indication of any axial fission product migration, and 3) ascertain if any axial fuel redistribution had occurred, e.g., formation of axial gaps or filling of dishes at the ends of the pellets.

The rods were positioned for various periods before and after the individual ramp tests in a parking position. In this position, the rods were partially withdrawn from the HBWR core such that the lower portions of the rods were exposed to thermal neutrons and were producing low power while the upper portions experienced no power generation. Irradiation in this position increased the general gamma activity in the lower third of most of the rods. This misleading activity increase is presumably due to fission products with half-lives of weeks or months. Because different groups of rods were irradiated for significantly different periods in the parking position and cooled for different periods, the activity increase is more significant in some rods than in others. Rods AC9 and S41 were ramped in the first group of ramp tests, which was irradiated for the shortest period and had the longest cooling time. Rods R1, R2, and AC10 were irradiated for significant periods in the parking position and cooled for the shortest period. As a result, the misleading activity was greatest in Rods R1, R2, and AC10 and minimal or negligible in Rods AC9 and S41. The gross gamma scan from Rod S42, which was not ramp tested, showed no misleading activity. For the purposes of using the gross gamma scans to compare with the calculated axial power distributions in IFA-518 and IFA-517, the results from Rods AC9 (negligible misleading activity) and S42 (no misleading activity) were used.

The normalized activity in the fuel in Rod AC9 is shown in Figure 70. Background activity was subtracted from the original signals before normalization, and low activity in the pellet-to-pellet interfaces was avoided. The calculated normalized axial power distributions (based on in-reactor neutron detectors) are also shown for a lower cluster rod without a thermocouple hole in IFA-518.1 at the beginning of life. Distributions for both the nonshielded (high LHGR) and shielded (suppressed LHGR) conditions are illustrated. Rod AC9 operated in the lower cluster of IFA-518.1 for approximately equal periods in the shielded and nonshielded conditions before ramp testing. Given the complex irradiation history and the uncertainties concerning fission product migration during ramping, irradiation in the parking position, and axial burnup depletion, the shape of the normalized gross gamma activity is very similar to an axial power curve representative of the combined operation in the shielded and nonshielded condition. It is concluded that the axial LHGR profiles calculated for IFA-518.1 that were based upon neutron detector measurements and neutron streaming effects are reasonable.(6)

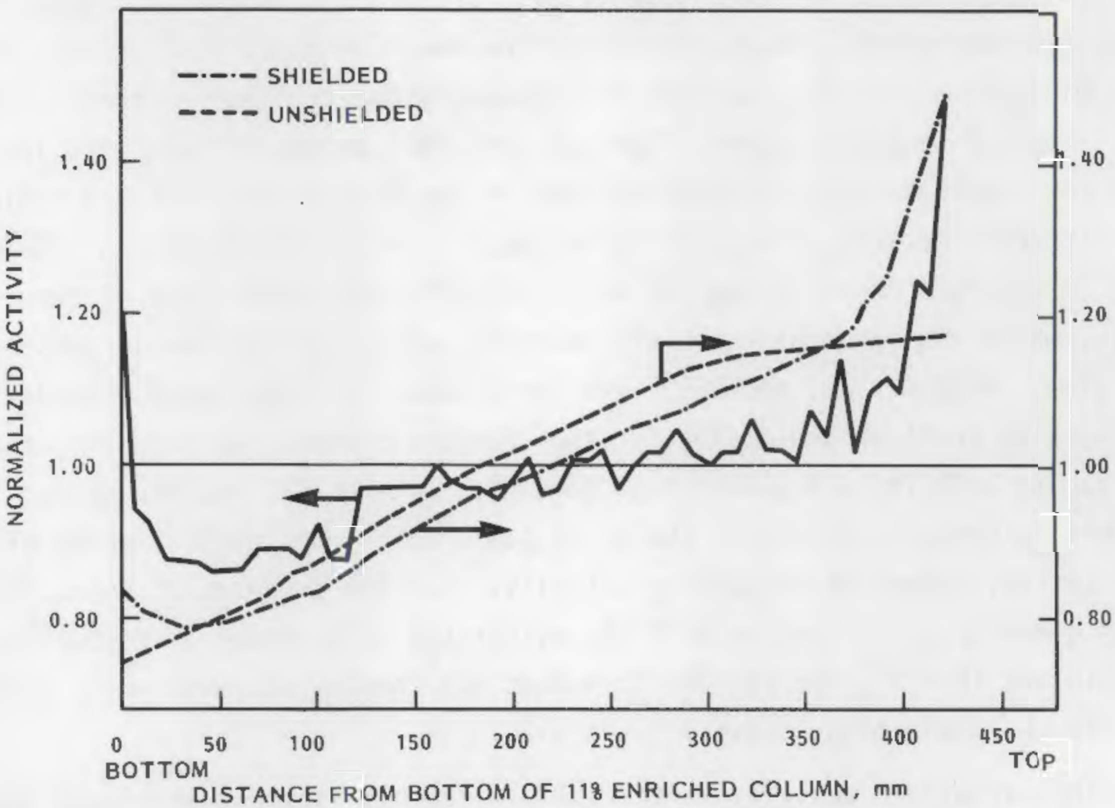

FIGURE 70. Normalized Gross Gamma Activity Distribution in Rod AC10 Compared with Calculated Power Profiles at Beginning of Life

The gross gamma scan for Rod S42 is shown in Figure 71. The location of the central fuel thermocouple tip is noted, and the bottom of the thermocouple well is ~25 mm below the tip. The general shape of the curve in the region without the thermocouple well confirms the relatively flat power profile (peak-to-average power ratio of 1.04) determined from the neutron detector measurements during steady-state operation.(7) Ignoring the effects of self-shielding on gamma ray attenuation, the activity at the thermocouple tip indicates that the local LHGR at that point was 97% of the average LHGR in the rod. The reduced activities above and below the thermocouple tip were caused by lower fissile atom density regions known to have existed from the time of manufacture. Segregation of the fine fraction to near the bottom of the thermocouple well with corresponding segregation of the coarse fraction to the top of the column resulted in lower fuel densities in these regions during the fuel loading.

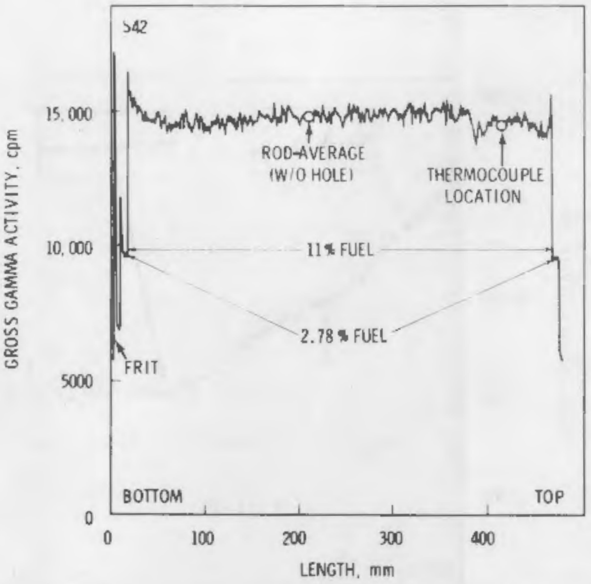

FIGURE 71. Gross Gamma Activity Distribution in Rod S42

The misleading activity caused by irradiation in the parking position prevented comparison between rods for any significant axial migration of fission products. However, spectral scans for long-lived ^{137}Cs indicated varying degrees of migration in the different types of rods as discussed in Section 4.3.4.

The gross gamma scans indicated that significant axial gaps--gaps greater than 1.3 mm (0.05 in.)--were not formed in any of the rods with pellet fuel. In a rod fueled with dished pellets, the pellet interfaces can normally be identified very easily by decreases in activity in gross gamma scans. This is true if 1) the dishes have not been filled with fuel and/or 2) fission products have not migrated to the interfaces. In Rod R1, which was ramped to 71 kW/m, the pellet interfaces were easily identified by decreases in activity over the lower half of the fuel stack. Some interfaces in the upper portion of the fuel column were partially or entirely obliterated (Figure 72), which indicates that the latter dishes were filling due to fuel movement over at least the upper portion of the fuel column. This general trend is consistent with the slightly higher LHGR (3% to 6%) in the upper portion of the column as

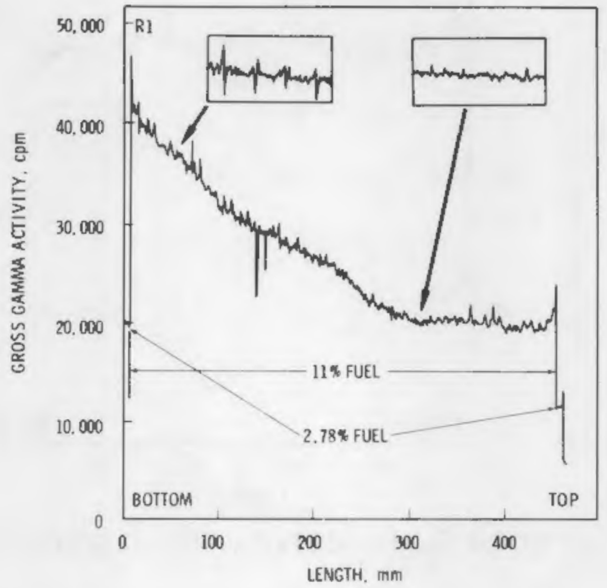

FIGURE 72. Gross Gamma Activity Distribution in Rod R1

compared with the lower portion. The interfaces in Rod R2, which was ramped to 74 kW/m, were also generally distinguishable as activity decreases. It might be expected that the interfaces in Rod R2 would be less distinguishable in gross gamma scans due to higher fuel temperatures and more fuel moving to the dishes. However, ceramographic evidence presented later in Figure 84 shows that, although dish filling did occur in both Rods R1 and R2, the decreases in activity at the original pellet interfaces were generally caused by transverse cracking of a sintered central core of fuel that formed during the ramp test and reopened at the position of the old interfaces during the final shutdown.

Distinct pellet interfaces were also indicated by activity decreases in the axial gamma scans in Rods AC9 and AC10 even though the pellets in these rods were originally flat-ended. As with the dished-pellet reference rods, ceramographic evidence indicated that the activity decreases were primarily caused during the final shutdown by transverse cracking of a sintered central core of fuel that had formed during the ramp test.

The fuel column lengths for the rods with pellet fuel were determined from the gross gamma scans. It was assumed that the fuel column length corresponded to the half-peak position at each end of the fuel column, including the low enrichment pellets. Relocation of small quantities of spheres to locations beneath the lower 2.78% enriched pellet and the lower alumina insulator pellet did not permit measurement of the fuel column length for the sphere-pac rods. However, estimates were made by comparing the pre- and post-test plenum lengths from the neutron radiographs. Fuel column length measurements are compared to preirradiation measurements determined from neutron radiographs in Table 8. The changes that occurred during the testing are also tabulated in the table. All the changes were relatively small (~0.1 to 0.2%); however, the fuel columns in the reference rods were longer after testing while the columns in the annular-coated and sphere-pac rods were shorter. The fuel column lengths in both the ramped and nonramped sphere-pac rods were the same, indicating that the change in Rod S41 occurred before the ramp test.

4.3.4 Spectral Gamma Scanning

Rods R1, R2, AC10, S41, and S42 were axially scanned for ^{137}Cs as described in Section 3.6.3. The axial distribution of ^{137}Cs in ramped Rod R1 is shown in Figure 73. Significant axial migration to the pellet interfaces in the lower portion of the fuel column is indicated by the activity peaks at

TABLE 8. Fuel Column Length Changes

Rod Number	As-Built Length, mm (in.)[a]	Postramp Length, mm (in.)	Change mm (in.)	Change %
R1	461.7 (18.180)	462.5 (18.209)[b]	+0.7 (+0.029)	+0.15
R2	461.0 (18.150)	462.0 (18.187)[b]	+0.9 (+0.037)	+0.20
AC9	464.9 (18.305)	464.0 (18.269)[b]	-0.9 (-0.036)	-0.19
AC10	465.4 (18.325)	465.1 (18.312)[b]	-0.3 (-0.013)	-0.06
S41	465.6 (18.330)	465.1 (18.310)[c]	-0.5 (-0.020)	-0.11
S42	464.6 (18.290)	464.1 (18.270)[c]	-0.5 (-0.02)	-0.11

(a) Measured from preirradiation neutron radiographs; estimated precision is ±0.13 mm (0.005 in.).

(b) Measured from postramp gamma scans; estimated precision is ±0.13 mm (0.005 in.).

(c) Measured from postramp neutron radiographs; estimated precision is ±0.25 mm (0.010 in.).

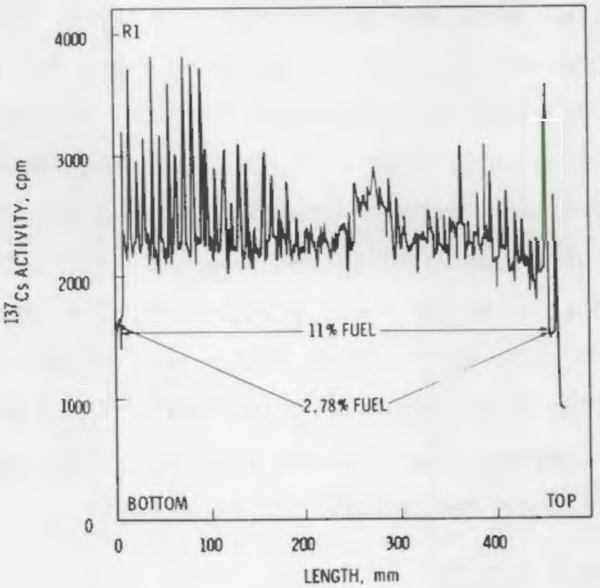

FIGURE 73. Axial Distribution of ^{137}Cs in Rod R1

the interfaces. The ^{137}Cs activity distribution at points away from the pellet interfaces was relatively flat for this long-lived isotope, which indicates that this general axial distribution of ^{137}Cs is typical of the relatively flat steady-state axial power profile. The flat power and even ^{137}Cs distribution also indicate that the ^{137}Cs that concentrated at the pellet interfaces in the lower part of the rod was originally relatively evenly distributed along the length of the fuel column. Cesium-137 also migrated to the high surface area Zircaloy frit in the lower end plug and to the region of the alumina insulator that was just above the 2.78% enriched pellet at the top of the fuel stack.

In Rod R2, ^{137}Cs did not concentrate at pellet-pellet interfaces; but it did concentrate at several regions along the length of the rod that were approximately one to three pellets in length (Figure 74). The general ^{137}Cs distribution, as evidenced by observing the minimums in the distribution, was relatively flat. Because the peak-to-average steady-state LHGR in the rods was ~1.15, significant ^{137}Cs axial migration to the lower portion of the rod occurred as a result of the ramp test. Rod R2 was ramped to the highest LHGR.

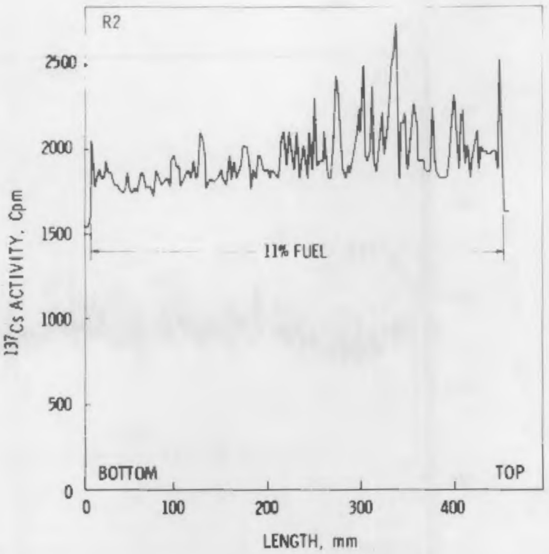

FIGURE 74. Axial Distribution of ^{137}Cs in Rod R2. Data were unavailable from computer tape and were plotted by hand; therefore, less detail is shown than in the other gamma scans.

In ramped Rod AC10, the pellet-to-pellet interfaces were fairly well-defined by minimums in the ^{137}Cs distribution (Figure 75). The axial distribution of ^{137}Cs does not have an axial peak-to-average of about 1.15, as would be expected from the steady-state irradiation. Thus, significant ^{137}Cs redistribution from the top to the bottom of the fuel stack is indicated. The low-enrichment pellet at the bottom of the stack had the highest activity.

The axial distributions of ^{137}Cs in Rods S41 and S42 are shown in Figures 76 and 77, respectively. Some axial migration occurred to the low fuel density regions immediately below and in the region of the thermocouple well in ramped Rod S41, and ^{137}Cs also migrated to the very bottom of the fuel column and the upper part of the frit in the lower end plug. The ^{137}Cs distribution in nonramped Rod S42 was relatively flat, which confirms the steady-state power profile.

4.3.5 Eddy-Current Examination

Eddy-current signals did not indicate any incipient cladding defects in any of the power-ramped rods (Section 3.6.4). This Harwell result confirmed the eddy-current results obtained at Halden.

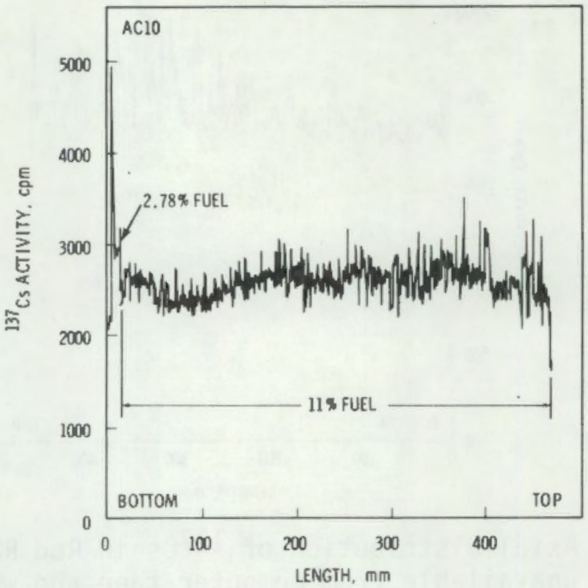

FIGURE 75. Axial Distribution of ^{137}Cs in Rod AC10

4.3.6 Profilometry

Profilometry measurements were made at both the Halden and Harwell facilities. Because the preramp and postramp measurements were made at the same azimuthal position at Halden, these results are used in this report (see Section 4.2.3).

Five of the ramped fuel rods had V-groove notches machined in the upper and lower end plugs to determine the length of the rods. Preirradiation measurements were made at Kjeller, Norway, on the as-built rods, and postramp measurements were made at Harwell. The measurements (see Table 9) reflect very small changes in rod length (0.10 to 0.22 mm). Rod length increases of >0.2 mm had been expected for all the rods due to the measured in-reactor irradiation-induced growth. In addition, a rod length increase of ~0.3 mm had been expected in Rod R1 due to the measured length increase after the ramp test. Neither of these changes was confirmed by the postirradiation measurements. Significant length variances between the V-grooves as a function of azimuthal position were known to have been present in the rods before irradiation. It is felt that these variances, differences in measurement techniques and equipment, and a lack of cross-calibration between the two sites at which the measurements were made render the measurements of little value. They are included in this report, however, for completeness.

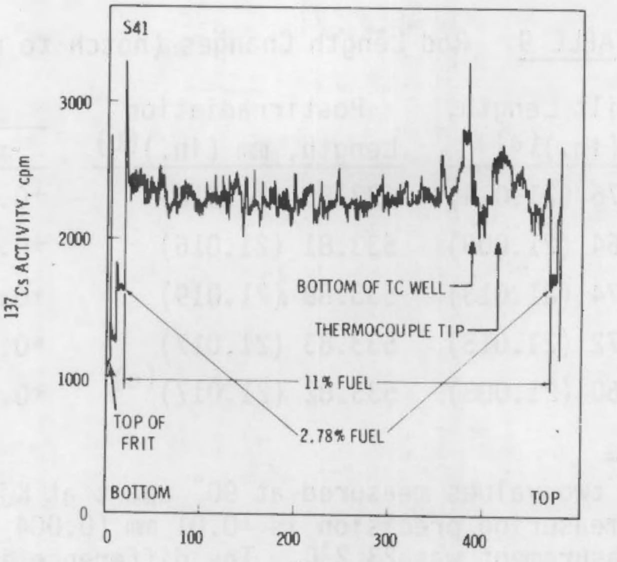

FIGURE 76. Axial Distribution of ^{137}Cs in Rod S41

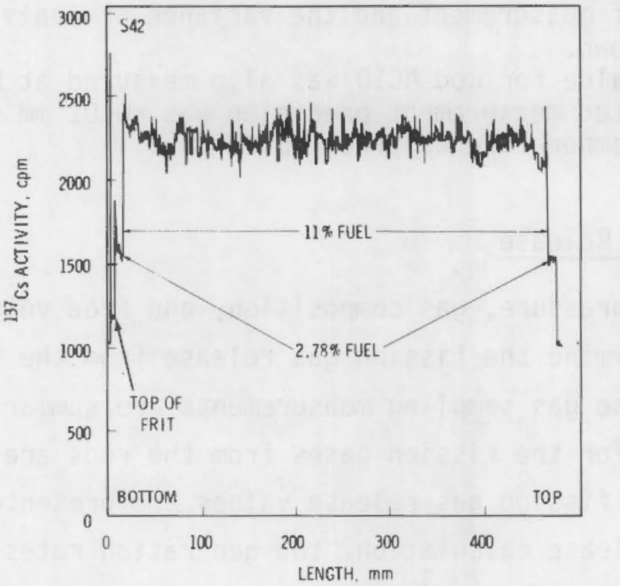

FIGURE 77. Axial Distribution of ^{137}Cs in Rod S42

TABLE 9. Rod Length Changes (notch to notch)

Rod Number	As-Built Length, mm (in.)(a)	Postirradiation Length, mm (in.)(b)	Difference	
			mm (in.)	%
R1	533.76 (21.014)	533.86 (21.018)	+0.10 (0.004)	+0.02
R2	533.64 (21.009)	533.81 (21.016)	+0.17 (0.007)	+0.03
A6	533.74 (21.013)	533.89 (21.019)	+0.15 (0.006)	+0.03
AC9	533.72 (21.013)	533.83 (21.017)	+0.11 (0.004)	+0.02
AC10	533.60 (21.008)	533.82 (21.017)(c)	+0.22 (0.009)	+0.04

(a) Average of two values measured at 90° apart at Kjeller, Norway. Estimated measuring precision is ±0.01 mm (0.004 in.). Temperature at time of measurement was 23.2°C. The difference in the two length measurements varied from 0.01 mm to as high as 0.08 mm.

(b) Average of at least three measurements made at different azimuthal positions around the rod at Harwell. Estimated precision of the measurement is ±0.01 mm (0.0004 in.). The temperature of cladding at the time of measurement and the variance of individual measurements are not known.

(c) A single value for Rod AC10 was also measured at Halden (533.64 mm); the estimated measurement precision was ±0.01 mm (0.0004 in.), and the cladding temperature was from 35 to 38°C.

4.3.7 Fission Gas Release

Internal rod pressure, gas composition, and free volume were measured for seven rods to determine the fission gas release from the fuel (Section 3.6.6). The results of these gas sampling measurements are summarized in Table 10; isotopic contents for the fission gases from the rods are given in Table 11; and the calculated fission gas release values are presented in Table 12. For the fission gas release calculation, the generation rates used were 26.9 cm^3 (STP)/MWd for xenon and 4.1 cm^3 (STP)/MWd for krypton and the burnup values used were those given in Section 4.3.9.

The low values for oxygen and nitrogen (Table 10) in the gas from all the rods indicate that there was no significant leakage during sampling. The low values for carbon monoxide and carbon dioxide in Rods AC9 and AC10 show that there were no significant chemical reactions between the fuel and the graphite coating, even at the high fuel temperatures experienced during the power-ramp

TABLE 10. Summary of Gas Sampling Results

Item	R1	R2	A6	AC9	AC10	S41	S42
	Rod Number						
Hydrogen, vol%	---	0.04	---	---	---	---	0.03
Helium, vol%	18.19	9.83	15.96	17.30	17.18	58.1	90.42
Oxygen, vol%	0.06	0.02	0.14	0.04	---	---	0.07
Carbon monoxide/ nitrogen, vol%	0.21	0.38	0.50	0.30	0.25	0.02	0.36
Argon, vol%	---	0.014	0.025	---	---	0.04	0.13
Carbon dioxide, vol%	0.12	0.03	---	0.02	0.11	0.01	---
Krypton, vol%	10.71	10.06	11.19	10.84	10.85	5.5	1.22
Xenon, vol%	70.17	79.60	72.17	71.50	71.61	36.40	7.80
Pressure, kPa (psi) at 0°C	462.5 (67.07)	635.7 (92.19)	531.6 (77.10)	485.1 (70.36)	532.0 (77.15)	716.6 (103.93)	432.0 (62.66)
Void volume, cm^3	7.70	7.97	10.40	10.65	10.53	8.15	8.20

TABLE 11. Isotopic Contents of Fission Gases

Rod	Krypton, %				Xenon, %				
Number	$^{83}\mathrm{Kr}$	$^{84}\mathrm{Kr}$	$^{85}\mathrm{Kr}$	$^{86}\mathrm{Kr}$	$^{130}\mathrm{Xe}$	$^{131}\mathrm{Xe}$	$^{132}\mathrm{Xe}$	$^{134}\mathrm{Xe}$	$^{136}\mathrm{Xe}$
R1	13.84	26.91	6.45	52.82	0.01	11.38	17.94	32.03	38.62
R2	13.81	26.92	6.44	52.82	0.00	11.41	17.93	32.03	38.61
A6	14.11	27.30	6.69	51.90	--	11.38	17.82	32.00	38.79
AC9	14.06	27.30	6.77	51.88	0.02	11.55	17.81	31.87	38.75
AC10	14.23	26.95	6.74	52.08	0.02	11.61	18.09	31.59	38.68
S41	14.22	26.92	6.86	52.01	0.02	11.55	17.76	31.42	39.25
S42	14.19	27.22	6.53	52.05	--	11.44	18.71	31.03	38.83

TABLE 12. Fission Gas Release Values

Rod Number	Ramping LHGR, kW/m	Burnup, MWd/kgM	Fraction Released		
			Xe	Kr	Xe + Kr
R1	70.6	7.1	0.40	0.40	0.40
R2	74.1	9.7	0.47	0.38	0.46
A6	66.5	10.7	0.46	0.46	0.46
AC9	67.2	10.8	0.42	0.41	0.42
AC10	69.3	10.6	0.46	0.46	0.46
S41	70.9	7.1	0.34	0.34	0.34
S42	(a)	7.0	0.04	0.05	0.04

(a) Rod S42 was not ramped.

tests. For the reference and annular-coated-pressurized rods, the fraction of fission gas released correlates well with the ramping LHGR, i.e., the higher the ramping LHGR, the higher the release fraction. However, releases from the fuel rods with annular fuel were higher than expected (see Section 5.3.1).

The fission gas release value from nonramped sphere-pac Rod S42 was much lower than expected based upon the in-reactor pressure sensor that was operative during steady-state irradiation.(7) Based upon the measured release value, the absolute values of the in-reactor pressure measurements have been adjudged to be in error for Rod S42.

4.3.8 Ceramography

Eleven ceramographic sections were prepared from five of the HBWR fuel rods (Table 13). Transverse sections were taken from the ramped reference, annular-coated, and sphere-pac rods to characterize fuel restructuring at an axial position that was equivalent to a ramping LHGR of ~69 kW/m (a LHGR that was common to all three rods). Photomacrographs of the sections from Rods R1, AC9, and S41 are shown in Figure 78. Fuel fragments from Rod R1 and microspheres from the outer nonrestructured region of Rod S41 fell out during specimen preparation. Radial strips in the as-polished (AP) and etched (E) conditions for each section are shown at higher magnification for Rods R1 and AC9 in Figures 79 through 82, and an as-polished strip for Rod S41 is shown in Figure 83. The location of each strip is noted in Figure 78.[a]

TABLE 13. Ceramographic Sections

Rod Number	Section Type	Typical LHGR During Ramping, kW/m
R1	Transverse	68.7
	Longitudinal	66.6
R2	Transverse	77.1
	Longitudinal	73.2
AC9	Transverse	68.7(a)
	Longitudinal	66.6
S41	Transverse	72.5(a)
	Transverse	69.3
	Longitudinal	70.1
S42	Transverse(a)	(b)
	Longitudinal	(b)

(a) Section taken adjacent to tip of centerline thermocouple.
(b) Rod S42 was not ramped. Typical maximum LHGRs during steady-state operation at the points of sectioning were ~42 kW/M.

---

[a] Due to the optics of the metallographic instrument, the images of the higher magnification strips are a mirror image of the photomacrograph image. This is true for all ceramographs illustrated in this report.

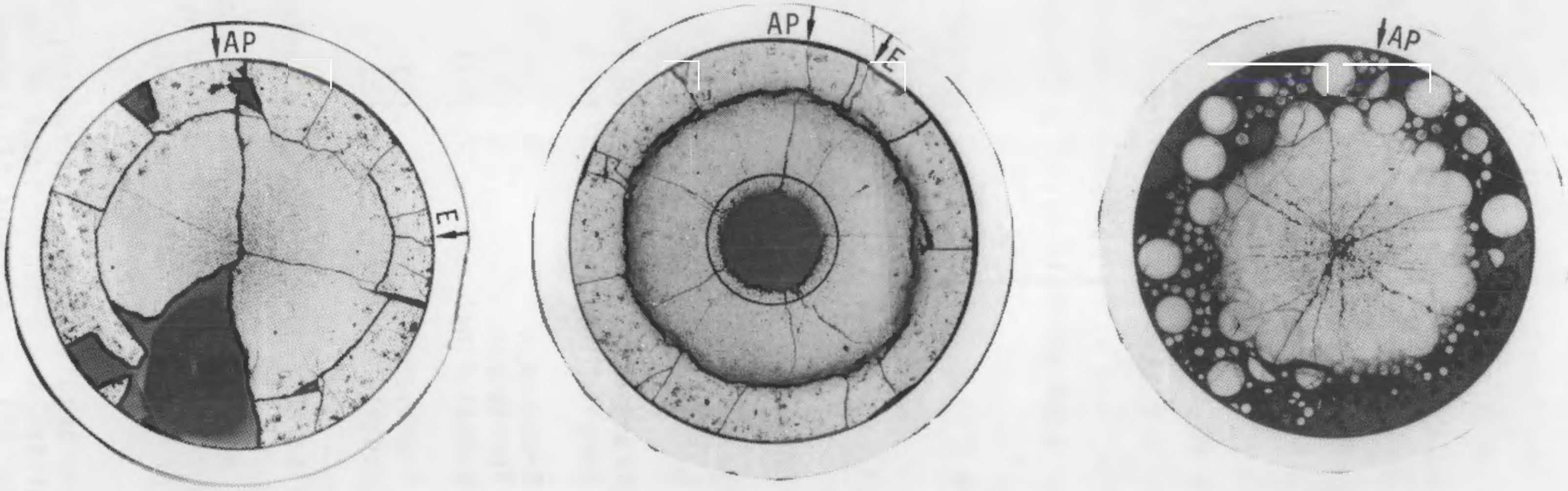

Reference

Annular-Coated

Sphere-pac

FIGURE 78. Photomacrographs of Transverse Sections from Rods R1, AC9, and S41 at the Location Equivalent to an LHGR of 69 kW/m (5.2X)

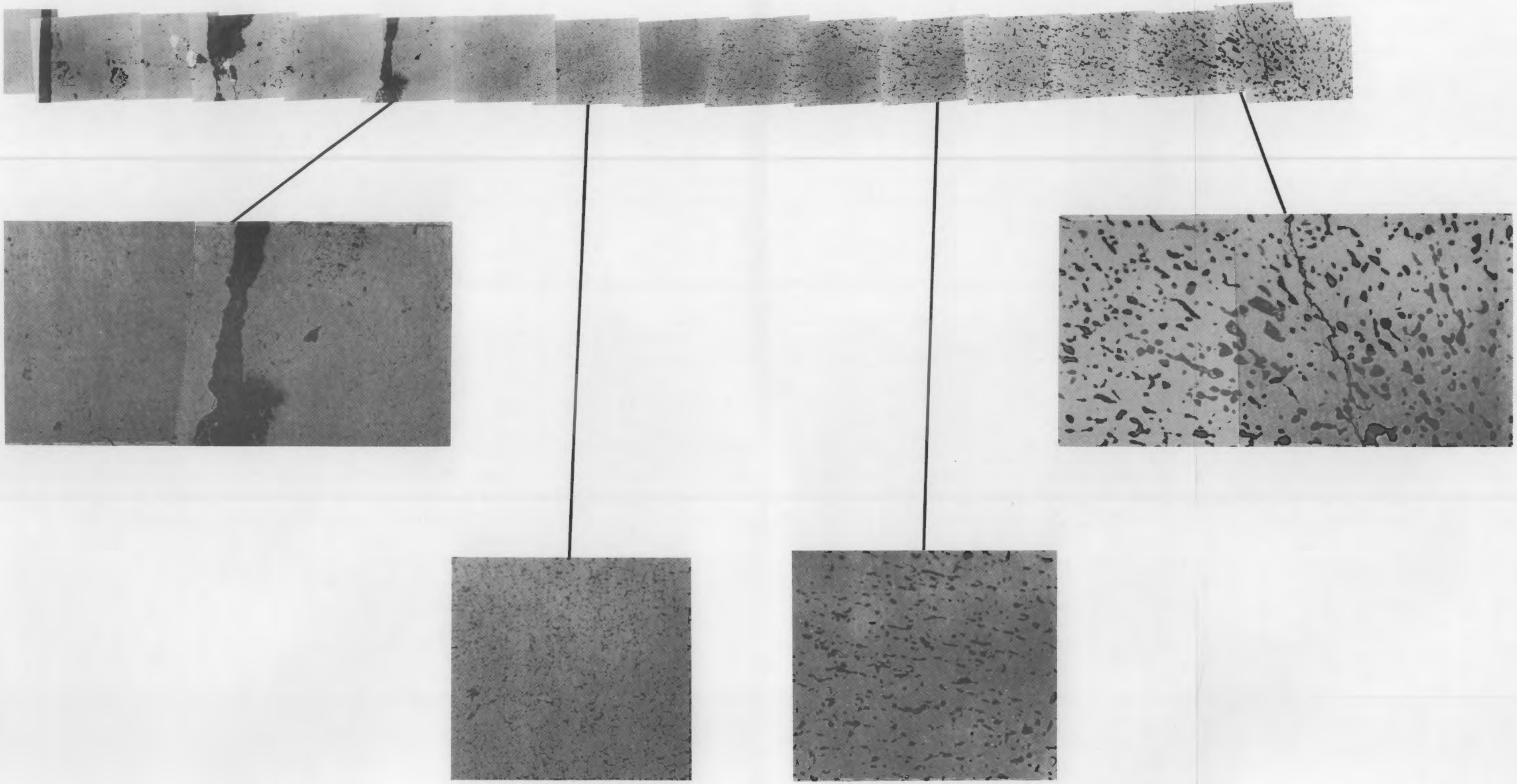

FIGURE 79. As-Polished Radial Strip from Transverse Section of Rod R1 (strip at 62.5X; selected areas at 167X)

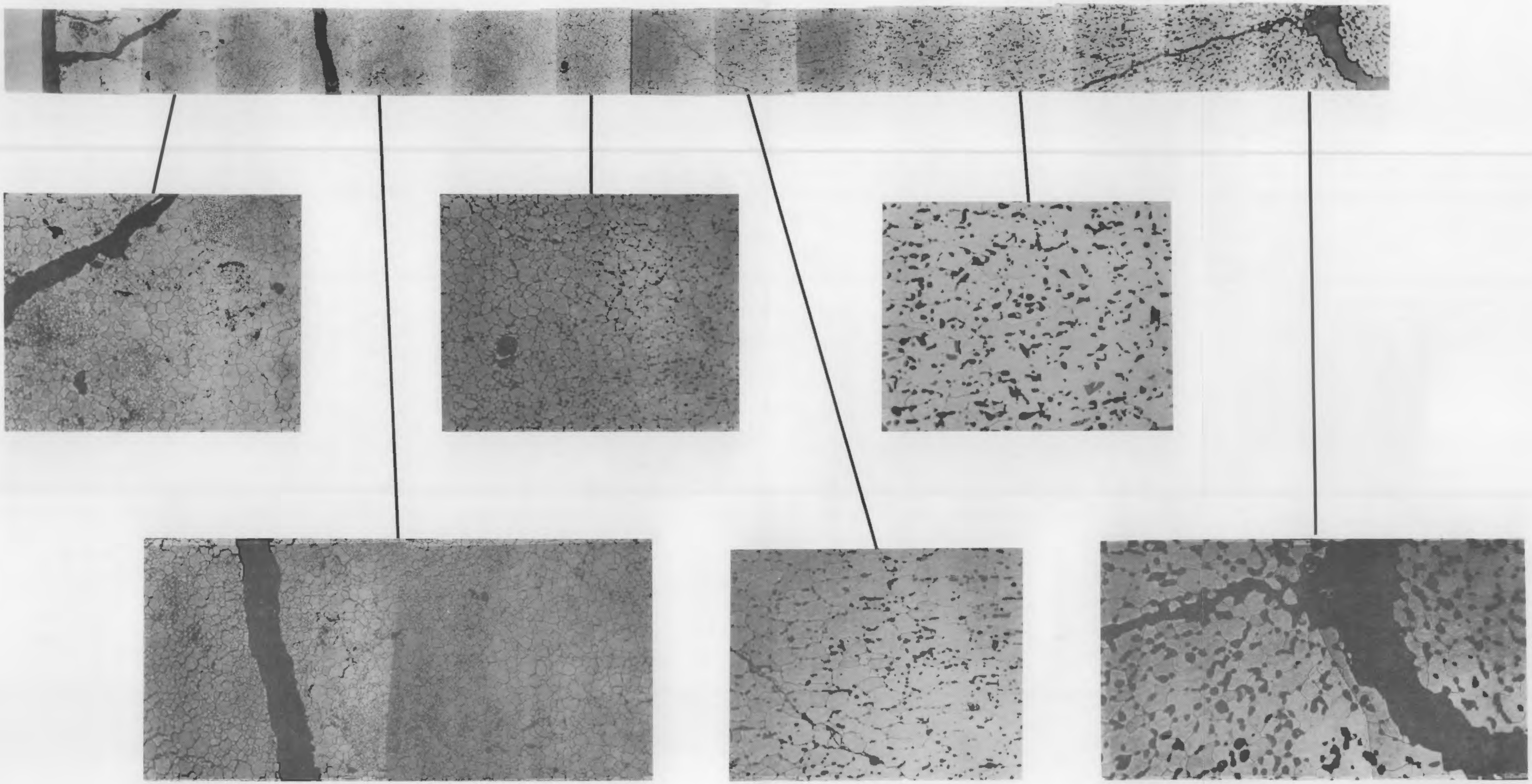

FIGURE 80. Etched Radial Strip from Transverse Section of Rod R1 (strip at 62.5X; selected areas at 167X)

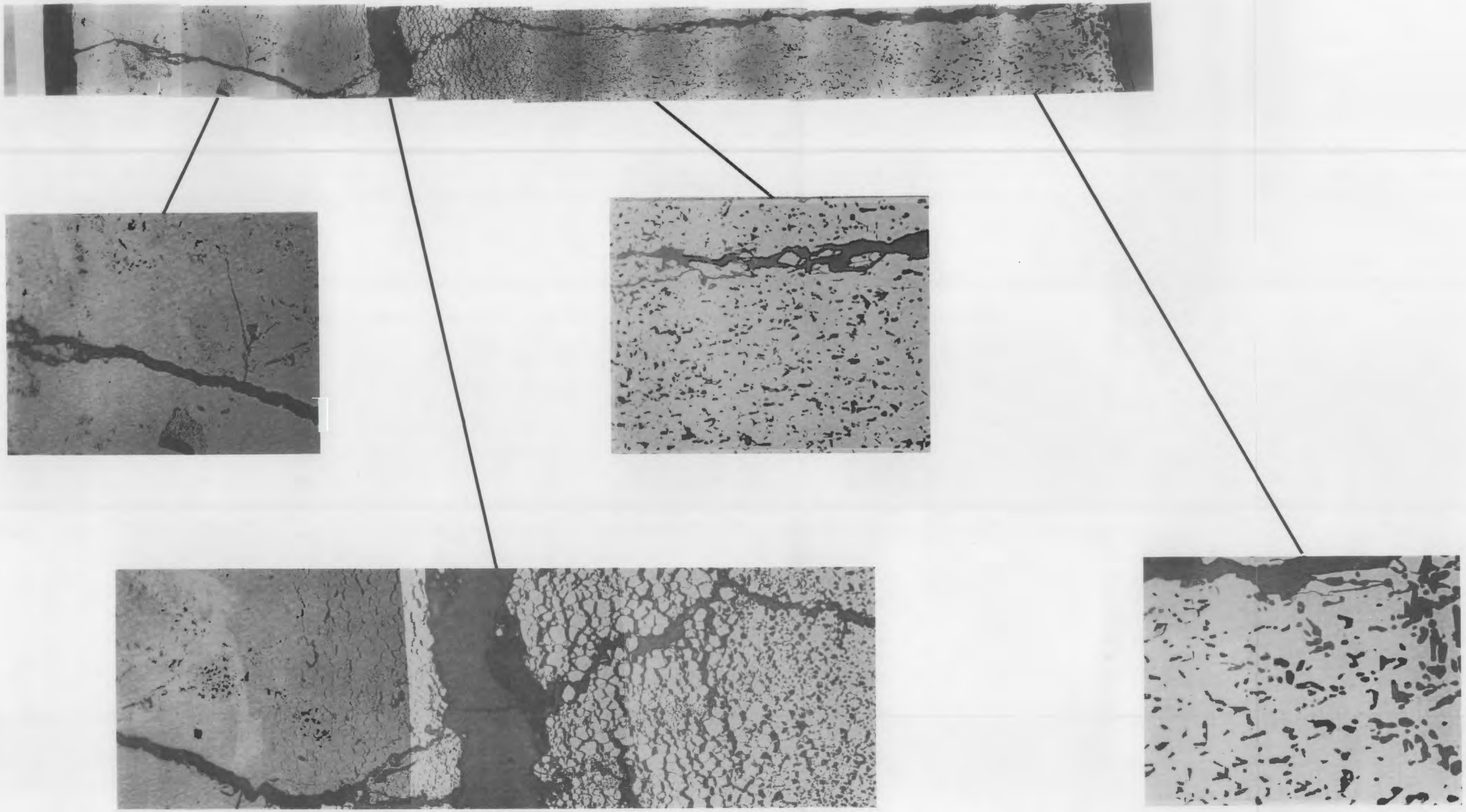

FIGURE 81. As-Polished Radial Strip from Transverse Section of Rod AC9 (strip at 62.5X; selected areas at 167X)

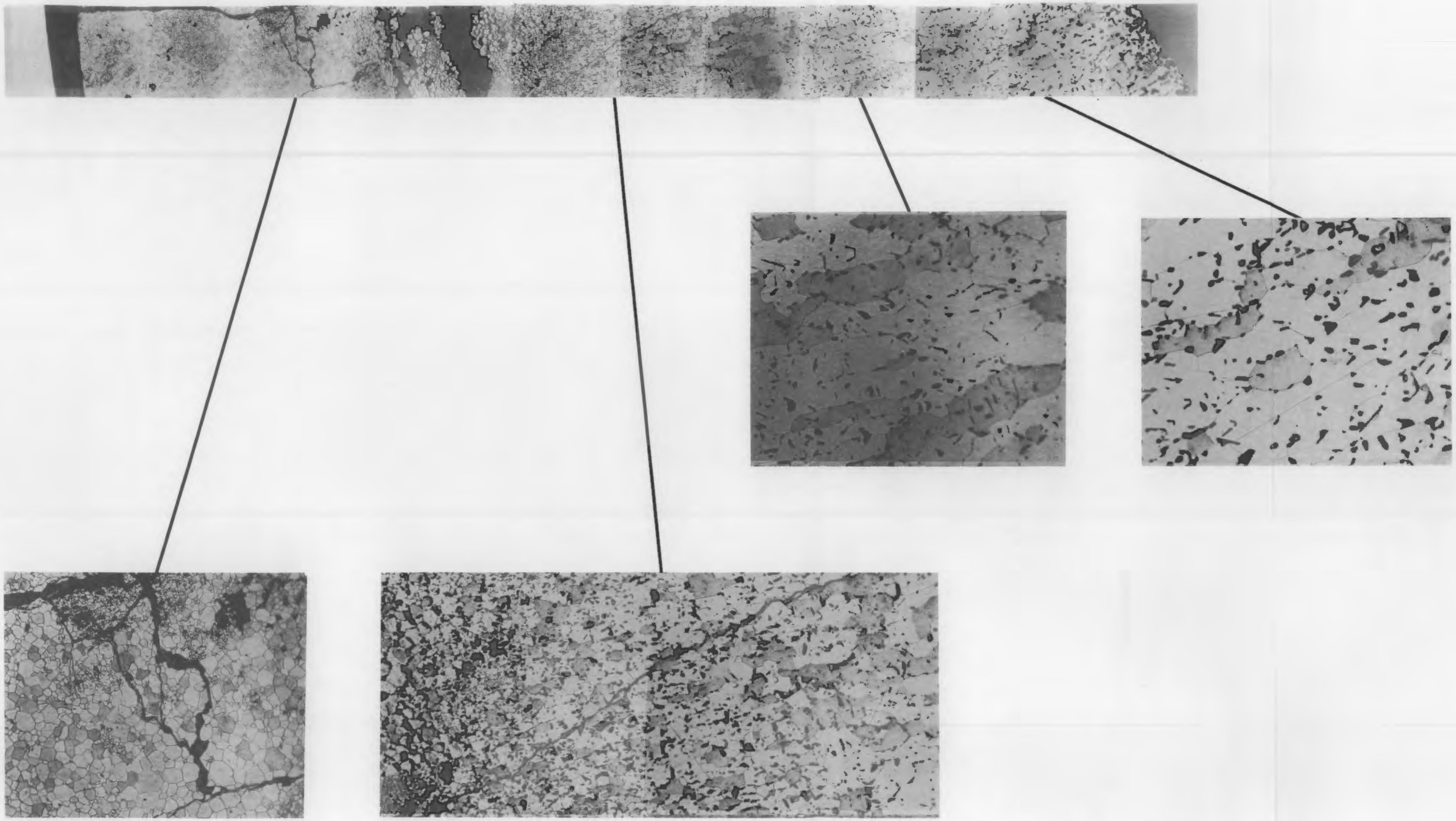

FIGURE 82. Etched Radial Strip from Transverse Section of Rod AC9 (strip at 62.5X; selected areas at 167X)

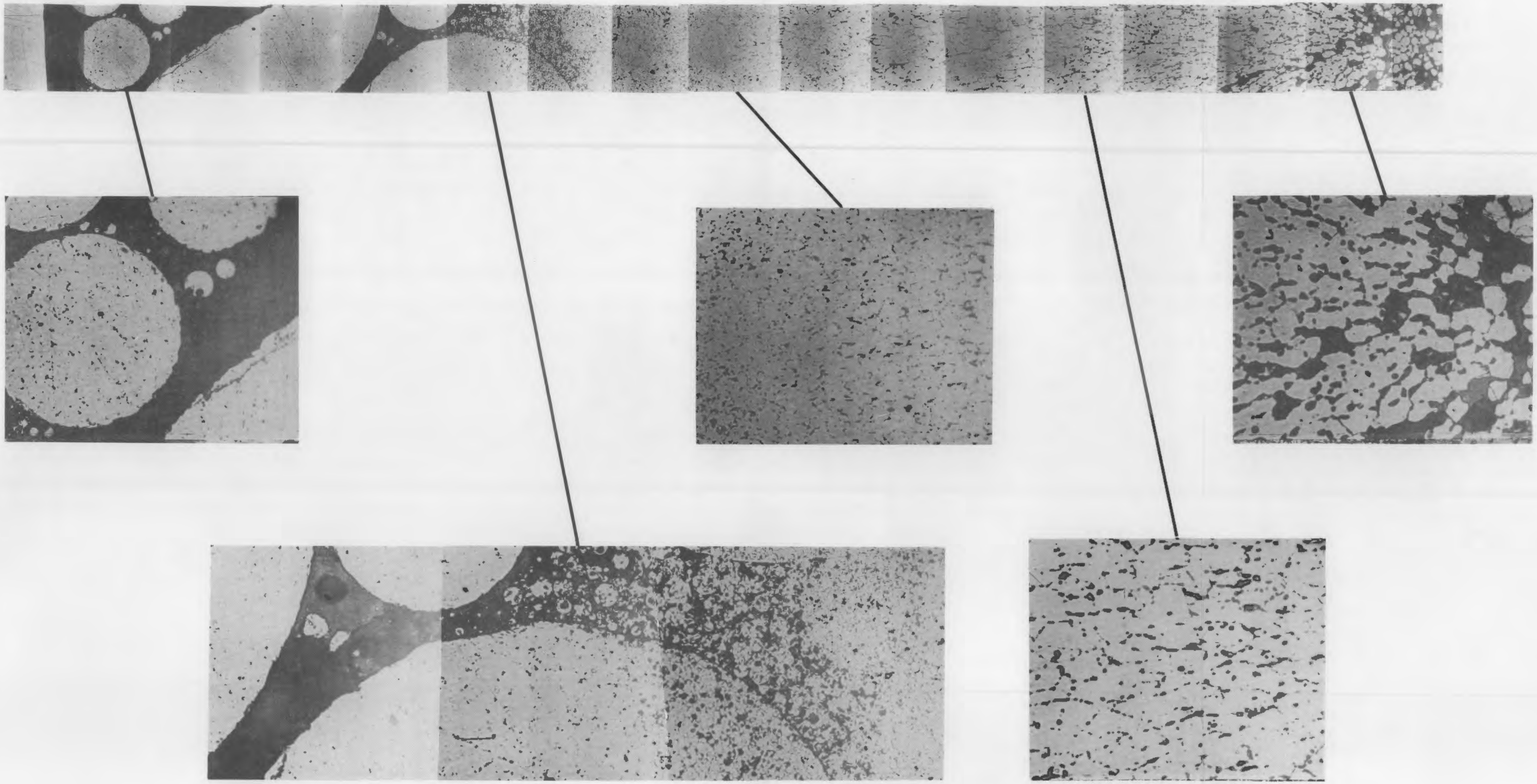

FIGURE 83. As-Polished Radial Strip from Transverse Section of Rod S41 (strip at 62.5X; selected areas at 167X)

Longitudinal sections were also taken from the three types of ramped rods to characterize axial restructuring. The longitudinal samples were ground to the centerline of the fuel rod. The specimen locations were selected based upon a review of the NDE data. The location of the specimen for Rod R1 was based upon an indication of significant obliteration of the rocking pattern (Section 4.2.3), i.e., possible significant mechanical interaction, at a position 75 to 150 mm from the lower weld (see Figure 14). The location of the specimen for Rod AC9 was chosen to quantify central hole closure as well as the maximum degree of closure observed in neutron radiographs. The maximum hole closure occurred in the twenty-third pellet from the bottom of the fuel stack (Figure 68). The location of the specimen for Rod S41 was selected to be representative of transverse cracks observed in the neutron radiographs (Section 4.3.1). Photomacrograhs of these sections are shown in Figure 84.

Radial strips in the as-polished and etched conditions are shown at higher magnification for Rods R1 and AC9 in Figures 85 through 88, and a diametral strip for Rod S41 in the as-polished condition is shown in Figure 89. The locations of the strips are noted in Figure 84.

The cladding from the specimen for Rod AC9 was examined in the etched condition to ascertain if there was any evidence of a graphite/Zircaloy reaction (Figure 90). No evidence of a reaction zone was observed. Similar examinations of the cladding from Rods R1 and R2 also revealed no evidence of any reaction zones.

Transverse sections were taken from ramped Rod S41 and nonramped Rod S42 to verify the position of the thermocouple wells within the beds of spheres. Both thermocouple wells were located properly near the centerline of the fuel rod. Photomacrographs of the specimens are shown in Figure 91.

A longitudinal specimen from nonramped Rod S42 was taken to characterize the fuel restructuring and axial crack formation that was observed in the neutron radiographs after operation at normal LHGRs. A photomacrograph of the specimen is shown in Figure 92, and a radial strip in the as-polished condition is shown in Figure 93.

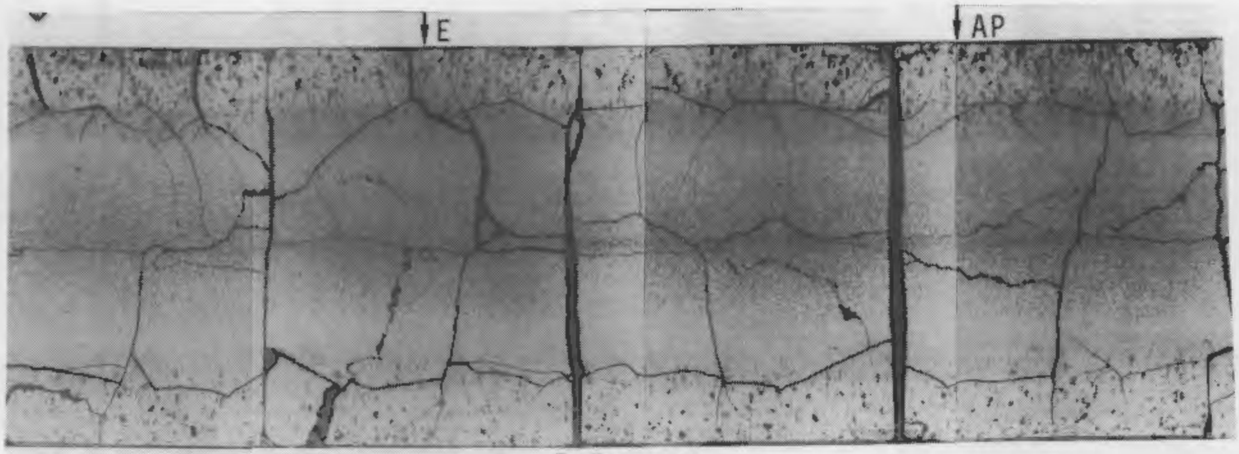

Reference

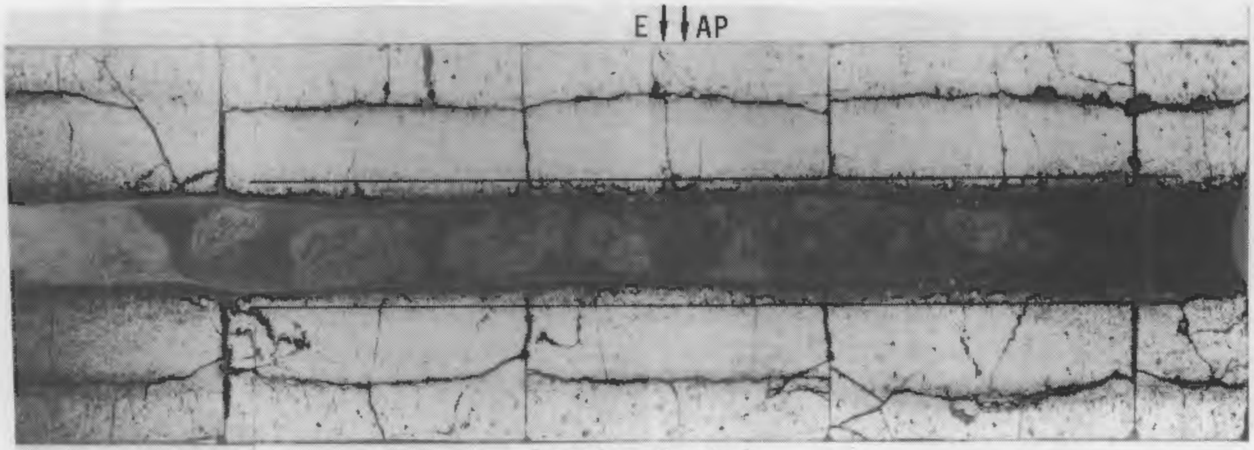

Annular-Coated

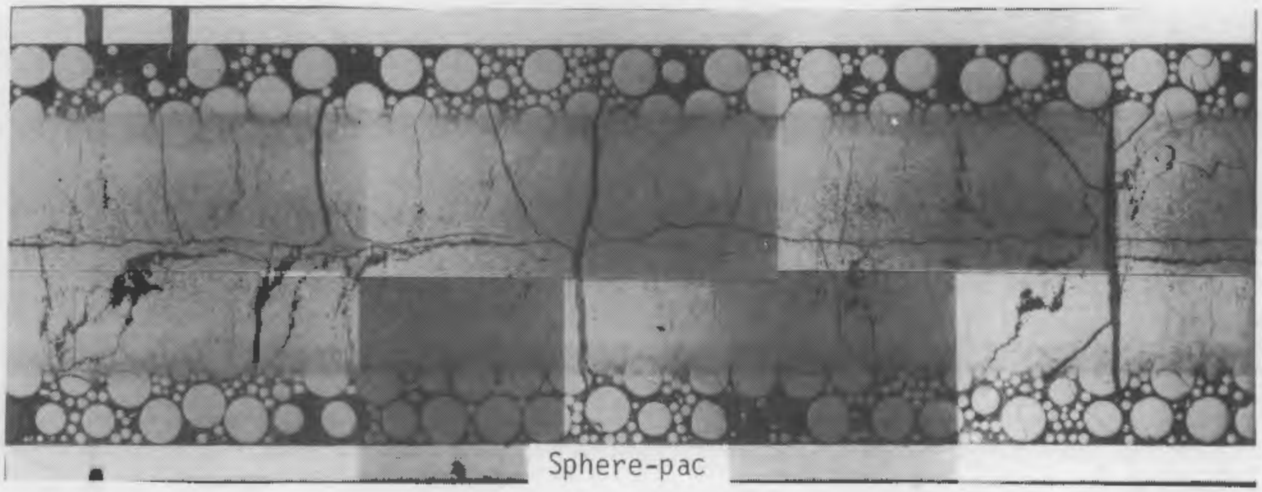

Sphere-pac

FIGURE 84. Photomacrographs of Longitudinal Sections from Rods R1, AC9, and S41 (5.1X). The lines on the AC9 photograph represent the original hole diameter.

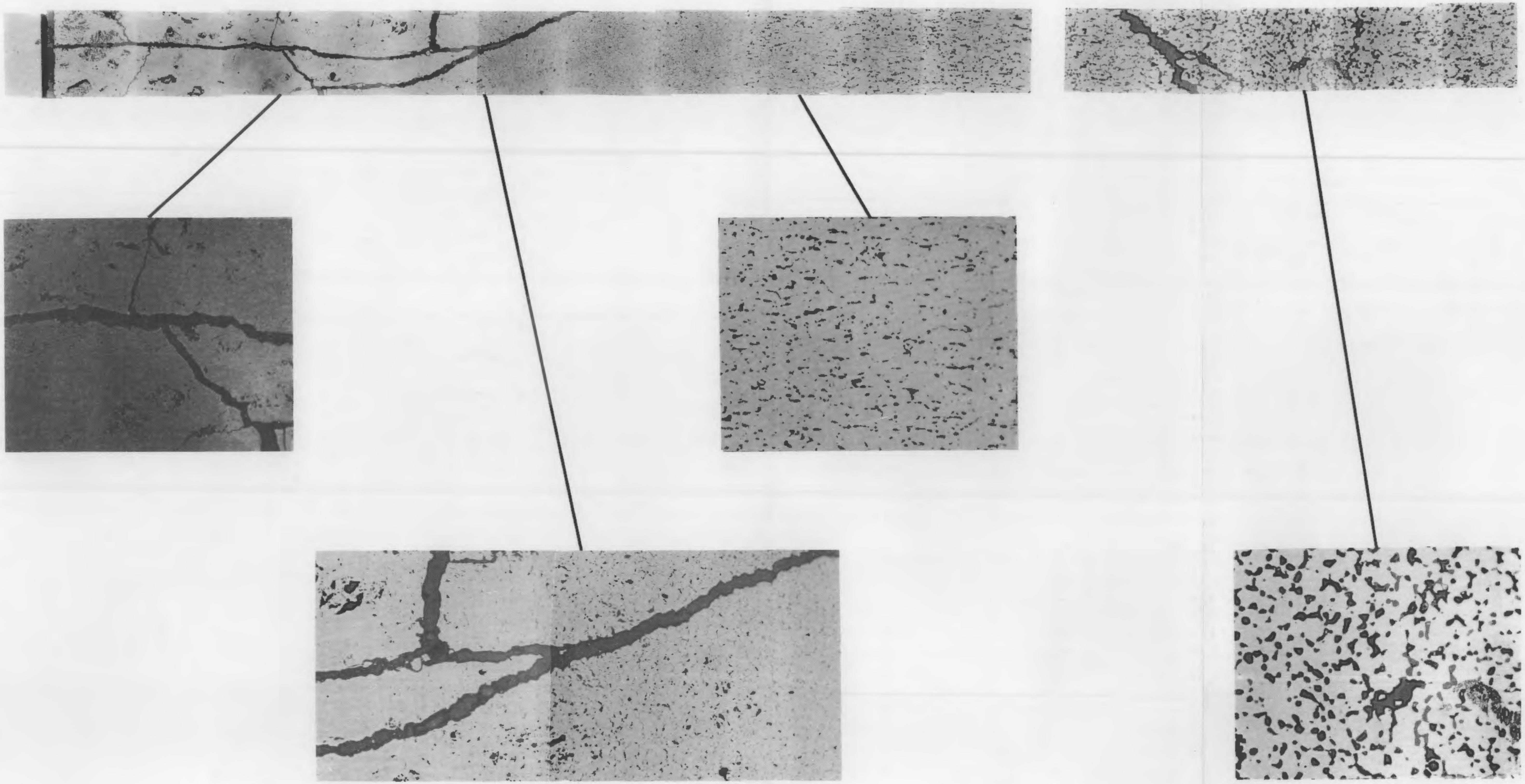

FIGURE 85. As-Polished Radial Strip from Longitudinal Section of Rod R1 (strip at 62.5X; selected areas at 167X)

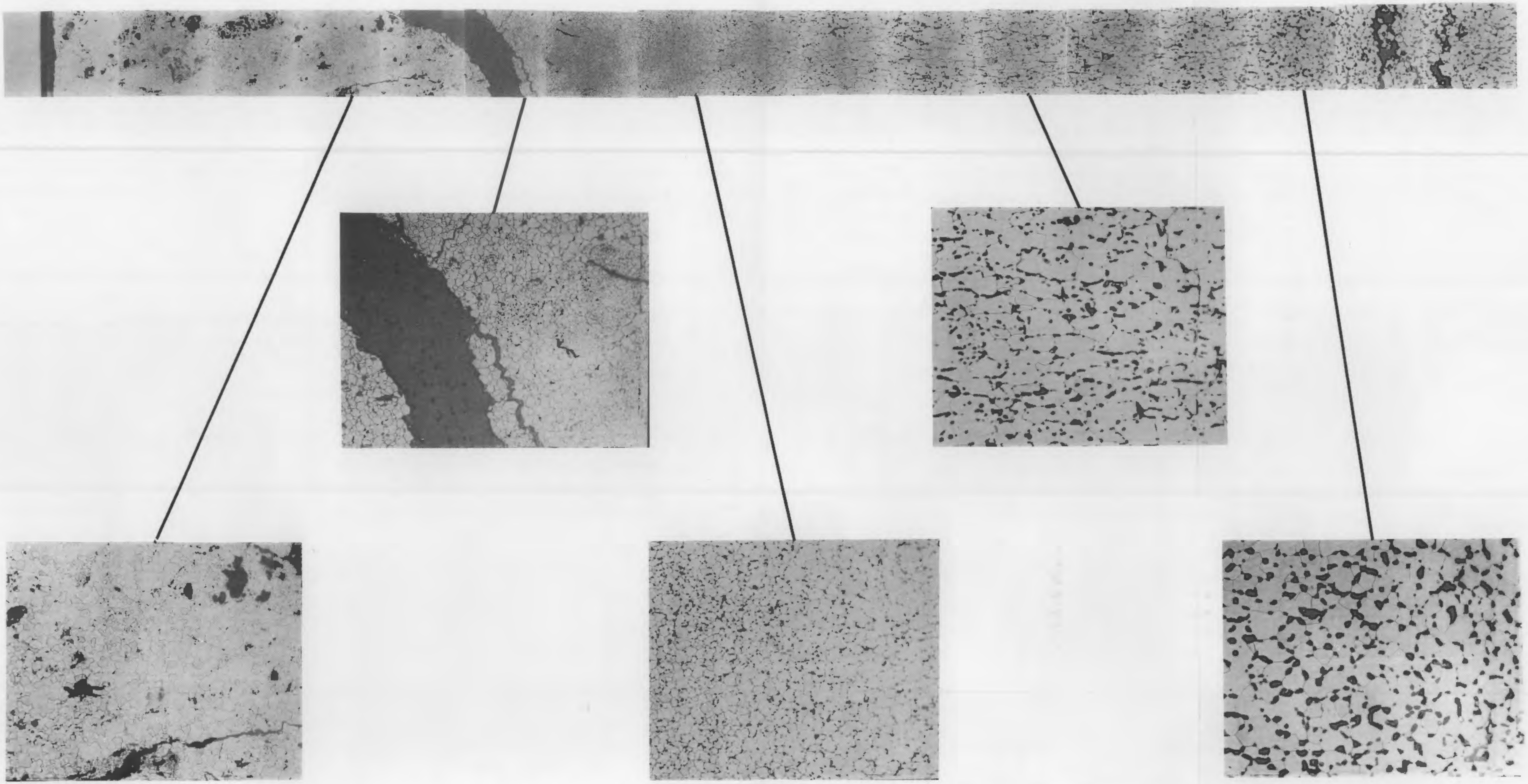

FIGURE 86. Etched Radial Strip from Longitudinal Section of Rod R1 (strip at 62.5X; selected areas at 167X)

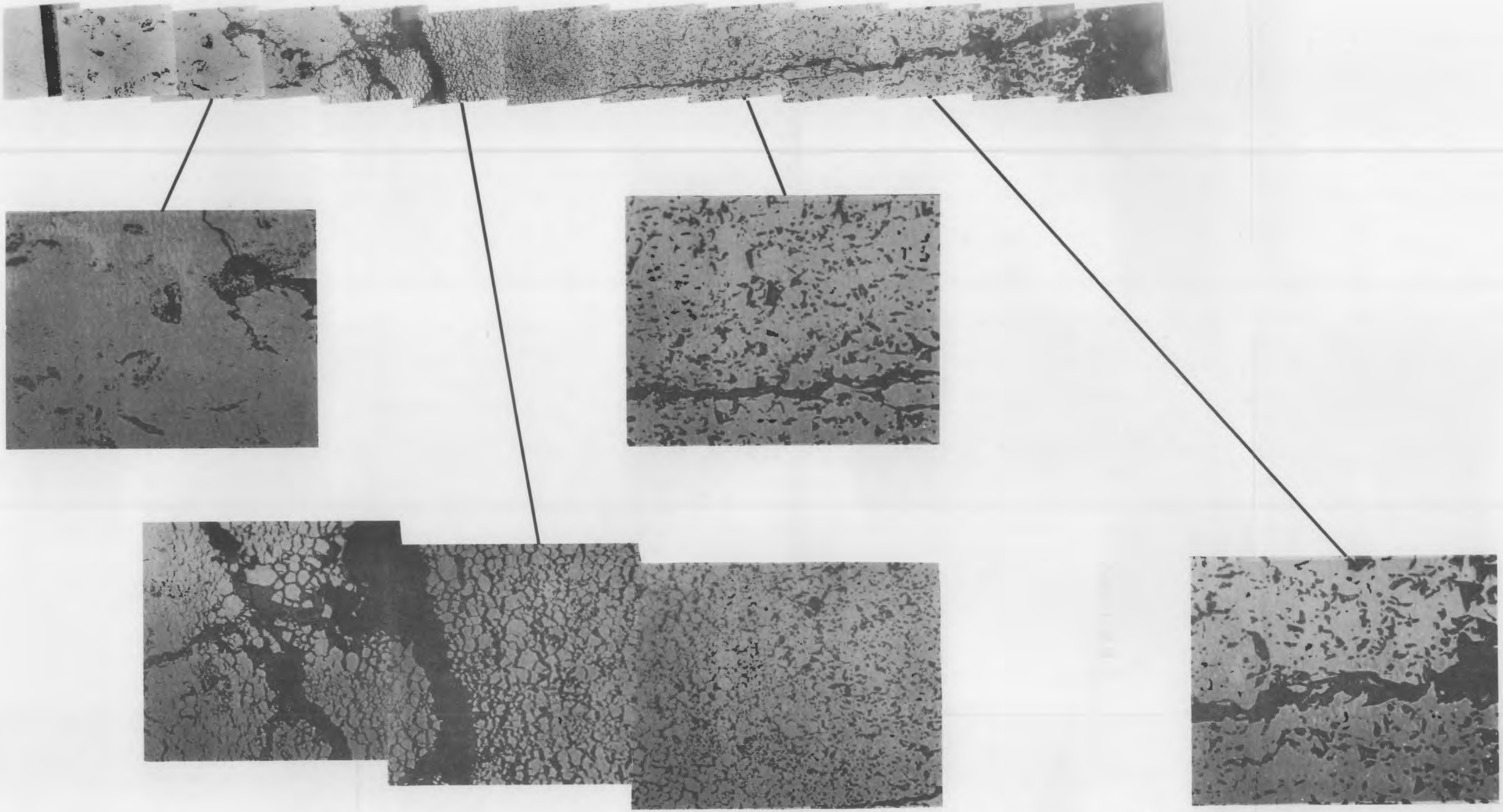

FIGURE 87. As-Polished Radial Strip from Longitudinal Section of Rod AC9 (strip at 62.5X; selected areas at 167X)

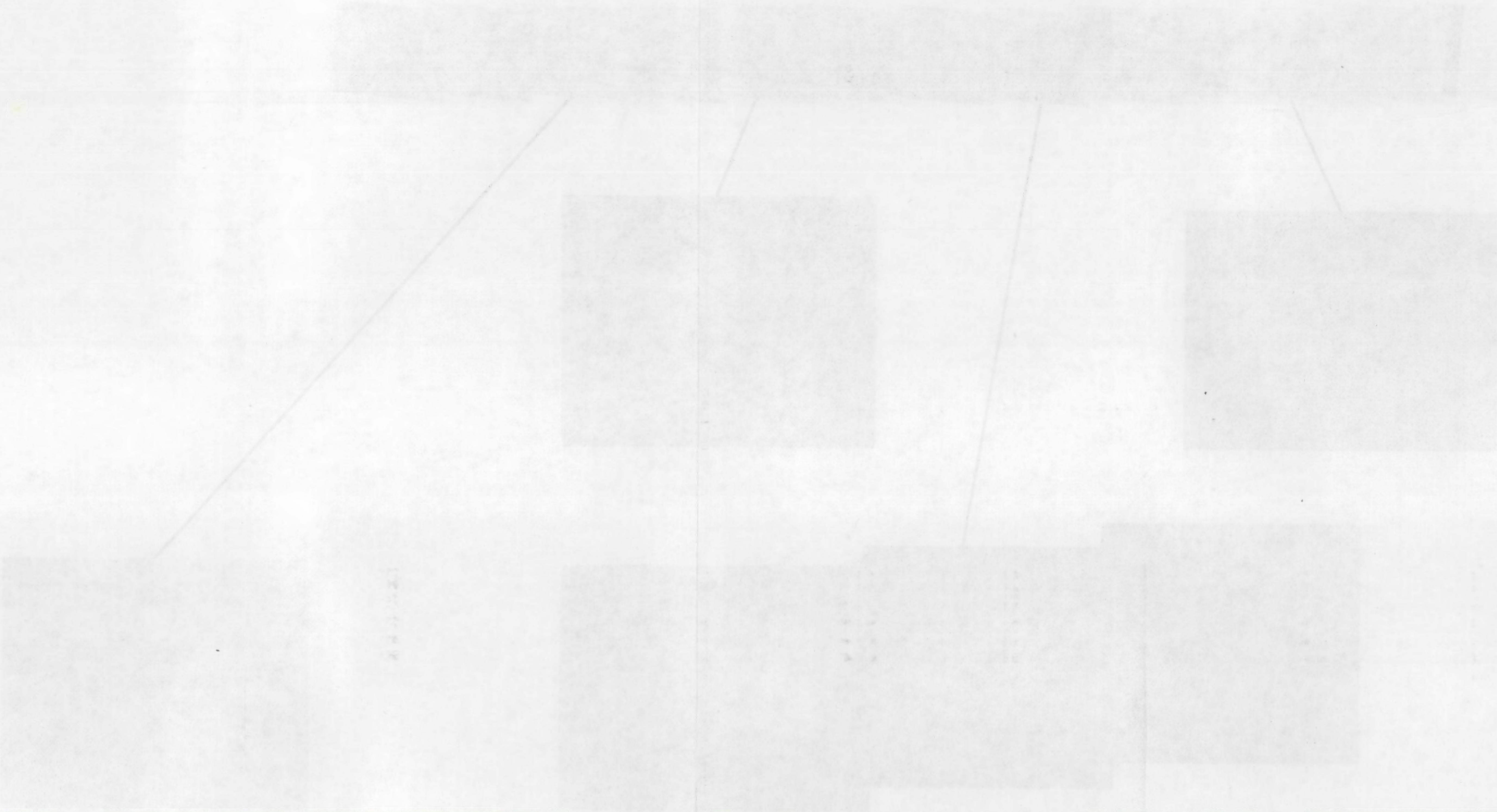

FIGURE 67. As-Polished Radial Strip from Longitudinal Section of Rod ACS (Strip at 62.5X; selected areas at 125X)

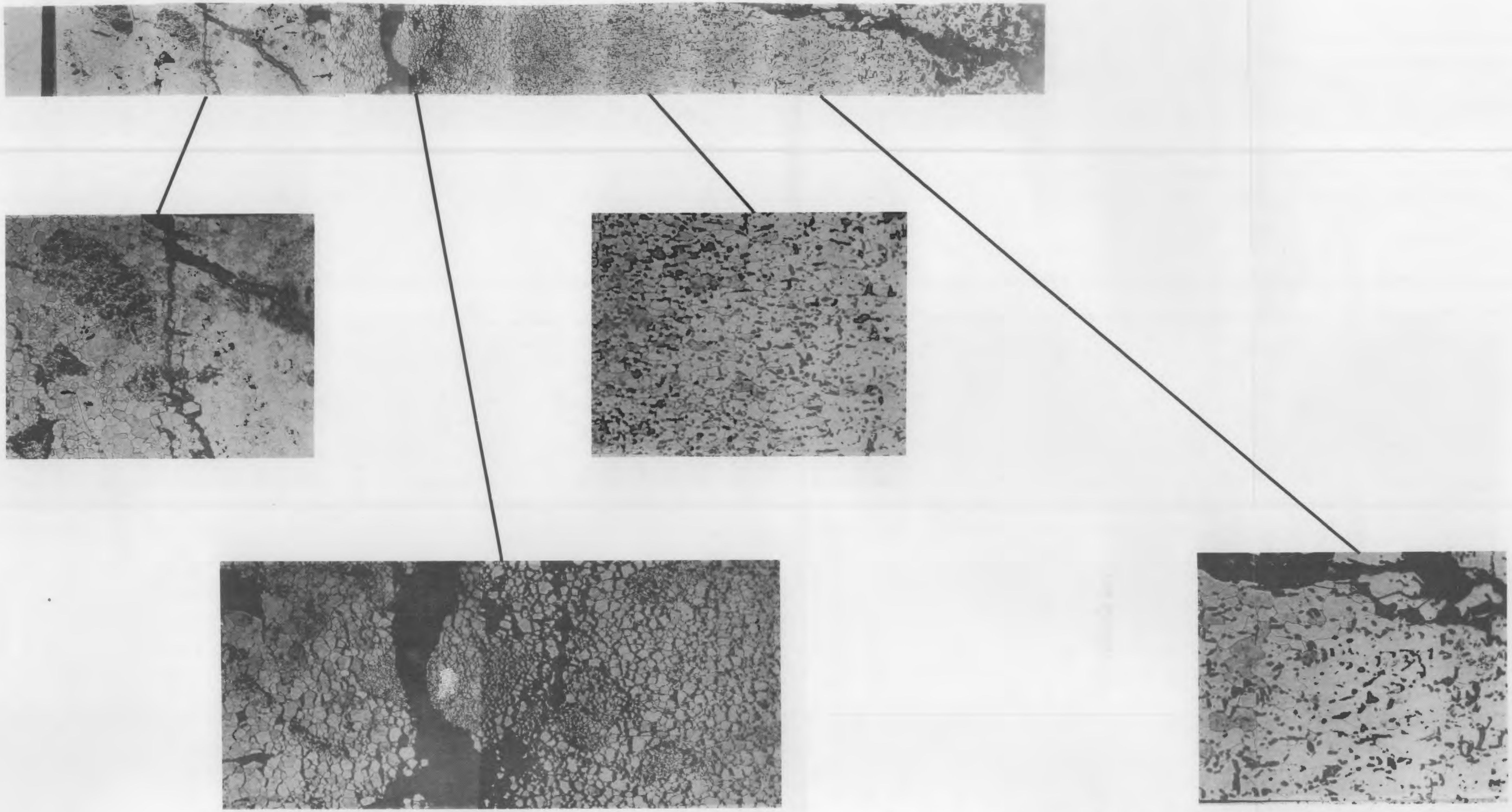

FIGURE 88. Etched Radial Strip from Longitudinal Section of Rod AC9 (strip at 62.5X; selected areas at 167X)

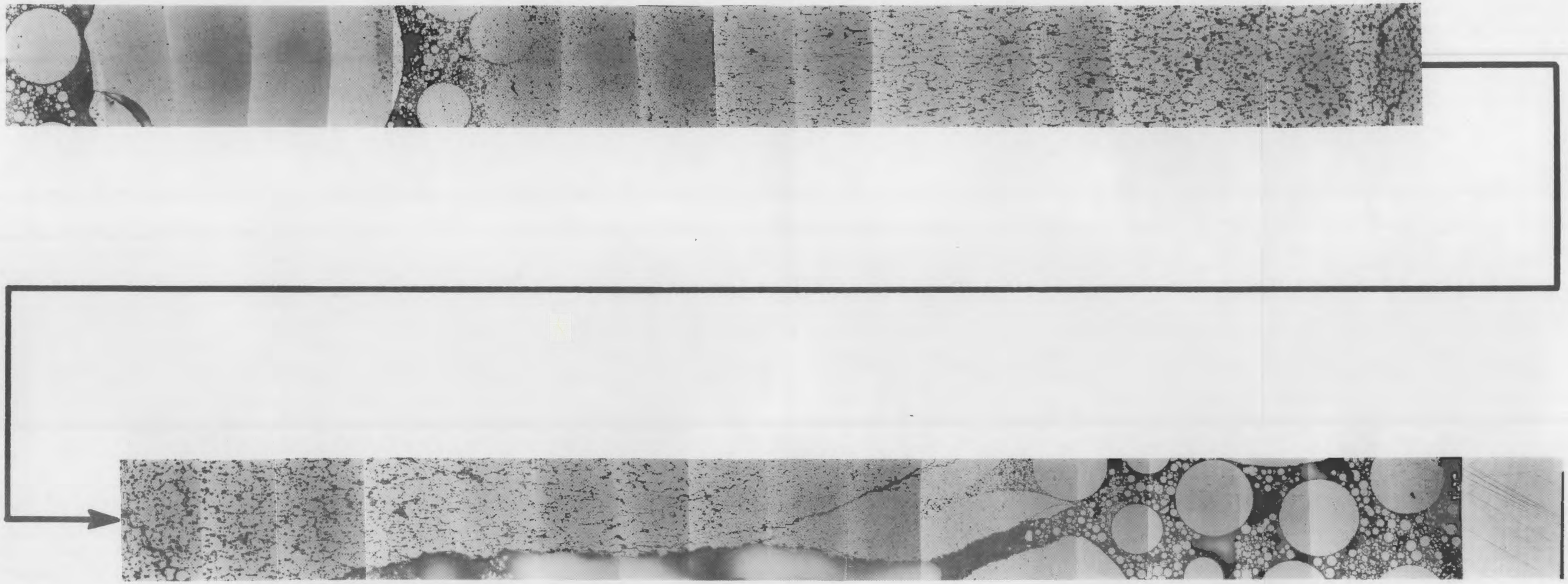

FIGURE 89. As-Polished Diametral Strip from Rod S41 (62.5X)

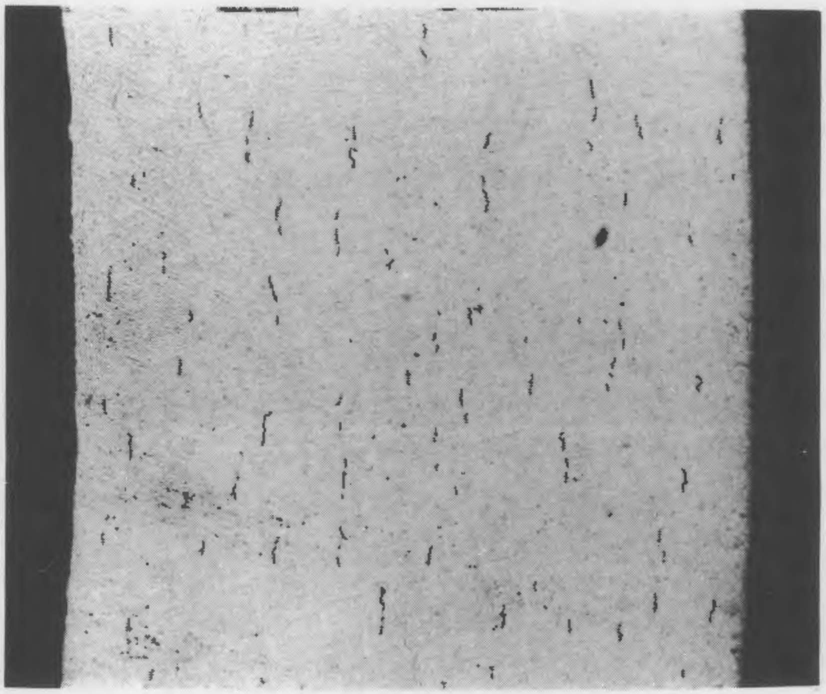

FIGURE 90. Etched Cross Section of Cladding from Rod AC9 (100X)

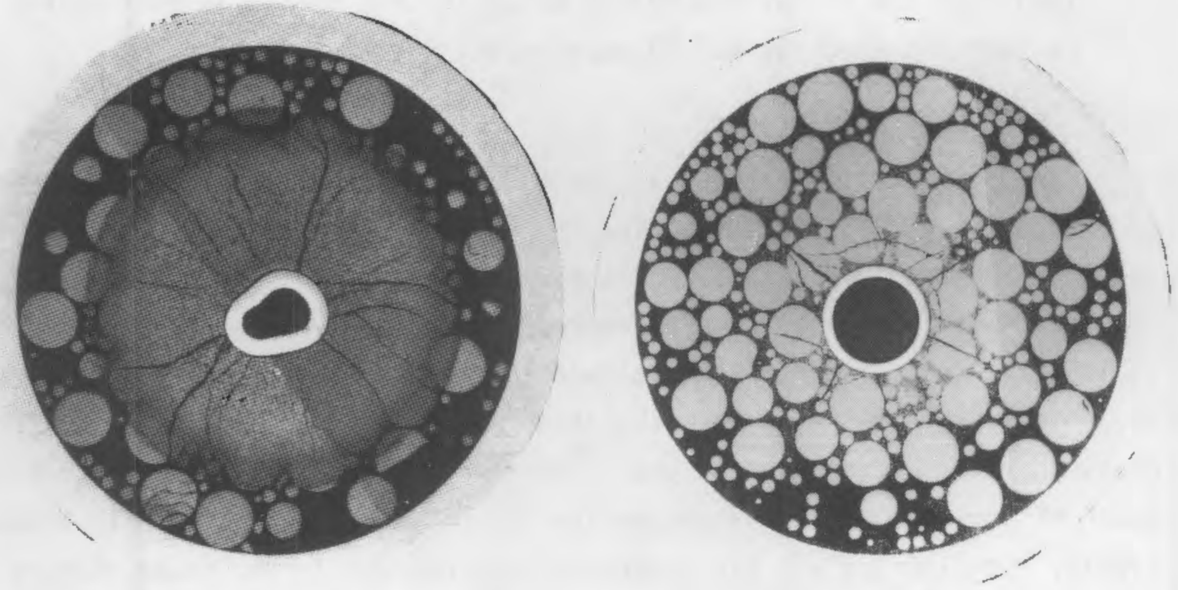

FIGURE 91. Photomacrographs of Thermocouple Wells in Rods S41 and S42 (6.4X)

Transverse and longitudinal sections from reference Rod R2, which had been ramped to very high LHGRs, were taken to characterize the restructuring. Photomacrographs are shown in Figure 94; and radial strips in the as-polished and etched conditions are shown in Figure 95. The locations of the strips are noted on the photomacrographs.

The relationships between the fuel structures, operational factors, and other PIE results are discussed in Section 5. However, a few general observations are worth noting at this point:

- The dominant feature in both the transverse and longitudinal sections from the ramped annular-coated rods was a large midradius circumferential crack in each fuel pellet. This circumferential crack was also observed in the neutron radiographs (Section 4.3.1).
- The central portion of the fuel in all the ramped rods exhibited extensive grain and pore (bubble) growth. In the reference rods, this restructuring was sufficient to fill the dishes.
- In the nonramped sphere-pac rod, the central portion of the fuel sintered to form a mass in which it was difficult to identify original spheres. Complex cracking occurred in this sintered central core of fuel, but the transverse cracks noted in this region in the neutron radiographs (Section 4.3.1) were easily identifiable.

4.3.9 Burnup Analyses

Burnup samples were taken at the middle of the fuel columns from reference Rods R1 and R2 to characterize the steady-state burnups in the IFA-517.1 assembly and the lower cluster of the IFA-518.1 assembly, respectively. The burnup values from these samples represent the rod-average burnups (see Table 14). Comparisons of the calculated rod-average burnups for Rods R1 and R2, which were calculated from the steady-state power histories, with the measured values determined by the ^{148}Nd method (Table 15) indicate that the power history values are 4% and 3% low for IFA-517.1 and IFA-518.1, respectively. Considering all the uncertainties involved in the power history calculations,(6,7) the comparisons are considered very good. The measured

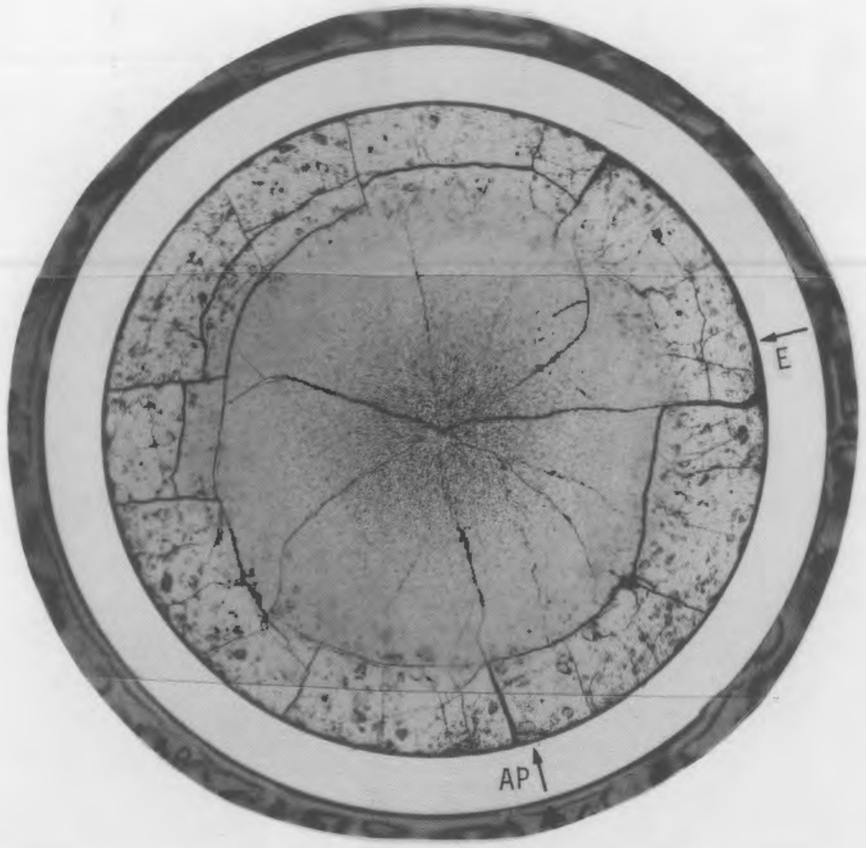

FIGURE 94. Photomacrograph of As-Polished Transverse Section from Rod R2 (5.1X)

FIGURE 95. As-Polished and Etched Radial Strips from Rod R2 (62.5X)

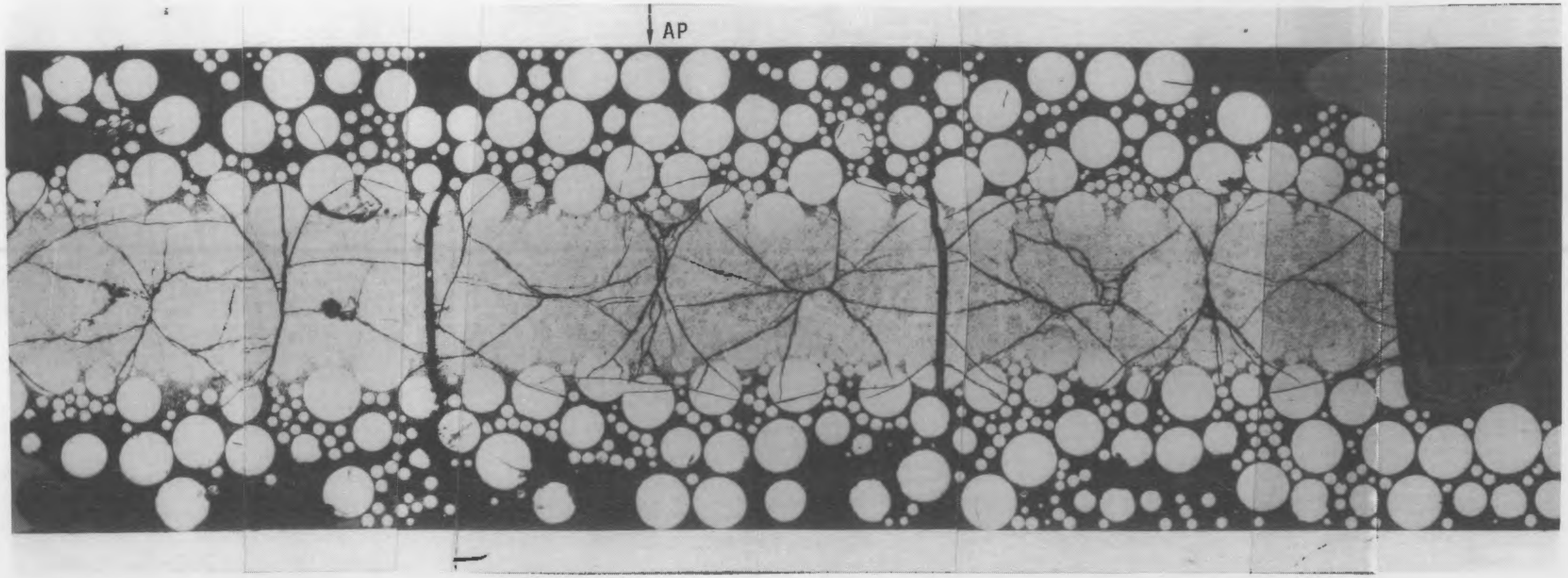

FIGURE 92. Photomacrographs of Two Longitudinal Sections from Nonramped Rod S42 (8.5X)

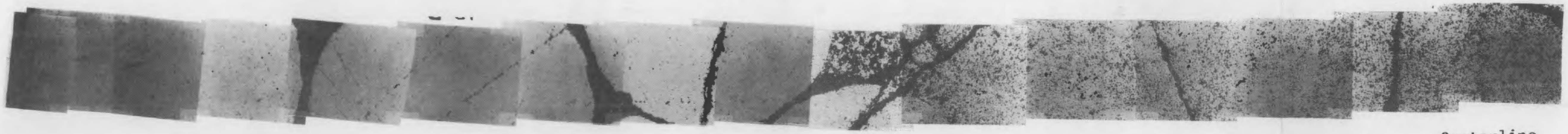

FIGURE 93. As-Polished Radial Strip from Rod S42 (62.5X)

TABLE 14. Final Rod-Average Burnup Values

	Rod Number						
Rod-Average Burnup Values	R1	R2	A6	AC9	AC10	S41	S42
Value from power history, MWd/kgM	6.8	9.3	10.3	10.5	10.3	6.8	6.8
^{148}Nd Value, at.%	0.80	1.09	---	---	---	---	---
^{148}Nd Value, MWd/kgM$^{(a)}$	7.1	9.7	---	---	---	---	---
Normalized value	---	---	10.7	10.8	10.6	7.1	7.1

(a) Calculation assumed 190 MeV/fission.

TABLE 15. Mass Spectrometric Analysis of Burnup Samples

Rod Number	Uranium Isotope	Uranium wt%	Neodymium Isotope	Neodymium wt%	Burnup, at.% (1σ)
R1	234	0.08 ±0.01	142	0.29 ±0.01	0.80 (±0.2)
	235	10.30 ±0.02	143	29.50 ±0.06	
	236	0.23 ±0.01	144	23.05 ±0.05	
	238	89.40 ±0.18	145	19.83 ±0.04	
			146	15.37 ±0.03	
			148	8.57 ±0.04	
			150	3.42 ±0.02	
R2	234	0.07 ±0.01	142	0.36 ±0.01	1.09 (±0.03)
	235	9.95 ±0.05	143	28.64 ±0.06	
	236	0.29 ±0.01	144	24.47 ±0.05	
	238	89.70 ±0.18	145	19.46 ±0.04	
			146	15.19 ±0.03	
			148	8.43 ±0.04	
			150	3.38 ±0.02	

burnup values from Rods R1 and R2 and the burnup values calculated from the power histories for all the rods were used to normalize and provide the final burnup values for the five rods for which burnup was not determined chemically. The final normalized burnup values determined in this way were listed in Table 1.

4.3.10 Longitudinal Cladding Examination

Longitudinal cladding specimens were prepared from annular-coated, annular, sphere-pac, and reference rods as described in Section 3.6.9. These specimens were prepared primarily to examine the inner cladding surface for 1) graphite (annular-coated rods), 2) fission product deposition (all types of rods), and 3) evidence of mechanical interaction (sphere-pac rods). After longitudinal slitting of the fuel rod sections, one-half of the resultant clamshell was lifted away to reveal the fuel structure. Photographs were taken, and the fuel was then removed for visual examination of the cladding inner surface.

The fuel structure from both halves of a clamshell sample taken near the bottom of ramped annular-coated Rod AC10 is shown in Figure 96. Similar photographs of a clamshell sample taken near the top of the fuel stack from ramped annular-coated Rod AC9 are shown in Figure 97. For both specimens, some fuel fragments adhered to the inner surface of the graphite-coated cladding on the half of the clamshell that was lifted away. Only the annular-coated rods exhibited this behavior. The fuel fragments were very easily removed, indicating that they were only slightly bonded. Sintering of individual pellet interfaces in the central or core portion of the fuel occurred in the fuel stack from the Rod AC9 sample; apparently most of the interfaces were open in the Rod AC10 specimen. The general barrel shape of the surface of the midradius circumferential cracks observed in the neutron radiographs (Section 4.3.1) was obvious in the fuel from Rods AC9 and AC10. The plenum region and upper portion of the fuel stack from Rod AC10, a region near the upper portion of the fuel stack from Rod AC9, and a region near the bottom of the fuel stack from Rod AC10 are shown in Figure 98. The only area in which graphite on the inner surface of the cladding could be positively identified was in the plenum region from Rod AC10 (Figure 98a). The surface of the cladding (graphite?) adjacent to the fuel was typically covered with a heavy deposit of a mottled black material that was heavier near the bottom of the fuel stack.

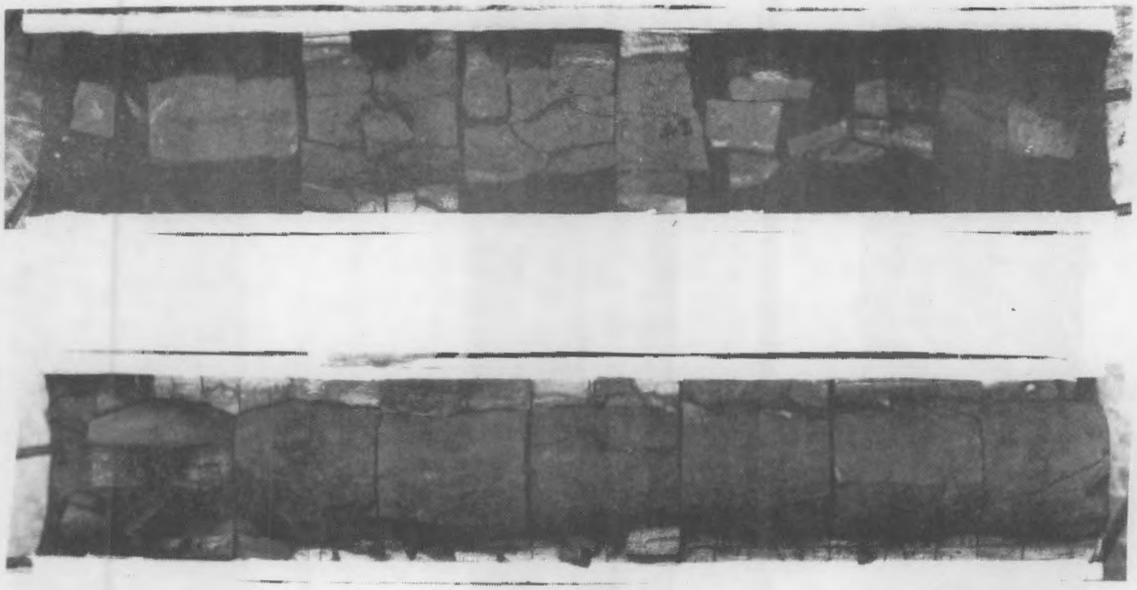

FIGURE 96. Fuel Structure in Bottom Clamshell Sample from Rod AC10 (2.4X)

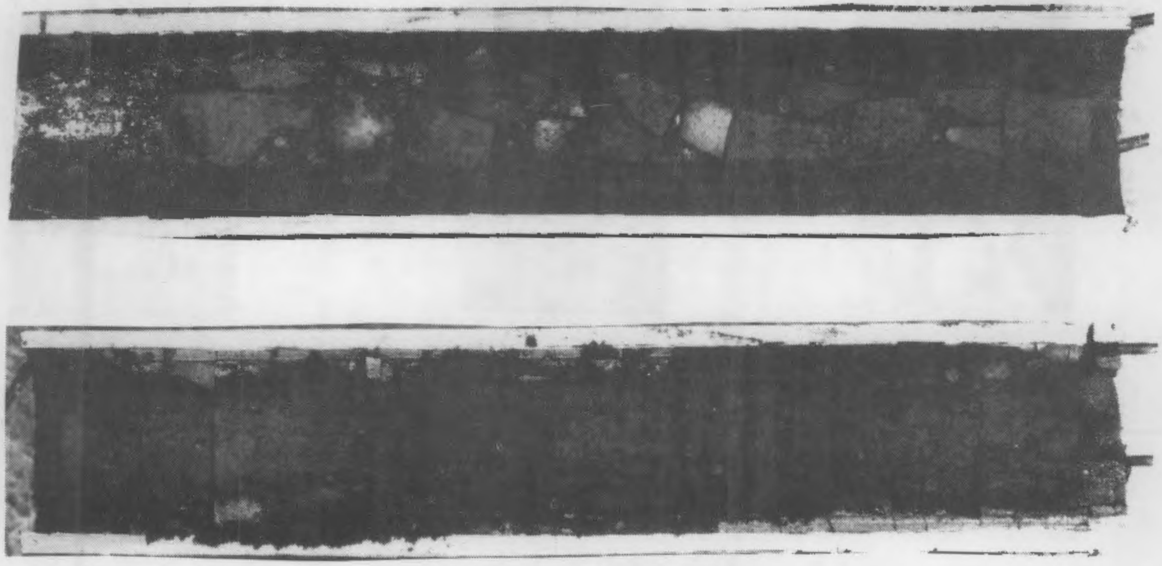

FIGURE 97. Fuel Structure in Upper Clamshell Sample from Rod AC9 (2.4X)

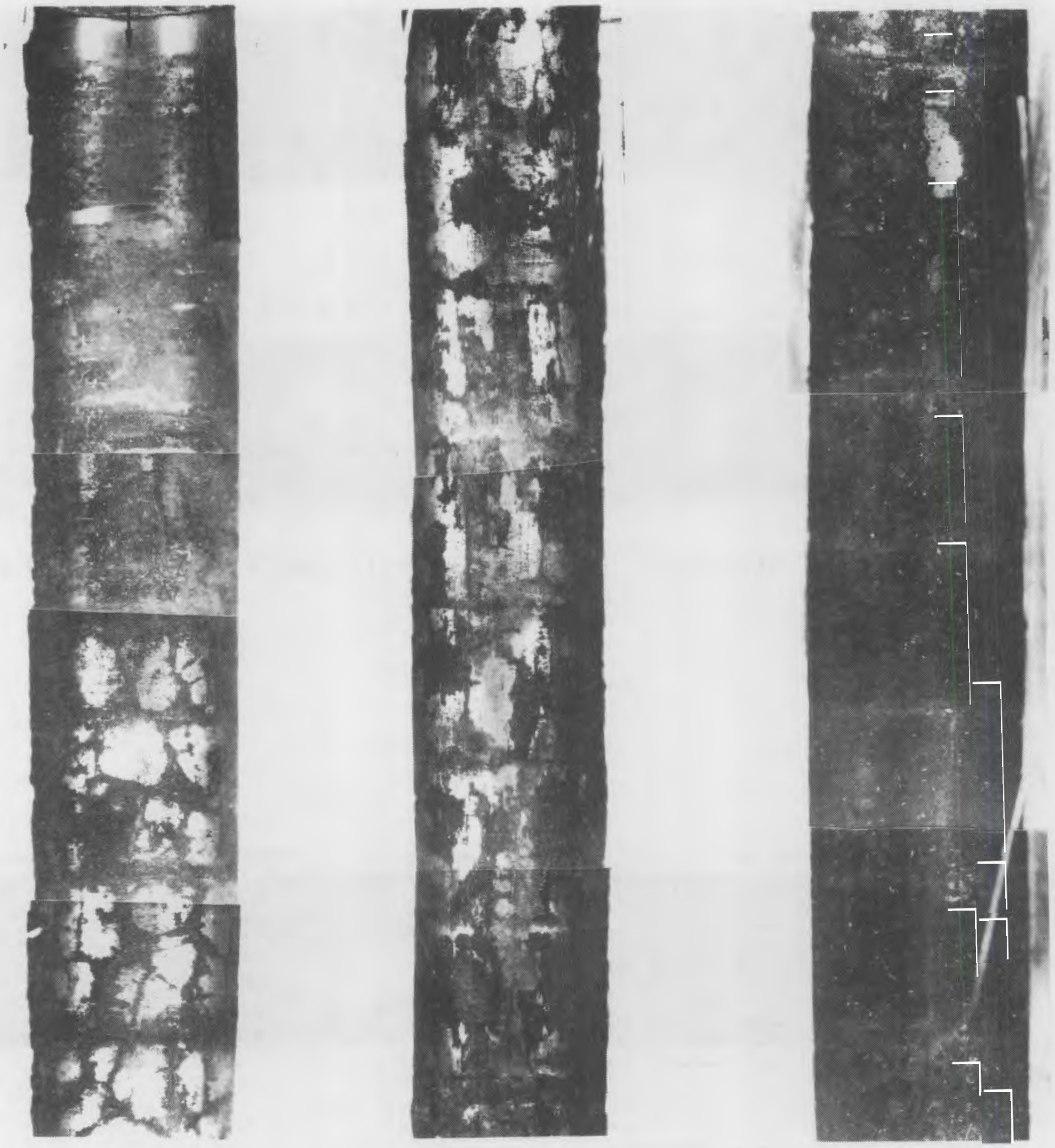

(a) (b) (c)

FIGURE 98. Inner Surface of Cladding from Annular-Coated Rods at a) Plenum Region of Rod AC10, b) Upper Region of Fuel Stack of Rod AC9, and c) Lower Region of Fuel Stack of Rod AC10 (2.8X)

Smaller specimens were sectioned from the longitudinal clamshells for examination on the SEM. The character of the surface of the fission-product/ UO_2 deposit is shown in Figure 99. This surface deposit appeared quite crystalline, unlike the smooth surface of the as-fabricated graphite coating. These specimens were so highly radioactive from fission products that they could not be examined in the energy dispersive x-ray mode on the SEM; therefore, scrapings of the graphite coating and the fission product deposit were used. Fission products such as Cs, I, Ba, Cd, In, and Mo were detected on the surface of the scrapings adjacent to the fuel. No fission products were detected on the surface of the scrapings adjacent to the cladding. On the latter samples, zirconium was not present in any significant amount, indicating that the scrapings were truly representative of what was on the cladding. Because carbon cannot be detected using the energy dispersive x-ray technique, it was concluded that the major portion of the material on the surface of the scrapings adjacent to the cladding was graphite and that the graphite was effective in preventing fission products from reaching the cladding.

The fuel structure and the appearance of the cladding surface from ramped annular Rod A6 at a location near the bottom of the fuel stack are shown in Figure 100. The central fuel core sintered at pellet interfaces, and the barrel shape of the midradius crack observed in the neutron radiographs of the annular-coated rods is obvious. Apparently, the annular fuel behaves the same during a ramp test whether the rod is coated or noncoated. The inner surface of the cladding from Rod A6 did not show the heavy deposit of black mottled material that was observed in the annular-coated rods; however, some fission product/UO_2 deposits did occur on the cladding and the location of the original pellet interfaces could be identified by rings of the deposit. The character of the surface of the fission product/UO_2 deposit from SEM examination is shown in Figure 101. The crystallite size was similar to that observed for the deposit on the annular-coated rods; however, there was significantly less material.

The fuel structure and the appearance of the inner cladding surface from ramped reference Rod R1 are shown in Figure 102. There was evidence of sintering of the pellet interfaces in the central portion of the fuel even though

FIGURE 99. SEM View of Fission Products on Graphite Coating from Rod AC10 (1250X)

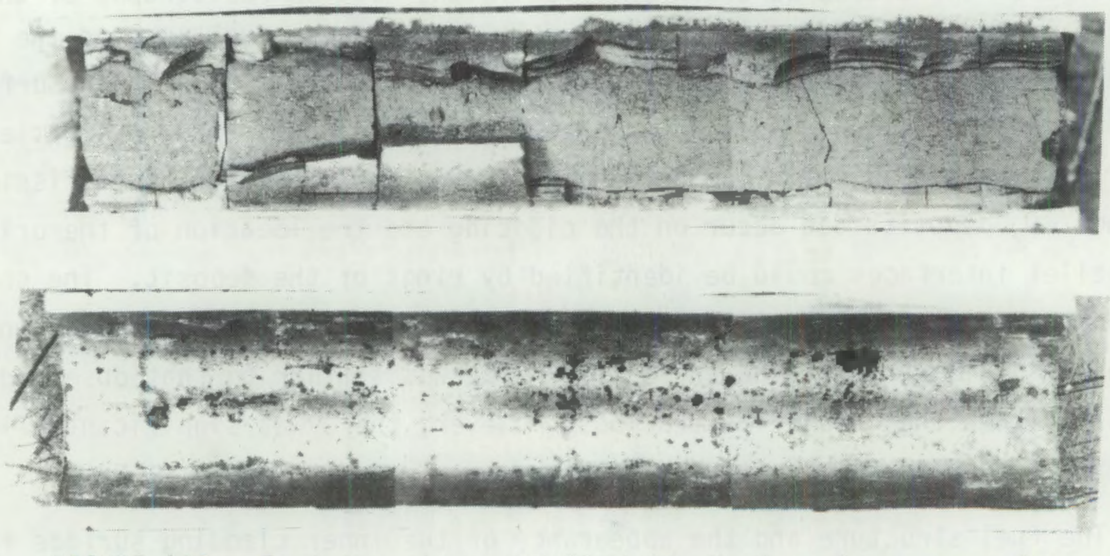

FIGURE 100. Fuel Structure and Cladding Surface Appearance from Rod A6 (2.3X)

FIGURE 101. SEM View of Fission Products on Inner Cladding Surface from Rod A6 (1250X)

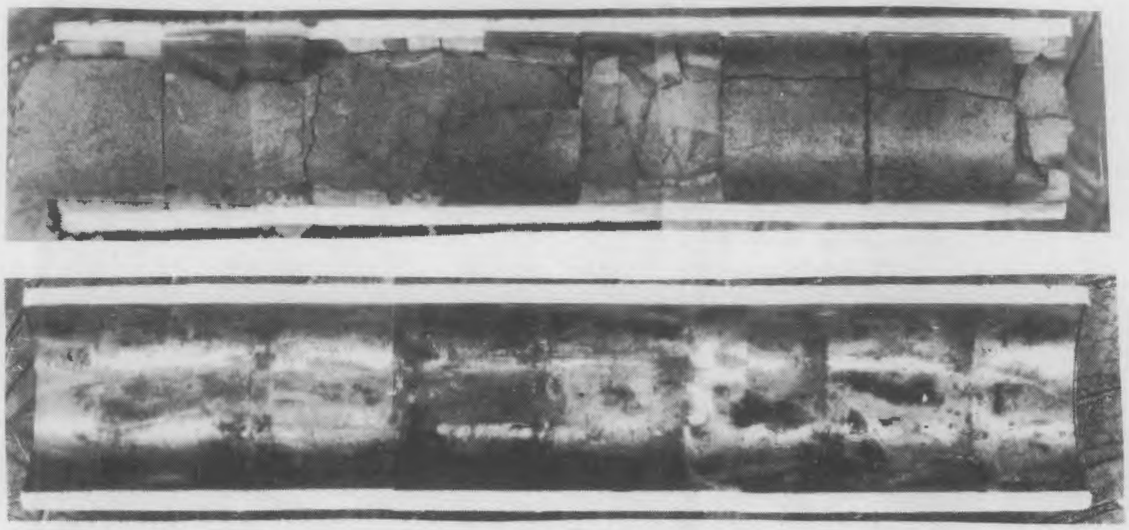

FIGURE 102. Fuel Structure and Cladding Surface Appearance from Rod R1 (2.1X)

the pellets were originally dished. The fission product deposits on the inner surface of the cladding were heavier than in Rod A6 but did not have the appearance of the heavy black deposits that occurred in the annular-coated rods. The location of the original pellet interfaces could also be detected by rings of the deposit on the cladding surface. The character of the deposit from SEM examination is shown in Figure 103. The crystallite size and appearance were similar to those in Rod A6.

The fuel structure and the appearance of the inner cladding surface from ramped sphere-pac Rod S41 are shown in Figure 104. Both large- and medium-sized spheres protruded from the sintered central core of fuel. The spheres in the annular region between the core and the cladding were obviously relatively loose, and most fell away from the specimen when the upper clamshell was removed. The location of the transverse cracks in the central core that were noted in the neutron radiographs (Section 4.3.1) were also apparent even

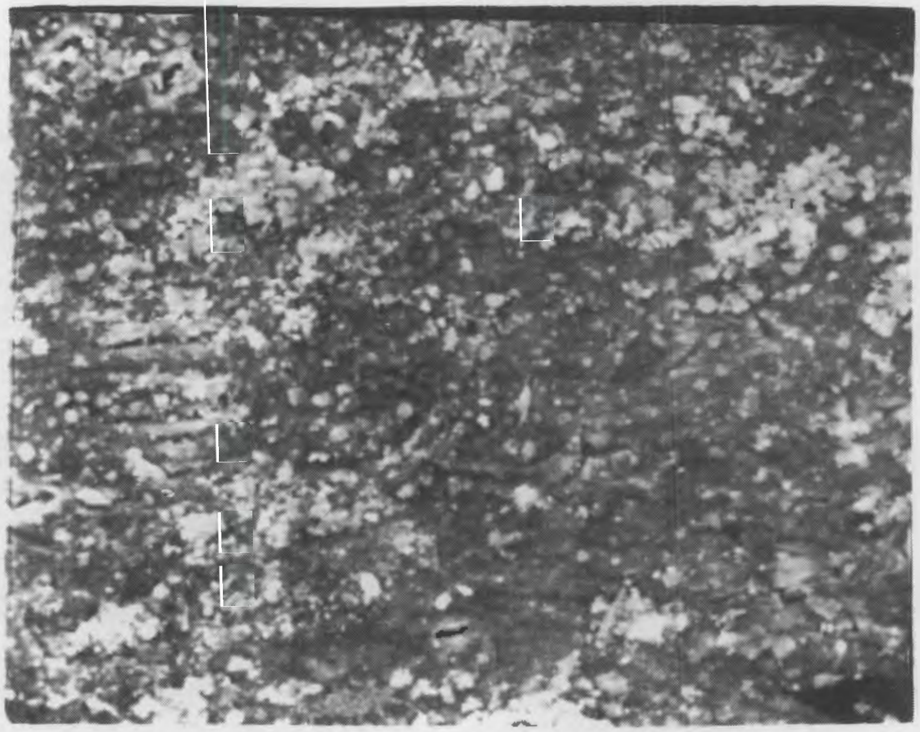

FIGURE 103. SEM View of Fission Products on Inner Cladding Surface from Rod R1 (1250X)

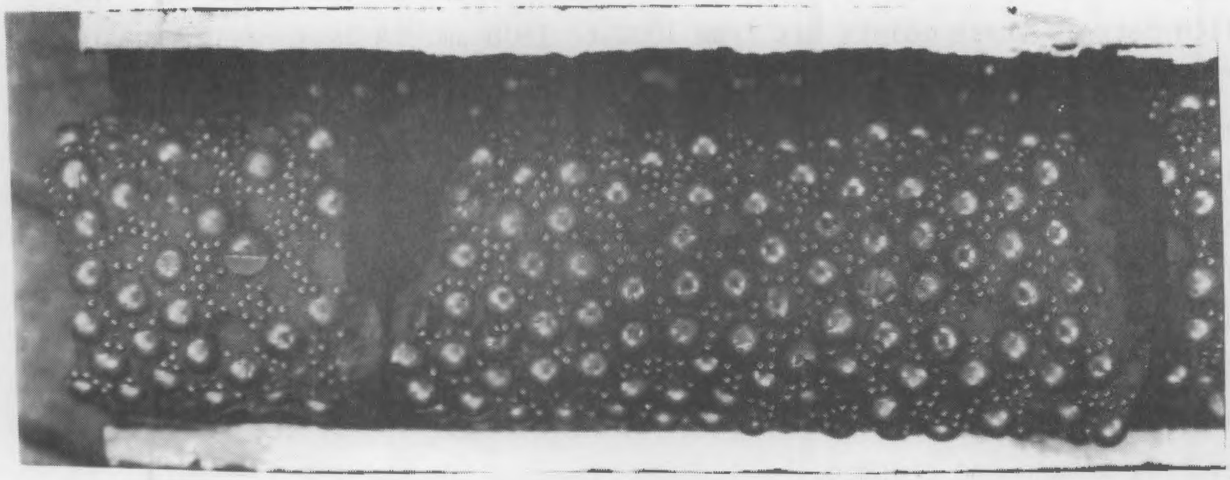

a) Fuel (5.8X)

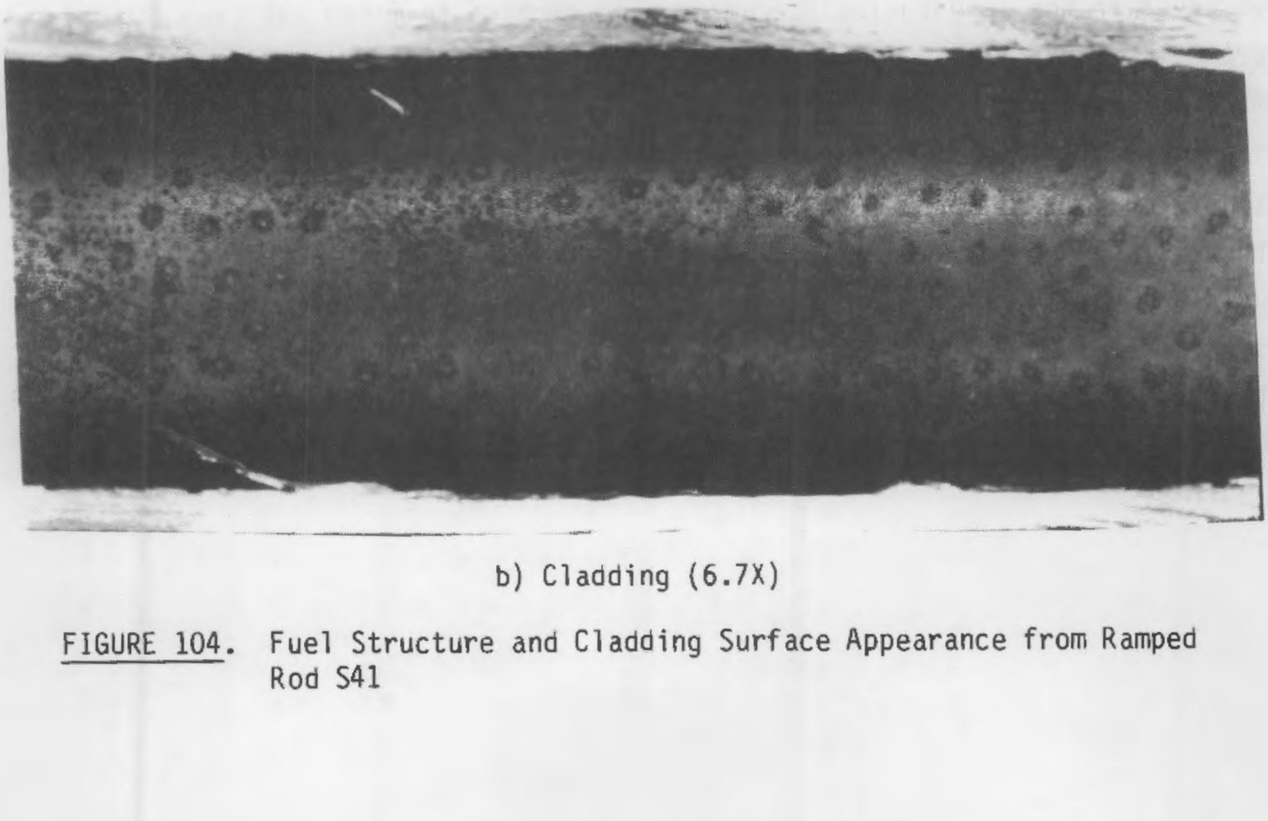

b) Cladding (6.7X)

FIGURE 104. Fuel Structure and Cladding Surface Appearance from Ramped Rod S41

though there had obviously been some rotation of the central core fragments during specimen preparation. A regular pattern of large dark spots with a lighter center area was visible on the inner surface of the cladding. The pitch between these points was from 1000 to 1600 µm. A less regular pattern of smaller dark spots was also apparent on the cladding. The larger spots conform to the pattern of what would be expected if the large 1200- to 1400-µm diameter spheres were in contact or nearly in contact with the cladding. The less regular, smaller spots conform to what might be expected if the medium-sized (~400-µm diameter) or small (~25 to 40 µm-diameter) spheres were in contact with the cladding. SEM photographs of two of the large spots on the cladding (Figure 105) reveal that these spots are composed of spheres stuck to the cladding surface; the spheres in the central portion of the spots were severely broken and crushed.

The appearance of the inner cladding surface from nonramped Rod S42 is shown in Figure 106. The structure of the sintered core could not be obtained because the core was very friable and fell apart during specimen preparation, which was not unexpected given the complicated cracking of the core that was observed in the longitudinal ceramographic section from Rod S42 (see Figure 92). Therefore, a comparison of the cores from Rods S41 and S42 cannot be made. The points of contact between the large spheres and the cladding were observed; however, points of contact between the cladding and the medium-sized spheres were not obvious. SEM photographs of the contact points reveal that these spots are composed of spheres stuck to the cladding surface (see Figure 107a, b, and c). The spheres in the central portion of the spot were severely broken. After the fuel was etched away, SEM examination revealed that small spheres were trapped and embedded in the cladding, producing several dimples with diameters in the range from 5 to 15 µm (see Figure 107d and e).

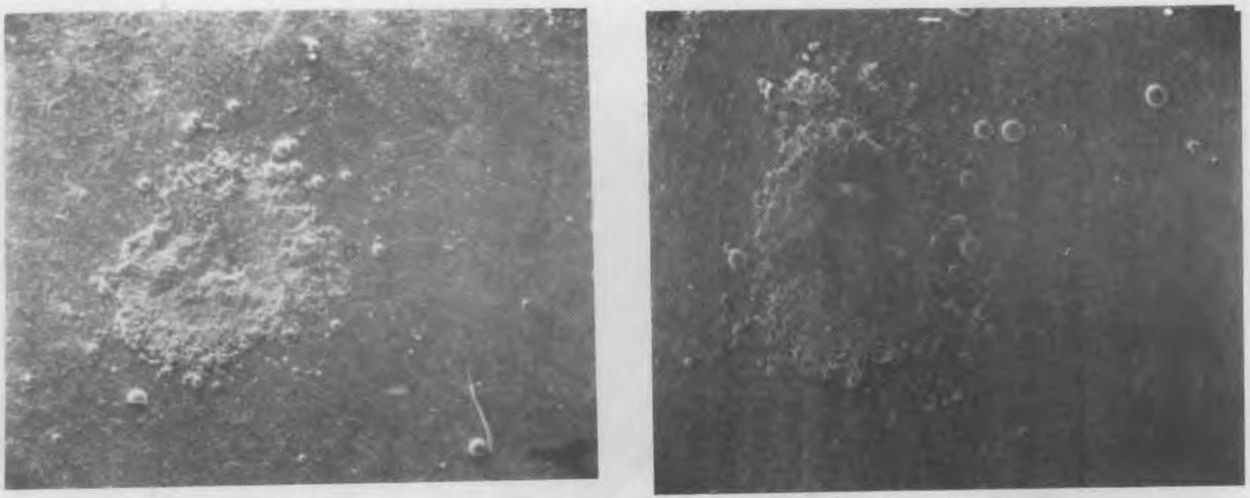

a) Region 1, 109X

d) Region 2, 109X

b) Region 1, 435X

e) Region 2, 435X

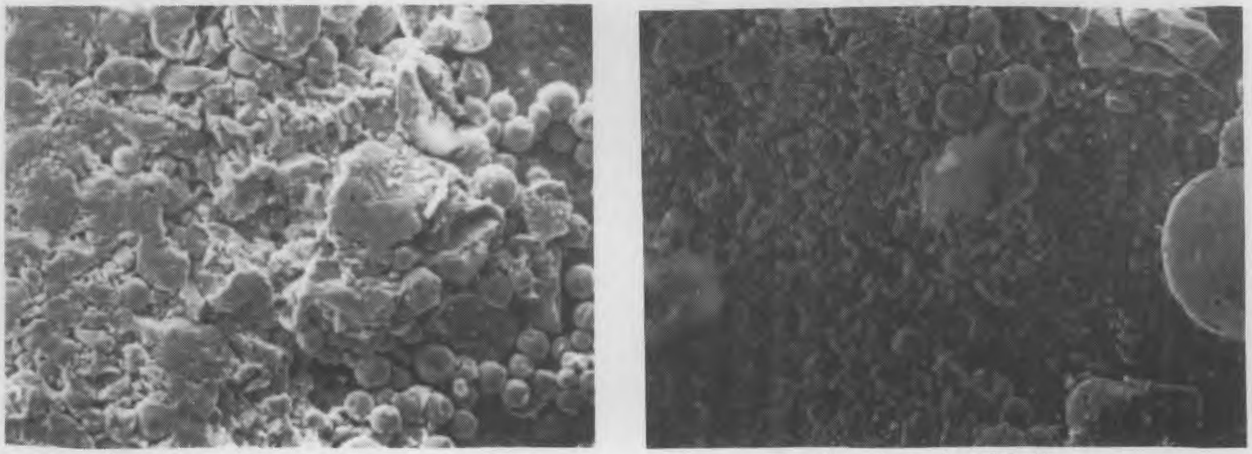

c) Region 1, 850X

f) Region 2, 850X

FIGURE 105. SEM Views of Large Areas of Crushed Spheres That Adhered to the Cladding of Rod S41 (letters on micrographs indicate location of area at the next higher magnification)

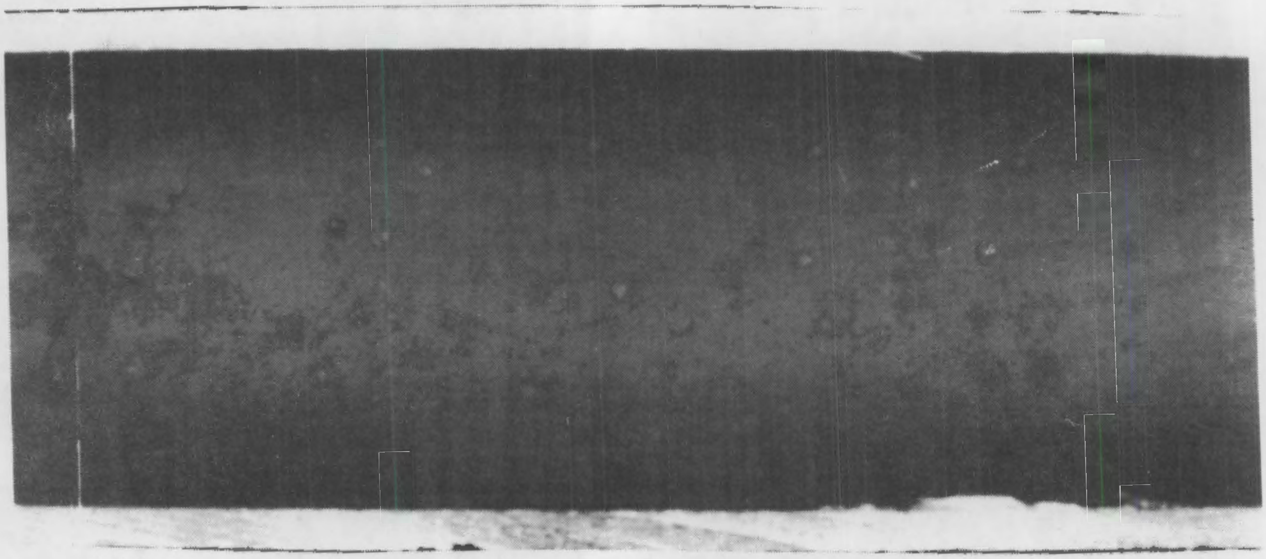

FIGURE 106. Cladding Inner Surface Appearance from Nonramped Rod S42 (6.7X)

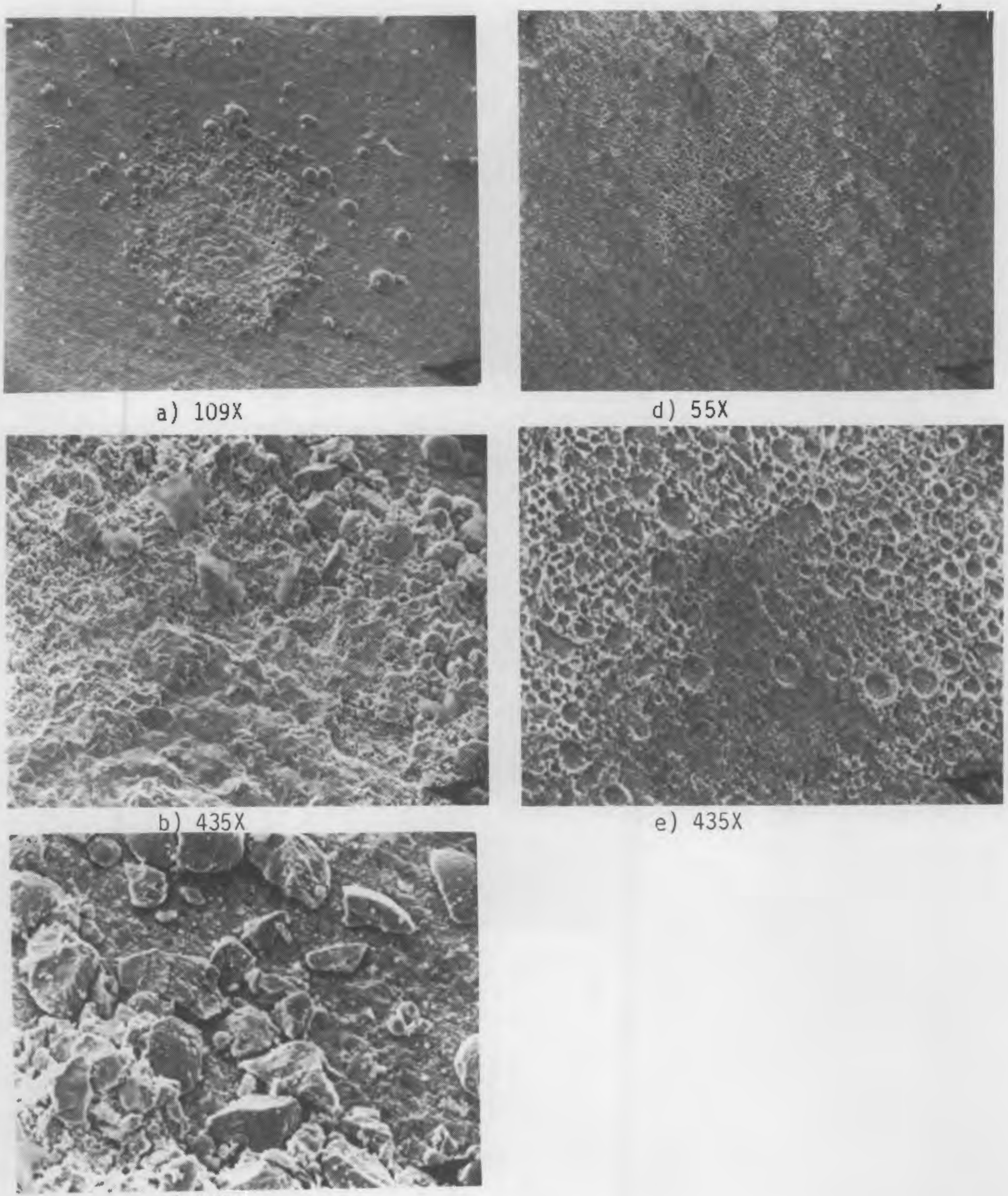

a) 109X

d) 55X

b) 435X

e) 435X

c) 850X

FIGURE 107. SEM Views of Crushed Spheres That Adhered to Cladding of Rod S42 Before (a, b, c) and After (d, e) Etching (letters on micrographs indicate location of area at the next higher magnification)

5.0 DISCUSSION OF RESULTS

Descriptions of the experiments, methods of examination, and the results of the testing and examination of 11 experimental fuel rods irradiated in the HBWR have been described in the three previous sections. In this section, the results are evaluated in terms of the chemical, mechanical, and thermal behavior, especially with respect to PCI. The behaviors of the fuel rods containing design features that are expected to alleviate PCI failures are compared with the reference dished-pellet design and with each other.

5.1 CHEMICAL BEHAVIOR

Chemical reactions between the coating and the fuel in graphite-coated rods could generate significant quantities of CO and/or CO_2, resulting in fuel rod overpressurization. A reaction between the graphite coating and the Zircaloy cladding could embrittle the cladding. Chemical reactions between fission products and the Zircaloy cladding are known to promote stress corrosion cracking (SCC) and PCI failures. The reaction between fission products and the Zircaloy cladding is common to all the fuel rod types that were tested; however, the presence of the graphite coating is expected to reduce the fission product-Zircaloy reaction. A uniform deposition of fission products on the cladding in the sphere-pac fuel rods is also expected to reduce the propensity for PCI failure. These three types of chemical reactions (graphite-fuel, graphite-cladding, and fission product-cladding) are discussed below with respect to the available PIE results and applicable irradiation histories.

5.1.1 Graphite-Fuel Reaction

Based on thermodynamic considerations, the fuel and graphite in the coated rod designs will not react significantly at the normal temperatures that occur in the graphite coating during steady-state or power-ramp conditions. However, graphite that might abrade from the coating during rod fabrication and relocate in the central portion of the rod could encounter temperatures high enough to result in the formation of CO and CO_2. Graphite-coated rods instrumented with pressure sensors to monitor internal rod pressure during steady-state operation in the HBWR to burnups of 10 to 12 MWd/kgM have shown no significant pressure increase that can be attributed to a graphite-fuel reaction.(6,12) The postramping gas analysis of two annular-coated rods showed no significant quantities of CO or CO_2 in the plenum gas (Section 4.3.7, Table 10) even though the fuel temperatures were significantly higher and the volume of fuel at the elevated temperatures was greater than those encountered during steady-state irradiation in the HBWR or those expected during commercial operation. Therefore, there was no significant graphite-fuel reaction during the steady-state or power-ramp irradiations.

5.1.2 Graphite-Cladding Reaction

The cladding from the ceramographic sections taken from Rod AC9 was examined in the etched condition (see Figure 90) for evidence of a chemical reaction between the graphite coating and the cladding. Normal hydride platelets were observed throughout the cross section of the cladding, but no evidence of a reaction product was found on or near the inner surface of the cladding. Rod AC9 had been power-ramped at a burnup of 10.8 MWd/kgM. Thus, it can be concluded that at normal graphite-Zircaloy operating temperatures and after moderate exposure periods there is no evidence of a graphite-cladding reaction that might embrittle the Zircaloy cladding.

5.1.3 Fission Product-Zircaloy Reactions

Because there were no rod failures during the ramp tests, regions of cladding failure could not be examined for evidence of fission product-Zircaloy reactions that might cause failure. Therefore, other results (e.g., eddy-current, visual, and ceramographic examinations) were used to provide indirect evidence of any fission product-Zircaloy interactions.

Eddy-current examination of all the ramped rods (Sections 4.2.2 and 4.3.5) revealed no evidence of incipient cracks on the inner cladding surface that might be attributed to SCC. Likewise, no x-marks that might be associated with localized areas of high strain were observed visually on the exterior surface of the cladding (Section 4.3.2). Therefore, explicit locations could not be identified for in-depth ceramography. The lack of incipient cracks and x-marks is probably due to the absence of cladding creepdown in the HBWR, which resulted in lower cladding stresses during the ramp test, and the proven SCC resistance of the cladding used in the tests.(13)

As discussed in Section 4.3.10, the graphite coating in the annular-coated rod was effective in preventing fission products from reaching the cladding during the 8 h at the terminal ramping LHGR.

5.2 MECHANICAL AND PRESSURE BEHAVIOR

Mechanical interaction between the fuel and the cladding produces stresses in the cladding that, in combination with chemical attack, can lead to a breach of the cladding, i.e., a PCI failure. Because none of the ramped fuel rods failed during testing, a direct comparison between the fuel rod types cannot be made based on a fail/no-fail criterion. Evaluations of the mechanical interaction of the different fuel rod types are presented below in terms of their elongation behavior during ramping for the rods that were power-ramped and the PIE results for the power-ramped rods and the one nonramped rod. The pressure behavior in Rod AC10 is also described.

5.2.1 Basis for Evaluation of Elongation Signals During Ramping

The measured elongation sensor signal, E_R, for a rod during a ramp test is dependent upon several mechanisms and may be generally expressed as:

$$E_R = f(\alpha) + f(\epsilon_E) + f(\epsilon_c) + f(\epsilon_p) + f(P) \qquad (1)$$

where $f(\alpha)$ = contribution to E_R caused by cladding free thermal expansion or contraction

$f(\epsilon_E)$ = contribution to E_R caused by elastic deformation of the cladding due to FCMI

$f(\epsilon_c)$ = contribution to E_R caused by possible creep of the cladding due to FCMI

$f(\epsilon_p)$ = contribution to E_R caused by plastic deformation (yielding) of the cladding due to FCMI

$f(P)$ = contribution to E_R in those rods that experienced liftoff of the sensor due to internal pressure (see Appendix B).

The effect of each of these functions on the elongation sensor signal, methods of evaluating the mechanical interaction in the fuel rods, and behavior after liftoff of the sensor are described in the following sections.

Contribution of Cladding Free Thermal Expansion to the Elongation Signal

The contribution to E_R from cladding free thermal expansion/contraction is caused by the lengthening/shortening of the rod due to an average temperature increase/decrease in the cladding as the LHGR is increased/decreased. The derived expansion/contraction signal is the difference between the actual free thermal expansion/contraction in the cladding and that of a Zircaloy stay rod that supports the fuel rod and the linear variable differential transformer (LVDT) sensor housing. Thus, the signal is always less than what would be calculated from expansion/contraction of the cladding alone. Over the temperature range of interest, the signal is linear with a slope of 0.0015 to 0.0030 mm per kW/m during the ramp tests. Some variation in slope occurred from test to test due to differing amounts of subcooling in the heavy-water coolant, but the amount of subcooling usually remained constant for any particular ramp test.

Contribution of Elastic Deformation to the Elongation Signal

Prior to any yielding of the cladding during a ramp test, the cladding elongation due to FCMI will be elastic. After subtracting the cladding thermal expansion/contraction component from E_R and assuming no contribution from f(P), the contribution to the elongation signal (in terms of strain) caused by axial elastic deformation of the cladding can be described by the Generalized Hooke's Law

$$\varepsilon_z = \frac{1}{E}[\sigma_z - \nu(\sigma_\theta + \sigma_r)] \qquad (2)$$

where ε_z = observed axial strain
E = Young's modulus (~82 GPa at 265°C)(11)
ν = Poisson's ratio (0.265 at 265°C)(11)
σ_z = axial stress
σ_θ = hoop stress
σ_r = radial stress.

Using the thick-walled tubing equations,

$$\sigma_r = \frac{Pr_i^{\,2}}{r_o^{\,2} - r_i^{\,2}} \left(1 - \frac{r_o^{\,2}}{r^2}\right) \tag{3}$$

$$\sigma_\theta = \frac{Pr_i^{\,2}}{r_o^{\,2} - r_i^{\,2}} \left(1 + \frac{r_o^{\,2}}{r^2}\right) \tag{4}$$

at the midwall cladding radius r, where r_o and r_i are the inside and outside radii of 6.16 and 5.26 mm,$^{(8,9)}$ respectively, $\sigma_r = -0.075\ \sigma_\theta$. By substitution,

$$\varepsilon_z = \frac{1}{E}(\sigma_z - 0.25\ \sigma_\theta) \tag{5}$$

at stress levels less than those required for yielding. Thus, a tensile stress in the axial direction results in elastic rod elongation, and a tensile stress in the hoop direction results in elastic rod shortening (Poisson's shortening). If the hoop stress is less than four times the axial stress, i.e., $\sigma_\theta/\sigma_z < 4$, the rod will be longer than the original length; and if $\sigma_\theta/\sigma_z > 4$, the rod will be shorter than the original length. If the cladding is elastic during a power-ramp test and the elongation rate tends to increase, σ_θ/σ_z is becoming smaller; and the effect of the axial stress is increasing. Similarly, if the elongation rate tends to decrease, σ_θ/σ_z is becoming larger; and the effect of the hoop stress is increasing. These comments apply only to the stress ratio and not to the absolute stress values.

Thus, for elastic deformation in the cladding, a method exists for estimating the changing effect of the hoop and axial stresses: by examining the amount and direction of changes from the estimated cladding free expansion line (see Section 4.1). In the limit, if one of the principal stresses can be determined to be insignificant, the method can be used to estimate the minimum value of the remaining principal stress. The method applies only to the general stress conditions in the cladding; localized conditions (e.g., at ridges) are not calculable and may be different for the different fuel types.

Contribution of Cladding Creep Deformation to the Elongation Signal

If high stress levels are maintained in the cladding for a sufficient time, axial and/or hoop creep can occur, resulting in permanent deformation of the cladding and a contribution to E_R. It is not possible to separate creep strain from strain caused by yielding during the ramp tests; however, the approximate magnitude of the cladding creep can be estimated.

Solution of the MATPRO(11) creep equation for Zircaloy cladding using the maximum observed permanent deformation (+0.06% in Rod R1) indicated a required stress in excess of the 0.2% yield stress. Thus, either the equation is not valid at the stress levels encountered in Rod R1 or a small amount of yielding occurred at stress levels lower than the 0.2% yield stress. Because the permanent strains are low and the difference between creep and yielding cannot be ascertained, the component to the elongation signal that might be caused by creep will be assumed to be zero; and all permanent deformation will be attributed to yielding.

Contribution of Cladding Plastic Deformation to the Elongation Signal

It is not possible to tell at what exact point any permanent elongation contributed to E_R, but useful stress ratio information can be ascertained. For those rods that exhibited permanent axial strain during the ramp tests, the incremental strain at the yield condition can be estimated using the von Mises-Hencky criteria for the yield condition as modified for anisotropy by Hill:(14)

$$\delta\epsilon_z^p = \delta\lambda\left[\sigma_z - \frac{R}{R+1}\sigma_\theta - \frac{1}{R+1}\sigma_r\right] \tag{6}$$

where $\delta\epsilon_z^p$ = incremental plastic strain in the axial direction

$\delta\lambda$ = a constant of proportionality

R = an anisotropy factor = 1.58.(15)

If $\sigma_r = -0.075\ \sigma_\theta$, then

$$\delta\varepsilon_z^p = \delta\lambda(\sigma_z - 0.58\ \sigma_\theta) \qquad (7)$$

For the limiting condition of yielding with no axial strain, $\sigma_\theta/\sigma_z = 1.72$. This condition is also illustrated in Figure 108, where the yield curve in the axial-hoop tensile quadrant of the three-dimensional yield surface at the plane for $\sigma_r = -0.075\ \sigma_\theta$. For $\sigma_\theta/\sigma_z > 1.72$ (Zone A), the cladding will experience permanent shortening with a corresponding increase in diameter. For $\sigma_\theta/\sigma_z < 1.72$ (Zones B and C), the cladding will experience permanent lengthening with the strain in the hoop direction also dependent upon the hoop-to-axial stress ratio. If $\sigma_\theta/\sigma_z > 0.68$ (Zone B), the cladding will increase in diameter; if $\sigma_\theta/\sigma_z < 0.68$ (Zone C), the cladding will decrease in diameter.

Thus, if permanent lengthening or shortening occurs, a method exists to estimate the relative importance of the axial and hoop stresses and the sign of the permanent hoop strain. The latter is of particular importance because permanent diametral deformations could not be determined from the profilometry data (Section 4.3.6).

Contribution of Internal Pressure to the Elongation Signal

For those rods where the liftoff pressure of the elongation sensor was exceeded during the ramp tests (Appendix B), the elongation sensor signal contained not only thermal and mechanical components but also a contribution due to pressure changes in the rod. The sign of the pressure contribution was opposite that of thermal expansion. The calibration factor (MPa/mm) for the bellows on the sensor is not known, and the pressure changes indicated by the sensor after liftoff are only the differential above the liftoff pressure. These differential changes are probably relatively small in magnitude compared to the liftoff pressure, e.g., a few tenths of a megapascal compared to liftoff pressures of 2.0 to 2.6 MPa.

During periods when the pressure signal was present in the overall elongation sensor signal, it was impossible to ascertain the elongation changes. However, if certain assumptions were made concerning the elongation, trends in the internal rod pressure could be estimated for some rods. These estimates of rod pressure are presented in Section 5.2.5.

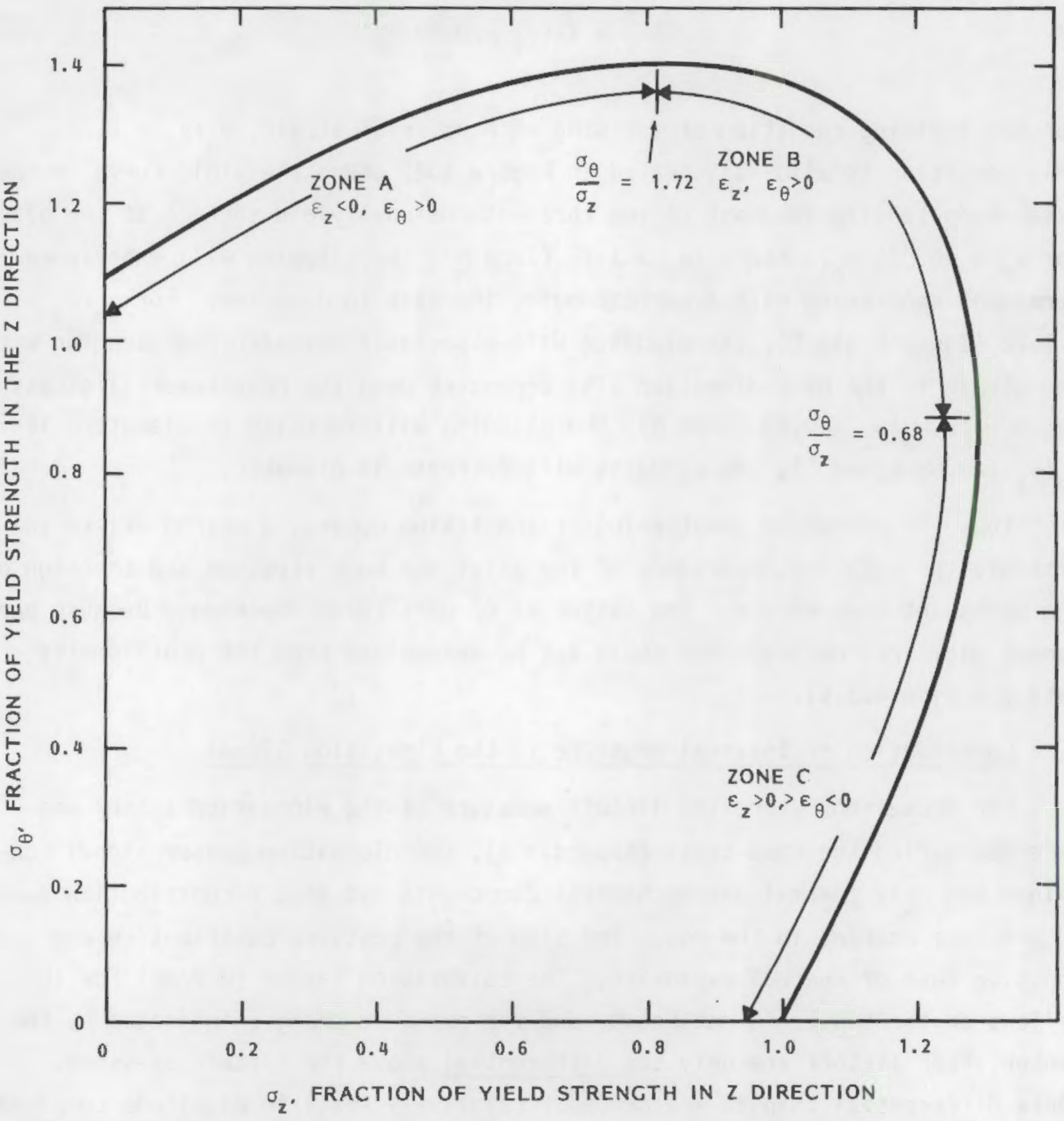

FIGURE 108. Yield Curves for σ_θ and σ_z in Terms of the Yield Strength (normalized) in the z Direction for $\sigma_r = -0.075\ \sigma_\theta$

5.2.2 Mechanical Behavior in Reference Fuel Rods During Power-Ramp Testing

Three reference rods with solid, dished-pellet fuel and elongation sensors (Rods R1, R2, and R3) were power-ramp tested at burnup levels of 7.1, 9.7, and 14 MWd/kgM, respectively. None of the fuel rods failed during the ramp tests; but all three rods experienced permanent lengthening as a result of the power-ramps. Comparison of preramp and postramp profilometry for the reference rods with the profilometry for annular-fueled and sphere-pac rods indicates that while conclusions concerning absolute changes in diametral strain cannot be made (Section 4.3.6), the reference rods (especially Rod R1) exhibited the greatest number of deviations from the rocking pattern, which indicates the greatest amount of localized FCMI in any of the rod types. The direction in the change of ovality as a function of fueled length was variable in the reference rods, which is also indicative of random localized FCMI. In the absence of definitive postirradiation measurements of rod diameter and length changes (Section 4.3.6) as a result of the ramp tests, the elongation measurements during the power-ramp tests provide the primary basis for evaluating the mechanical behavior in the reference rods. Of the three rods with elongation sensors, only Rod R1 did not have a contribution to the measured signal from the internal pressure during some portion of the ramp tests. The Rod R1 elongation is relied upon heavily in evaluating the mechanical behavior of the reference rods.

The detailed elongation sensor signal histories during the power-ramping of Rods R1, R2, and R3 are shown in Figures 3, 4, and 5, respectively. These elongation signal histories are also reduced in Figure 109 with key letters identifying specific points that are used in the following discussion. The letters common to each rod are:

- a = start of power ascension for preconditioning at 28 kW/m
- b = start of reactor-driven portion of power-ramp
- c = start of ^{3}He-induced portion of power-ramp
- d = start of 8-h hold at peak power
- e = start of power descension
- f = end of test.

Points of interest between the major points are noted with primes, e.g., c', d', and d".[a] Permanent axial deformation as a result of the power-ramp tests is indicated by a noncongruency of points a and f.

The elongation signal in Rod R1 was not affected by a pressure component during the ramp test. The signal in Rod R2 was affected from 3.5 h into the

---

[a] Some of the identified special points are not used in this section but are used in the discussion of pressure signals in Section 5.3.5.

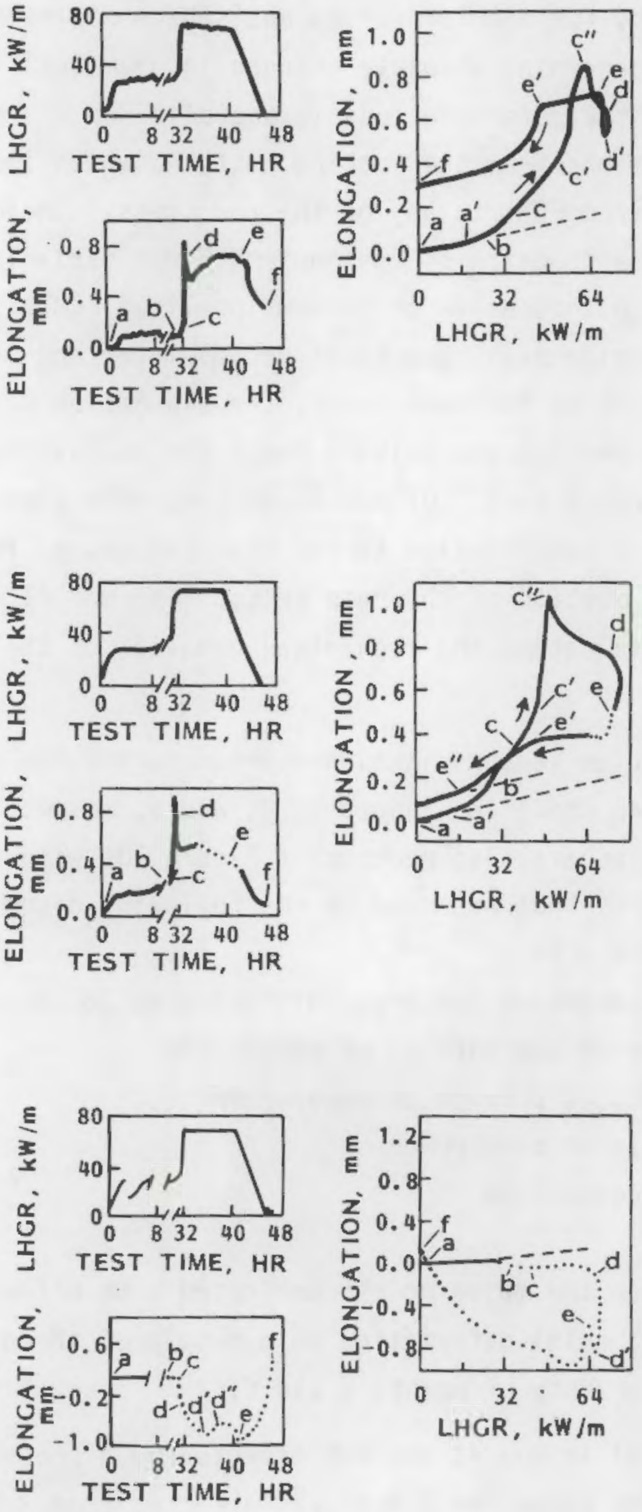

a) Rod R1

b) Rod R2

c) Rod R3 (note scale change)

FIGURE 109. Summary Plots of Elongation During Ramping in Rods R1, R2, and R3 (data affected by liftoff are shown with dotted lines; cladding thermal expansion, with dashed lines)

power-holding period until a LHGR of ~66 kW/m on the power descent. In Rod R3 (the highest burnup reference rod), the elongation sensor signal was affected by a pressure component during most of the period of interest (Appendix B).

Behavior During the Power Ascension

During the power ascent, the elongation behavior in both Rods R1 and R2 was similar. Fuel-cladding interaction started (point a' in Figure 109) at LHGRs lower than the previous steady-state LHGR, as it had on previous power ascensions during the base irradiation.(12) The LHGR at which interaction started was lower in the higher burnup Rod R2 than in Rod R1, i.e., 12 kW/m versus 21 kW/m. After interaction started, the initial interaction elongation rate was linear and nearly the same in both rods (points c to c') over a differential LHGR of ~33 kW/m. Both rods then experienced an increased rate of elongation (points c' to c") followed by very rapid inversion to contraction with increasing LHGR until the peak ramping LHGR was achieved (points c" to d). The high rate of elongation from points c to c' indicates that σ_θ/σ_z was decreasing rapidly and that the axial forces in the rods were dominant during this period. According to Equation (5), the minimum axial stress at point c" in both rods, assuming $\sigma_\theta = 0$ (which it probably was not), was ~130 MPa (19,000 psi). The change in the elongation rate from expansion to contraction at point c" indicates a major change in the force/stress condition in the cladding and the fuel. It occurred in both rods at a differential LHGR of ~40 kW/m after interaction started and at a similar amount of axial cladding strain (~0.16%).

The rod contraction with increasing LHGR can be interpreted in two ways. First, axial yielding or rapid creep in the fuel could reduce the axial force exerted by the fuel on the cladding. Second, radial forces caused by thermal expansion over a major portion of the fueled length of the rod could result in increasingly significant hoop stresses in the cladding. Because the fuel pellets were dished, the strength properties of the fuel should be determined by the fuel temperature at the edge of the dishes. This temperature would be significantly lower than would be expected to permit yielding or rapid creep of the fuel. Postirradiation ceramography did show that the dishes were filled; a solid central core of fuel was probably present after the 8-h holding period.

However, it is probable that the dish filling occurred by fuel creep during the 8 h and not during the last 5 min of the power-ramp. Therefore, the second interpretation--significant radial forces caused by fuel thermal expansion--would seem to be the reason for the contraction from points c" to d. As will be shown later, estimates of the cladding hoop stress in both Rods R1 and R2 at the end of the 8-h holding period were also relatively high, which supports the interpretation of increasing radial forces in the fuel during the latter stages of the ramp. Probably both the axial and radial forces were increasing during the entire power-ramp.

Behavior During the Peak-Power Holding Period and the Power Descent

During the first hour of the peak-power holding period, the elongation behavior in Rods R1 and R2 was similar; the rods contracted rapidly. This contraction was presumably due to fuel creep in the central hotter portion of the fuel that filled the dishes and whatever other space was available, e.g., crack volume. The axial forces in the fuel during the initial part of the power hold were apparently determined by the hotter central portion of the fuel. The stress ratio σ_θ/σ_z was increasing during this period.

During the last 7 h of the holding period, the elongation in Rod R1 increased rapidly at first and then attained an essentially constant value (points d' to e). Up until the time of a pressure component to the elongation signal in Rod R2, it behaved similarly. The stress ratio σ_θ/σ_z was decreasing during this period. Assuming that the axial and hoop stresses were both decreasing or that the axial stress was nearly constant during this period, the decreasing stress ratio indicates that the hoop stress was decreasing more rapidly than the axial stress. The length increase in Rod R1 from points d' to e corresponds to a minimum decrease in hoop stress of 128 MPa (18,600 psi) if it is assumed that 1) the axial stress did not change, 2) the stress change is elastic, and 3) the stress change occurred equally along the length of the fuel column.

An interesting phenomenon apparently occurred in Rod R3 between points d' and d". The rapid increase in the elongation signal during this short period (less than the 2-s data sampling period) indicated that a portion of the fuel column slipped with a recovery of rod shortening that was caused by the hoop stress. Apparently the effect of the hoop stress on rod length was wholly or partially reduced while the effect of the axial stress was not completely recovered. The process may have continued slowly over a greater length at times greater than d".

During the power descent, the elongation signals from Rods R1 and R2 were similar in shape and were also similar to signals from Rod AC9. Initially, the rod elongation that was greater than cladding free contraction increased with decreasing LHGR (points e to e'). Assuming, as for Rod AC9, that both the axial and hoop stresses in the cladding are being reduced by fuel thermal contraction and that the entire fueled length is being affected, the hoop stress was decreasing more rapidly than the axial stress. The rods then contracted to the cladding free thermal contraction curve (points e' and e") and then as cladding thermal contraction to zero power (points e" to f). Assuming $\sigma_\theta = 0$ at point e', σ_z for Rod R1 (Figure 110) at point e' = 45 MPa (6,500 psi). A linear extrapolation from point e' to point x indicates that σ_z at point x = 86 MPa (12,500 psi); and, from Equation (5), σ_θ at point e = 190 MPa (27,500 psi). For Rod R2 (Figure 109), σ_z = 30 MPa (4400 psi) at point e', σ_z = 70 MPa (10,200 psi) at point e, and, because the signal was affected by a pressure component and an extrapolation is required, σ_θ was at least 120 MPa (17,000 psi) at point e. The lower cladding stresses for Rod R2 than for Rod R1 are probably associated with the higher LHGR and resultant higher temperatures and weaker fuel. The cladding stress values and corresponding compressive stresses in the fuel indicate that the axial forces in the fuel-cladding system are controlled by higher temperature, weaker fuel and that the radial forces are controlled by lower temperature, stronger fuel. The hoop stresses estimated for Rod R1 at the end of the power-holding period are more than three times those in Rod AC9 and similar in magnitude to those estimated in sphere-pac Rods S40 and S41. The estimated axial stresses in Rod R1 are significantly higher than in Rod AC9 and similar in magnitude to the sphere-pac rods.

The changing rod lengths and stress ratios during the power-holding period provide an opportunity to estimate the stresses during the holding period. If it is assumed that there was no change in the axial cladding stress from points d' to e (Figure 109) for Rod R1 and that the stresses were elastic, the

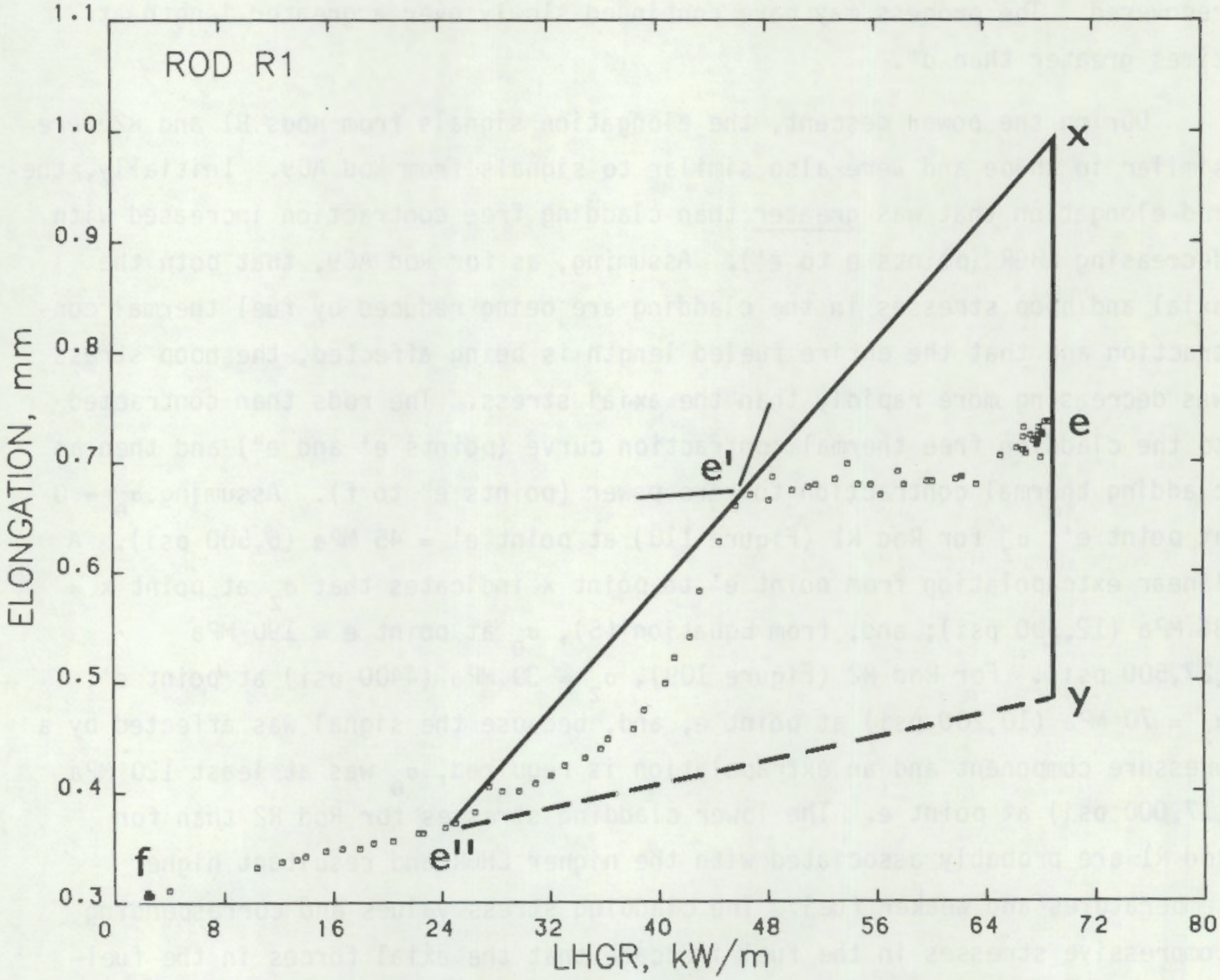

FIGURE 110. Rod Elongation During Power Descension in Rod R1 and Method of Extrapolation to Determine Cladding Stresses

hoop stress at point d' is the sum of the estimated hoop stress at point e (190 MPa) and the decrease in hoop stress as calculated above for the last 7 h of the power-holding period (128 MPa) or 318 MPa (46,100 psi). This value is probably higher than what would be required for yielding or creep of the cladding in the diametral direction.

The stresses in Rod R1 at the end of the power-ramp can be estimated by assuming that the stresses were elastic and that an exponential extrapolation (to point q in Figure 111) of the elongation attributed to the hoop stress decrease from points d' to e is valid. The first assumption is probably not

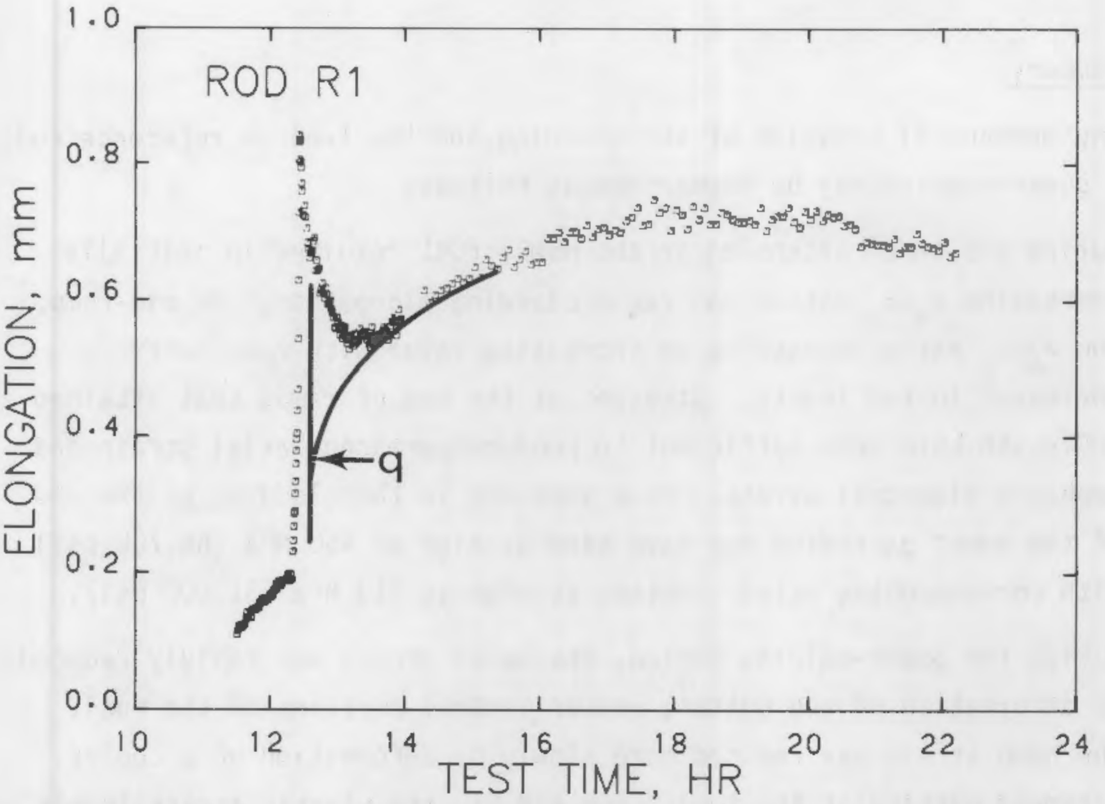

FIGURE 111. Method of Extrapolation to Estimate Cladding Stresses in Rod R1 at the End of the Power-Ramp

valid and the second assumption is certainly open to question; however, the estimate is provided to illustrate that the axial and hoop stresses were very high during the ramp testing of the reference rods. The extrapolation corresponds to a hoop stress reduction from the end of the power-ramp to the end of the power-holding period of ~270 MPa. Summing this value to the estimated stress at the end of the power hold (190 MPa), the estimated hoop stress at the beginning of the 8-h hold is 460 MPa (66,700 psi). The corresponding axial stress at point q varies from 160 to 213 MPa (23,000 to 31,000 psi), depending upon whether it is assumed that axial yielding has occurred prior to or after the end of the ramp.

The above analysis of the reference rods during ramping has shown that yielding of the cladding in the axial and probably the hoop directions occurred during ramp testing as a result of high stresses in both directions. The cladding reached the yield condition in Zone B (Figure 108) with σ_θ/σ_z between 0.68 and 1.72 at the time of yielding.

Summary

The mechanical behavior of the cladding and the fuel in reference rods during power-ramping may be summarized as follows:

- During the power ascension in the HBWR, FCMI resulted in initially decreasing σ_θ/σ_z ratios and rapid cladding elongation. At mid-ramp, the σ_θ/σ_z ratio changed to an increasing value with resultant decreases in rod length. Stresses at the end of ramps that attained LHGRs >66 kW/m were sufficient to produce permanent axial strain and probably diametral strain. Hoop stresses in the cladding at the end of the power ascension may have been as nigh as 460 MPa (66,700 psi) with corresponding axial stresses as high as 213 MPa (31,000 psi).
- During the power-holding period, the axial stress was rapidly reduced by deformation of the hotter, weaker central portions of the fuel. The hoop stress was reduced more slowly by deformation of a cooler, stronger portion of the fuel. For Rod R1, the elastic stress levels after the 8-h holding period were estimated to be σ_z = 86 MPa (12,500 psi) and σ_θ = 190 MPa (27,500 psi).
- During the power descension, the hoop stress was relieved more rapidly than the axial stress.

5.2.3 Mechanical Behavior in Annular-Fueled Rods During Power-Ramp Testing

The measurements of elongation during the power-ramp tests provide the primary basis for evaluating the mechanical behavior in the rods with annular fuel. (None of the rods failed, and PIE and profilometry did not reveal direct mechanical behavior data.) Of the rods containing elongation sensors, only Rod AC9 had a pure elongation signal that was free from the effect of internal pressure (Appendix B); however, useful mechanical data can be obtained from the instrumentation.

The detailed elongation sensor signal histories during the power-ramping of Rods A6, AC9, AC11, and ACP27 were shown in Figures 6, 7, 8, and 9, respectively. These elongation signal histories are reduced in Figure 112 with key

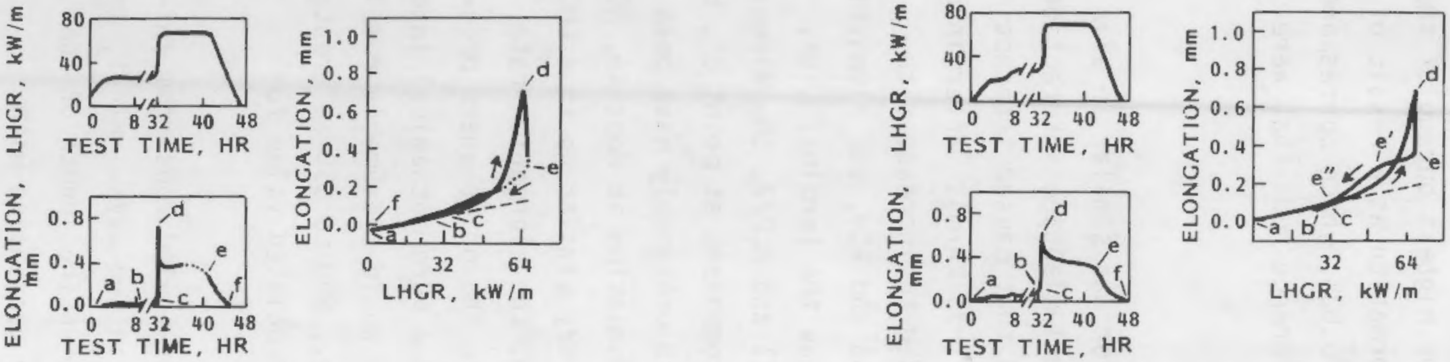

a) Rod A6

b) Rod AC9

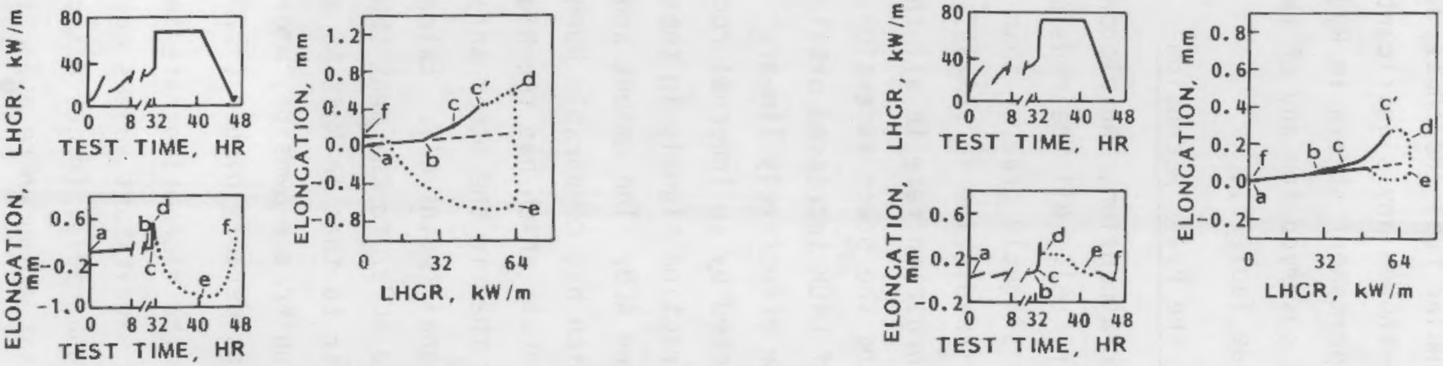

c) Rod AC11 (note scale change)

d) Rod ACP27 (note scale change)

FIGURE 112. Summary Plots of Elongation During Ramping in Rods A6, AC9, AC11, and ACP27 (data affected by liftoff are shown with dotted lines; cladding thermal expansion, with dashed lines)

letters to identify specific points that are used in the subsequent discussion. Only one rod with annular fuel--Rod AC11, which had the highest burnup of the annular-fueled rods--showed any significant axial deformation as a result of the ramp test. The permanent strain in Rod AC11 was +0.02%, which corresponds to the minimum value observed for any of the three reference rods that were power-ramp tested (see Table 5).

Behavior During the Power Ascension

During the power ascension, the elongation behavior was similar in all the rods with annular fuel. All the rods commenced fuel-cladding interaction at LHGRs equal to or slightly greater than those LHGRs that caused interaction during steady-state irradiation in IFA-517 or IFA-518 (~35 kW/m). After interaction began, the elongation rate in all the rods tended to increase with increasing LHGR during the power ascension. In Rods A6 and AC9, the elongation rate as a function of LHGR increased until ~5 kW/m below the terminal LHGR, where the rate became effectively linear. In Rods AC11 and ACP27, the elongation signal was affected by an internal rod pressure component at point c', but pure mechanical interaction signals in these rods would presumably have been similar to Rods A6 and AC9. The amount and rate of elongation in Rods A6, AC9, and ACP27, all of which had comparable burnups, were very similar up to a LHGR of 60 kW/m. In Rod AC11, which had the highest burnup, the elongation rate increase was greater than in the other three rods up to the point where pressure affected the signal (point c'). Extrapolation of a pure mechanical interaction signal for Rod ACP27 to the peak LHGR (point d) would presumably result in a magnitude similar to that in Rods A6 and AC9, i.e., 550 to 650 μm greater than that for cladding free expansion, whereas an extrapolated value for Rod AC11 would be considerably higher (~1200 μm).

The increase in the elongation rate in the annular-fueled rods from initially rather low to significant values can be viewed in two ways. First, it could be that axial and radial forces acting along the entire length of the rod are producing a situation where σ_θ/σ_z is gradually decreasing with probably high stresses in both directions. Second, it could be that primarily axial forces are gradually affecting longer lengths of the rod as the LHGR is increased until the entire fueled length is affected, with σ_θ/σ_z decreasing rapidly as the peak LHGRs are approached. When mechanical interaction started, the initial elongation rates in the reference rods were significantly greater and steepened more rapidly than in the annular-fueled rods (see Figure 109). This suggests that a smaller length of rod was initially affected in the annular-fueled rods. The flat-ended annular pellets should expand at the peak fuel temperatures at the surface of the central hole while the dished reference pellets should expand at a lower rate. Thus, the absence of an initially steeper elongation rate after interaction starts in the annular-fueled rods indicates that longer lengths of the rod are being affected by primarily axial stresses.

Cladding stresses in annular-fueled rods during the power ascension and the power-holding period cannot be exactly quantized because two of the three variables in Equation (5) are not known. However, the stresses in Rod AC11 exceeded the yield criterion because permanent elongation was observed. Three pieces of information provide evidence for a relatively low σ_θ/σ_z at the end of the ramp in Rod AC11 and the other annular-fueled rods:

- similar elongation behavior
- cladding expansion rate
- diameter reduction.

Elongation data for those portions of the ramp tests unaffected by a pressure component suggest that the behavior in all the annular-fuel rods was similar, i.e., axial interaction increased gradually with an unknown but relatively constant radial component during the power ascension. If it is assumed that the difference in elongation between point d and the thermal expansion line in Figure 112b for Rod AC9 is due solely to axial interaction, the minimum axial stress is 84 MPa (12,190 psi). Similarly, from an extrapolation for Rod AC11 (Figure 112c), the minimum axial stress is ~194 MPa (28,000 psi), i.e., ~51% of the yield strength. The relatively low permanent axial strain in Rod AC11 (~0.02%) indicates permanent axial deformation at stresses considerably less than the engineering yield strength of 380 MPa for a 0.2%

strain.(11) Perhaps a value between 50% and 60% of the 0.2% yield strength is more appropriate, in which case the minimum axial stress value of 194 MPa calculated above is very close to the yield condition and σ_θ/σ_z in the cladding would have a value considerably less than 1.0.

If the measured cladding expansion rate is nearly equal to what would be expected from solely axial forces caused by thermal expansion of the fuel, σ_θ/σ_z would be low in the annular-fueled rods. During irradiation in IFA-518.1 at a burnup of 10 MWd/kgM, the measured central fuel temperature in Rod AC9 increased 27.9°C per kW/m. Assuming that the flat-ended fuel pellets expand axially proportional to the central fuel temperature during the ramp test and that the coefficient of expansion is 1.6×10^{-6} mm/mm-°C, the calculated expansion rate of the fuel stack ($\dot{L}_{TE}$) is 0.208 mm per kW/m. The measured elongation rate for the rod ($\dot{L}_m$) is the sum of $\dot{L}_{TE}$ and the elastic compression rate of the fuel stack ($\dot{L}_f$) caused by the axial stress in the cladding, i.e.,

$$\dot{L}_m = \dot{L}_{TE} + \dot{L}_f \tag{8}$$

The minimum axial stress at the end of the power ascension (68.4 kW/m) in Rod AC9 as calculated above for Rod AC11 was 84 MPa (12,200 psi). The resulting axial force in the cladding is 8600N, and the axial force in the fuel is -8600N. Starting at 64.0 kW/m, the measured elongation curve was essentially linear up to the peak LHGR. The minimum axial stress as determined above at 64 kW/m is 34 MPa (4890 psi), and the compressive force in the fuel is -3440N. Assuming that the force is distributed over a 1-mm wide annular portion of fuel adjacent to the hole and because of the high fuel temperature Young's modulus is 1.38 GPa (2×10^7 psi), the calculated $\dot{L}_f$ equals -0.087 mm per kW/m over the LHGR range from 64.0 to 68.4 kW/m. Thus, the indicated value for $\dot{L}_m$ is 0.121 mm per kW/m; and the measured value over the same range in Rod AC9 is 0.115 mm per kW/m. Because the values for $\dot{L}_m$ are similar, a low σ_θ/σ_z value is indicated for the Rod AC9 cladding and presumably for all the annular-fueled rods during ramp testing.

Rod AC11 was the only rod for which the profilometry data showed a decrease in rod diameter over essentially the entire fueled length at all four azimuthal orientations (see Figures 37 through 40). Although there are uncertainties in the profilometry data (Section 4.3.6), this result certainly indicates permanent diametral reduction of the cladding in Rod AC11 and a low σ_θ/σ_z value at the end of the power ascension.

The evidence indicates that σ_θ/σ_z was <0.68 (Zone C in Figure 108) in the cladding of annular-fueled rods at the end of the power ascension during power-ramp testing in the HBWR. Because of the lack of cladding creepdown in the HBWR, radial thermal expansion of the fuel is not sufficient to induce high hoop stresses in the cladding of annular-fueled rods during a ramp test up to a burnup level of 16 MWd/kgM.

Behavior During the Peak-Power Holding Period and the Power Descent

During the peak-power holding period in Rod AC9 and the first 5 h of the holding period in Rod A6 (the only periods of "pure" elongation signal for any of the annular-fueled rods), the magnitude of elongation decreased rapidly (points d to e in Figure 112). The majority of the elongation recovery occurred within the first hour of the holding period. This rapid decrease in elongation at constant power indicates that the stress ratio σ_θ/σ_z in the cladding was increasing.

As will be explained in Section 5.2.5, the central hole volume of the annular fuel also decreased significantly during this period. The rapid increase in σ_θ/σ_z and the concurrent decrease of the hole diameter is indicative of decreases in the tensile axial stress/strain in the cladding and compressive axial stress in the fuel by fuel movement into the central hole under the influence of a relatively constant, possibly increasing, radial force. This interpretation is supported by the axial behavior of the flat-ended fuel pellet previously proposed in which significant axial elongation of the fuel and cladding occurs during the power ascension due to thermal expansion of the hotter central portion of the fuel. The hotter central portion of the fuel would be the weakest and, if stressed, would be the most likely to flow into the available space in the hole to relieve the stress, thus creating a smaller central hole during the holding period.

As depicted in the neutron radiographic and ceramographic data for Rod AC9 (Figures 63, 64, and 84), the shape of the hole changed from cylindrical to that of an hourglass along the length of individual pellets during the period when the hole volume decreased. If the central fuel temperature/strength was the same along the length of a pellet, a smaller cylindrical hole would be expected. The hourglass shape was probably caused by a corresponding shape of the outer cylindrical surface of the pellet that resulted from differential axial thermal expansion in the pellet. A variable fuel-cladding gap would have resulted in relatively higher heat transfer across the gap at the ends of the pellet compared with the heat transfer at the wider gap at the midplane of the pellet. Lower fuel temperatures, slightly higher strength, and less flow into the hole would have occurred at the ends of the pellet compared to the midplane of the pellet and an hourglass-shaped hole would have resulted (see Figure 67).

The amount of volume recovered by the elastic relaxation of the axial cladding strain in Rod AC9 corresponds to only 0.08% of the volume that was inside the rod along the fueled length. The hole volume decreased by ~5% of the volume that was inside the rod along the fueled length. However, the porosity in the central portion of the fuel after ramping (Figure 82) was considerably greater than the 5 to 6% in the as-fabricated fuel. Pressure in the bubbles in the fuel also contributed to deformation of the fuel into the central hole, which indicates that thermal-expansion-induced forces are not the only forces acting during the ramp testing and that the sources of stress/strain in the fuel are very complex.

During the power descension in Rod AC9, the mechanical component of the measured elongation signal (the measured signal less the thermal expansion component) initially increased slightly with decreasing LHGR (points e to e' in Figure 113) and then decreased with decreasing LHGR until the free contraction value (point e") was reached at approximately the LHGR at which PCI was initiated on the power ascension. The measured elongation signal at lower LHGRs followed the cladding free thermal contraction (points e" to f). If it is assumed that the mechanical component of the measured elongation signal that increased with decreasing LHGR (points e to e') is typical of the entire

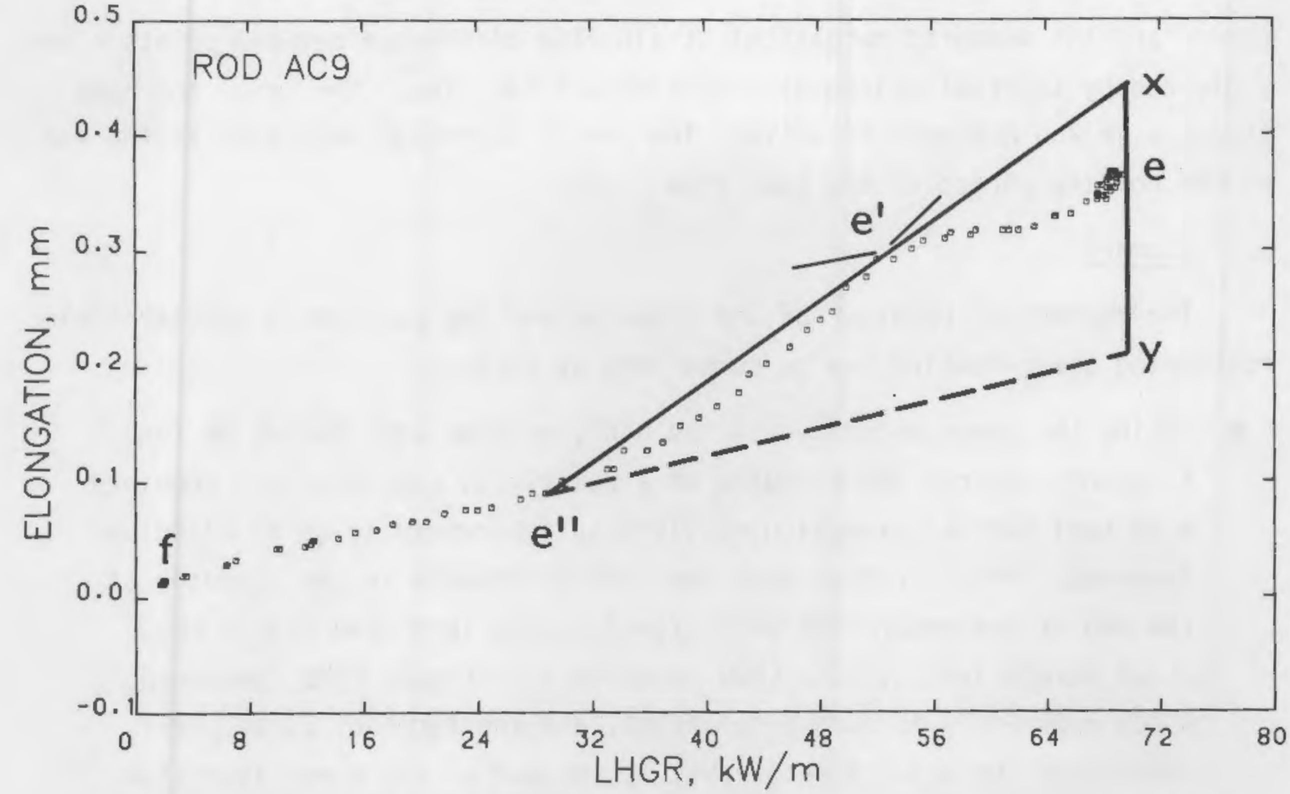

FIGURE 113. Rod Elongation During Power Ascension in Rod AC9 and Method of Extrapolation to Determine Cladding Stresses

fueled length of the rod and is caused solely by differential fuel-cladding contraction in the axial and radial directions, σ_θ/σ_z in the cladding is decreasing. That is, both σ_z and σ_θ are decreasing, but σ_θ is decreasing faster than σ_z. If it is further assumed that σ_θ is reduced to zero at e' and that the elastic differential thermal contraction is linear between points e', e", and x (Figure 113), the axial stress in the cladding at the end of the power-holding period can be estimated from Equation (5) where ϵ_z equals the difference between points x and y in Figure 113 divided by the fueled length. The axial stress computed in this manner is 38 MPa (5525 psi). The fact that the contraction curve is not linear between points e' and e" is interpreted to mean that smaller lengths of the fuel rod are being stressed as the LHGR is reduced. This is similar to what was proposed to be occurring during the power ascension. From Equation (5), the hoop stress (σ_θ) at the end of the holding period is 47 MPa (6800 psi) using the calculated axial stress and the measured mechanical strain (the difference between points e and y divided by the fueled length) (see Figure 113). Thus, the axial and hoop stresses in Rod AC9 were relatively low and of a similar magnitude at the end of the holding period of the ramp test.

Summary

The mechanical behavior of the cladding and the fuel in an annular-fueled rod during power-ramping may be summarized as follows:

- During the power ascension in the HBWR, wedging and locking of fuel fragments against the cladding at a relatively few locations combined with fuel thermal expansion resulted in predominantly axial cladding stresses. Radial forces were low. Hoop stresses in the cladding at the end of the power-ramp were significantly less than 68% of the axial stress levels. The LHGR at which significant FCMI commenced, which apparently is burnup dependent, and the terminal power level determined the axial stress level at the end of the power ascension. If the increase in LHGR above the power for interaction is sufficient, axial yielding or rapid creep during the power-ramp or the initial portion of the high-power holding period can result in permanent axial elongation with a presumably permanent decrease in fuel rod diameter. The presence of the graphite coating on the cladding apparently had little, if any, effect on the general axial stresses during the power ascension.
- During the initial portion of the high-power holding period, the axial stress in the cladding was rapidly reduced primarily by deformation of the hot central portion of the fuel into the central hole. The hoop-to-axial stress ratio rapidly increased during this period. Although it is not possible to absolutely determine the hoop stress in the cladding, it apparently remained relatively constant but could have conceivably been increasing slightly. At the end of an 8-h peak-power hold, the elastic axial and hoop stresses in the cladding were approximately equal at 35 to 50 MPa (5000 to 7250 psi).

- During the power descent, the cladding stresses were rapidly reduced with the radial stress being relieved more rapidly than the axial stress.

For commercial annular-fueled rods that have experienced only small amounts of cladding creepdown, the mechanical behavior of a rod during a power increase would be expected to be similar to that described above, i.e., axially dominant cladding stresses with only minor hoop stresses. For commercial annular-fueled rods that have experienced significant cladding creepdown or significant fuel swelling (high-burnup rods), the radial force and resultant higher cladding hoop stress can be expected to be more significant.

5.2.4 Mechanical Behavior in Sphere-Pac Fuel Rods During Power-Ramp Testing

Two sphere-pac fuel rods (Rods S40 and S41) were power-ramp tested at a burnup of ~7 MWd/kgM. Both rods were instrumented with elongation sensors, and the elongation behavior of both rods was similar although Rod S40 experienced a small permanent axial shortening (-0.02% strain). Comparison of preramp and postramp profilometry for the two rods with the reference and annular-fueled rods indicates that conclusions concerning absolute changes in diametral strain cannot be made (Section 4.3.6). However, the sphere-pac rods exhibited only minimal deviations from the rocking pattern and the greatest amount of change in ovality. The ovality changes generally increased along the length of the rod, being greatest at the top of the rod, and were generally along a single generatrix along the length of the rod. In the absence of definitive postirradiation measurements of rod diameter and length changes (Section 4.3.6) as a result of the ramp tests, the elongation measurements during the tests provide the primary basis for evaluating the mechanical behavior in the sphere-pac rods. The elongation signals measured during ramping of the sphere-pac rods were not affected by an internal rod pressure component during the ramp tests (Appendix B).

Detailed elongation sensor signal histories during the power-ramping of Rods S40 and S41 are shown in Figure 10 and 11, respectively. These elongation signal histories are reduced in Figure 114 with key letters identifying specific points that are used in the following discussion.

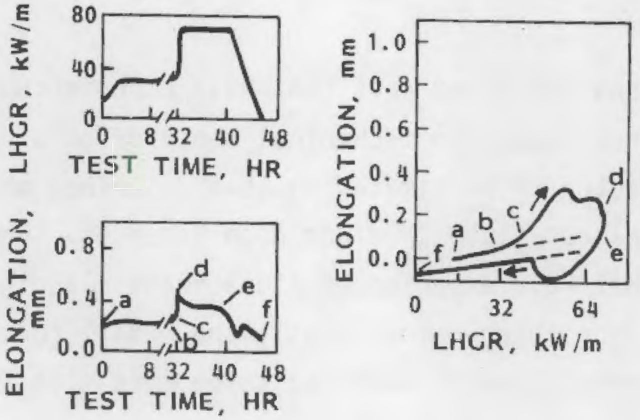

a) Rod S40

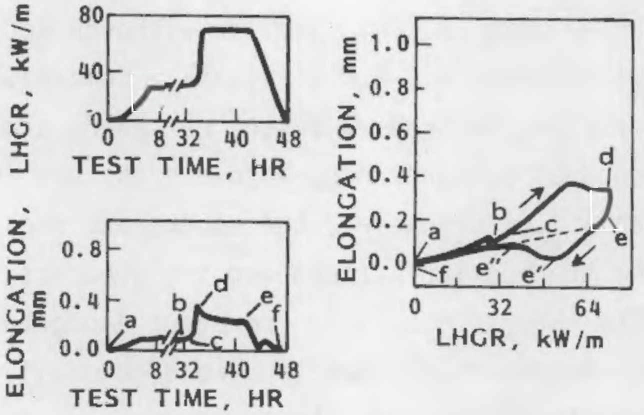

b) Rod S41

FIGURE 114. Summary Plots of Elongation During Ramping in Rods S40 and S41 (data affected by liftoff are shown with dotted lines; cladding thermal expansion, with dashed lines)

Permanent axial shortening of Rod S40 occurred as a result of the ramp test, i.e., the difference between points a and f. Rod S40 was the only rod from these FPIP tests to exhibit shortening of the cladding during power-ramping. The amount of axial strain was small (-0.02%) and indicates permanent hoop strains in the cladding with $\sigma_\theta/\sigma_z > 1.72$, i.e., in Zone A of Figure 108.

Behavior During the Power Ascension

During the power ascensions, the elongation in both sphere-pac rods was similar. Initially, the rate of elongation was equal to or very near the rate of free thermal expansion of the cladding. At LHGRs nearly equivalent to the previous steady-state LHGR (~30 to 35 kW/m), FCMI was initiated in both rods, as evidenced by the departure of the elongation rate from the cladding free expansion rate. During the rapid ^{3}He-induced portion of the ramp (points c to d), the elongation rate in both rods initially increased, which indicates that σ_θ/σ_z was decreasing, and then decreased, which indicates that σ_θ/σ_z was increasing. Although both the axial and hoop stresses were probably increasing during the power ascension, it is not possible to calculate either stress directly because two of the three variables are not known [see Equation (5)] and an independent measurement of cladding diameter was not made. However, the increasing σ_θ/σ_z during the latter portion of the ramp indicates that the hoop stress in the sphere-pac rods was much greater during the power ascension than in the rods with annular fuel. If it is assumed that the highest cladding stress levels and permanent shortening in Rod S40 occurred during the latter part of the power ascension or the initial stages of the power-holding period, the cladding stress levels can be estimated. If, because permanent shortening occurred in Rod S40 and, therefore, according to Equation (7), $\sigma_\theta/\sigma_z \geq 1.72$ at the yield condition, σ_θ/σ_z is assigned a value of 2.0 at point c'; and, if it is further assumed that the cladding is still elastic at point c', the hoop stress in the cladding of Rod S40 at point c' is equivalent to 170 MPa (25,000 psi). Similarly, the axial stress is 85 MPa (12,500 psi). Using a cladding uniaxial yield strength value in the range from 190 to 230 MPa, as was estimated for the annular-fueled rods (Section 5.2.3), the estimated hoop stress at point c' is a significant fraction of that estimated for the yield condition. Because both σ_θ and σ_z can be expected to increase between points c' and d, the above estimates of cladding stress and the explanation of yielding are reasonable.

Behavior During the Peak-Power Holding Period and the Power Descent

During the power descent, both sphere-pac rods became shorter than the thermal contraction line. If the contraction is assumed to be elastic, this indicates that $\sigma_\theta/\sigma_z > 4$ during the initial portion of the descent and represents a more rapid reduction of the cladding axial stress than the hoop stress during the power-holding period. For Rod S41, if it is assumed that $\sigma_z = 0$ at point e' and the rate of differential fuel-cladding contraction in the radial direction was constant between e and e", the line e"-e' can be extrapolated to the power-holding LHGR to provide values for the hoop stress at point e' and at the end of the power-holding period (point e). These values are 67 MPa (9700 psi) at point e' and 192 MPa (27,800 psi) at point e, and the corresponding axial stress at point e is 60 MPa (8,700 psi). For these assumptions, these are minimum hoop stress values that can be calculated. The assumption that $\sigma_z = 0$ at point e' is consistent with the formation of the transverse cracks observed in the central zone of the ramped Rod S41 (Figure 84). Thus, it is indicated that the hoop stress values in sphere-pac rods after holding for 8 h at ~70 kW/m are near the yield condition.

An evaluation of the mechanical interaction in sphere-pac rods during normal operation has been presented previously(12) based upon the measured elongation behavior in the HBWR and limited PIE results. In summary, the evolution of the mechanical behavior in the sphere-pac rods during normal operation consists of 1) the crushing of small spheres located between the large spheres and the cladding (Figure 107) and between the large spheres themselves to partially relieve axial and radial stresses in the cladding during the initial rise to power; 2) the embedding of crushed spheres into the cladding to anchor the bed of spheres axially; 3) the sintering of a central core of fuel during the initial steady-state operation, which further relieves the cladding stresses; 4) during the power descent, the formation of transverse cracks in the sintered central core, resulting in short portions of the fuel column that are effectively retained in the same axial position by the anchors formed during step (2) and 5) as a result of the four steps listed, a fuel rod that does not experience significant FCMI during subsequent power ascensions until the previous peak LHGR is exceeded. The rod is effectively conditioned to the previous LHGR.

The postulated high stress levels, especially for hoop stress, after holding 8 h at the peak ramping LHGR indicate that the mechanism that results in conditioning during steady-state irradiation is not operative during power-ramp testing. The degree of crushing of small spheres that were originally located between the cladding and the large spheres is apparently capable of accepting only a small amount, if any, of additional deformation in order to reduce the cladding stress level during power-ramping. The formation of the large sintered zone in the central portion of the fuel also effectively removed a large volume of the small spheres that were originally trapped between the large spheres in the center of the bed; thus, these smaller spheres were no longer present to relieve the load on the cladding.

Summary

The mechanial behavior of the cladding and the fuel in a sphere-pac fuel rod during power-ramping may be summarized as follows:

- During the power ascension, significant FCMI was initiated at an LHGR that was approximately equal to the previous steady-state LHGR to which the rod was exposed. As the LHGR increased, both axial and hoop stresses were created in the cladding by differential fuel/cladding thermal expansion. At the highest LHGRs, the cladding hoop stress increased more rapidly than the axial stress. If the hoop stress is sufficiently high, it can result in axial shortening and a diametrial increase in the cladding, presumably by yielding of the cladding.
- Stress relief in the cladding during an 8-h power hold apparently occurred in both the axial and hoop directions. During this period, σ_θ/σ_z continued to increase and the elastic hoop stress at the end of an 8-h hold may have been as high as 192 MPa (27,800 psi).
- During the initial portion of the power descent, the axial stress was rapidly reduced by the formation of transverse cracks in the hotter central portion of the fuel; and $\sigma_\theta/\sigma_z > 4$.

The power-ramp testing of sphere-pac fuel rods in the HBWR is a good simulation of the mechanical aspects of PCI behavior because cladding creepdown and/or fuel swelling/relocation are not required to promote FCMI, as is the case for rods with pellet fuel. For this reason, the lack of cladding failure during power-ramp testing of Rods S40 and S41 in the HBWR is noteworthy.

5.2.5 Pressure in Annular-Fueled Rods That Experienced Elongation Sensor Liftoff

Two of the rods that contained annular fuel (Rods AC11 and ACP27) experienced liftoff of the elongation sensor during the power ascension portion of the power-ramp tests. Thus, the measured elongation signal contained a contribution from the internal rod pressure (see Appendix B and Figures 8 and 9). During the period of sensor liftoff, nothing can be definitively concluded concerning fuel rod elongation; however, if assumptions are made concerning the elongation behavior during these periods, Equation (1) can be solved to determine trends in the internal rod pressure.

The sensor in Rod ACP27 experienced liftoff at a LHGR of ~60 kW/m during the power ascension. Prior to liftoff, the elongation behavior in Rod ACP27 was very similar to that in Rod AC9. In addition, both rods experienced similar peak ramping LHGRs at similar burnup levels: 70 and 71 kW/m and 9.5 and 10.8 MWd/kgM for Rods ACP27 and AC9, respectively. If it is therefore assumed that the elongation behavior in Rod ACP27 was the same as for Rod AC9 during the period of liftoff, Equation (1) can be solved for the pressure component of the elongation sensor signal. This pressure component is not the absolute pressure, but it indicates the pressure above the liftoff pressure (in this case, the pressure above 2.01 MPa in the operating fuel rod). In addition, the response to the pressure after liftoff was not calibrated; and, therefore, the pressure component provides only an indication of the internal rod pressure changes as a function of time.

The derived pressure signal for Rod ACP27 as a function of test time is shown in Figure 115. The measured elongation signal, the calculated thermal expansion signal for Rod ACP27, and the mechanical interaction signal for Rod AC9 are also shown. The large pressure decrease in the derived pressure signal within the first hour of the power-holding period is very interesting. Fission gas release from the fuel would be expected to cause a continuing increase in the pressure as the time at power increased, albeit with a decreasing rate. The sudden decrease in the pressure signal is interpreted to indicate a decreasing volume of the central hole. With the transfer of high-temperature gas from the central hole to a lower temperature region elsewhere

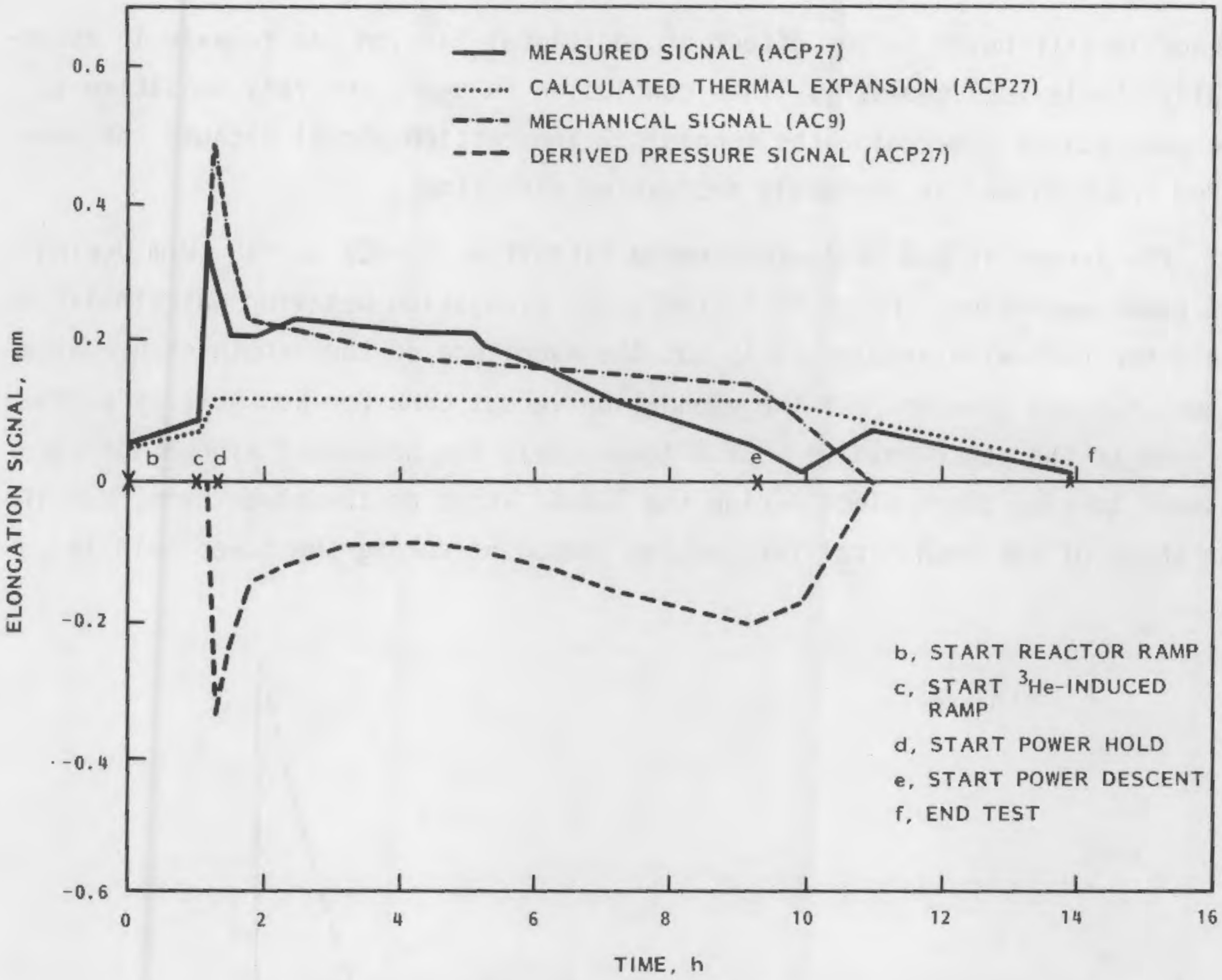

FIGURE 115. Derived Pressure Signal in Rod ACP27

in the fuel rod, e.g., the midradius circumferential fuel cracks, the average temperature of the gas and therefore the pressure in the rod decreased even though the number of gas molecules in the gas volume probably increased during the same period due to fission gas release. The closure of the central hole obviously occurred quite rapidly. It is noteworthy that the maximum mechanical interaction signal at the beginning of the power-holding period could be much larger or as much as 0.2 mm smaller and still result in the same conclusion concerning when the central hole closed. That is, the analysis for Rod ACP27 is not very sensitive to the assumption of a mechanical interaction signal in ACP27 that is equivalent to that which occurred in Rod AC9. The gradual rise in the rod pressure signal in the last 6 h of the power-holding period is attributed to the effect of additional fission gas release in essentially stable fuel geometry. This conclusion is again not very sensitive to the assumptions concerning the mechanical interaction signal because the measured "raw" signal is obviously decreasing with time.

The sensor in Rod AC11 experienced liftoff at a LHGR of ~48 kW/m during the power ascension. Prior to liftoff, the elongation behavior was similar to the other rods with annular fuel; but the magnitude of the length change at a given LHGR was greater. If the elongation versus LHGR for Rod AC11 is extrapolated to the power-holding LHGR (Figure 116), the permanent elongation is assumed to have taken place during the latter stage of the power ramp; and if the shape of the mechanical interaction component during the power hold is

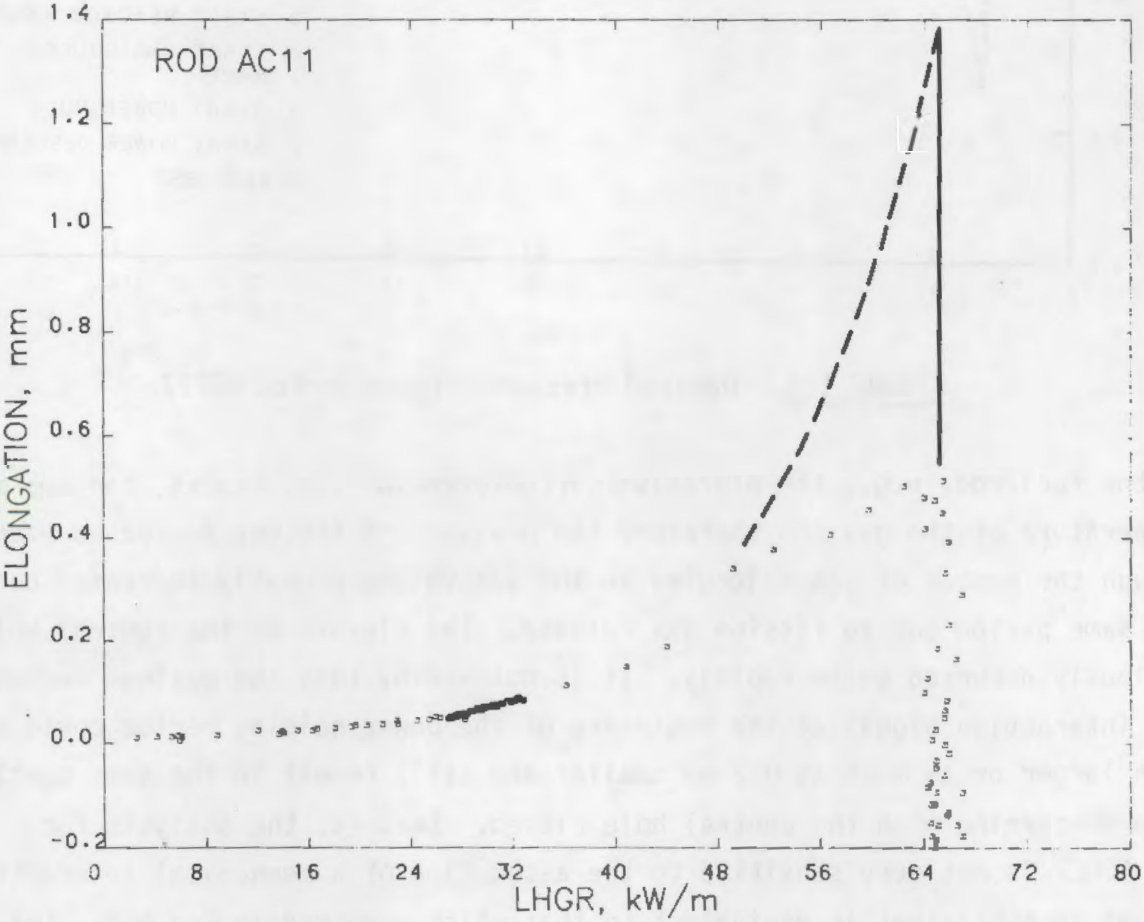

FIGURE 116. Extrapolation of Elongation Signal in Rod AC11

similar to that which occurred in Rod AC9, Equation (1) can be solved for the pressure component of the elongation signal. The derived pressure signal for Rod AC11 as a function of test time is shown in Figure 117. As for Rod ACP27, the decrease in the pressure signal immediately after the start of the power-holding period indicated that the central hole closed, and the steady rise in pressure after the initial decrease indicates continued fission gas release. For Rod AC11, the derived pressure signal is much more sensitive to the assumptions used to derive the signal, especially if the actual mechanical interaction component was less than the extrapolated value. This sensitivity is presumably due to the higher fission gas inventory and release in the higher

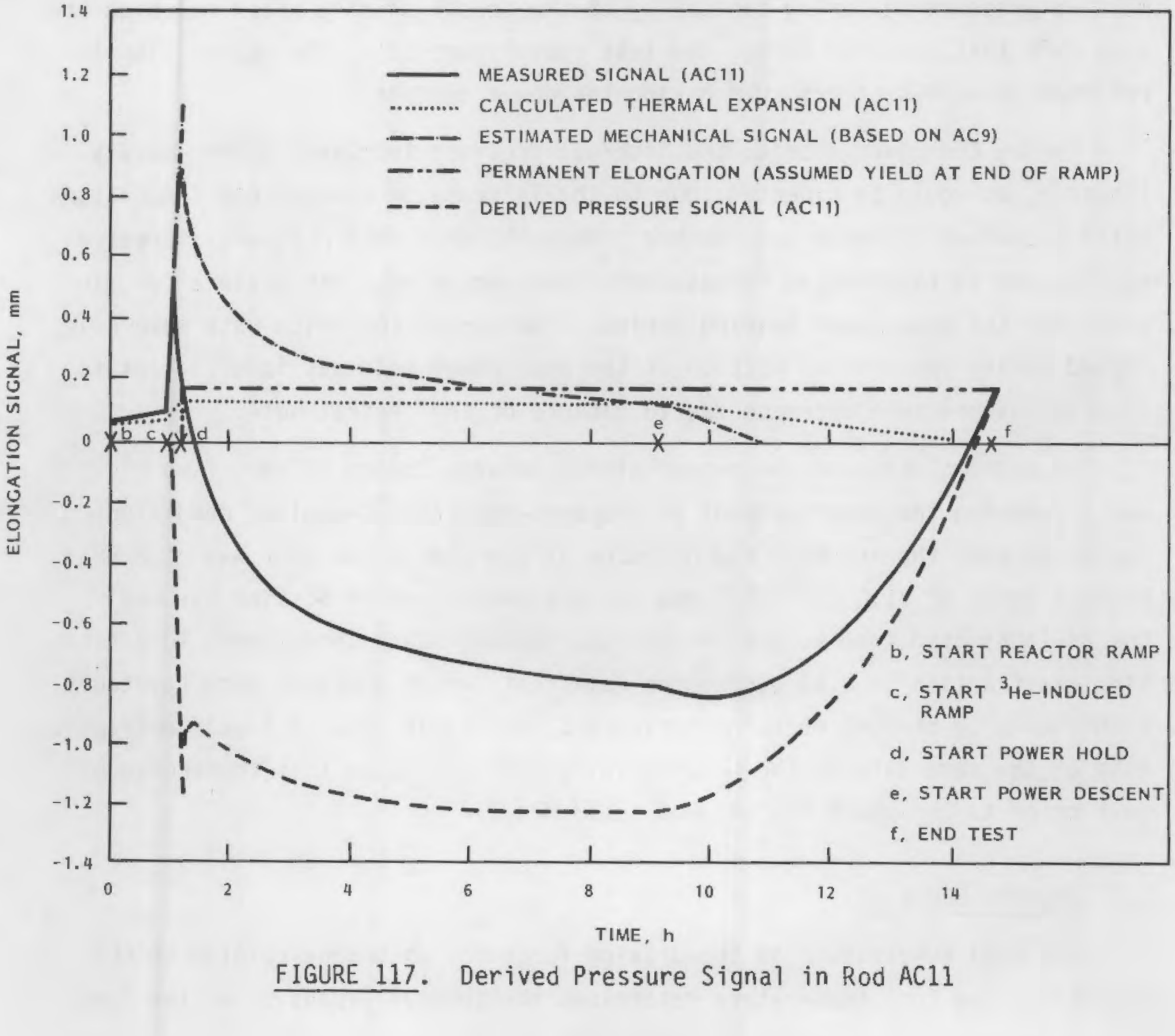

FIGURE 117. Derived Pressure Signal in Rod AC11

burnup Rod AC11. Nevertheless, the derived result indicates that, as with Rod AC9, the central hole closure occurred very rapidly after achieving the power-holding LHGR. This result is consistent with the rapid reduction in the axial cladding strain for rods with annular fuel that was postulated to have occurred due to deformation of the hot central portion of the fuel (Section 5.2.3).

5.2.6 Pressure in Annular-Coated Rod AC10 During Power-Ramp Testing

Rod AC10 contained a pressure sensor for measuring the internal gas pressure during power-ramping. The internal pressure in the fuel rod exceeded the maximum pressure measuring capability of the sensor shortly after reaching the peak LHGR that occurred during the test (see Figure 12). The sensor signal returned at a LHGR of ~25 kW/m during the power descent.

During the power ascent, the internal pressure increased approximately linearly, as would be expected, due to the increase in average gas temperature until a LHGR of ~53 kW/m was reached. Above 53 kW/m, the pressure increased rapidly due to fission gas release until the sensor went off scale a few minutes into the peak-power holding period. The period for which data were collected during the initial portion of the peak-power hold was insufficient to observe any pressure decrease due to closure of the central hole.

An extrapolation of the sensor signal between 25 and 12 kW/m (see Figure 12) during the power descent to the zero-power/240°C-coolant condition indicated that the internal rod pressure at the end of the test was ~1.2 MPa. Using a value of 31.0 cm^3 (STP)/MWd for the generation of fission gas and the as-fabricated free volume in the rod, this pressure corresponds to a fission gas fraction of 0.44 during the ramp test, which compares very favorably with the value of 0.46 measured during PIE (see Table 12). A linear extrapolation of the same data to the power-holding LHGR indicates that the pressure just prior to the power descent was ~2.23 MPa (325 psi).

5.3 THERMAL BEHAVIOR

The fuel temperature is the driving force for phenomena related to PCI failures. The fuel temperature determines the thermal expansion of the fuel, which in turn determines the radial and axial stresses in the fuel rod cladding. It also determines the release of fission products (including krypton and xenon), which increases the internal pressure in the fuel rod, and the species that affect SCC (e.g., iodine and cadmium). The results obtained from PIE of the ramped rods, as they pertain to thermal considerations, are discussed below.

5.3.1 Comparison of Annular-Pellet and Reference Fuel Temperatures During Ramping

During steady-state irradiation in the HBWR, fuel temperature measurements up to burnups of 10 to 12 MWd/kgM have shown that the centerline temperature at a given LHGR was lower in annular-coated and annular fuel than in dished-pellet reference fuel.(6) It was not possible to obtain thermocouple data during the power-ramp tests; therefore, no direct fuel temperature measurements could be made. Estimates of the thermal conditions of the fuel during ramping are inferred from other indicators, e.g., evaluations of restructuring from the ceramographic sections and fission gas release measurements.

Comparison of ceramographic sections from annular-coated and reference rods at a nearly equivalent ramping LGHR of 69 kW/m (Figure 78) shows that restructuring and grain growth have occurred in the central regions in both fuel types as a result of the ramp tests. The dishes were completely filled in reference Rod R1 (Figure 84) and evidence of sintering at pellet-pellet interfaces was present in both Rods R1 (Figure 102) and AC9 (Figure 97) as well as in annular Rod A6 (Figure 100). Comparisons of the fuel types indicate that the largest amount of grain growth occurred in Rod AC9 (Figures 82 and 87). The cross section of Rod AC9 showed a relatively wide midradius circumferential crack in the fuel, and adjacent regions on both sides of this crack exhibited a significant degree of grain boundary separation (Figures 81 and 82). The midradius crack and areas of grain boundary separation were also evident in the longitudinal section from Rod AC9 (Figures 87 and 88). A midradius crack was also evident in the fuel cross section from Rod R1 (Figures 79 and 80); however, this crack was much narrower than the one in Rod AC9 and very little grain boundary separation occurred in regions adjacent to the crack.

For both the annular-coated and reference fuel types, the midradius circumferential crack formed either at or very close to the maximum radius at which grain boundary bubbles of fission gas were detected. From the outer surface to the center of the fuel in Rod R1 (Figure 79 and 80), the fuel structure changed from 1) an as-fabricated structure, 2) to grain boundary bubble precipitation, 3) to the midradius circumferential crack, 4) to greater grain boundary bubble precipitation, 5) to equiaxed grain growth with fewer but larger grain boundary bubbles, 6) to larger elongated grains with some white inclusions of presumably noble metal fission products and even larger gas bubbles, and 7) finally, at the fuel center, a region similar to region (6) but containing generally equiaxed grains. This gradual change in structure indicates that if the midradius crack was present at power it did not pose a significant heat transfer barrier and was therefore not very wide. A significant radial compressive force on the fuel would tend to keep such a crack closed. Because even narrow cracks are a heat transfer barrier, it is possible that the midradius crack in Rod R1 was not present at power and formed during the power/temperature descent due to differential contraction between the thermally stressed as-fabricated and the stress-free restructured regions of the fuel, i.e., at the weak point where grain boundary bubbles reduced the strength of the fuel.

By comparison, the fuel structure in Rod AC9 (Figure 82) changed rather dramatically at and across the midradius crack. The fuel on either side of the circumferential crack was characterized by significant grain boundary separation in the radial direction. The midradius circumferential crack in Rod AC9 was significantly wider than in Rod R1. A narrow band of fuel with large grain boundary bubbles and grains with the original grain size was located immediately adjacent to the region of grain boundary separation on the side of the circumferential crack closest to the center of the rod. There is little or no evidence of a transition region of small grain boundary bubbles to equiaxed grain growth in Rod AC9 as was evidenced in Rod R1. Instead, the structure changed dramatically from small grains with large grain boundary bubbles to large elongated grains with larger bubbles in the grain boundaries. The dramatic change in fuel structure in Rod AC9 indicates that a major heat transfer barrier was present in the region of the grain boundary separation, including the midradius crack, during portions of the ramp test. Whether the crack, observed at room temperature, was actually open at power and was the major heat transfer barrier is not known; but the integrated effect of grain boundary separation would have the same effect as a single wide midradius crack and would present a heat transfer barrier. Because of the presence of a significant midradius heat transfer barrier in the annular pellet, the central fuel temperatures during ramping were higher than would be expected based upon the steady-state irradiation results obtained at LHGRs of <42 kW/m. This is substantiated by the high fission gas release for the power-ramped annular-pellet rods when compared to reference Rod R1 (Table 12), especially when the differences in terminal ramping LHGR are considered.

The difference in behavior with respect to formation of midradius circumferential cracks in the annular and reference fuels is difficult to quantitatively explain, but a qualitative explanation is possible. Both types of rods should and do exhibit a region in the fuel in which the diffusion of atoms and/or intragranular fission gas bubbles result in the formation of a zone with significant quantities of fission gas precipitated on the grain boundaries. Obviously, for similar temperatures, the strength of the fuel in this region should be reduced with respect to the strength of the nonrestructured fuel; and, if sufficient tensile stress is present, the fuel would fracture along grain boundaries. Theoretically, during irradiation, nonrestrained and nonrestructured annular and solid reference fuel fragments should experience high midradius tensile thermal stresses in the circumferential direction on radial crack surfaces.(16) The radial crack surfaces were created by thermal stresses in the original fuel pellets during the initial power ascension. It would be expected that both fuel types should form some type of midradius circumferential cracks during the ramp test if the fuel fragments were radially nonrestrained. Therefore, similar thermal effects would also be expected for nonrestrained fragments, i.e., the formation of comparable midradius heat transfer barriers and drastic changes in structure across the thermal barrier. However, the power-ramp test results indicate that the fuel fragments in annular-pellet rods experienced low hoop stresses and were relatively nonrestrained during the ramp test (Section 5.2.3), which resulted in the formation of a radial heat transfer barrier. The fuel fragments in reference pellet rods, however, experienced significant hoop stresses and were restrained by the cladding (Section 5.2.2), which resulted in the existence of radial compressive forces and prevented formation of a significant heat transfer barrier.

Thus, it is postulated that differential fuel-cladding expansion in the HBWR was not sufficient to completely close the fuel-cladding gap in the rods with annular fuel during the ramp tests; and high fuel temperatures were experienced in these rods. In commercially irradiated annular fuel rods, sufficient cladding creepdown may occur to close the fuel-cladding gap; therefore, commercially irradiated annular fuel may be subjected to radial restraint sufficient to prevent the formation of the midradius thermal barrier during power-ramping. Fuel rod segments with annular fuel that are being commercially irradiated in Big Rock Point Reactor (BRPR) are scheduled to be ramp-tested and destructively examined to ascertain if the thermal barrier is formed during a power-ramp test.

5.3.2 Comparison of Sphere-pac and Reference Fuel Temperatures During Ramping

For sphere-pac fuel, restructuring and sintering takes place in the central portions of the fuel after steady-state operation at LHGRs ≤ 42 kW/m (Figures 92 and 93). Centerline fuel temperatures for the sphere-pac fuel were slightly below the temperatures in the reference fuel up to a burnup of 7 MWd/kgM.(7) Additional restructuring and sintering occurred to a larger radius as a result of the ramp tests in both fuel types (Figure 78). Temperatures were not measured during the ramp tests because the thermocouples could not be reconnected after the steady-state irradiation; however, comparison of the fission gas release fractions from Rod S41 and R1, which were ramped to identical conditions, showed that the release from the sphere-pac fuel was lower than from the reference fuel (Table 12). The area of the restructured zone, i.e., the area inside the grain boundary bubble precipitation radius, was smaller for Rod S41 than for Rod R1 (41% and 50%, respectively). These results indicate that the peak temperatures were lower in Rod S41 than in Rod R1 during the ramp tests.

5.4 OVERALL COMPARISON OF THE FUEL ROD TYPES DURING POWER-RAMP TESTING IN THE HBWR

Three general types of fuel rods were power-ramp tested in the HBWR: rods with annular-pellet, sphere-pac, and reference dished-pellet fuel. The rods with annular fuel also had the additional variables of noncoated cladding and cladding coated with graphite with and without helium pressurization. The following summary compares the behavior of the three general fuel rod types during power-ramp testing in the HBWR:

- All three ramped reference rods experienced permanent axial elongation, indicating that the cladding yielded or crept rapidly due to high axial stress levels. High hoop stresses and diametral strain were also indicated in the reference rods. After an 8-h hold at the peak ramping LHGR, the axial and hoop stresses in the cladding of reference rods were estimated to be ~86 MPa (12,500 psi) and 190 MPa (27,500 psi), respectively. The fuel thermal expansion in the radial direction and resultant hoop stresses in the reference fuel rods were greater than in the annular fuel rods.
- The rods with annular fuel exhibited the least amount of cladding stress during this power-ramping. Only one rod out of four tested (the rod with the highest burnup) had any permanent deformation as a result of power-ramp testing. During the period when the cladding stresses were the highest, i.e., immediately after achieving the peak ramping LHGR, the cladding stress in annular-fueled rods was primarily axial. The axial stress level was rapidly reduced by plastic deformation of the high-temperature central region of the fuel into the central hole in the fuel. This rapid plastic deformation may have been assisted by the formation of a midradius circumferential heat transfer barrier in the fuel that increased the central fuel temperature and plasticity. After 8 h at the peak ramping LHGR, the axial and hoop stresses for the annular-fueled rods were nearly equivalent from 35 to 50 MPa (5000 to 7500 psi). In rods with graphite-coated cladding, no CO or CO_2 formed that might have

overpressurized the rods. The graphite coating also prevented any significant amounts of fission products from reaching the cladding. There was no evidence that the graphite coating significantly affected the general FCMI behavior. It can be expected that significant amounts of cladding creepdown and/or fuel swelling will promote higher hoop stresses in rods with annular fuel that are irradiated in a commercial reactor and subsequently power-ramped. However, for comparison to reference rods, it should be noted that the reference rods irradiated in a commercial environment would be subject to the same amount of creepdown, thereby also promoting higher hoop stresses during power-ramp testing.

- The sphere-pac rods experienced significant hoop stresses during power-ramp testing in the HBWR, as evidenced by the permanent shortening in one of the two ramped rods. The mechanism for conditioning of sphere-pac rods to the previous peak-power level that was observed during steady-state irradiation is apparently not operative during power-ramping of irradiated rods. As a result, the hoop stresses after 8 h at the peak ramping LHGR were estimated to be ~192 MPa (27,800 psi) and permanent diametral strain is indicated. Axial stresses were estimated to be ~67 MPa (9700 psi). Fuel temperatures in the sphere-pac rods were lower than in the reference and annular designs, as evidenced by lower fission gas release and less central fuel restructuring. When comparing the mechanical behavior of sphere-pac rods to rods with either annular or reference pellets, the power-ramp testing of the sphere-pac rods in the HBWR is a good simulation because cladding creepdown and/or fuel swelling/relocation are not required to promote FCMI.

6.0 REFERENCES

1. Crouthamel, C. E. November 1977. Fuel Performance Improvement Program, Quarterly/Annual Progress Report, April-September 1977. COO-4066-4, Pacific Northwest Laboratory, Richland, Washington.

2. Crouthamel, C. E., and M. D. Freshley. January 1978. Fuel Performance Improvement Program, Semiannual Progress Report, April-September 1980. DOE/ET/34215-19, Pacific Northwest Laboratory, Richland, Washington.

3. Crouthamel, C. E., and M. D. Freshley. April 1981. Fuel Performance Improvement Program, Semiannual Progress Report, October 1980-March 1981. DOE/ET/34215-21, Pacific Northwest Laboratory, Richland, Washington.

4. Bailey, W. J., et al. December 1977. State-of-the-Technology Review of Fuel Cladding Interaction. COO-4066-2, Pacific Northwest Laboratory, Richland, Washington.

5. Bailey, W. J., and J. O. Barner. January 1978. Assessment of Fuel Concepts. COO-4066-3, Pacific Northwest Laboratory, Richland, Washington.

6. Guenther, R. J., and J. O. Barner. December 1981. Performance of Annular-Coated, Annular, Vipac, and Reference Test Rods During Steady-State Irradiation in HBWR IFA-518.1. DOE/ET/34215-23, Pacific Northwest Laboratory, Richland, Washington.

7. Cunningham, M. E., K. H. Rising, and J. O. Barner. March 1982. Fuel Performance Analysis of the HBWR IFA-517.1 Test Assembly. DOE/ET/34215-22, Pacific Northwest Laboratory, Richland, Washington.

8. Wagoner, S. R., J. O. Barner, and R. K. Welty. June 1979. Description and Characterization of HBWR Series H-1 Test Rods. COO-4066-11, Pacific Northwest Laboratory, Richland, Washington.

9. Guenther, R. J., J. O. Barner, and R. K. Welty. March 1980. Description and Characterization of HBWR Series H-2, H-3, and H-4 Test Rods. DOE/ET/34215-14, Pacific Northwest Laboratory, Richland, Washington.

10. Crouthamel, C. E., and J. O. Barner. June 1982. Fuel Performance Improvement Program, Semiannual Progress Report, April-September 1981. DOE/ET/34215-28, Pacific Northwest Laboratory, Richland, Washington.

11. Hagrman, D. L., G. A. Reymann, and R. E. Mason. February 1980. MATPRO-Version II (Revision 1), A Handbook of Materials Properties for Use in the Analysis of Light Water Reactor Fuel Rod Behavior. NUREG/CR-0497, TREE-1280, Rev. 1, Rev. 3, and Rev. 4, EG&G Idaho, Inc., Idaho Falls, Idaho.

12. Guenther, R. J., and J. O. Barner. September 1982. Performance of Annular-Coated-Pressurized, Annular-Coated, Sphere-pac, and Reference Test Rods During Steady-State Irradiation in HBWR IFA-518.2. DOE/ET/34215-27, Pacific Northwest Laboratory, Richland, Washington.

13. Cubicciotti, D., R. L. Jones, and B. C. Syrett. March 1980. Stress Corrosion Cracking of Zircaloys. EPRI NP-1329, SRI International, Menlo Park, California.

14. Hill, R. 1948. "A Theory of Yielding and Plastic Flow of Anisotropic Metals." In Proceedings of R. Soc. London 193A:281.

15. Hann, C. R., et al. March 1978. Transient Deformation Properties of Zircaloy for LOCA Simulation. EPRI NP-526, Vol. 2, prepared for the Electric Power Research Institute by Battelle, Pacific Northwest Laboratories, Richland, Washington.

16. Guha, R. M., J. L. Head, and J. R. Mathews. 1979. "Analysis of Crack Patterns in Fast Reactor Fuel Pellets." Nuclear Energy 18:39-45.

APPENDIX A

DATA PROCESSING

APPENDIX A

DATA PROCESSING

Two data recording systems were used in the power-ramping experiments. The CALIB system was limited to a maximum of two readings per minute and covered the entire time span of the power-ramping experiments. The data were converted to engineering units by the Halden Project. The FAST-SCAN system had a higher sampling frequency (capable of 30 readings per minute), but the data collection interval included primarily the reactor ramp, the ^{3}He depressurization ramp, and the first hour of the peak-power holding period. The 8-h hold and power descension were also sampled on the FAST-SCAN system for Rods R3, AC11, and ACP27. This system stored only digital signals to be converted to engineering units at PNL.

The objective was to obtain the average linear heat generation rates (ALHR) as a function of the cobalt neutron detector signal (NDCO). The CALIB data allowed calculation of ALHRs from the vanadium neutron detector (NDV) signals and a NDCO signal while the FAST-SCAN system provided only a NDCO signal for rod power. Using the cobalt detector was preferred because of its essentially instantaneous signal. Vanadium detectors have an inherent ~5-min delay time. To obtain correct LHGRs, three calculations were made: 1) correction of NDV signals for delay time, 2) calculation of ALHRs from corrected NDV values, and 3) development of a correlation between ALHR and NDCO, which was then applied to both data collection systems to obtain ALHRs from the NDCO signals.

CORRECTION FOR NDV DELAY TIME

For each time step, a corrected time was determined by adding the delay time to the current time. The corrected NDV value was obtained by interpolating between the data points that bracketed the corrected time. This value was associated with the current time to obtain the delay time correction.

CALCULATION OF ALHR FROM NDV SIGNAL

The power-ramping rig had six NDVs and one central NDCO (see Figure A.1). Four of the NDVs were in a coplanar array at the midpoint of the fuel. The other two NDVs were above and below one of the coplanar vanadium detectors. ALHRs were calculated from the corrected NDV signals according to the equation:

$$\mathrm{ALHR}_i = \left(\frac{\mathrm{KG}_i}{\mathrm{AL}_i}\right)\left(\frac{\mathrm{ND}_j + \mathrm{ND}_k}{2}\right) \cdot \overline{\mathrm{ND}} \cdot \mathrm{HE}$$

where ALHR_i = average linear heat generation rate of rod i (kW/m)

KG_i = factor for conversion from NDV signal to power (kW/m) for rod i

AL_i = axial length of the fuel column of rod i

ND_j, ND_k = signals from nearest vanadium detectors in planar array

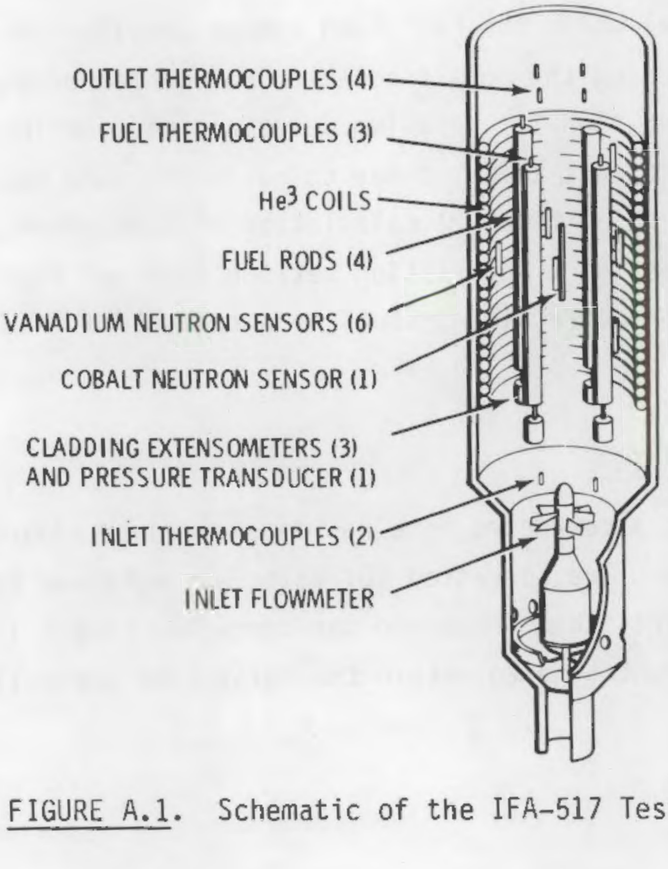

FIGURE A.1. Schematic of the IFA-517 Test Rig

$\overline{ND}$ = ratio of average axial NDV values to the ND_2

HE = a correction factor to account for the flux difference between the fuel rod and the NDV due to ^{3}He in the coils = 1.04 with ^{3}He and 1.00 without ^{3}He.

The KG factor can be calculated from the following equation;

$$KG_i = (KG_{517.1})\left(\frac{4\ M_i}{M_{517.1}}\right)(R_{1/4})\ (CD_i)\ (HF_i)$$

where $KG_{517.1}$ = a conversion factor from NDV signal to power (kW/nA); calculated for IFA-517.1 from a heat balance with four rods in rig = 0.796 kW/nA

M_i = corrected mass of fuel in test rod i (see Reference 6 for a discussion of the effect of a central hole on LHGR)

$M_{517.1}$ = mass of fuel in IFA-517.1 experiment = 1.484 kg

$R_{1/4}$ = fraction of power available for a single rod compared with a four-rod test rig = 0.267

CD_i = depletion constant for each test rod; ratio of fissile fuel remaining to initial fissile fuel

HF_i = hole factor i to account for the effect of thermocouple holes in fuel and center hole in annular fuel for rod i = 0.9596.

CORRELATION BETWEEN ALHR AND NDCO

ALHRs were plotted versus NDCO signals to develop a correlation as a function of ^{3}He pressure. Linear fits were obtained for two cases: 1) full ^{3}He pressurization and 2) no ^{3}He in the coils. Using these correlations, an equation was developed to calculate ALHR from NDCO signals as a function of normalized ^{3}He pressure for both data collection systems.

$$ALHR = [A - (A - B)NP](NDCO - C)$$

where A = slope of ALHR versus NDCO without ^{3}He

B = slope of ALHR versus NDCO with ^{3}He

C = residual current in detector at zero power, ~0.6 for most tests

NP = normalized pressure in ^{3}He coils, p/40 atm.

The above correlation could not be applied to the data for Rod R1 because the ^{3}He pressure signal was inadvertently omitted from the FAST-SCAN data set. Instead, the normalized pressure signal was replaced with a normalized time signal over the time range of the ^{3}He depressurization ramp, which did not introduce a significant error because the ^{3}He pressure drop was very close to being linear with time.

To complete the data processing, the FAST-SCAN data were spliced with the CALIB data to obtain a single data set that was applicable to the entire time span for each power-ramp test.

APPENDIX B

EVALUATION OF ELONGATION SENSOR LIFTOFF

APPENDIX B

EVALUATION OF ELONGATION SENSOR LIFTOFF

The elongation sensors in the bottom end plugs of the fuel rods were designed to perform two functions: 1) provide an elongation signal during testing and 2) provide an instantaneous signal in the event of a cladding breach. The latter function was provided by attaching the linear variable differential transformer (LVDT) magnetic core to a bellows that would collapse if the reactor coolant pressure entered the fuel rod. The pressure at which each bellows would start to collapse, i.e., the liftoff pressure, was measured for each sensor prior to fuel rod fabrication. If the fission gas release from the fuel in each test rod was high enough, the resultant internal rod pressure could also exceed the liftoff pressure. Thus, the indicated signal would not be a true elongation signal but a combination of an elongation signal and an internal fuel rod pressure signal. To properly interpret the elongation behavior during any particular test, it was necessary to determine if the liftoff pressure was exceeded.

During the fabrication of the elongation sensors, the bellows were first sealed with 1.01 MPa (10 atm) of helium at 20°C and then compressed slightly before being tack-welded. A characteristic exterior pressure was then required to initiate bellows collapse. This liftoff pressure ($P_{LO/20}$) was measured by the Institutt for Energiteknikk (IFE) for each sensor. If the differential pressure between the rod liftoff pressure and the internal pressure in the bellows is assumed to be the same at room temperature as it is for the sensor operating at 240°C during the test, the liftoff pressure at 240°C can be determined as follows:

$$P_{LO/240} = P_{LO/20} - P_{B/20} + P_{B/240}$$

where $P_{LO/240}$ = the liftoff pressure at 240°C

$P_{B/20}$ = the internal bellows pressure at 20°C = 1.01 MPa

$P_{B/240}$ = the pressure in the bellows at 240°C

$$= \left(\frac{273 + 240}{293}\right)(1.01) = 1.78 \text{ MPa.}$$

Table B.1 lists the measured liftoff pressures at 20°C and the calculated liftoff pressures at 240°C for the test rods discussed in this report. The following sections describe whether $P_{LO/240}$ was exceeded during testing for each fuel rod. Different methods are used for estimating whether $P_{LO/240}$ was exceeded depending upon the available data. Table B.2 summarizes the results of this analysis and indicates the region of valid elongation data for each ramped rod with an elongation sensor.

TABLE B.1. Liftoff Pressures for FPIP Fuel Rods with Elongation Sensors

Rod Number	Liftoff Pressure, MPa $P_{LO/20}$	 $P_{LO/240}$
R1	1.80	2.56
R2	1.35	2.11
R3	1.49	2.25
A6	1.38	2.14
AC9	1.60	2.36
AC11	1.40	2.16
ACP27	1.25	2.01
S40	1.85	2.61
S41	1.85	2.61

TABLE B.2. Results of Sensor Liftoff Analysis

Rod Number	Liftoff	Valid Elongation Signal Range
R1	No	Entire test
R2	Yes	Up to 3.5 h into test; below 56 kW/m - descent
R3	Yes	Up to 25 kW/m - ascent
A6	Yes	Up to 5.5 h into test; below 50 kW/m - descent
AC9	No	Entire test
AC11	Yes	Below 48 kW/m - ascent; below 4 kW/m - descent
ACP27	Yes	Below 58 kW/m - ascent; below 48 kW/m - descent
S40	No	Entire test
S41	No	Entire test

REFERENCE RODS R1, R2, AND R3

The reference rods contained an initial pressure of 0.10 MPa of helium. Rod R3 (the reference rod with the highest burnup) definitely experienced liftoff of the elongation sensor during the ramp test (see text Figure 5) and even during the latter portion of its steady-state irradiation.(12) Adequate fission gas was released during the ramp test to prevent reseating of the sensor at the zero-power/240°C-coolant condition. Using the average of the void volumes measured for Rods R1 and R2 and a fission gas generation value of 31 cm^3(STP)/MWd and setting the zero-power/240°C-pressure equal to the liftoff pressure, this lack of reseat in Rod R3 corresponds to a minimum fission gas release fraction of 0.52 and 92% fission gas in the rod gas.

For Rod R1 (the reference rod with the lowest burnup), a different method (compared to Rod AC9) of estimating whether the elongation sensor lifted off is needed because there was no sibling reference rod with a pressure sensor. The method selected involves assuming that the liftoff pressure was reached and then determining if the gas temperature required to reach this pressure was reasonable for the rod. For Rod R1, the final measured pressure during post-irradiation examination (PIE) was 0.463 MPa at 0°C, the measured void volume was 7.70 cm^3, and the liftoff pressure was 2.56 MPa at 240°C. The sum of the original upper and lower plenum volumes, which operated at 240°C, was 4.25 cm^3. If the volumetric average fuel temperature at the peak ramping LHGR was ~1200°C and the coefficient of expansion for the fuel is 1×10^{-5}, the fuel volume changed by ~1.4 cm^3. If one-third of this volume change reduced the plenum volume, two-thirds reduced the gap/dish/crack volume (which would operate at an average gas temperature of T_p) and the thermal expansion of the Zircaloy is neglected, then

$$2.56 = \left(\frac{4.25 - 0.47}{7.70 - 1.40}\right)\left(\frac{2.73 + 240}{273}\right)(0.463) + \left(\frac{3.45 - 0.93}{7.70 - 1.40}\right)\left(\frac{273 + T_p}{273}\right)(0.463)$$

and $T_p = 2736$°C.

This average gas temperature would require all the gas not in the plenum regions to be at or near the peak fuel temperature. Residual gas in the fuel-cladding gap and in fuel cracks would be at considerably lower temperatures. Therefore, it is not possible for the gas to be at 2736°C, and the assumption that the at-power pressure in the rod was equivalent to the liftoff pressure must be in error. Hence, the pressure did not reach the liftoff pressure. This conclusion is supported by the fact that there was no downward inflection in the elongation versus time curve (see text Figure 3) as was observed in Rod A6. A similar calculation for Rod AC9 yielded an average gas temperature of 1413°C for the gas that was not in the plenum regions. This value is quite reasonable for annular fuel, where a substantial volume of gas is at the peak fuel temperature; and it lends credibility to the calculational technique. All the data for the Rod R1 ramp test are valid elongation data.

Reference Rod R2 was ramped to the highest power, had the highest measured fission gas release, and had a burnup level between Rods R1 and R3. The calculated liftoff pressure was 2.11 MPa; the lowest of the reference rods. Using the method used above for Rod R1, the calculated average gas temperature in the portion of the gas volume that was not in the plenum was 952°C. Given the formation of a small central void in Rod R2 (where gas temperatures would be high), the 952°C temperature is relatively low. Taking this low gas temperature and the downward inflection of the elongation versus time curve at about 3 h into the peak-power hold (see text Figure 4), the pressure in Rod R2 is adjudged to have slightly exceeded the liftoff pressure during the ramp test. All data on the power ramp and up to the point of inflection and probably below ~66 kW/m on the power descension, where there is an upward inflection in the elongation versus LHGR curve, are valid elongation data.

ANNULAR ROD A6

Rod A6 was initially fabricated with a helium pressure level of 0.10 MPa. The fission gas release fractions from ramped Rods A6 and AC10 were identical at equivalent burnup; thus, the fuel temperature and peak pressure in Rod A6 were probably similar to those in Rod AC10 even though the ramping LHGR in Rod A6 was lower by ~3 kW/m. The sensor signal versus time for Rod A6 shows a downward inflection at ~5.5 h into the ramp (see text Figure 6), as would be expected if liftoff occurred. The peak pressure in Rod AC10 (and presumably in Rod A6) was determined to be in the range from 2.2 to 2.3 MPa (see next section). The calculated liftoff pressure for the sensor in Rod A6 is 2.14 MPa. Thus, all evidence points to liftoff having occurred in Rod A6 during the latter part of the ramp test. The elongation signal was valid throughout the first portion of the ramp test and most of the power descent.

ANNULAR-COATED RODS AC9 AND AC11

Rods AC9 and AC11 were also fabricated with a helium pressurization of 0.10 MPa. Because of the large gas volume in the central hole, the operating pressure in these rods was very sensitive to the power level.

The liftoff pressure in Rod AC11 (the annular-coated rod with the highest burnup) was definitely exceeded during the power-ramp test as evidenced by the large negative elongation indication during the power-holding period (see text Figure 8) and the return to the free cladding expansion line at ~4 kW/m during the power descent. The latter is interpreted to be the bellows reseating, i.e., reaching $P_{LO/240}$. Ignoring the small pressure increase caused by operation at 4 kW/m, the pressure in the rod at 240°C and zero power equals 2.16 MPa, which corresponds to a pressure of 1.15 MPa at STP. Using a fission gas production value of 31.0 cm^3 (STP)/MWd and the void volumes that were measured in Rods AC9 and AC10 during PIE (~10.6 cm^3), the calculated fission gas volume that was released from the fuel in Rod AC11 is 112 cm^3, which corresponds to a fission gas release fraction of 0.71 and a fission gas content in the rod gas of 91%. The calculated release fraction is larger than those observed during the ramping of rods with annular fuel at ~11 MWd/kgM (0.71 versus 0.42 to 0.46) (see Section 4.3.7).

Rods AC9 and AC10 experienced similar steady-state power histories; therefore, it can be assumed that the pressure conditions in both rods were similar prior to the power-ramp tests. Rod AC10 was power-ramped to a slightly higher LGHR than Rod AC9 (69 kW/m versus 67 kW/m) and had a slightly higher fission gas release (0.46 versus 0.42). Therefore, the peak pressures in Rod AC9 were probably lower than in Rod AC10 during the ramp test. The pressure transducer in Rod AC10 bottomed out while at the peak power due to fission gas release (see text Figure 12); however, linear extrapolation of data taken during the power descent indicates that the peak pressure in Rod AC10 was in the range from 2.2 to 2.3 MPa at a linear heat generation rate (LHGR) of 69 kW/m. The peak pressure during the ramping of Rod AC9 would be expected to be less than 2.2 MPa, and the calculated liftoff pressure for Rod AC9 was 2.36 MPa. Thus, the calculated pressure in Rod AC9 was less than the calculated liftoff pressure. In addition, there was no inflection in the sensor signal versus time for Rod AC9 that would indicate that the sensor lifted (see text Figure 7); thus, the signal is indicative of only an elongation signal.

ANNULAR-COATED-PRESSURIZED ROD ACP27

Rod ACP27 was initially pressurized with 0.45 MPa of helium. The liftoff pressure for the elongation sensor in Rod ACP27 (2.01 MPa) was the lowest of all rods that were ramped. During the last power ascension during the steady-state irradiation of sibling Rod ACP28, the pressure increased from 1.0 to

1.4 MPa with a power increase from 0 to 38 kW/m. The linearly projected pressure due just to the increase in power/temperature at the ramping power would therefore be ~1.7 MPa for Rod ACP27. Noting that annular-coated Rod AC10 had a measured pressure increase due to fission gas release during the power ascension of 0.7 MPa in going from just 55 to 65 kW/m (see text Figure 12), the sum of the power/temperature effect and fission gas release would be expected to have caused liftoff of the elongation sensor in Rod ACP27 at ~60 kW/m. The inflection in the elongation versus LHGR curve for Rod ACP27 at ~58 kW/m (see text Figure 9) is therefore attributed to liftoff. The elongation signals for Rod ACP27 are valid up to 58 kW/m during the ascension and below 48 kW/m on the power descension.

SPHERE-PAC RODS S40 AND S41

The sphere-pac rods were initially fabricated with a helium pressurization level of 0.45 MPa at room temperature. Two methods were used to estimate whether the liftoff pressure was exceeded in the sphere-pac rods. The first method estimated the volumetric average gas temperature in the fueled region, as used above for Rods R2 and R3. The result was a average temperature of 1200°C. Assuming a peak centerline fuel temperature during the ramp in excess of 2300°C, the volumetric average gas temperature would be expected to be in excess of 1400°C. Therefore, the first method would indicate that liftoff did not occur in the sphere-pac rods.

In the second method, the measured amounts of fission gas in ramped Rod S41 and nonramped Rod S42 and the slope of the pressure versus LGHR in Rod S42 at two burnup levels were used to estimate the pressure at the ramping power in Rod S41. If both rods are assumed to have released the same amount of gas during the steady-state irradiation, the final pressure at the end of the steady-state irradiation at 240°C in Rod S41 is estimated to be:

$$P_{240/ss} = P_{240/I} + \frac{(F_R)(V_G)(T_c + 273)}{(V_R)(T_{fab})}$$

$$= 0.90 \text{ MPa}$$

where $P_{240/ss}$ = the pressure at 240°C at the end of the steady-state irradiation

$P_{240/I}$ = the initial pressure at the start of the irradiation at 240°C = 0.84 MPa

F_R = measured fractional fission gas release in S42 at the end of the steady-state irradiation = 0.04

V_G = volume of fission gas generated at end of the irradiation at STP = 70.4 cm^3

T_c = coolant temperature = 240°C

V_R = measured total gas volume in S42 at the end of the irradiation = 8.2 cm^3

T_{fab} = temperature of gas at fabrication = 293K.

The slopes of the pressure versus LHGR curves for Rod S41 at zero burnup and the end-of-irradiation burnup were 0.0066 and 0.00737 MPa per kW/m, respectively. If these slopes are then plotted versus the pressure at 240°C at the two burnup levels and if the resultant curve is linearly extrapolated to the estimated pressure at 240°C at the end of the ramp test, the operating temperature dependency while at power at the end of the ramp test can be estimated. The equation for the slope versus pressure is:

$$\text{slope} = -3.2 \times 10^{-3} + 0.0117(P_{240})$$

The slope computed for the temperature dependency of the pressure after the ramp is 0.0126 MPa per kW/m. If the pressure at 240°C after the ramp test ($P_{240/R}$) is determined in the same way as the pressure after steady-state irradiation for Rod S41 (with F_R = 0.34 and V_R = 8.15 cm^3), $P_{240/R}$ = 1.35 MPa. Thus, the pressure at power at the end of the 8-h hold, P_p, is estimated to be:

$$P_p = P_{240/R} + (0.0126)(\text{LHGR}) = 2.24 \text{ MPa}$$

where the LHGR is 70.9 kW/m.

Because the liftoff pressure at 240°C for both sphere-pac rods was 2.61 MPa, both methods indicate that the elongation sensors in the sphere-pac did not lift off and that the measured signal was actually an elongation signal throughout both ramp tests.

DOE/ET/34215-29
PNL-4337
UC-78

DISTRIBUTION

No. of
Copies

OFFSITE

6 Martin Langsam
DOE Contracting Officer
9800 S. Cass Avenue
Argonne, IL 60439

Dr. P. M. Lang
Office of Light Water Reactors
U.S. Department of Energy
Mail Stop B-107
Washington, DC 20545

Mr. A. S. Mehner
Office of Light Water Reactors
U.S. Department of Energy
Mail Stop B-107
Washington, DC 20545

183 DOE Technical Information Center

Mr. Howard L. Sobel
Section Head, Nuclear Materials
and Fuel Management Section
American Electric Power Service
Corporation
2 Broadway
New York, NY 10004

Mr. Benjamin L. Dow, Jr.
Arkansas Power and Light Company
P.O. Box 551
Little Rock, AR 72203

Mr. J. Barclay Andrews, II
Nuclear Power Generation
Division
Babcock & Wilcox Company
P.O. Box 1260
Lynchburg, VA 24505

No. of
Copies

Mr. Thomas A. Coleman
Nuclear Power Generation
Division
Babcock & Wilcox Company
P.O. Box 1260
Lynchburg, VA 24505

Dr. U. Decher
Combustion Engineering, Inc.
1000 Prospect Hill Road
P.O. Box 500
Windsor, CT 06095

Mr. R. N. Duncan
Combustion Engineering, Inc.
1000 Prospect Hill Road
P.O. Box 500
Windsor, CT 06095

Dr. D. O'Boyle
Commonwealth Edison Company
P.O. Box 767
Chicago, IL 60690

Dr. Min L. Lee
Chief Nuclear Engineer
Consolidated Edison Company
of New York, Inc.
4 Irving Place
New York, NY 10003

Dr. F. W. Buckman
Consumers Power Company
1945 W. Parnell Rd.
Jackson, MI 49201

Mr. D. B. Wehmeyer
Detroit Edison Company
2000 Second Avenue
Detroit, MI 48226

No. of
Copies

Mr. J. D. Kortheuer
Duke Power Company
P.O. Box 33189
Charlotte, NC 28242

Mr. Philip E. MacDonald
EG&G Idaho, Inc.
P.O. Box 1625
Idaho Falls, ID 83415

Dr. David Franklin
Electric Power Research
Institute
P.O. Box 10412
Palo Alto, CA 94303

Dr. J.T.A. Roberts
Electric Power Research
Institute
P.O. Box 10412
Palo Alto, CA 94303

Mr. J. R. Tomonto
Florida Power & Light Company
P.O. Box 013100
Miami, FL 33101

Dr. S. Armijo
Nuclear Energy Division
General Electric Company
175 Curtner Avenue
San Jose, CA 95125

Dr. H. W. Schadler, Manager
Metallurgy Laboratory
General Electric Company
Research and Development Center
P.O. Box 8
Schenectady, NY 12301

Mr. Gordon Bond
GPU Service Corp.
260 Cherry Hill Road
Parsippany, NJ 07054

No. of
Copies

Mr. D. J. Groetch
Manager, Advanced Development
Activity
Knolls Atomic Power Laboratory
Box 1072, F3, 12
Schenectady, NY 12301

Mr. William J. Tunney
Long Island Lighting Company
175 E. Old Country Road
Hicksville, NY 11801

Mr. R. G. Ballinger
Massachusetts Institute of
Technology
Room 8139
77 Massachussetts Avenue
Cambridge, MA 02139

Professor Michael Driscoll
Massachusetts Institute of
Technology, NW 13-201
77 Massachusetts Avenue
Cambridge, MA 02139

Mr. Charles Tyrone
Mississippi Power & Light
P.O. Box 1640
Jackson, MS 39205

Mr. S. W. Wilczek, Jr.
Niagara Mohawk Power Corporation
300 Erie Boulevard West
Syracuse, NY 13202

Mr. Roger O. Anderson
Northern States Power, G08
414 Nicollet Mall
Minneapolis, MN 55401

Mr. Dennis Coleman
Nuclear Associates International
6003 Executive Boulevard
Rockville, MD 20852

No. of
Copies

Mr. Peter A. Aucoin
Nuclear Assurance Corporation
24 Executive Park West
Atlanta, GA 30329

Dr. Joseph K. Gasper
Manager, Reactor and Computer
Technical Services
Omaha Public Power District
1623 Harney
Omaha, NE 68102

Mr. G. F. Daebeler
Philadelphia Electric Company
2301 Market Street
P.O. Box 8699
Philadelphia, PA 19101

Mr. Richard R. O'Laughlin
Nuclear Fuel Manager
Public Service Company of
Indiana
1000 East Main Street
Plainfield, IN 46168

Mr. B. H. Koske
Energy Conversion Engineer
Public Service Company of
New Mexico
P.O. Box 2267
Albuquerque, NM 87103

Mr. Kashmiri L. Mahna
Public Service Electric
and Gas Company
P.O. Box 570, Room 3347
Newark, NJ 07101

Professor A. Sesonske
School of Engineering
Purdue University
West Lafayette, IN 47907

Mr. John Hallam
Manager, Computer Engineering
Quadrex Corporation
1700 Dell Avenue
Campbell, CA 95008

No. of
Copies

Mr. Daniel D. Whitney
Sacramento Municipal Utility
District
6201 S. Street
P.O. Box 15830
Sacramento, CA 95813

Professor A. K. Miller
Department of Materials Science
and Engineering
Stanford University
Stanford, CA 94305

Mr. Philip D. Brown
Nuclear Engineer
Fuel Cycle Services
Tennessee Valley Authority
409 Krystal Building
Chattanooga, TN 37401

Mr. Ralph O. Meyer
Core Performance Branch
U.S. Nuclear Regulatory
Commission
MS P-1114
Washington, DC 20555

Mr. Melvin Silberberg
Chief, Fuel Behavior Branch
U.S. Nuclear Regulatory
Commission
MS 1130SS
Washington, DC 20555

Mr. David Dziadosz
Virginia Electric and
Power Company
Post Office Box 26666
Richmond, VA 23261

Mr. R. S. Miller
Nuclear Fuel Division
Westinghouse Electric
Corporation
P.O. Box 3912
Pittsburgh, PA 15230

No. of
Copies

Dr. Elwyn Roberts
Manager, Irradiation Testing
Westinghouse Electric
Corporation
P.O. Box 355
Pittsburgh, PA 15230

Dr. J. C. Turnage
Yankee Atomic Electric Company
20 Turnpike Road
Westborough, MA 01581

ONSITE

DOE Richland Operations Office

H. E. Ransom

26 Exxon Nuclear Company, Inc.

S. J. Beard
G. J. Busselman
M. H. Campbell
C. E. Crouthamel
O. L. Kruger
K. R. Merckx
J. N. Morgan
J. F. Patterson
N. Kjaer-Pederson
G. L. Ritter
G. A. Sofer
L. Van Swam
R. K. Welty

No. of
Copies

Exxon Nuclear Company, Inc. (contd)

H. E. Williamson
K. N. Woods (10)
Records File
Library

Washington Public Power Supply System

D. L. Larkin

26 Pacific Northwest Laboratory

W. J. Bailey
J. O. Barner (5)
C. E. Beyer
L. R. Bunnell
M. E. Cunningham
S. K. Edler
M. D. Freshley
R. J. Guenther
C. R. Hann
P. E. Hart
D. D. Lanning
C. L. Mohr
F. E. Panisko
R. D. Widrig
R. E. Williford
Publishing Coordination YO(2)
Technical Information (5)